Strengthening mechanisms associated to anisotropic precipitates in an Al-Li-Cu alloy of third generation

Thomas Dorin

To cite this version:

Thomas Dorin. Strengthening mechanisms associated to anisotropic precipitates in an Al-Li-Cu alloy of third generation. Materials. Université de Grenoble, 2013. English. NNT : 2013GRENI031 . tel-01200540

HAL Id: tel-01200540
https://theses.hal.science/tel-01200540

Submitted on 16 Sep 2015

HAL is a multi-disciplinary open access archive for the deposit and dissemination of scientific research documents, whether they are published or not. The documents may come from teaching and research institutions in France or abroad, or from public or private research centers.

L'archive ouverte pluridisciplinaire **HAL**, est destinée au dépôt et à la diffusion de documents scientifiques de niveau recherche, publiés ou non, émanant des établissements d'enseignement et de recherche français ou étrangers, des laboratoires publics ou privés.

UNIVERSITÉ DE GRENOBLE

THÈSE

Pour obtenir le grade de

DOCTEUR DE L'UNIVERSITÉ DE GRENOBLE

Spécialité : **Matériaux, Mécanique, Génie civil, Electrochimie (2MGE)**

Arrêté ministériel : 7 août 2006

Présentée par

Thomas Dorin

Thèse dirigée par **Alexis Deschamps** et
codirigée par **Frédéric De Geuser**

préparée au sein du **Laboratoire des Sciences et Ingénierie des Matériaux et des Procédés**
dans **l'École Doctorale Ingénierie – Matériaux Mécanique Energétique Environnement Procédés Production (I-MEP2)**

Microstructure et mécanismes de durcissements associés à la phase T_1 dans un alliage Al-Li-Cu de troisième génération

Thèse soutenue publiquement le **26 novembre 2013**,
devant le jury composé de :

Dr. Joël Douin
Directeur de recherche au CEMES, Toulouse (Président)
Pr. Michel Perez
Professeur à l'INSA de Lyon (Rapporteur)
Pr. Christopher Hutchinson
Associate professor à l'université Monash, Australie (Rapporteur)
Pr. Alexis Deschamps
Professeur à Grenoble INP (Directeur de thèse)
Dr. Frédéric De Geuser
Chargé de recherche au SIMAP (Co-encadrant)
Dr. Christophe Sigli
Ingénieur de recherche à Constellium (Encadrant industriel)
Pr. Aude Simar
Professeure à l'université catholique de Louvain, Belgique (Examinatrice)
Pr. Pierre Guyot
Collaborateur bénévole au SIMAP (Invité)

Remerciements

Ces trois années de thèse ont été jalonnées d'un grand nombre de rencontres. Avant d'entrer dans le vif du sujet, je vais maintenant remercier les personnes sans qui je ne serais pas arrivé au bout de ce travail.

Tout d'abord, je tiens à remercier sincèrement mes trois encadrants de thèse : Alexis, Frédéric et Christophe. Merci pour votre disponibilité permanente au cours de ces trois années. Je remercie en particulier Alexis et Frédéric pour m'avoir transmis leur passion de la recherche. Vous m'avez appris la rigueur et la motivation indispensables pour mener à bien un projet de recherche. Je vous remercie aussi pour des moments de partage plus informels. Par exemple, la tradition du café du matin avec Fred et d'autres thésards, je pense en particulier à Quentin, Laurent, Eva et Rosen.

Merci Christophe pour ces moments enrichissants partagés au cours de différents séminaires européens. Je me rappelle notamment d'un restaurant à Aachen où nous avons partagé un bon plât de moules! Enfin, un grand merci à mon directeur de thèse, Alexis, et plus particulièrement pour l'accueil que tu m'as réservé au sein de ta famille à mon arrivée à Melbourne. Je me souviendrai toujours de ces bons moments partagés au cours de ces 3 mois passés en Australie. Je me remémore souvent cette fois où tu m'as sauvé la vie (au sens littéral du terme) quand j'ai fait une chute d'une dizaine de mètre sur une falaise magnifique des Arapiles. Ces 3 mois passés en Australie ont été très enrichissant d'un point de vue personnel et professionnel. De plus, ce séjour a été l'occasion de rencontrer Chris Hutchinson grâce à qui je vais pouvoir retourner en Australie pour un post-doc.

Je souhaite aussi remercier les membres de mon jury de thèse. Le président Joël Douin, les rapporteurs Michel Pérez et Christopher Hutchinson, l'examinatrice Aude Simar et enfin Pierre Guyot en tant qu'invité. Merci à tous d'avoir été présent pour ma soutenance et merci pour les discussions animées qui ont suivies ma présentation. Je tiens à remercier Pierre pour l'intérêt qu'il a porté à mon travail de thèse et pour les discussions que nous avons menées ensemble.

Je vais maintenant remercier les différentes personnes que j'ai pu côtoyer au sein du laboratoire SIMAP et en premier lieu les permanents de l'équipe PM : Marie qui m'a accepté dans son bureau pendant la majeure partie de ma thèse. Merci pour ta joie et ta bonne humeur permanente qui ont toujours rendues mes journées au laboratoire très agréables, puis dans le désordre Frédo, Gilles, François, Fabien, Bruno, Jean-Louis, Marc V. & D.B., Guillaume B & P, Yves, Joël, Patricia, Catherine, Muriel, Mireille, Raphaël, Christelle. Merci à tous pour m'avoir assisté dans mon travail ou tout simplement pour avoir partagé de bons moments ensemble autour d'un café ou d'une part de gâteau. Je tiens aussi à remercier nos secrétaires Virginie, Nathalie (pour ses bons gâteaux !!) et Sanie, sans oublier l'équipe de techniciens pour leur disponibilité et leur expertise technique toujours nécessaire : Magali, Alain, Stéphane, Colin, Bruno et Roman. Enfin merci à toute l'équipe du CMTC : Florence, Frédéric, Stéphane, Francine, Joëlle, Rachel, Graziella…

Il me reste à remercier toute l'équipe des non-permanents : Merci pour tous les bons moments que nous avons pu partager ensemble au sein ou à l'extérieur du laboratoire ! Je suis bien sûr obligé de mentionner les pauses de midi et ces parties de tarots endiablées ! Pour ceux qui ne le savent pas encore, l'apprentissage du tarot est nécessaire à tout thésard entrant dans le groupe PM. Vous pouvez notamment demander à Eva et à Rosen qui en ont fait les frais ! Parmi les taroteurs, il y a ceux qui sont partis vers d'autres horizons : Guilhem, Jean-Jean, Quentin, Jean, Coraly (je serais bientôt à classer dans cette catégorie). Et ceux grâce à qui la tradition perdurera : Laurent, Nico, Eva, Rosen, Simon, Maxime, Fanny, Audrey, Ismaël… Merci aussi à Romain, Natasha, Sinh, Men Yang, Quinquang, Kitti, Benjamin, Mahmoud, Souad, Hassan, Aymen, Bassem, Mohamed…

Avant de terminer, je tiens à remercier les personnes avec qui j'ai pu travailler en dehors du laboratoire SIMAP et tout particulièrement Williams Lefebvre du laboratoire GPM de Rouen pour m'avoir accueillis et consacré du temps. Merci aussi à Matthew Weyland de l'université Monash (Australie) et à Noël Brunetière de l'université de Poitiers.

Et pour finir, merci à ma famille pour m'avoir toujours soutenu et pour continuer à le faire ! Si je suis arrivé jusque là c'est en grande partie grâce à vous…et surtout, je remercie chaleureusement ma compagne, Kate, pour avoir été présente à mes côtés dans les bons comme dans les mauvais moments. Merci d'avoir cru suffisamment en notre couple pour venir t'installer en France et nous voilà maintenant reparti ensemble vers de nouvelles aventures au pays des kangourous.

Le mot de la fin sera pour ma Mamie, qui s'est éteinte quelques jours avant ma soutenance de thèse. Je tiens tout particulièrement à te remercier pour avoir été présente à mes côtés depuis ma petite enfance et pour m'avoir donné la force de donner le meilleur de moi-même le jour de la soutenance… Cela aura été ta dernière leçon…

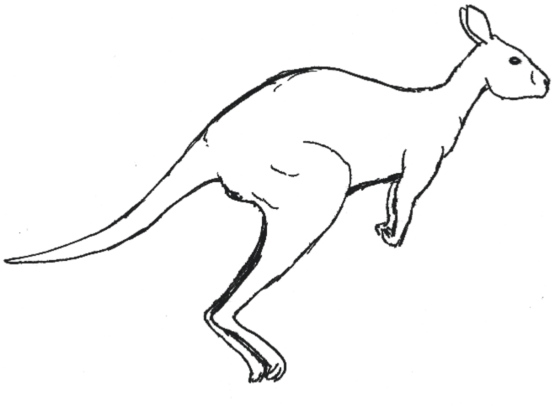

Résumé étendu

Motivations

Ce chapitre résume, en Français, le document de thèse qui est écrit en anglais. Chaque chapitre est résumé de manière à faire ressortir les principaux résultats et conclusions importantes. Le choix d'effectuer la rédaction du manuscrit entièrement en anglais a été motivé par différentes raisons. Tout d'abord, les chapitres centraux de la thèse ont été écrits sous formes d'articles et il nous a donc semblé cohérent d'écrire l'ensemble de la thèse en anglais pour assurer une continuité au manuscrit. Ensuite, la thèse a été effectuée dans le cadre d'un contrat CIFRE avec Constellium qui favorise la publication en anglais pour une diffusion du travail à un niveau international. Enfin, un des rapporteurs du jury de thèse qui est un spécialiste dans le domaine provient d'un pays anglophone.

Plan

1. Introduction

1.1 Contexte industriel

L'évolution des matériaux utilisés dans le domaine de l'aéronautique se fait de manière à diminuer la consommation en carburant tout en réduisant l'impact environnemental. Les dernières générations d'alliages Al-Li-Cu ont une combinaison optimale de propriétés telles qu'une faible densité, une bonne limite d'élasticité et ténacité et offrent une stabilité de ces propriétés dans le temps. Ces solutions répondent aux challenges actuels des manufacturiers de l'aéronautique et sont donc une solution de choix pour ces industriels. Cette étude porte sur un alliage de ce type et qui est proposé par Constellium : l'alliage AA2198.

1.2 Objectifs

Les alliages appartenant à la famille des Al-Li-Cu sont durcis grâce à la formation de la phase T_1-Al_2LiCu. La phase T_1 précipite sous forme de plaquettes dans les plans {111} de la matrice CFC de l'aluminium. Les objectifs de ce travail de thèse sont les suivants :

- Mettre en place une procédure de caractérisation de la phase T_1
- Explorer un grand nombre de microstructures et de limites d'élasticité
- Tester et améliorer les modèles de limite d'élasticité existants
- Comprendre les mécanismes de durcissement associés à la phase T_1 et leur influence sur les phénomènes de plasticité

1.3 Présentation du manuscrit

Le manuscrit de thèse est rédigé entièrement en anglais et les principaux chapitres de la thèse sont écrits sous forme d'articles. Le premier chapitre est une étude bibliographique générale permettant de replacer l'étude dans son contexte global. Des états de l'art plus spécifiques sont effectués dans les articles inclus dans chaque chapitre. Le deuxième chapitre permet de présenter le matériau étudié ainsi que les techniques de caractérisation qui ont été utilisées au cours de ce travail. Les trois chapitres suivants représentent le cœur du travail et ont été rédigés sous forme d'articles. Le troisième chapitre permet d'expliquer la mise en place d'une stratégie de caractérisation adaptée à la phase T_1. Une étude systématique de la microstructure sur une large combinaison de paramètres et de la limite d'élasticité résultante est ensuite explorée dans le quatrième chapitre afin de comprendre le lien entre la microstructure de la phase T_1 et la limite d'élasticité. Les modèles d'élasticité de la littérature sont ensuite testés sur la base de nos mesures expérimentales pour être ensuite améliorés de manière à modéliser l'incrément de limite d'élasticité lié à la phase T_1 de manière la plus physiquement correcte possible. Le cinquième chapitre décrit l'étude des mécanismes de durcissement liés à la phase T_1 en termes d'interactions dislocation/précipité ainsi que le lien entre précipitation et phénomènes de plasticité. Une discussion est effectuée dans chaque chapitre mais une discussion plus générale est conduite à la fin du manuscrit de manière à conclure sur l'ensemble du travail réalisé.

2. Principaux résultats

2.1 Chapitre I : Revue bibliographique

Ce chapitre permet tout d'abord de replacer l'étude dans son contexte général. Les différentes classes d'alliages d'aluminium sont décrites avec une attention particulière portée aux alliages à durcissement structural de la série 2XXX qui sont au cœur de cette étude.

2.1.1 Contexte général

Les alliages à durcissement structural et plus particulièrement les alliages de la série 2XXX ont été utilisés abondamment dans l'industrie aéronautique depuis le début du 20ème siècle [1]. Le phénomène de durcissement structural dans les alliages d'aluminium a été découvert au début du 20ème siècle et est maintenant abondamment utilisé dans l'industrie [2]. Le phénomène de durcissement apparait pendant un revenu à basse température (en général entre 100°C et 250°C). Les alliages de la famille Al-Cu-Li permettent un gain important en poids tout en conservant des bonnes propriétés mécaniques et ont donc été progressivement introduits dans le domaine de l'aéronautique [3,4]. Il y a eu principalement trois générations d'alliages Al-Cu-Li avec une diminution du rapport Li/Cu (voir Figure 1). La troisième génération d'alliage a une composition en Li typiquement comprise entre 0.75wt% et 1.8wt% [5].

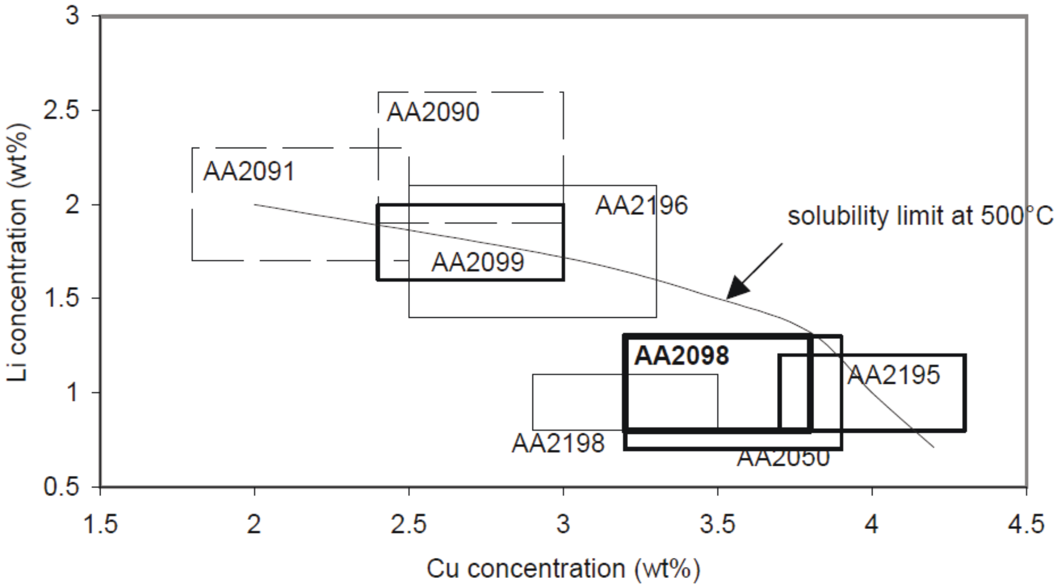

Figure 1: Evolution des compositions d'alliages entre la deuxième et la troisième génération d'alliages Al-Li-Cu. (extrait de Warner [5])

2.1.2 Précipitation durcissante dans les Al-Cu-Li

Les phases présentes dans les alliages d'aluminium sont généralement divisées en trois groupes : les intermétalliques, les dispersoides et les précipités. Le phénomène de durcissement qui apparait pendant le traitement de revenu se fait grâce à la formation de précipités de taille nanométrique. Une bonne compréhension des phénomènes de précipitations intervenant dans ces alliages est donc décisive.

Dans l'alliage AA2198, les précipités pouvant se former proviennent principalement des systèmes binaires Al-Cu (GP-zones, θ'', θ' et Ω) et Al-Li (δ') et des systèmes ternaires Al-Cu-Mg (GPB-zones, S'/S) et Al-Cu-Li (T_1,T_B) [6,7]. Toutefois, la formation de la phase T_1–Al_2LiCu qui germe sur les dislocations, se fait de manière prédominante si l'alliage est suffisamment pré-déformé [8]. La structure de la phase T_1 est hexagonale et a été récemment établie dans deux études séparées par Donnadieu et al. [9] et Dwyer et al. [10].

Un des buts premiers de ce travail de thèse est de comprendre le lien entre la microstructure de la phase T_1 et l'incrément de limite d'élasticité. Si on considère la morphologie de la phase T_1, les paramètres importants sont les suivants : la densité, le diamètre et l'épaisseur des plaquettes ainsi que la fraction volumique en précipités. La variation des paramètres du traitement thermomécanique (tel que la pré-déformation [11,12], la température [13,14] ou la durée de traitement [15]) est utilisée comme un outil puissant permettant de faire varier les différents paramètres de la phase T_1 de manière indépendante.

2.1.3 Contributions au durcissement et modélisation de la limite élasticité

Le durcissement d'un métal est induit par la présence d'obstacles au mouvement des dislocations. Les obstacles qui sont généralement considérés sont les suivants : les autres dislocations, les précipités, les joints de grains et la solution solide. Dans le cas des alliages d'aluminium à durcissement structural, la principale contribution au durcissement est apportée par la présence de précipités. Lorsque une dislocation interagit avec un précipité, elle peut soit le cisailler soit le contourner (voir Figure 2). Dans le cas des précipités sphériques une transition cisaillement/contournement, quand les précipités atteignent une taille critique, correspond généralement au pic de dureté du matériau. Les modèles de limite d'élasticité sont bien définis dans le cas d'une distribution de précipités quasi-sphériques. La Figure 3 montre l'évolution de la limite d'élasticité en fonction du rayon moyen des précipités. La limite d'élasticité augmente dans un premier temps proportionnellement à $\sqrt{f_v R}$ et décroit par la suite en fonction de $\sqrt{f_v}/_R$.

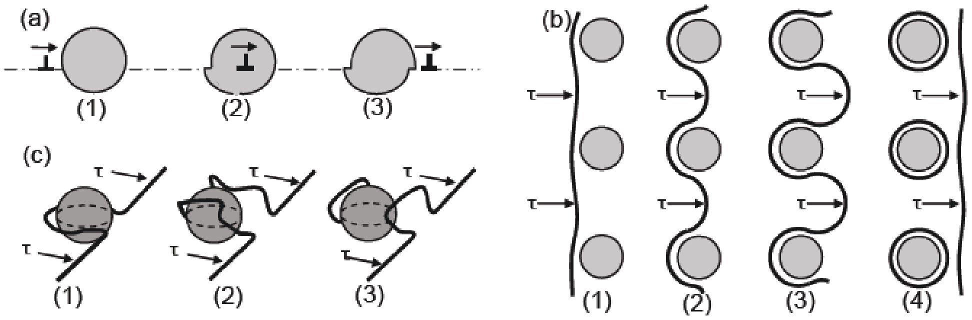

Figure 2: Schéma montrant les trois principaux mécanismes d'interaction dislocation/précipité [16].

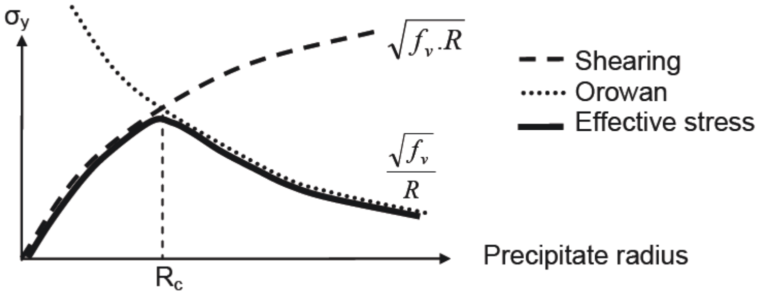

Figure 3: figure montrant l'évolution de limite d'élasticité en fonction du rayon des précipités dans le cas d'une distribution de précipités sphériques (extrait de Fribourg [17]).

Dans le cas des alliages Al-Cu-Li, les précipités T_1 ont une forme de plaquettes. Deux modèles ont d'abord été proposés dans la littérature [18,19] pour modéliser l'incrément de limite d'élasticité induit par les précipités T_1. Ces modèles sont basés sur le mécanisme de contournement. Cependant les précipités T_1 sont maintenant connus comme étant cisaillables (Figure 4), et la pertinence de ces premiers modèles est donc remise en question. Un troisième modèle, basé sur le mécanisme de cisaillement a été proposé par la suite par Nie et Muddle [20]. Ce modèle prend en compte la création d'une interface supplémentaire entre le précipité et la matrice au cours du mécanisme de cisaillement :

$$\Delta\tau = \frac{1.211 D {\gamma_i}^{3/2}}{t^2}\sqrt{\frac{b f_v}{\Gamma}} \tag{1}$$

Où t et D sont les épaisseur et diamètre moyens des précipités T_1, γ_i est l'énergie d'interface précipité/matrice, b est le vecteur de Burgers, f_v est la fraction volumique de précipités et Γ est la tension de ligne de dislocation.

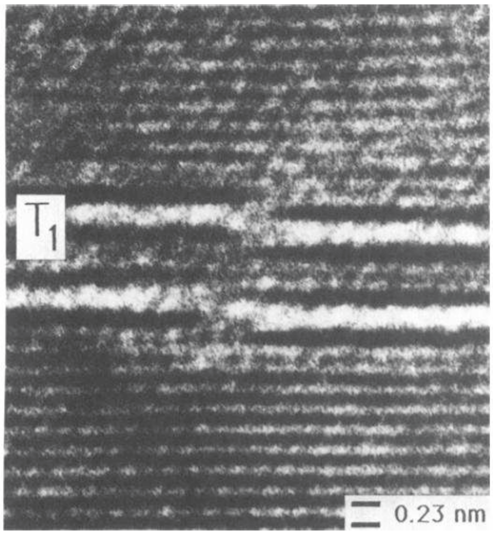

Figure 4: observation en microscopie électronique à haute résolution dans un axe de zone <110> d'un précipité T_1 cisaillé (extrait de Howe et Lee [21]).

2.2 Chapitre II : Matériau et techniques expérimentales

2.2.1 L'alliage AA2198

L'alliage AA2198 appartient à la technologie AIRWARE qui est proposée par Constellium [22]. La composition de l'alliage 2198 est détaillée dans le Tableau 1.

Tableau 1: Composition de l'alliage AA2198 en poids pourcent (données communiquées par Constellium)

AA2198	*Cu*	*Li*	*Mg*	*Ag*	*Zr*	*Al*
Min	2.9	0.8	0.25	0.1	0.04	bal
Max	3.5	1.1	0.8	0.5	0.18	bal

Une série de traitements thermomécaniques est généralement appliquée à l'alliage AA2198 de manière à obtenir les propriétés désirées. Tout d'abord, un premier traitement de coulée est effectué, suivent ensuite un laminage à chaud puis un laminage à froid. Une remise en solution suivie d'une trempe sont ensuite conduites. Une étape de détensionnement permet de relaxer les contraintes internes présentes dans l'alliage à la suite de la trempe. Les traitements de vieillissement (naturel et artificiel) sont les traitements cruciaux qui vont déterminer les propriétés finales de l'alliage. Un traitement thermomécanique typique est présenté sur la Figure 5.

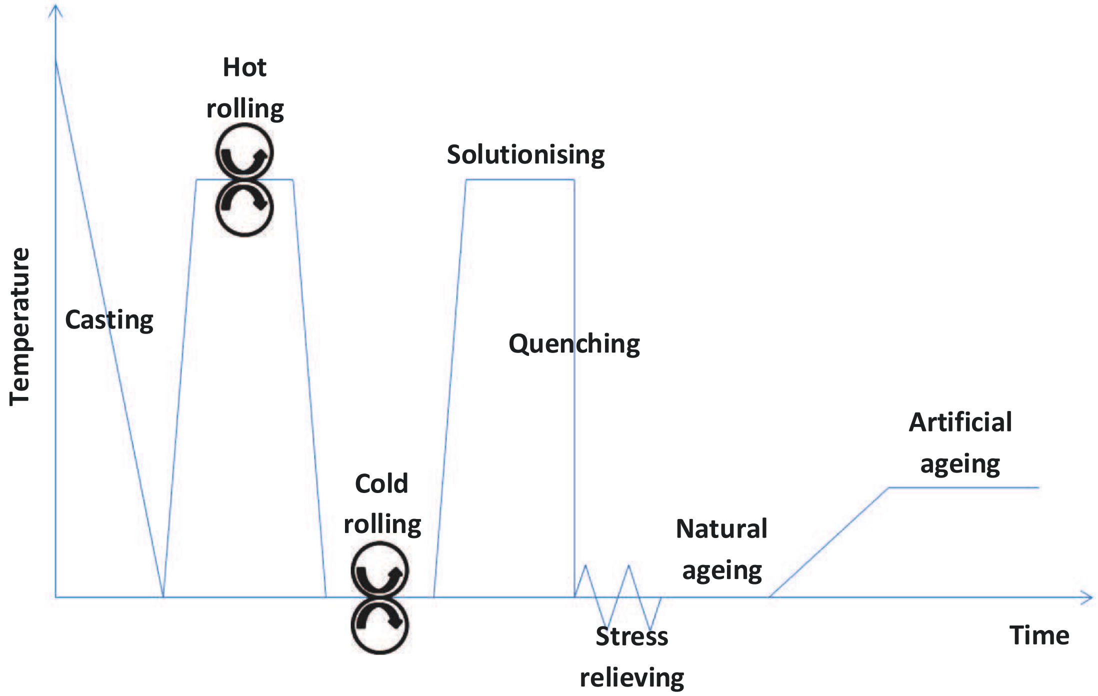

Figure 5 : Schéma du procédé thermomécanique industriel pour les alliages de la série 2xxx.

2.2.2 Méthodes expérimentales

Les principales techniques expérimentales utilisées pendant la thèse sont les suivantes : microscopie électronique en transmission conventionnelle (TEM) et à champ sombre annulaire à grands angles (HAADF) ; calorimétrie différentielle à balayage (DSC) ; diffusion des rayons X aux petits angles (SAXS ;. microscopie optique en contraste Nomarski ; microscopie confocale à balayage ; essais de traction et essais Bauschinger. Le principe des techniques, la préparation des échantillons ainsi que le traitement des données sont présentés dans ce chapitre.

2.3 Chapitre III : Mise en place d'une procédure de caractérisation de la phase T_1

Le but de ce chapitre est de mettre en place une procédure complète de caractérisation de la phase T_1 dans l'alliage AA2198 en termes de morphologie (diamètre et épaisseur) et en terme de fraction volumique au cours d'un revenu en température bi-palier (18h à 155°C et ensuite 190°C). La diffusion des rayons X aux petits angles (SAXS) est utilisée pour extraire l'évolution du diamètre moyen et de l'épaisseur moyenne des précipités de manière in-situ. La méthode qui est utilisée pour extraire le diamètre et l'épaisseur est extraite d'un travail récent par De Geuser et al. [23]. La microscopie électronique en transmission est utilisée pour calibrer l'évolution de diamètre qui est obtenue en SAXS.

La calorimétrie différentielle à balayage (DSC) est utilisée dans cette étude pour estimer la fraction volumique de précipités. Un flux de chaleur obtenu en DSC, à partir d'un échantillon ne contenant initialement pas de précipités, est présenté sur la Figure 6a. Les pics exothermiques et endothermiques qui sont présents sur le signal de DSC sont dus respectivement à la formation et la dissolution de phases. Avant de pouvoir effectuer des mesures quantitatives, il est nécessaire de bien comprendre les transformations de phase qui interviennent au cours de la rampe. Afin de mettre en évidence ces transformations, nous avons reproduit la même rampe en température en SAXS in-situ de manière à corréler l'apparition des pics avec la formation ou la dissolution de phases connues. Des images SAXS au cours de la rampe sont présentées sur la Figure 7. L'évolution de l'épaisseur des plaquettes au cours de la rampe est présentée en parallèle au flux de chaleur de DSC sur la Figure 6b. La succession des deux principaux pics exothermiques (B et C sur la Figure 6a) est associée à la précipitation puis à l'épaississement de la phase T_1.

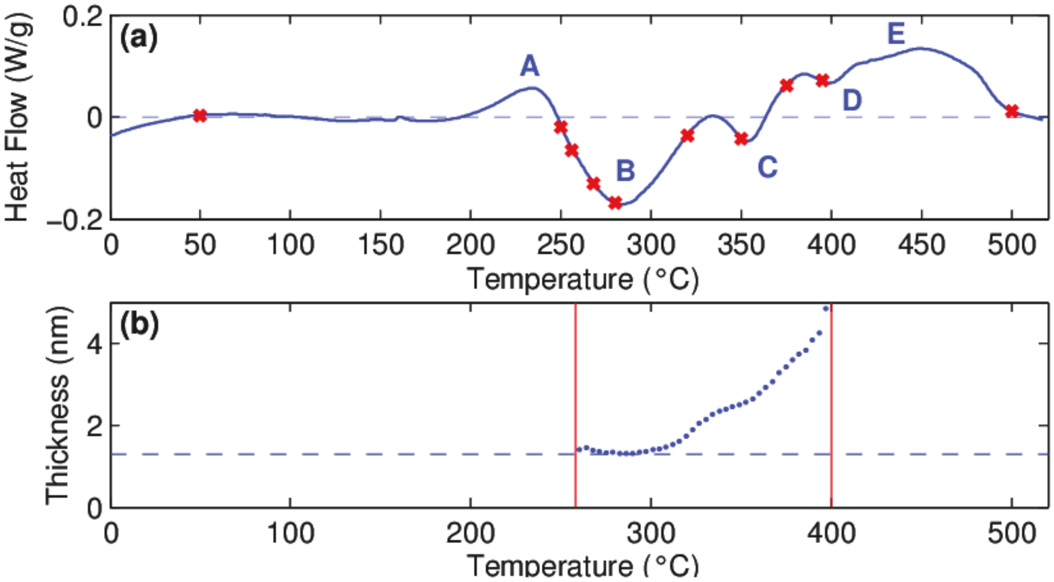

Figure 6: (a) flux de chaleur enregistré au cours d'une rampe de DSC de 50K/min de 0°C à 520°C à partir d'un échantillon ne contenant pas de précipités et (b) évolution de l'épaisseur moyenne des précipités T_1 au cours de la même rampe température effectuée in-situ en SAXS.

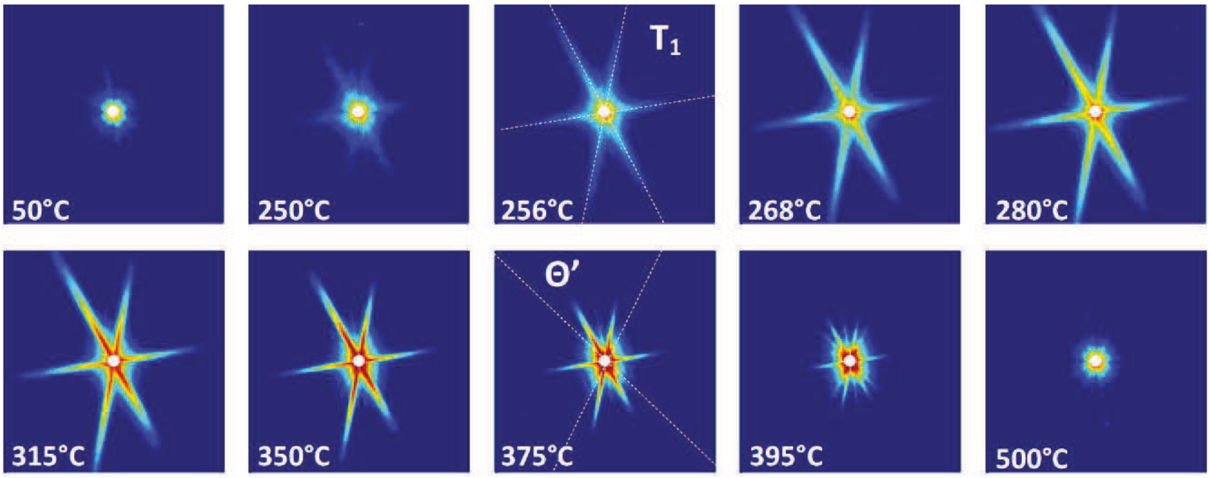

Figure 7: images SAXS extraites au cours d'une rampe à 50K/min de 50°C à 500°C à partir d'un échantillon ne contenant pas de précipités.

Les observations précédentes ont permis de mettre en évidence que les réactions se passant au cours de la rampe de DSC incluent presque exclusivement la phase T_1. Par conséquent, la fraction volumique de précipités en présence dans l'échantillon avant la rampe de DSC est proportionnelle à l'intégrale globale du flux de chaleur de DSC. L'évolution de la fraction volumique est ensuite calibrée grâce à des observations en HAADF-STEM.

La densité numérique de précipités peut ensuite être déduite à partir des évolutions de diamètre, épaisseur et fraction volumique:

$$N \propto \frac{4 * f_v}{\pi * t * D^2} \tag{2}$$

Où N est la densité numérique de précipités. Les évolutions de l'ensemble des paramètres caractéristiques de la phase T_1 pendant le revenu bi-palier sont représentées sur la Figure 8.

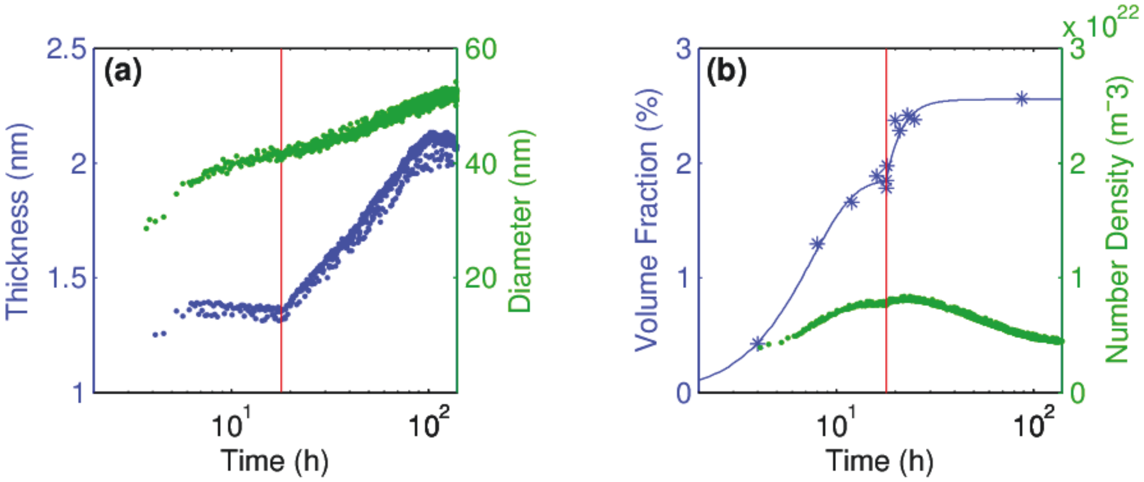

Figure 8: Evolutions des paramètres caractéristiques de la phase T_1 au cours d'un revenu bi-palier (18h à 155°C et 190°C) (a) évolution du diamètre et de l'épaisseur des T_1 (en nm) et (b) évolution de la fraction volumique (en %) et de la densité numérique de précipités (en m^{-3}).

2.4 Chapitre IV : Quantification et modélisation du lien entre microstructure et limite d’élasticité.

Dans ce chapitre, une étude du lien entre microstructure et limite d’élasticité est effectuée. La stratégie utilisée consiste à faire varier les paramètres du traitement thermomécanique (pré-déformation, température et durée du traitement) de manière à faire varier les paramètres de la microstructure des précipités T_1 (diamètre, épaisseur et fraction volumique). L’évolution de la limite d’élasticité au cours des traitements thermomécaniques effectués, est systématiquement mesurée.

2.4.1 Création d’une base de données expérimentale

La variation de la pré-déformation permet de faire varier la densité de sites de germination disponibles pour la phase T_1 car cette phase germe sur les dislocations. Le contrôle de la pré-déformation permet de faire varier la densité numérique ainsi que le diamètre moyen des précipités. Les cinétiques de précipitation à 155°C ont été suivies en SAXS in-situ pour 3 pré-déformations : 0.5%, 2.5% et 12%. Des images ont été extraites à des temps caractéristiques pendant le revenu permettant de mettre en évidence les différences de cinétique d’apparition des T_1 quand le niveau de pré-déformation varie (voir la Figure 9). Pour ces trois pré-déformations, les précipités T_1 se maintiennent à une épaisseur constante (de 1.3nm) qui correspond à la formation de précipités d’une seule maille seulement. Pour activer l’épaississement des plaquettes il est nécessaire d’augmenter la température de traitement et pour cela nous utilisons les résultats obtenus au cours du chapitre précédent avec un traitement bi-palier (voir Figure 8).

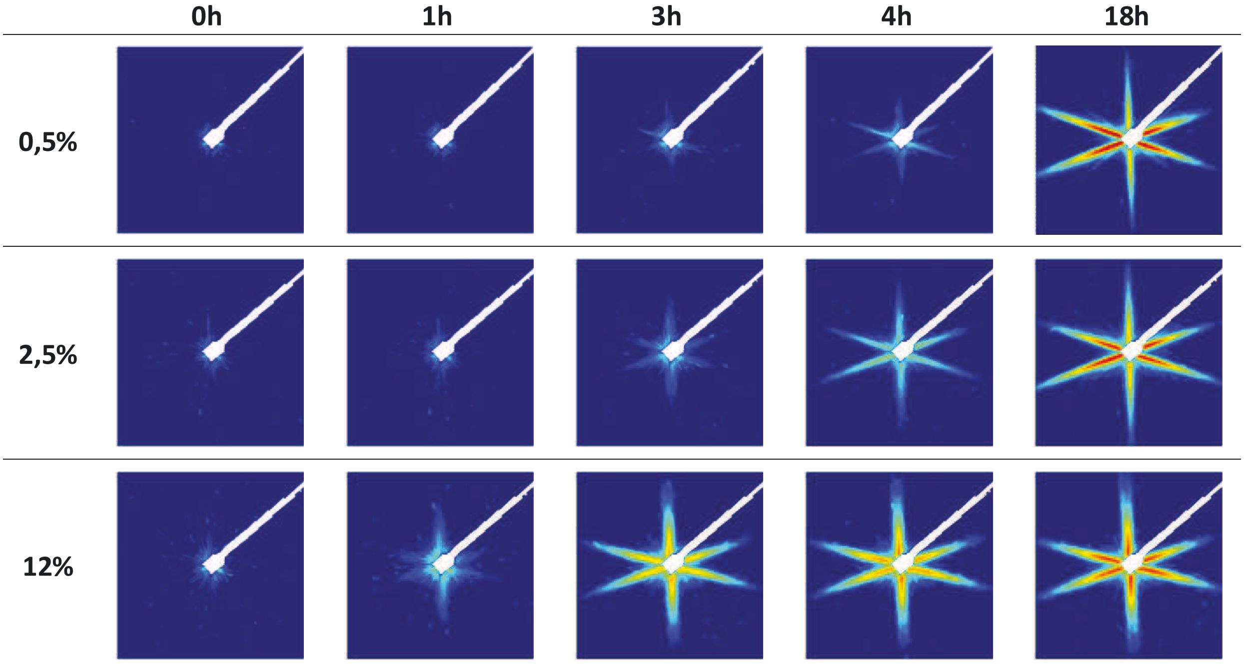

Figure 9: images mesurées en SAXS à différents temps de revenu à 155°C pour les trios pré-déformations suivantes: 0.5%, 2.5% et 12%.

La procédure de caractérisation qui a été mise en place au chapitre précédent nous permet d’extraire les évolutions de tous les paramètres caractéristiques des précipités T_1 permettant ainsi d’enrichir une base de données expérimentales qui pourra être ensuite utilisée pour tester des modèles de limite d’élasticité.

2.4.2 Modèles de limite d'élasticité

Deux modèles de limite d'élasticité basés sur le mécanisme de contournement ont été proposés par Nie et Muddle [18] et Zhu et Starke [19]. La capacité de ces modèles à prédire l'évolution de la limite d'élasticité au cours du traitement bi-palier est évaluée. La Figure 10 montre l'évolution expérimentale de la limite d'élasticité avec les évolutions prédites par les deux modèles. La prédiction par ce type de modèle n'est pas satisfaisante et ne semble donc pas convenir au durcissement par des précipités T_1. En effet, pour pouvoir modéliser correctement la contribution apportée à la limite d'élasticité par les précipités T_1, il est nécessaire de considérer le caractère cisaillable de ces précipités.

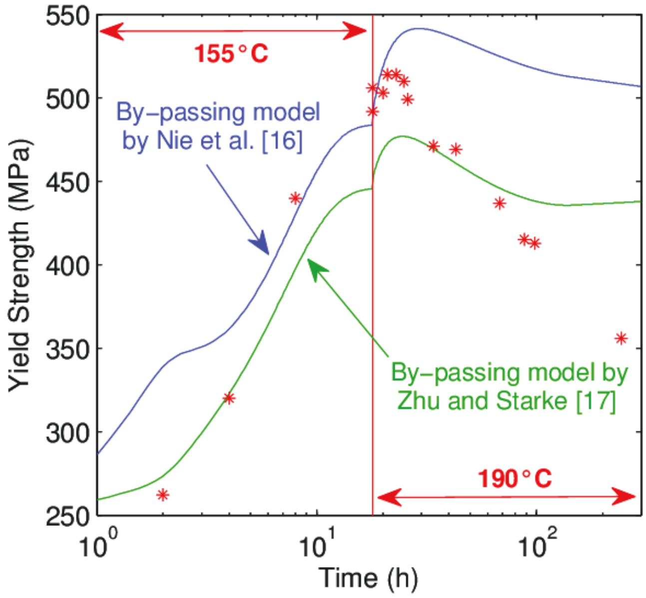

Figure 10: Limite d'élasticité mesurée expérimentalement au cours du traitement bi-palier (symboles), et prédictions obtenues avec les deux modèles basés sur le mécanisme de contournement (courbes).

Nie et Muddle [20] ont ensuite proposé une approche alternative qui prend en compte la création d'une nouvelle interface matrice/précipité au cours du mécanisme de cisaillement (se référer au chapitre I, équation (1)). La Figure 11 montre un schéma du mécanisme de cisaillement.

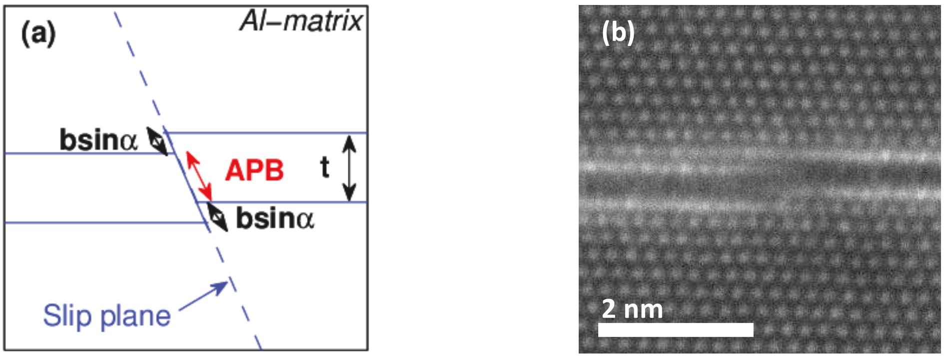

Figure 11: (a) schéma d'une plaquette cisaillée observée debout révélant la création d'une nouvelle interface matrice/précipité et de la création d'une paroi d'antiphase. (b) Image d'un précipité T_1 cisaillé en HAADF-STEM en axe <110>.

Nous proposons d'étendre et de modifier le modèle proposé par Nie et Muddle en incluant la création d'une paroi d'antiphase au cours du mécanisme de cisaillement (comme précisé sur la Figure 11). L'équation modifiée prend en compte l'énergie surfacique d'interface γ_i et l'énergie surfacique de la paroi d'anti-phase γ_{APB} :

$$\Delta\tau_{T1} = \frac{0.762 D \gamma_{eff}^{3/2}}{t^2}\sqrt{\frac{bf_v}{\Gamma}} \tag{3}$$

$$\text{avec}\ \gamma_{eff} = 2\sin(\alpha)\gamma_i + \left(\frac{t}{b\sin(\theta)} - \sin(\alpha)\right)\gamma_{APB}$$

La Figure 12 montre l'évolution expérimentale de la limite d'élasticité au cours du traitement bi-palier ainsi que les évolutions prédites par Nie et Muddle et par le modèle modifié ci-dessus. Dans les deux cas les prédictions sont très proches de l'évolution expérimentale. Cependant notre modèle modifié semble mieux modéliser la transition au pic de limite d'élasticité. Les énergies de surface sont utilisés comme paramètres de fit. Le résultat des fits nous donnent : $\gamma_i = 0.08$ J/m^2 et $\gamma_{APB} = 0.007$ J/m^2.

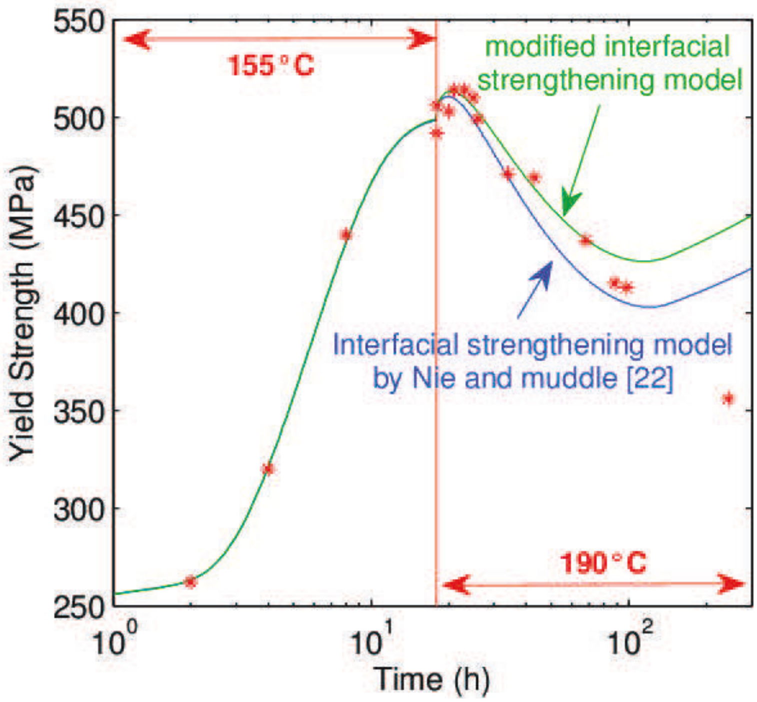

Figure 12: Limite d'élasticité mesurée expérimentalement au cours du traitement bi-palier (symboles), et prédictions obtenus avec les deux modèles prenant en compte le mécanisme de cisaillement (courbes).

La figure ci-dessus montre que la prédiction de la décroissance en limite d'élasticité autour du pic de durcissement est possible en considérant seulement le mécanisme de cisaillement. Par conséquent, il semble que ce mécanisme reste dominant, y compris après la transition. Cependant, on peut remarquer que ces modèles ne permettent pas de prédire les temps très sur-vieillis ce qui laisse penser qu'une transition de mécanisme de durcissement intervient aux temps très longs après le pic de durcissement.

2.5 Chapitre V: Etude des mécanismes de durcissement et phénomènes de plasticité liés à la phase T_1

Dans ce chapitre, l'influence des précipités T_1 sur les phénomènes de plasticité est etudiée. Dans cette optique, les mécanismes d'interaction entre les dislocations et les précipités T_1 sont observés et discutés. Ensuite l'influence de la microstructure de T_1 sur les phénomènes de localisation de la plasticité est étudiée.

2.5.1 Observation en HAADF-STEM

Des observations sont tout d'abord conduites en HAADF-STEM sur un échantillon sur-vieilli 18h à 155°C et 70h à 190°C puis déformé plastiquement 2%. La présence de nombreux précipités T_1 épaissis est alors révélée. La Figure 13 montre un précipité T_1 de deux épaisseurs caractéristiques et cisaillé en trois endroits. Les événements de cisaillement observés sont seulement d'un vecteur de Burgers. Ainsi, il semble qu'il est énergétiquement plus favorable pour une dislocation de cisailler le précipité à un autre endroit plutôt que de le cisailler deux fois au même endroit. Ce mécanisme de cisaillement simple des T_1 évite une localisation catastrophique de la déformation au niveau microscopique comme mis en avant récemment par Deschamps et al. [24].

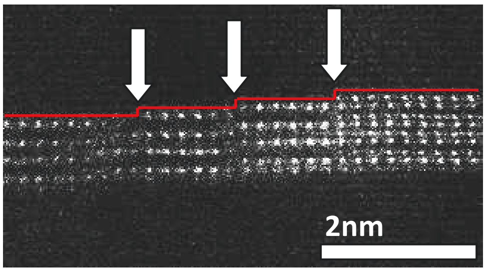

Figure 13: image HAADF-STEM en axe de zone <112> d'un précipité T_1 épais cisaillé sur un échantillon vieilli 18h à 155°C et 70h à 190°C et déformé plastiquement 2%.

2.5.2 Essais mécaniques

Des essais de traction sont tout d'abord conduits sur des échantillons revenus à différents temps au cours d'un traitement bi-palier. Le taux d'écrouissage $\theta = \frac{d\sigma}{d\varepsilon}$, calculé à partir de ces courbes de traction, est tracé en fonction de $\sigma - \sigma_y$ (où σ_y est la imite d'élasticité) sur la Figure 14a. Le taux d'écrouissage initial est estimé par interpolation et tracé en fonction du temps de traitement sur la Figure 14b. L'augmentation du taux d'écrouissage observé est caractéristique d'une transition cisaillement/contournement.

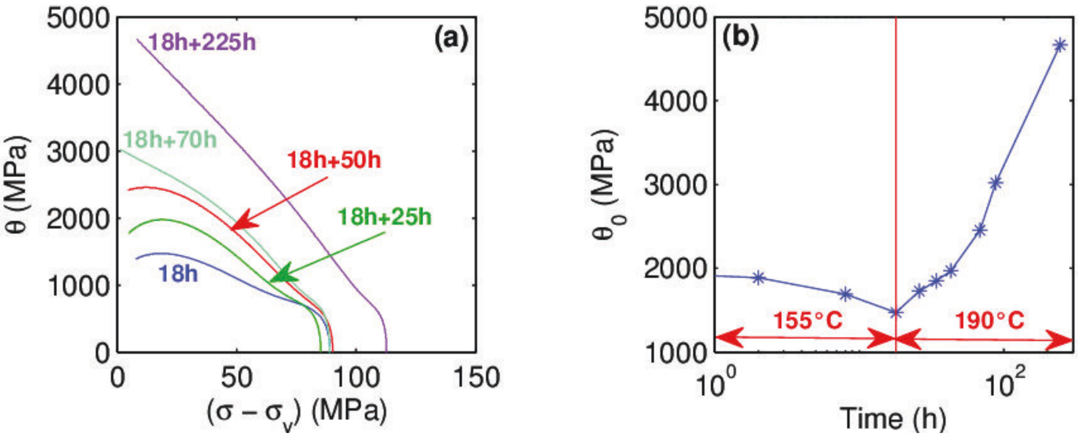

Figure 14: (a) évolution du taux d'écrouissage en fonction du temps de traitement au cours du traitement bi-palier et (b) évolution du taux d'écrouissage initial en fonction du temps de traitement.

2.5.3 Localisation de la plasticité

La localisation de la plasticité dans des bandes de cisaillement est observée en microscopie confocale à balayage sur différents temps de traitement. Une disparition des bandes de cisaillement en fonction du temps de traitement révèle une homogénéisation de la déformation plastique. Une telle homogénéisation est liée à une transition cisaillement/contournement. En effet, l'apparition de boucles de dislocation autour des précipités crée un champ de contrainte important autour des précipités permettant de dévier les dislocations en mouvement et ainsi d'homogénéiser la déformation plastique. La Figure 15 montre deux images prises en microscopie confocale mettant en évidence la disparition des bandes de glissement entre un état revenu 18h à 155°C et un état revenu 18h à 155°C puis 70h à 190°C.

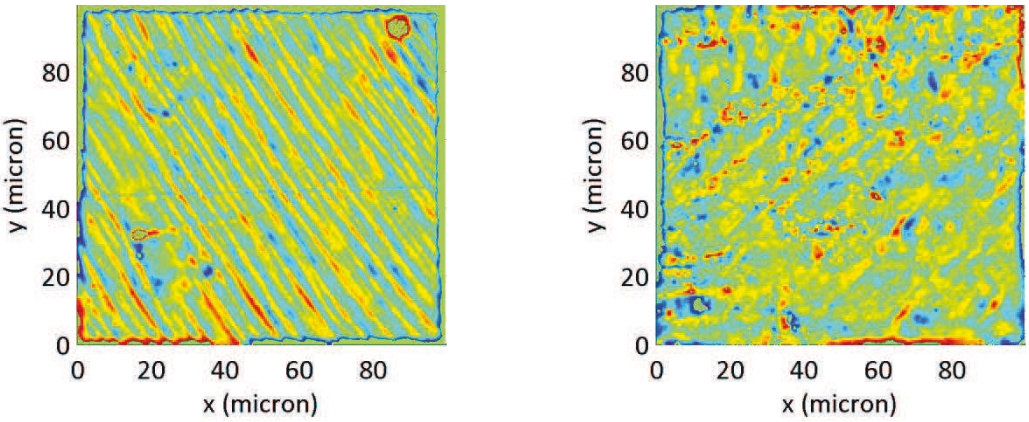

Figure 15: (a) image de bandes de cisaillement sur un état revenue 18h à 155°C et (b) absence de bandes de cisaillement sur un état revenu 18h à 155°C puis 70h à 190°C.

L'ensemble de nos observations semble confirmer qu'une transition cisaillement/contournement intervient dans le cas des précipités T_1 longtemps après le pic de limite d'élasticité. Cette transition semble graduelle avec probablement une combinaison de mécanismes dans la plupart des cas.

3. Bilan général

Ce travail de thèse a permis d'acquérir une meilleure compréhension des phénomènes de durcissement liés à la phase T_1 dans les alliages Al-Li-Cu de dernière génération. Une nouvelle méthode de caractérisation de la phase T_1 a tout d'abord été proposée. Une base de données expérimentale a ensuite pu être générée. Cette base de données a été utilisée pour tester différents modèles de limite d'élasticité proposés dans la littérature. Un modèle énergétique prenant en compte la création d'une nouvelle interface matrice/précipité et d'une paroi d'antiphase, lors du cisaillement, a permis de décrire de manière très précise l'évolution de la limite d'élasticité pour de nombreuses microstructures de T_1. Ce modèle permet notamment de modéliser la transition au pic de durcissement et le début de la décroissance en limite d'élasticité, sans invoquer une transition cisaillement/contournement. Cette transition semble intervenir seulement pour des états fortement sur-vieillis. Le paramètre critique contrôlant cette transition est encore inconnu et des efforts supplémentaires notamment en simulation de type Ab Initio permettraient de mieux comprendre les différentes énergies intervenant lors du cisaillement de T_1.

4. Bibliographie

1. Starke Jr, E. A., Staley, J. T.: Prog. Aerospace Sci. 32, 131-172 (1996)
2. Williams, J. C., Starke Jr, E. A.: Acta Mater. 51, 5775-5799 (2003)
3. Polmear, I. J.: Mat. Trans., 12-31 (1996)
4. Rioja, R. J., Liu, J.: Met. and Mat. Trans. A 43A, 3325-3337 (2012)
5. Warner, T.: Mat. Sci For. 519-521, 1271-1278 (2006)
6. Hardy, H. K., Silcock, J. M.: J.Inst. Met. 84, 423-428 (1955-56)
7. Sainfort, P., Dubost, B.: J. de phys. 48, 407-413 (1987)
8. Decreus, B., Deschamps, A., De Geuser, F., Donnadieu, P., Sigli, C., Weyland, M.: Acta Mater. 61, 2207-2218 (2013)
9. Donnadieu, P., Shao, Y., De Geuser, F., Botton, G. A., Lazar, S., Cheynet, M., de Boissieu, M., Deschamps, A.: Act. Mater. 59, 462-472 (2011)
10. Dwyer, C., Weyland, M., Chang, L. Y., Muddle, B. C.: Appl. Phys. Lett. 98 (2011)
11. Cassada, W., Shiflet, G. J., Starke Jr., E. A.: Met. Trans. A 22A (1991)
12. Gable, B. M., Zhu, A. W., Csontos, A. A., Starke Jr., E. A.: J. of L. Met., 1-14 (2001)
13. Csontos, A. A., Starke Jr, E. A.: Met. and Mat. Trans. A 31A, 1965-1976 (2000)
14. Csontos, E. A., Starke, A. A.: Int. J. of Plast. 21, 1097-1118 (2005)
15. Decreus, B., al: Precipitation evolution in AA2198 and AA2196 Al-Li-Cu alloys. In : PTM 2010 - International Conference on Solid-Solid Phase Transformations, Avignon (2010)
16. Guyot, P.: Phil. Mag. 24(190), 987-993 (1971)
17. Fribourg, G.: Couplages entre précipitation et plasticité dans un alliage d'aluminium 7xxx : application à des traitements thermomécaniques de réduction des distorsions dans des composants aéronautiques. Phd Thesis. Institut Polytechnique de Grenoble, France (2009)
18. Nie, J. F., Muddle, B., Polmear, I. J.: Trans Tech Publ. 217-222, 1257-1262 (1996)
19. Zhu, A. W., Starke, E. A.: Acta Metall. Inc. 47(11), 3262-3269 (1999)
20. Nie, J. F., Muddle, B. C.: J. of Phase eq. 19(6), 543-551 (1998)
21. Howe, J. M., Lee, J., Vasudevan, A. K.: Met. Trans. A 19A, 2911-2920 (1988)
22. Daniélou, A., Ronxin, J. P., Nardin, C., Ehstrom, J. C.: Proceedings of the 13th international conference on aluminium alloys, Pittsburgh, PA: TMS, Warrendale, PA. (2012)
23. De Geuser, F., Bley, F., Deschamps, A.: J. of App. Cryst. 45, 1208-1218 (2012)
24. Deschamps, A., Decreus, B., De Geuser, F., Dorin, T., Weyland, M.: Acta Mater. 61(11), 4010-4021 (2013)

General introduction

Industrial context

One of the greatest discoveries of the 20th century in metallurgy was probably made by Alfred Wilm when exploring the age-hardening ability of Al-Cu alloys. The strength increment arising during a heat treatment is now known to stem from the formation of nano-precipitates. Such heat treatments have now spread to many metallic systems and are industrially used in a wide range of applications from packaging to transportation.

The early generations of cast and wrought Al-alloys were mainly based on the Al-Cu-Mg, Al-Mg-Si and Al-Zn-Mg systems. The addition of Li as a primary alloying element in Al-Cu alloys is more recent. Li significantly reduces the alloys' density while enhancing its modulus. Due to Li's high solubility in Al, it was primarily added in large amounts with the purpose of creating high specific strength (strength/weight) Al-alloys for military aircrafts. However, the early generations of Al-Li-Cu alloys encountered significant drawbacks such as poor toughness and poor property stability, thus limiting their use. Three generations of Al-Li-Cu alloys have been developed with a gradual diminution of the Li/Cu ratio. The current generation contains less than 1.8wt% in Li and less than 5wt% in Cu with minor additions of Mg, Ag and Zr. They are used in both military and commercial airplanes mainly in wing and fuselage skins. The recent progress in Al-Li-Cu alloys has been driven by the apparition of a strong competitor to metals in aerospace, namely composite materials that also provide enhanced solutions to aeroplanes manufacturers. Nowadays, lighter solutions are in demand in order to reduce fuel consumption and the environmental footprint of the aeroplane. New generations of Al-Li-Cu alloys offer an optimal combination of properties such as low density, high strength, good damage tolerance and very long time property stability thus making them a prime choice of material for the current and next generation of aircrafts. The AIRWARE solution is currently proposed by Constellium and addresses the current challenges faced in the aeronautic sector. The main scope of this PhD study is based on one of these alloys, which is provided by the Constellium Vorrepe Research Center, and named hereafter as the AA2198 alloy.

State of the art

• *From the nano-scale to the macro-scale*

The early investigations on age-hardening in Al-alloys were mainly empirical. The impact of many additional alloying elements on the macroscopic mechanical response was evaluated. The understanding of the precipitation phenomenon was enhanced with the development of recent cutting-edge characterisation technologies. In order to develop new Al-alloys solutions, it is critical to understand the mechanisms involved on a nanometre range and their impact on the macroscopic properties.

• *The main contribution to strength in Al-Cu-Li alloys: the T_1 phase*

The strength increment of a material is induced by the obstacles to dislocation motion. Many obstacles can be encountered in Al-alloys such as solute elements, grain boundaries, other dislocations and precipitates. In the last generation of Al-Li-Cu alloys, such as the AA2198 alloy, the main strengthening contribution arises from the precipitation of the T_1-Al_2LiCu phase. The kinetics of precipitation of this phase, as well as the influence of alloy chemistry on the precipitation sequence, has been the subject of a former PhD thesis at SIMAP laboratory in collaboration with Constellium Research Centre. The T_1 phase forms as semi-coherent platelets along the $\{111\}$ planes of the Al FCC structure. The particularity of this phase lies within its strong anisotropy with a high aspect ratio (~ 100). Its thickness is only a few atomic planes and is of the order of 1nm while its diameter can grow up to a few 100 nm. The strong anisotropy of the T_1 phase makes it difficult to characterise accurately and at the beginning of this project a complete characterisation procedure suited to systematic evaluation was not available.

• *Lack of experimental and modelling data on strengthening by anisotropic plate-like precipitates*

The interaction mechanisms between dislocations and the T_1 precipitates is decisive as it controls the related macroscopic strength response of the alloy. The two main strengthening mechanisms that are generally considered when a moving dislocation encounters a precipitate are by-passing and shearing. When a precipitate is by-passed, a loop of dislocation is left around the precipitate and when sheared, the precipitate is cut to the extent of one Burgers' vector. In the case of near-spherical precipitates, a transition from shearing to by-passing generally corresponds to the material's peak strength when the precipitates reach a critical size. In this case, the yield strength models are well established. However, in the case of platelets precipitates such as the T_1 phase, the evolution of the strengthening mechanisms as a function of the precipitates' morphology is less understood. Due to the current lack of understanding and complexity of the strengthening mechanisms involved in the case of platelets precipitates, only a very few attempts of yield strength modelling can be found in the literature. Furthermore, the ability of the existing models to predict the yield strength has been poorly investigated due to a lack of experimental data in terms of the T_1 morphological parameters and volume fraction evolution during an age-hardening treatment.

Thesis Strategy

The main objective of this PhD work is to understand the relationship between the characteristics of the T_1 phase and the yield strength increment. The different steps and tools to achieve this goal are described as follows:

- ***Set-up a characterisation procedure of the T_1 phase***

The first step is to provide a suitable characterisation procedure in order to define, fully and accurately, the T_1 morphology. The important parameters that characterise the T_1 phase are its thickness, diameter, number density and volume fraction. We developed a new strategy that involves a wide range of state-of-the-art characterisation techniques such as Small-Angle-X-Ray-Scattering (SAXS), Conventional and High Angular Annular Dark Field Scanning Transmission Electron Microscopy (CTEM and HAADF-STEM) and Differential Scanning Calorimetry (DSC).

- ***Explore a wide range of T_1 microstructures***

Once a characterisation scheme is clearly established, it becomes possible to explore a wide range of T_1 microstructures. For this purpose we set up a strategy to design the thermo-mechanical treatment as a way of controlling the variation of the T_1 morphological parameters independently. As T_1 precipitates are known to nucleate on dislocations, varying the amount of cold working prior to the age-hardening treatment is a good way to vary the precipitates' density and diameter. The age-hardening temperature is then used in order to control the activation of the precipitate thickening process and thus vary the precipitates' thickness distribution. Finally varying the duration of the age-hardening treatment permits us to manage the completion of precipitation and thus the T_1 volume fraction. The variation of the thermo-mechanical parameters and associated influence on the T_1 microstructural parameters is summed up in Table 1. As a result, varying the thermo-mechanical treatment is an efficient tool to create of a wide range of T_1 microstructures thus resulting in a systematic experimental data base of microstructure / properties relationships.

Thermo-mechanical treatment →	Pre-strain	Temperature	Duration
T_1 microstructure →	Density/Diameter	Thickness	Volume Fraction

Table 1: Thermo-mechanical treatment parameters and associated variations on T_1 microstructural parameters.

- ***Test and improve the existing yield strength models***

A few models have been proposed in the literature to model the yield strength increment in the presence of the T_1 phase. However, the testing of the models remained limited due to a shortage of experimental data. Most of the existing models are adapted from the Orowan yield strength model which is classically used in the case of by-passed spherical precipitates. However, it is recognised that the T_1 phase is shearable when it consists of one unit cell. An alternative energetic approach of the shearing mechanism has been proposed by Nie and Muddle. We propose first testing the existing models and then further developing the existing model, which can be applied to any type of T_1 microstructures.

- ***Understand the strengthening mechanisms in terms of dislocation/precipitate interaction***

The final aim of this work is to fully describe the strengthening mechanisms involved in the presence of T_1 precipitates. Both experimental and modelling results will be used conjointly to depict the interaction mechanisms between dislocations and precipitates. The evolution of the strengthening mechanisms as a function of the precipitates morphology and the impact on the resulting yield strength will also be discussed. Two different approaches can be conducted to investigate the strengthening mechanisms. The direct approach consists in observing the result of an interaction between a dislocation and a precipitate. HAADF-STEM is a powerful technique, which is suited to the observation of shearing events on T_1 precipitates. However, this technique only permits local observations and does not reveal by-passed precipitates. As a consequence, an indirect approach is more powerful in the investigation of the strengthening mechanisms. The interaction mechanisms (by-passing or shearing) are known to have a direct influence on strain hardening and on the localisation of plasticity. As a result, we propose an investigation of the plasticity behaviour as a way of studying the strengthening mechanisms. We will look at the work-hardening behaviour by using both tensile and Bauschinger tests. The localisation of plasticity into slip lines will then also be investigated with Nomarski type observations and the Confocal Laser Scanning Microscopy (CLSM) technique.

Presentation of the manuscript

This manuscript has been written essentially as a collection of successive articles. The first chapter consists of a general literature review aiming to introduce the subject. The second chapter details the materials and experimental procedures used in the thesis. Each of the three main chapters that follow contains at least one article that has been or will be submitted to a peer-reviewed journal (chapters III to V). As a consequence, they contain their own state of the art and associated set of references. Particular care has been taken in order to avoid redundancy between the general literature review proposed in chapter I and each of the individual reviews proposed in the other chapters. A consequence of such a manuscript format is that each of the articles can be taken individually. However, we have aimed to express continuity in between the different chapters and will then bring all the results together in a final discussion and conclusion.

- ***Background and methodology***

The two first chapters give a general framework of the study. A general literature review (chapter I) goes back to the basics of aluminium alloys and their historical use in the aerospace industry. An insight is then given into the precipitates that can be encountered in current Al-Li-Cu alloys. The different contributions to strengthening are also given in this chapter. The second chapter is methodological. Details on the investigated AA2198 alloy and thermo-mechanical treatment conditions are presented. The characterisation techniques are then explained in terms of the principles, set-up, sample preparation, use and data analysis.

- ***Core of the PhD work***

Chapter III details the characterisation procedure employed to extract the T_1 microstructural data using a combination of SAXS, CTEM, HAADF-STEM and DSC. Chapter IV focuses on the understanding of the microstructure/strength relationships by exploring a wide range of T_1 microstructures while recording the yield strength evolution. The yield strength modelling is also included in this chapter. Chapter V contains two articles and focuses on the impact of T_1 precipitation on the plasticity mechanisms. An HAADF-STEM study of the sheared T_1 precipitates was conducted as a part of this PhD; the results were included in a paper by Deschamps et al.. This paper is included as an appendix.

- ***Discussion and conclusion***

This part will bring together all the results in order to discuss and conclude on the general influence of the T_1 precipitates on the strength increment and associated strengthening mechanisms. The improvements and limitations will be explored in order to propose indications for future studies of this system.

- ***Appendix***

The first appendix presents an independent study on the Relationship between the grain texture and the spatial dispersion of hardness during ageing. The second appendix is a recent paper published by Deschamps et al. on the influence of precipitation on plastic deformation of Al-Cu-Li alloys.

Enjoy!

General Content

Chapter I: Literature review

Chapter V: Investigation on the strengthening mechanisms of the T_1 precipitates and influence on the plasticity behaviour 111

Chapter I: Literature review

The main aim of this chapter is to present a literature review in order to show the general context of the study. I will start from generalities on Aluminium alloys and then give an idea of the industrial context and the history of the use of Aluminium alloys in the aerospace industry. An overview will then be given on the precipitates that are usually encountered in industrial Al-Cu-Li alloys. More emphasis will be given to the T_1-phase and the impact of the thermo-mechanical treatments on the precipitation behaviour of this phase will be described. The different contributions to strengthening will then be emphasized in terms of yield strength modelling. More detailed and specific literature review will be included in each chapter of the manuscript.

1. Generalities

1.1 Aluminium Alloys Designation System

Pure Aluminium has extremely poor mechanical properties. Most commonly, the addition of alloying elements combined with the proper thermo-mechanical processing, will confer the desired properties depending on the application. A century of using wrought and cast Aluminium alloys has resulted in a wide range of alloys developed for specific applications, which are narrowed down to eight families depending on their main alloying element. This nomenclature was developed by the Aluminium Association [1] and is called the International Alloy Designation System (IADS) as shown in Table 2. The first digit in the designation number describes the main alloying element; the following digits are used to differentiate all the specific industrial Al-alloys.

Family	Main alloying element
1XXX	None
2XXX	Copper
3XXX	Manganese
4XXX	Silicon
5XXX	Magnesium
6XXX	Magnesium and Silicon
7XXX	Zinc and Magnesium
8XXX	Other alloying elements

Table 2: The eight families of Al-alloys [1]

1.2 Heat-treatable Al-alloys

Al-alloys that experience an increase of their strength during a heat treatment are named heat-treatable Al-alloys. This increase of strength is mainly due to the formation of secondary particles which are called precipitates. The most well known precipitation-hardened Al-alloy is probably the Al-Cu alloy which is hardened by the GP-zone, θ'' and θ'-Al_2Cu precipitates. The classes of alloys which can be considered as heat treatable are the following: 2XXX, 6XXX, 7XXX and 8XXX Al-alloys.

1.3 Temper designation system

Another designation system was soon introduced in the IADS in order to classify the heat treatable Al-alloys series. The temper designation system that is used for most wrought Al-alloys is shown in Table 3. It consists of one letter, which gives the ageing condition and is generally followed by one or more digits that give more precise ageing characteristics of the alloy. The F, O, H, W and T letters stand for respectively, as-fabricated, annealed, cold-worked, solution heat-treated and heat-treated conditions. Classical tempers that are used for 2xxx alloys are T3 when the alloy is solutionized and cold-worked and T8 when the alloy has been solutionized, cold-worked and heat treated to peak strength. Additional digits are sometimes added in order to give more details on the secondary treatments, for instance, the TX51 designation specifies that the cold work has induced a permanent deformation between 0.5 -3% [2].

Suffix letter: F, O, H, T or W indicates basic treatment condition	**First suffix digit indicates secondary treatment used to influence properties**	**Second suffix digit for condition H only indicates residual hardening**
F-As fabricated		
O-Annealed-wrought products only		
H-Cold-worked strain hardened	1-Cold-worked only	2-1/4 hard
	2-Cold-worked and partially annealed	4-1/2 hard
	3-Cold-worked and stabilized	6-3/4 hard
		8-hard
		9-extra hard
W-Solution heat-treated		
T-Heat-treated stable	1-Partial Solution + natural ageing	
	2-Annealed cast products only	
	3-Solution + cold-worked	
	4-Solution + natural ageing	
	5-Artificially aged only	
	6-Solution + artificial ageing	
	7-Solution + stabilizing	
	8-Solution + cold-work + artificial ageing	
	9-Solution + artificial ageing + cold work	

Table 3: Temper designation system for most wrought Aluminium alloys. [3]

2. Aluminium Alloys in the aerospace industry

2.1 History

Aluminium has not always been the prime choice for aircraft designers. In the early ages of airplanes, the structure of the aircraft was mainly made out of wood which was, at the time, the best material for strength/weight ratio (specific strength) [3]. In the early 20th century, precipitation hardening was discovered in Al-Cu alloys. The first use of Aluminium in flying applications suffered serious corrosion issues. It is only when the anodising process was discovered that the poor corrosion resistance of Al-alloys could be overcome. After this, Al-alloys were gradually introduced into the structure of aircrafts and have been the main components in airframes since then. However, the composite materials appeared in the middle of the 20st century and have been increasingly introduced into the aircraft's structure. The use of composites increased exponentially in the 1990s and a decade ago the future of Al-alloys in the aerospace industry was highly uncertain. As a consequence, aluminium manufacturer had to come up with lighter and more reliable Al-alloys and processes. Nowadays, thanks to years of research, new generation of Al-alloys are currently and will remain a competitive choice of materials in the foreseeable future. Improvement in specific strength is no longer the only indicator of improved performance; durability and damage tolerance are examples of determining properties for aerospace applications. Nowadays, the essential characteristics lie in optimising the material but also the manufacturing technologies while reducing the environmental impact [4].

The highest specific strength is given by the 2XXX and 7XXX series Al-alloys, which are dominant as structural materials in the aerospace sector. The improvement of the yield strength for the Al-alloys in the aerospace domain is shown schematically in Figure 1. Today's strongest Al-alloy is the 7055-T7751 which is used for upper wings.

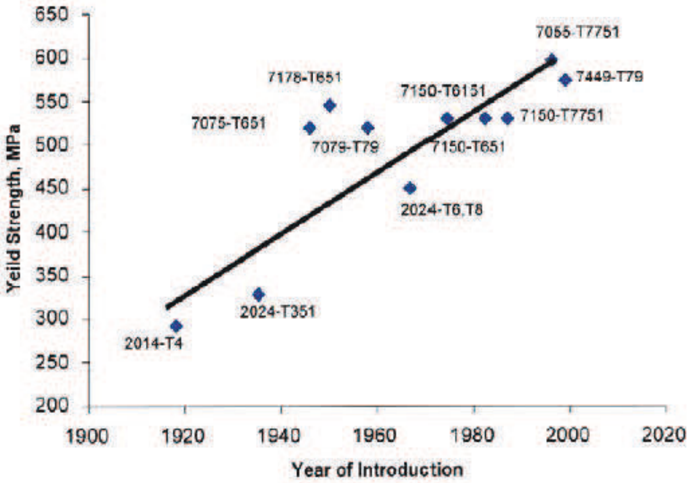

Figure 1: Yield strength of some Al-alloys used in the aerospace industry as a function of the year of introduction (taken from Williams and Starke [4]).

2.2 The Al-Li alloys

In order to achieve a decrease in weight, Al-Li alloys were gradually introduced [5,6]. Indeed, each weight percent of Li added lowers the density of the alloy by approximately 3% while increasing the modulus by approximately 6%. Li can also participate to the formation of hardening precipitates and it imparts higher fatigue crack growth resistance. There has been schematically three generations of the Al-Li alloys, the nominal compositions of the key Al-Li alloys are reported in Table 4. The first Al-Li-Cu alloy was patented by Alcoa in 1945, and the first application was in a military aircraft in 1958. The key feature of the second generation of Al-Li alloys is the Li content which is above 2wt%. These new solutions provided alloys with lower density and higher modulus but also encountered significant drawbacks such as a high anisotropy of the material properties [7,8]. As a consequence, the current third generation of Al-Li alloys represents a compromise with a lower Li content, typically between 0.75 to 1.8wt% and less than 5wt% in Cu. As a result, the Cu/Li ratio is increased compared to the second generation alloys (see Figure 2). This new generation of alloys was primarily launched for military and spatial applications but is currently used in commercial airplanes structure.

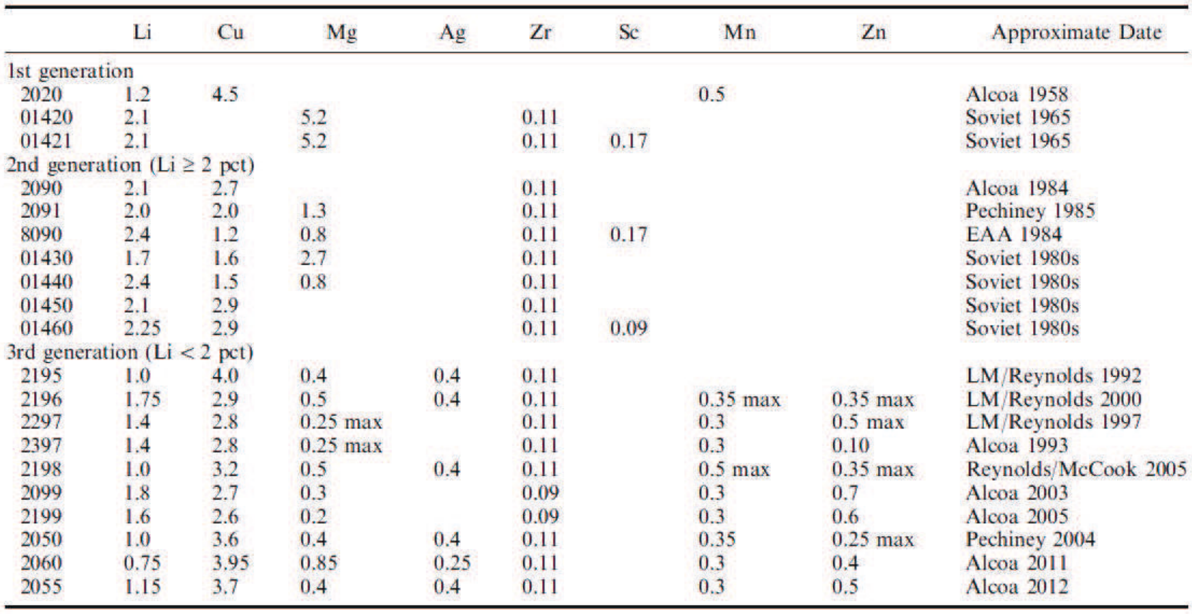

	Li	Cu	Mg	Ag	Zr	Sc	Mn	Zn	Approximate Date
1st generation									
2020	1.2	4.5					0.5		Alcoa 1958
01420	2.1		5.2		0.11				Soviet 1965
01421	2.1		5.2		0.11	0.17			Soviet 1965
2nd generation (Li ≥ 2 pct)									
2090	2.1	2.7			0.11				Alcoa 1984
2091	2.0	2.0	1.3		0.11				Pechiney 1985
8090	2.4	1.2	0.8		0.11	0.17			EAA 1984
01430	1.7	1.6	2.7		0.11				Soviet 1980s
01440	2.4	1.5	0.8		0.11				Soviet 1980s
01450	2.1	2.9			0.11				Soviet 1980s
01460	2.25	2.9			0.11	0.09			Soviet 1980s
3rd generation (Li < 2 pct)									
2195	1.0	4.0	0.4	0.4	0.11				LM/Reynolds 1992
2196	1.75	2.9	0.5	0.4	0.11		0.35 max	0.35 max	LM/Reynolds 2000
2297	1.4	2.8	0.25 max		0.11		0.3	0.5 max	LM/Reynolds 1997
2397	1.4	2.8	0.25 max		0.11		0.3	0.10	Alcoa 1993
2198	1.0	3.2	0.5	0.4	0.11		0.5 max	0.35 max	Reynolds/McCook 2005
2099	1.8	2.7	0.3		0.09		0.3	0.7	Alcoa 2003
2199	1.6	2.6	0.2		0.09		0.3	0.6	Alcoa 2005
2050	1.0	3.6	0.4	0.4	0.11		0.35	0.25 max	Pechiney 2004
2060	0.75	3.95	0.85	0.25	0.11		0.3	0.4	Alcoa 2011
2055	1.15	3.7	0.4	0.4	0.11		0.3	0.5	Alcoa 2012

Table 4: History of the nominal compositions of key Al-Li alloys (taken from Rioja and Liu [5]).

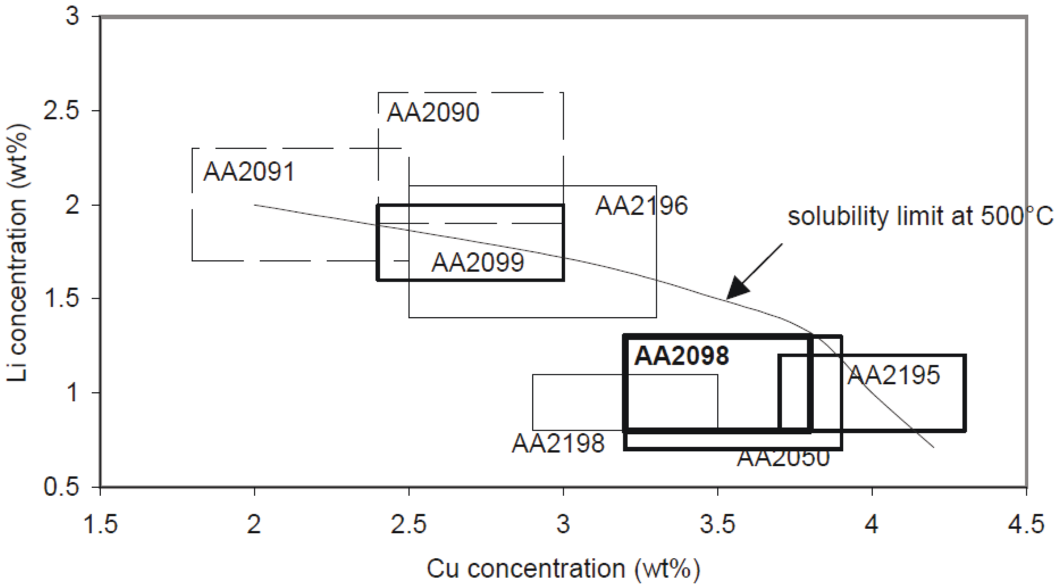

Figure 2: Comparison of compositions in wt%Cu and wt%Li for the second and third generation of Al-Li-Cu alloys. It can be noticed that the third generation of Al-Li alloys (bottom right hand corner) possess a higher Cu/Li when compared to the second generation Al-Li alloys (taken from Warner [9]).

A wide range of additional alloying elements is usually added to Al-Li alloys in order to obtain the desired properties. The main alloying additions involved in the 3rd generation of Al-Li alloys together with their impact are listed in Table 5. The numerous alloying elements highlights that a careful choice of composition is essential in achieving the expected properties.

Alloying element	Impact
Li and Mg	Density reduction, solid solution and precipitation strengthening
Cu and Ag	Solid solution and precipitation strengthening
Zn	Solid solution strengthening and corrosion resistance
Zr and Mn	Formation of dispersoids → Control of the grain size and texture
Fe and Si	Impurities which form intermetallics, detrimental to mechanical properties
Ti	Grain refiner
Na and K	Impurities

Table 5: Main alloying elements which are typical of the third generation of Al-Li alloys [5].

Nowadays, although the development of higher performance alloys continues, an upcoming challenge to improve the airplane structure is to optimise materials' utilisation [9].

3. Precipitation in the 'third generation Al-Li-Cu alloys'

The last generation of 2XXX Al-alloys are hardened by precipitation. Understanding and controlling precipitation is thus decisive in order to obtain the desired properties. From now on, the last generation of Al-Li alloys will be referred to as Al-Li-Cu alloys.

The Al-Li-Cu system involves numerous phases that can be divided into three main groups: intermetallics, dispersoids and precipitates. The intermetallics are coarse particles that form during solidification, due to the presence of impurities such as Fe and Si. They are usually detrimental to the alloy properties. Dispersoids are fine particles that form during homogenisation, which role is to prevent recrystallisation during the thermo-mechanical treatments. The addition of Zr in Al-Li-Cu alloys is a common way to form the spherical β'-Al_3Zr dispersoids. No further details will be given on intermetallics and dispersoids as they are not the focus of the current study, the emphasis will be on the strengthening precipitates that form in industrial Al- Li-Cu alloys.

It is well established that the T_1-Al_2LiCu phase is the main strengthening phase in Al-Li-Cu alloys [10]. Nevertheless, a number of other precipitates form due to the numerous alloying elements [11]. The complex precipitation sequence in Al-Li-Cu alloys was first highlighted by Hardy and Silcock [12] who identified a number of phases using X-Ray diffraction (see Figure 3). In the current Al-Li-Cu alloys, the precipitation sequence is even more complicated than the one described by Hardy and Silcock due to their complex composition. For examples, the use of alloying elements such as Mg and Ag greatly impacts the precipitation sequence. As a consequence, phases from the binary Al-Cu and Al-Li and from the ternary Al-Cu-Mg and Al-Cu-Li systems are usually encountered. The main phases that come up in these alloys are summed up in Table 6. A schematic diagram of a classic microstructure is given in Figure 4.

Despite the apparent complexity of the precipitation sequence in the Al-Li-Cu alloys, it is recognised that the T_1 phase is predominant if pre-stretching is applied prior to the heat treatment [13,14,15,16,17,18,19,20]. To give a fair view of the precipitates that are present in Al-Li-Cu alloys, only the most common precipitates will be described in this part.

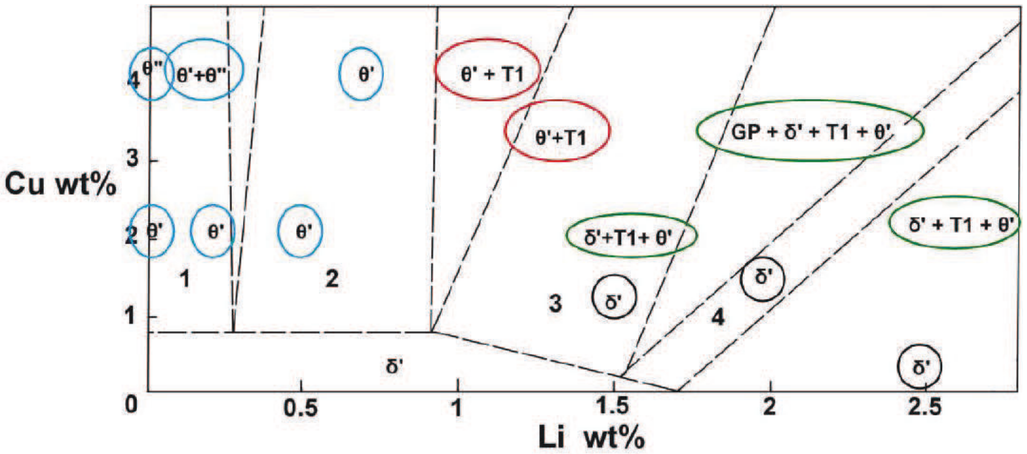

Figure 3: Precipitates observed by Hardy and Silcock in different Al –Li-Cu alloys after a heat treatment of 16 hours at 165°C (taken from Decreus [21]).

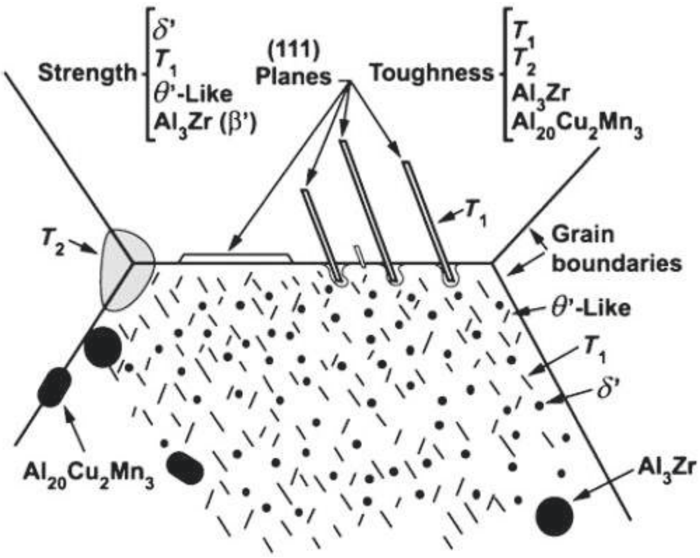

Figure 4: schematic view of the microstructure of third generation Al-Li alloys (taken from Rioja and Liu [5])..

System	Phase	Bulk Composition	Morphology	Orientation	Crystal structure
Al-Cu	GP-I zone	Cu	Disc (mono-layer of Cu)	$[100]_{Al}$	-
	GP-II zone	Al-Cu	Disc (bi-layers of Cu)	$[100]_{Al}$	-
	θ'	Al_2Cu	Platelet	$[001]//[100]_{Al}$	Tetragonal
	Ω	Al_2Cu	Platelet	$(111)//(111)_{Al}$	Orthorhombic
Al-Li	δ'	Al_3Li	Spherical	$(111)//(111)_{Al}$	L12
Al-Cu-Mg	GPB-I zone	Cu-Mg	-	-	-
	GPB-II zone	$Al_{10}Cu_3Mg_3$	Needle	$[100]//[100]_{Al}$	Orthorhombic
	S'	Al_2CuMg	Needle	$[100]_S//[100]_{Al}$ $[010]_S//[021]_{Al}$	Orthorhombic
	σ	$Al_5Cu_6Mg_2$	Cubical	$(100)//(100)_{Al}$ $[100]//[100]_{Al}$	Cubic
Al-Cu-Li	T_B	$Al_{7.5}LiCu_4$	Platelet	$(001)//(001)_{Al}$ $[100]//[110]_{Al}$	Tetragonal
	T_1	Al_2CuLi	Platelet	$(0001)//(111)_{Al}$ $[10\bar{1}1]//[110]_{Al}$	Hexagonal
Al-Cu-Li-Mg	T_2	$Al_2Cu(LiMg)_3$	-	-	-

Table 6: Bulk composition, morphology, orientation relationship and crystal structure of most of the precipitates that can be found in industrial 2xxx alloys [22].

3.1 The Al-Cu phases

The Al-Cu alloy is the first heat-treatable alloy that was discovered. As a consequence, its precipitation sequence has been studied extensively in the literature and is now well-established. The generally accepted precipitation sequence in Al-Cu alloys is the following [23]:

SSSS → GPI-zones → GPII-zones (θ'') → θ' → θ-Al_2Cu

Figure 5 shows the Al-rich side of the Al-Cu phase diagram, the solvus lines of the metastable phases (GP-zones, θ'', θ') and of the equilibrium phase θ are depicted. This phase diagram highlights that the Cu content and ageing temperature are decisive parameters in order to control precipitation in Al-Cu alloys.

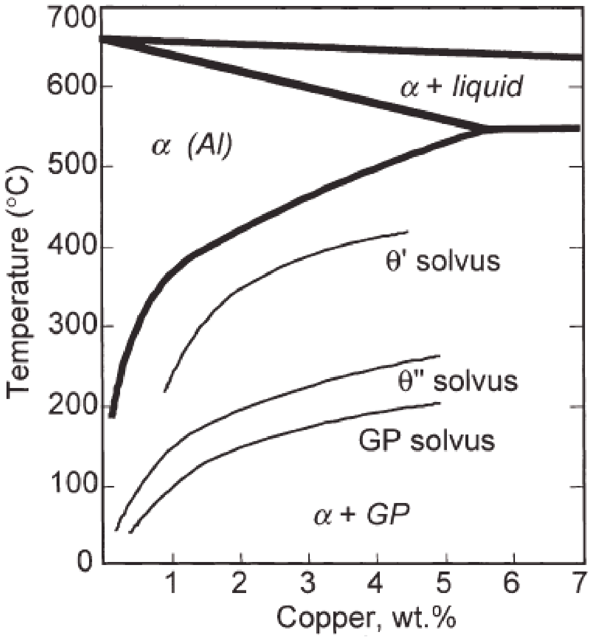

Figure 5: Al-rich side of the Al-Cu phase diagram, showing the solvus boundaries for the metastable GP-zones, θ'' and θ' and the stable θ phase, (taken from Ringer and Hono [24]).

The θ phase is highly unlikely to appear at the common heat treatment temperature (<200°C). As a consequence, the GP-zones form during natural ageing. Subsequently, the θ''-phase which is also referred as GPII-zone will form. The precipitation of the θ' phase occurs during the artificial ageing treatment.

3.1.1 The GP-zones

The Guinier-Preston zones (GP-zones) are the result of the supersaturated solid solution decomposition in the early stage of the ageing treatment. They were first observed by both Guinier [25] and Preston [26] in 1938 by performing X-Ray diffraction experiments on Al-Cu alloys. More generally, GP-zones are observed in a wide range of Al-alloys under different morphologies (needles, plates or spheres) depending on their interfacial energy with the matrix [27]. GP-zones are always the result of clustering of solute elements; they are coherent with the Al matrix and their size ranges from 1 to 10nm. In Al-Cu alloys, the GP-zones are often referred as GPI and GPII zones. GPI-zones usually consist of a single layer of Cu atoms on a {100} plane of the FCC structure even if there are a few examples of multi-layers GPI-zones [28]. In the literature, the GPII-zones are also referred to as θ’’. The latter consists of two single-layers of Cu with three Al layers in between. A model for the structure of one-layer, multi-layers GPI-zones and GPII-zones was proposed by Ringer and Hono [24] (Figure 6). More recently, Decreus et al. [10] observed GPI and GPII-zones in an AA2198 using a High Angular Annular Dark Field Scanning Transmission Electron Microscope (HAADF-STEM) (Figure 7).

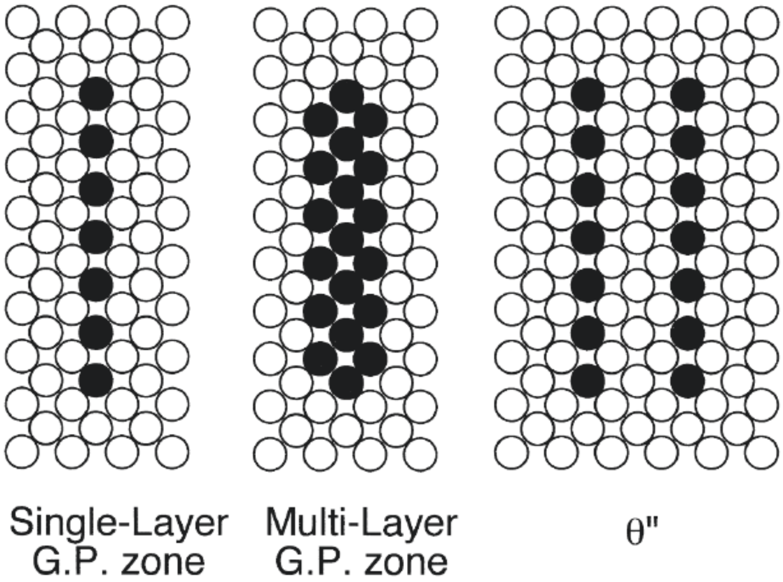

Figure 6: Schematic diagrams of the structure of single-layer and multilayer GP zones and θ’’ precipitates (taken from Ringer and Hono [24]).

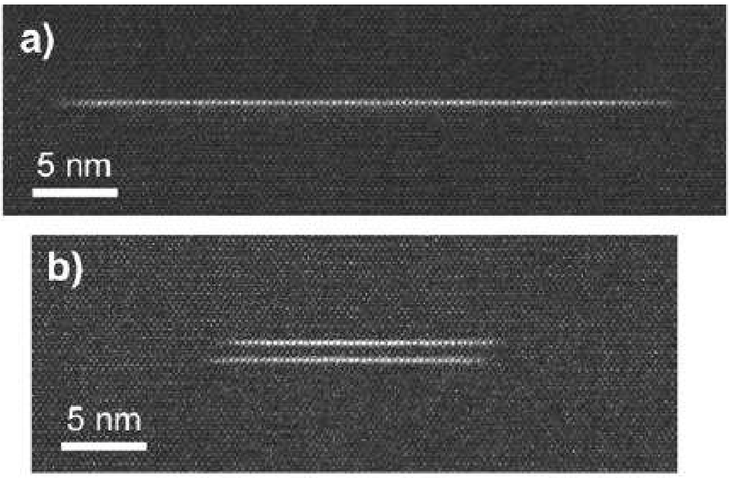

Figure 7: HAADF images in the <110> zone axis of a AA2198 aged 15 h at 155 °C, showing details of precipitates lying on the {100} matrix planes: (a) GPI-zone; (b) GPII-zone (taken from Decreus et al. [10]).

3.1.2 The θ’ phase

The θ’ phase is the main strengthening phase in the Al-Cu system. It is a semi-coherent metastable precipitate which has a well-established tetragonal crystal structure with lattice parameters a=0.404nm and c=0.580nm [23] (Figure 8 a). They appear as platelets in the {001} planes of the Al-FCC structure. Their shape and orientation give rise to streaks along the <100> directions when observed in the diffraction mode in TEM (Figure 8 b). Figure 8 c shows a bright field image taken along a <100> zone axis of an AA2219 sample, age-hardened at peak strength; two variants of θ’ are observed edge-on. The nucleation of θ’ is heterogeneous on the dislocations. As a result, cold working prior to heat treatment significantly enhances θ’ precipitation.

There are very few studies which focus on θ’ precipitates when forming in Al-Li-Cu alloys as its role in strengthening is of second order compared to the role of the T_1 precipitates in these alloys. The structure of the θ’ phase in Al-Li-Cu alloys has been investigated by Yoshimura et al. using TEM [29], they highlighted the impact of the Li content on the structure of the θ’ phase. Indeed, θ’ in high Li content alloys seems to exhibit a different structure and may act as a precursor to the T_B phase. Nevertheless, in low Li alloys (<2wt%), the structure of the θ’ phase is similar to the one found in the binary Al-Cu system.

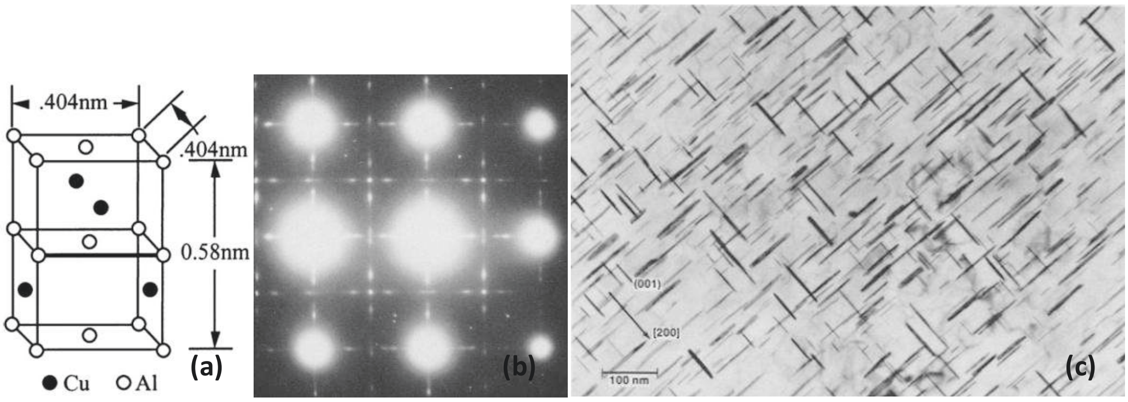

Figure 8: a) Model of the structure of θ’. b) Selected Area Diffraction (SAD) Pattern along a <100> Axis and c) Corresponding Bright Field image, on an AA2219 T87 sample. Two variants of the θ’ phase are observed edge-on (taken from Papazian [30]).

3.1.3 The Ω phase

The addition of Mg and Ag in Al-Cu alloys is known to promote the Ω-Al_2Cu phase at the expense of the θ’ phase. It was first reported by Auld [31] who named it θ'_M. In following publications, it was soon referred to as the Ω phase. This phase has been argued to be monoclinic [31], hexagonal [32], orthorhombic [33,34] and tetragonal [35]. What seems more likely is that this phase forms as thin, hexagonal plates on the {111} planes of the Al matrix [33]. The hexagonal structure has been evidenced, by Kerry and Scott [32], using electron diffraction. The composition of the Ω-phase has been noted to be highly similar to that of θ’, with segregation of Mg and Ag at the interphase. The shape of the Ω-phase is very similar to the Al_2LiCu-T_1 phase that also forms on the {111} planes. In Al-Cu-Mg-Li-Ag alloys, the Ω-phase is gradually replaced by the T_1 phase when the Li content is increased [15]. The pre-deformation applied prior to ageing has also proved decisive on the Ω/T_1 competition [15]. Indeed, pre-deformation tends to favour T_1 formation at the expense of Ω. A study by Ringer et al. [15], focuses on the competition between the T_1 and Ω phases depending on the alloy composition and pre-deformation. The use of Differential Scanning Calorimetry revealed that the Ω precipitation peak shifts towards higher temperature when pre-deformation is applied. This is relevant of the impact of pre-deformation that tend to inhibit Ω precipitation.

Figure 9: Dark Field image along a <112> zone axis of the Ω phase observed edge-on in an Al-Cu-Mg-Ag sample (taken from Knowles and Stobbs [33]).

3.2 The Al-Li system: the δ' phase

The accepted precipitation sequence in this system is [22,36]:

SSSS → δ'-Al_3Li → δ-AlLi

The δ' phase forms easily in the Al matrix due to its high coherency with the Al matrix. When the Li concentration is sufficient it forms immediately during or after quenching from the solution treatment. The δ phase is unlikely to form at the classical heat treatment temperatures.

The δ' precipitates are spherical with the $L1_2$ crystal ordering on the Al FCC structure. The space group of δ' is $Pm\bar{3}m$ and the lattice parameter is a=0.405nm. The Li content in Al-Li-Cu alloys determines the extent of the presence of δ' particles in the as-quenched state, Yoshimura et al. [37] investigated two Al-3.2wt%Cu alloys with a Li content of 1.6wt% and 2.4wt%. Figure 11 shows two SAD patterns along a <100> zone axis for the two alloys. Figure 11 (a) reveals only reflections corresponding to the Al FCC-structure while Figure 11 (b) shows lattice spots corresponding to the precipitation of δ'. As a result, the δ' phase is not considered to form in low-Li Al-Li-Cu alloys.

In Al-Li-Cu alloys of low Li content, the precipitation of T_1 is favoured to the expense of δ'. Nevertheless, although δ' cannot be found in its spherical shape, it may form coherently around the β' dispersoids and around the θ' precipitates [38]. Figure 12 shows two images taken in HAADF-STEM along the <110> zone axis of θ' precipitates in an AA2198 sample age-hardened at peak strength.

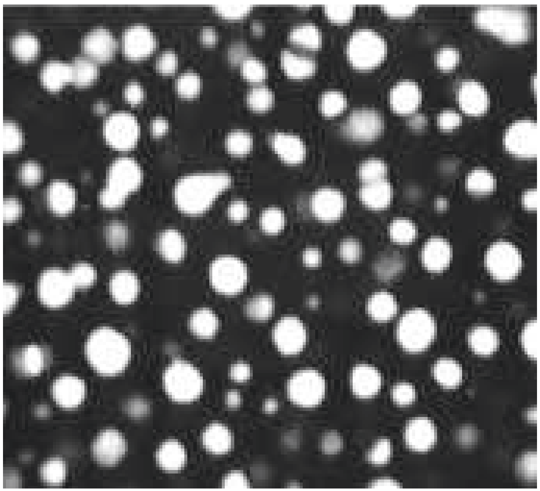

Figure 10: Dark field observation of δ′ precipitates (taken from Gregson and Flower [39]).

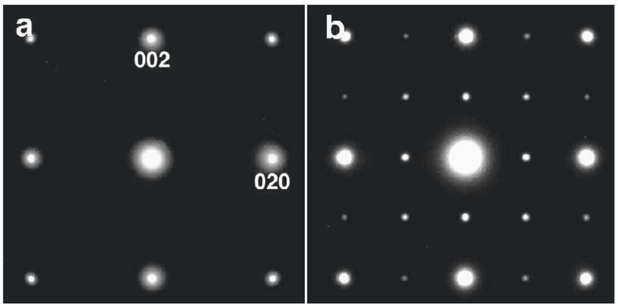

Figure 11: SAD patterns of the as-quenched Al–Li–Cu alloys taken along a <100> zone axis. (a) 1.6 wt%-Li alloy, showing only fundamental reflections; (b) 2.4 wt%-Li alloy, showing super-lattice spots from the presence of δ′ (taken from Yoshimura et al. [37]).

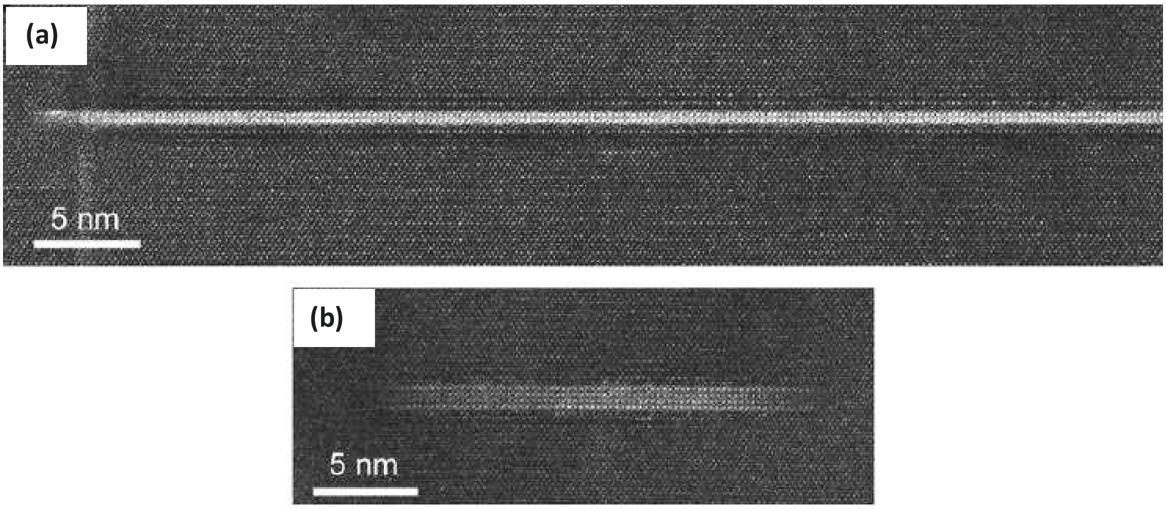

Figure 12: (a) Thin θ′ precipitate with evidence of wetting by a thin δ′ layer; (b) Same precipitate of larger thickness. All platelets are normal to the [001] Al direction (taken from Decreus et al. [10]).

3.3 The Al-Cu-Mg phases

The generally accepted precipitation sequence is as follows [27]:

SSSS → co-clusters → GPB-zones → GPBII-zones (S'') → S' → S-Al_2CuMg

The initial hardening stage has originally been attributed to the formation of GPB zones but it is now accredited to the formation of Cu-Mg co-clusters [40,41,42]. The subsequent hardening stage is attributed to the formation of GPB-zones, GPBII-zones, S' and S phases [40,43,44].

3.3.1 The GPB zones

When studying Al-Cu-Mg alloys, Bagaryatsky [45] revealed the presence of GP-zones like particles, composed in equal proportion of Cu and Mg. The name GPB-zone (Guinier Preston Bagaryatsky-zone) was given by Silcock [21], in order to distinguish them from the Cu GP-zones. In the same way as GP-zones, a distinction is made between GPBI and GPBII-zones [27], with GPBII-zones acting as a precursor to the S' phase. There are numerous models that attempt to define the structure and shape of the GPBI-zones. Bagaryatsky [45] described the GPBI-zones as an arrangement of Cu and Mg atoms in the {100} planes having a similar arrangement as for the stable S-phase. Instead, Silcock [21], using small-angle X-ray scattering (SAXS), interpreted the GPBI-zones to form as rod-like particles of 1-2nm in diameter and 4-8nm in length along the <100> direction of the Al matrix. As predicted by Silcock [21], the rod-like morphology of the GPBI-zones has been confirmed in ensuing TEM studies [40,46,47]. Atom-probe tomography was also used in parallel to TEM in following studies [40,46,48,49]. It has been noted that GPBI-zones do not form during natural ageing or short artificial ageing times which lead to their consideration as small precipitates with distinct structure and shape rather than clusters. The crystallography of GPBI-zones has been identified recently using HAADF-STEM combined with ab initio simulations [50]. The GPBI-zones were found to consist in an agglomeration of sub-nanometer-size, rod like structural units with the orthorhombic structure along the <100> direction of the Al matrix (Figure 13 (b)). The structure of the GPBI-zones has been confirmed by first principles energy calculations [51].

The S''-phase has been reported in many publications [41,43,45,52] and it has been referred to as GPBII-zones [53,54]. In a recent study by Kovarik et al. [55], using HRTEM imaging combined with ab initio simulations, the structure of the S''-phase was determined to be a strained version of the S phase with a modified orientation relationship (see Figure 14).

In the AA2198, due to the presence of both Cu and Mg, GP-zones and GPB-zones can theoretically be formed in the early stages of the SSSS decomposition.

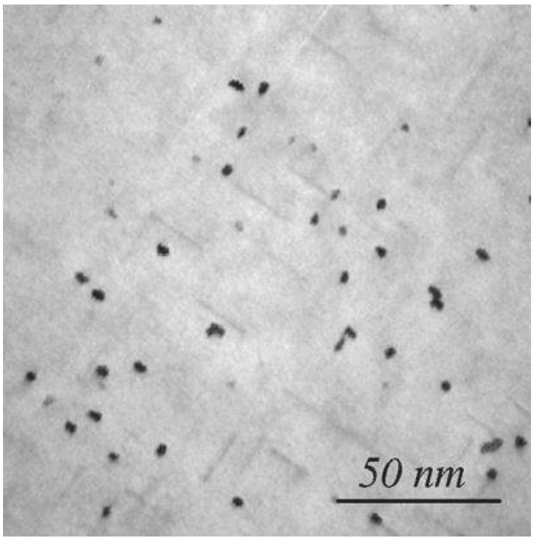

Figure 13: Needle-shaped GPB zones in an Al-2.99wt%Cu-0.98wt%Mg alloy aged 96h at 180°C (taken from Kovarik et al. [50]).

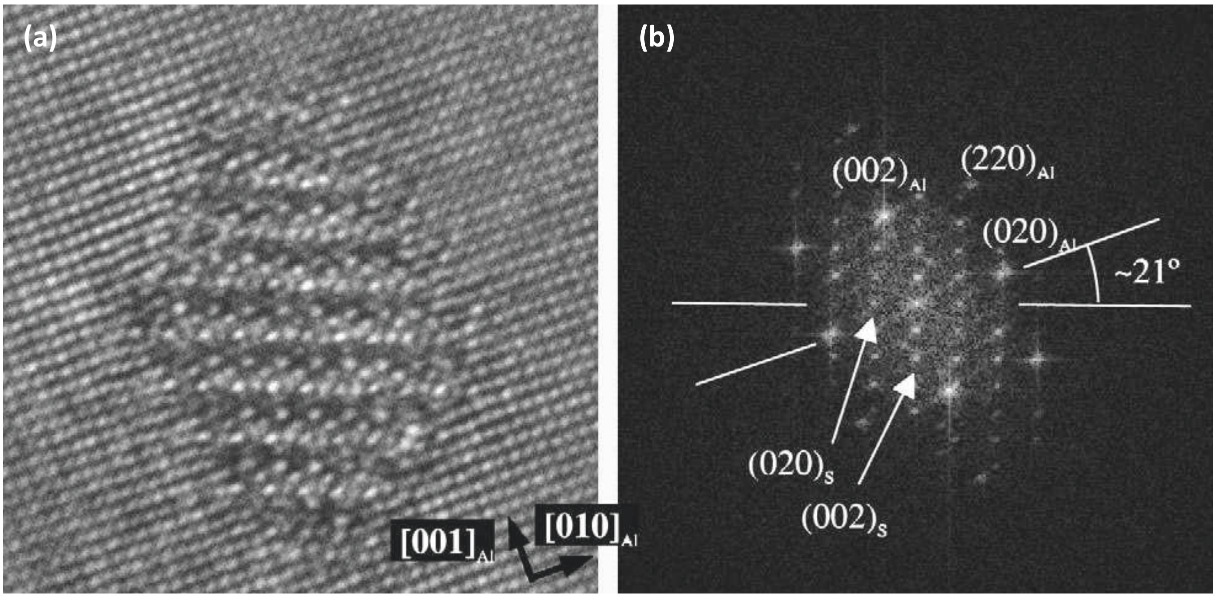

Figure 14: (a) HRTEM image of the S''-phase, along the <110> zone axis and corresponding FFT spectrum (taken from Kovarik et al. [55]).

3.3.2 The S'/S phase

The S' and S phases are often considered to be the same phase as they only slightly differ in lattice parameters. The difference between these two structures is attributed to the degree of coherency with the Al matrix but they exhibit very similar crystal structure [27]. As a consequence, the indication S is usually used to denote this phase. As proposed by Perlitz and Westgren in 1943 [56], on the basis of XRD work, the S phase is orthorhombic. The lattice parameters of this phase were later measured by Mondolfo [57] as, a=0.4nm, b=0.925nm and c=0.718nm. The S phase forms predominantly as laths in the {210} habit planes and along the <100> directions of the Al matrix [57].

Depending on the temperature and duration of the heat treatment the larger dimension of the S-phase can grow up to 1µm [58]. This phase nucleates either homogenously in the grains or heterogeneously on dislocations [59,60]. S-phase particles that nucleated on dislocation loops are shown in Figure 15 (a). Figure 15 (b) is a dark field image of S laths which are observed edge-on. A recent work by Styles et al. [61], has revealed the existence of two distinct S-phases which were called S1 and S2. The two phases were found to have different lattice parameters while exhibiting the same crystal structure. Styles et al. [61] suggested that S1 is a lath-shaped phase while S2 is a rod-shaped phase as observed in TEM (see Figure 16).

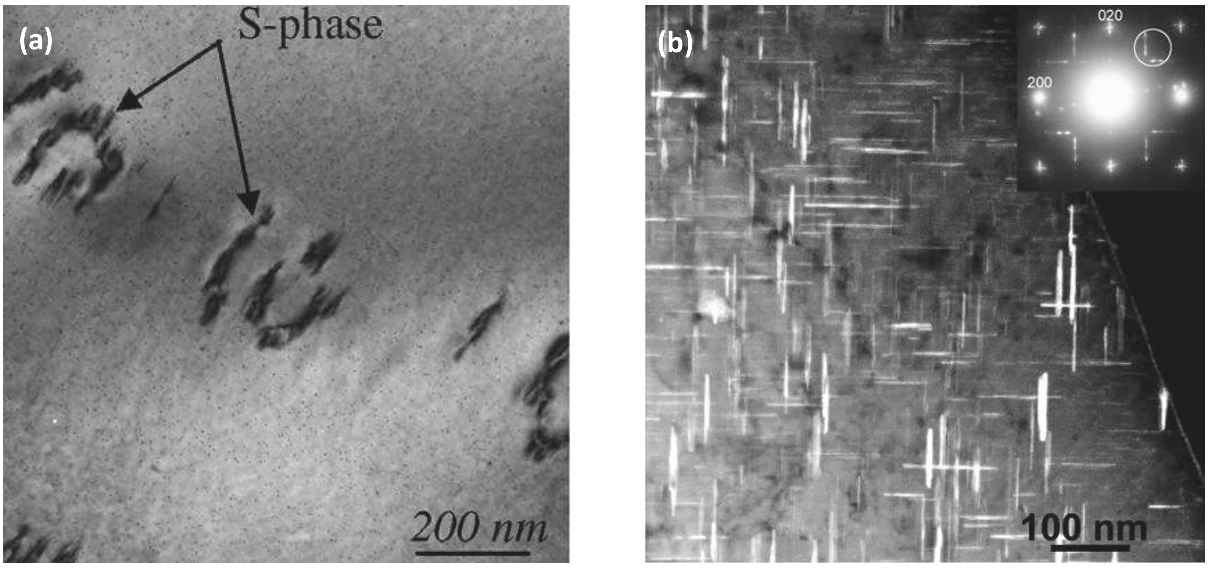

Figure 15: (a) S-phase particles that nucleated on dislocation loops observed in a Al-2.99wt%Cu-0.98wt%Mg alloy aged 96h at 180°C (taken from Kovarik et al. [50]). (b) Dark field image along a <100> zone axis of S-phase laths in a 2024 alloy aged 300 min at 190°C. The laths are observed edge-on. (taken from Tolley et al. [44]).

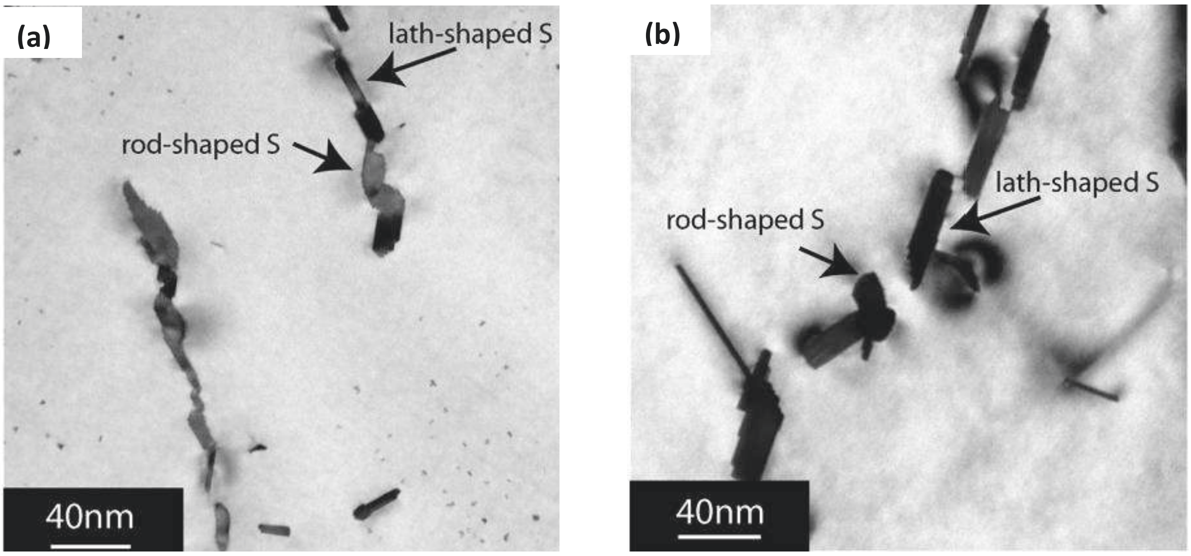

Figure 16: Bright field images recorded in TEM of a high purity Al-2.5Cu-1.5Mg (wt%) alloy in the <100> zone axis. The two distinct shapes of the S phase are observed. (taken from Styles et al. [61])

3.4 The Al-Li-Cu phases

The most common precipitation sequence for this system is

SSSS → T_1-Al_2CuLi

Although the T_1 phase is generally dominant, the T_B –$Al_{7.5}LiCu_4$ phase might form. This phase will not be described in details as its presence is usually associated to high temperature precipitation or grain boundaries. The determinant impact of the thermo-mechanical treatment parameters (pre-deformation, heat treatment temperature and duration) on the T_1 formation kinetics will be discussed in the following.

3.4.1 The T_1 phase

It is well-established in the literature that the T_1 phase is the main strengthening phase in Al-Li-Cu alloys. It is an equilibrium phase from the ternary Al-Li-Cu phase diagram. It was first reported by Hardy and Silcock [12] in 1955 as being hexagonal, with the space group P6/mmm and the lattice parameters a=0.4965nm and c=0.9345nm.

Several models have been proposed concerning the crystal structure of the T_1 precipitates. The first study of the crystal structure of T_1 was performed by Huang and Ardell [62]. They justified their structure by comparing predicted X-Ray intensities for various models with the X-Ray intensities measured by Hardy and Silcock [12] and to electron diffraction experiments. Their structure was based on the fact that the lattice number c defined by Hardy and Silcock was almost perfectly equal to $4*\{111\}_{AL}$. Hence a simple solution was to consider a four-layer structure. Figure 17 (a) shows the structure retained by Huang and Ardell, it consists of an ABCB stacking of planes with all the Li atoms going into the A and C layers without any Cu, and the B layer consisting of a random arrangement of Cu and Al.

This first model attempted by Huang and Ardell was followed by a number of studies using HRTEM that tried to compare this established model to experimental measurements. Three different studies [19,63,64] arrived at the same conclusion that the T_1 structure rather consists of an ABAB stacking of planes. Howe et al. proposed a refined structure as shown on Figure 17 (b).

In a following study using single-crystal X-Ray diffraction, Van Smaalen et al. [65] unravelled the structure of a bulk T_1. This structure is shown in Figure 17 (c). The global dimensions remain the same, but this new structure consists of corrugated atomic planes. Figure 17, clearly highlights the evolution in the models of the T_1 structure.

Two recent independent studies by Donnadieu et al. [66] and Dwyer et al. [67] have used the HAADF-STEM technique combined with ab initio calculations in order to study the structure of the T_1 precipitates when embedded in Al. The images obtained by HAADF-STEM show a Z contrast proportional to Z^n where n is approximately 1.7-2. As a consequence, this technique is perfectly suited to the case of T_1 precipitates which involve atoms of very different Z. The refined T_1 structure by Dwyer et al. [67] is displayed in Figure 18. The resulting structure is very similar with the bulk structure of Van Smaalen et al.; a small difference consists in the presence of an additional Al-Cu layer at the interface with the matrix. Following these studies, the structure of the T_1 phase can now be regarded as well-established.

It is well known in the literature that the T_1 precipitates nucleate on dislocations [13]. The impact of the pre-stretching applied prior to the heat treatment thus determines the precipitation kinetics of this phase. This aspect will be discussed in the following part.

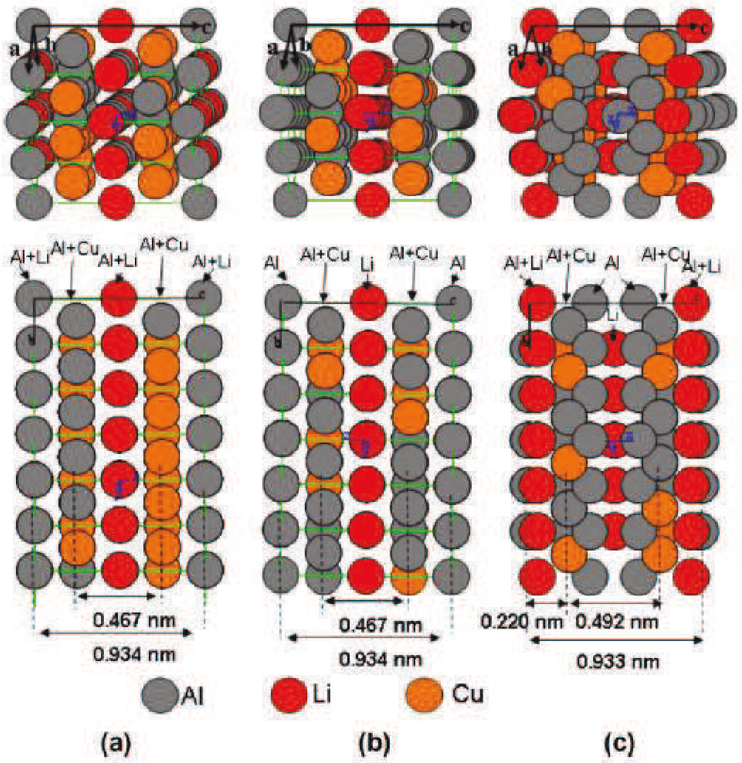

Figure 17: Atomic models for the T_1 phase: (a) Huang and Ardell [62], (b) Howe et al. [64], and (c) Van Smaalen et al. [65] (taken from Donnadieu et al.[66]).

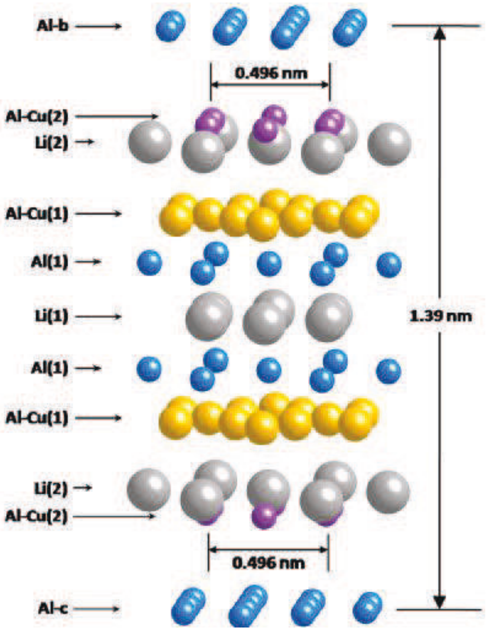

Figure 18: View of the structure of a T_1 precipitate embedded between two pure Al layers (taken from Dwyer et al. [67]).

3.4.2 *Influence of the thermo mechanical treatment on the T_1 microstructure*

One of the goals of the present work is to understand the relationship between the T_1 morphology and the resulting yield strength. When considering the morphology of the T_1 phase, the important parameters are the following: the number density, the mean diameter and thickness of the platelets and finally the volume fraction of the T_1 phase. The different parameters of the thermo-mechanical treatment that will greatly influence the resulting T_1 microstructure are the following: the amount of cold work applied prior to the final heat treatment, the temperature of the heat treatment and finally the duration of the heat treatment.

- ***Effect of pre-stretching***

It is well-established that dislocations act as preferential nucleation sites for the T_1 phase [13]. Consequently, the precipitation kinetics of the T_1 phase is strongly impacted if cold work is applied after the solution heat treatment and before artificial ageing [13,14,15,16,17,18,19,20]. Cassada et al. [13] have shown that 6h at 190°C are needed for an AA2090 sample, pre-deformed 6%, to reach a 1.8% T_1 volume fraction in comparison to 24h for a non-pre-deformed sample. In parallel, they measured the evolution of the yield strength and showed that 4h was needed to reach peak strength for the first sample versus 24h for the latter one.

If pre-deformation is applied, the T_1 phase precipitates at the expense of the other phases. But if no pre-deformation is applied, T_1 is no longer the dominant phase. As a result, when studying the impact of the T_1 phase on the mechanical behaviour, it is important to always apply cold work prior to the heat treatment. The competition between the precipitation of T_1 and θ' has been studied by Gable et al. [16] on an AF/C 458 sample. For a pre-deformation from 0 to 8%, the T_1 volume fraction evolves from 0.5% to almost 3% when the θ' volume fraction decreases from 1.14% to nearly 0% (Table 7).

Gable et al. [16] also highlighted that the same value of yield strength can be reached for different pre-deformations applied even if the T_1 microstructures were very different. As a consequence, it revealed that the relationship between the different parameters of the morphology of the T_1 phase and the increase in strength is not straightforward.

Pre-stretch (%)	**Ageing time (h)**	**Yield strength (MPa)**	**T_1 number density (/µm^3)**	**T_1 diameter (nm)**	**T_1 Volume fraction (%)**
0	120	454	272.6	158.7	2.53
2	35	452	754.7	86.8	2.12
4	20	451	963.1	55.6	1.64
6	15	452	1283.1	53.6	1.42
8	10	452	1478.3	40.1	0.94

Table 7: Measured yield strength for samples with different pre-stretch and ageing time performed on the alloy AF/C 458. The corresponding T_1 number density, diameter and volume fraction are also reported (from Gable et al. [16]).

In a recent PhD work, Decreus [68] also reported the effect of pre-stretch in an AA2198. The conclusion was the same with a faster kinetics for the pre-stretched samples: 100h at 155°C for the non-pre-stretched sample versus 15h for the 2% pre-stretched one to reach peak strength. The impact on ageing time is thus important from 0% to 2% but it seems that the impact on kinetics if a higher value of pre-stretch is applied becomes less important.

The impact of pre-stretching/natural ageing sequence is also to be considered. Indeed, we have mentioned before that precipitates such as GP-zones can form at room temperature after quenching. As a result, if pre-stretching is applied straight after quenching, the fraction of such precipitates will be minimal and if the pre-stretch is applied after a couple of days, the clustering would have already occurred. Decreus [68] concluded that this sequence has an impact on the hardness prior to the artificial ageing treatment with higher hardness for the sample stretched after a couple of days, but after the age-hardening treatment, the two different samples will reach the exact same peak strength. In summary, the moment when the pre-stretching is applied seems to have little impact on the resulting strength.

- ***Effect of the heat treatment temperature and duration***

The impact of the heat treatment temperature and duration is decisive upon the precipitation sequence. As a rule of thumb, longer time and higher temperature result in fewer and larger precipitates. In order to achieve the most advantageous microstructure for a given application, one must select the optimum temperature and duration.

Precipitation occurring on the grain boundaries results in poor fracture properties so this type of precipitation is generally to be avoided. Indeed, even if T_1 nucleates on dislocations that are distributed in the matrix, grain boundaries and sub-grain boundaries are also potential nucleation sites. The precipitation localisation on these latter sites is detrimental to the fracture behaviour of Al-Li-Cu alloys. Blakenship et al. [8] observed in a previous study a considerable reduction of grain boundary precipitation by lowering the heat treatment temperature from 165°C to 125°C. Csontos et al. [69,70] suggested the use of two consecutive heat treatments in order to lower this detrimental type of precipitation, but the impact on grain boundary precipitation of duplex ageing was finally found to be poor.

However, in recent studies, the performance of duplex or even triple ageing practices with different temperatures and durations was found to have a positive influence on some of the material’s properties. For instance, the duplex ageing executed by Csontos and Starke [69,70] on an AF/C-489 sample resulted in significant improvement of 85% in ductility with a limited loss of 4% in yield strength. Kolobnev et al. [71] also experimented duplex ageing on an Al-Li-Cu alloy and observed a considerable increase in fracture toughness, corrosion resistance and thermal stability in comparison to the same alloy aged at a single temperature. Although it is ineffective in lowering grain boundary precipitation, the duplex or even triple ageing practices give access to a wider range of microstructures which enables more freedom to create an alloy with specific mechanical properties.

Small angle X-Ray scattering (SAXS) has been proven to be a good way to follow the T_1 precipitation kinetics in-situ. De Geuser et al. [72] developed a method to extract the T_1 mean thickness and diameter evolution, in a AA2198 alloy, during a heat treatment at 155°C. In this ageing condition, the mean thickness of the T_1 precipitates was found to reach a constant value of 1.3nm, which corresponds to a distribution of single-layer T_1 precipitates.

Over-ageing is classically detrimental to the mechanical properties due to the coarsening of precipitates. Nevertheless, the T_1 phase exhibits a remarkable resistance to coarsening [73].

4. Strengthening contributions in Al-alloys

Strengthening of a metal is induced by the presence of obstacles to dislocation motion. Dislocation movement can be impeded by many types of objects such as: other dislocations, precipitates, grain boundaries, alloying elements in solid solution... In the case of Al-alloys, the strengthening contributions mainly come from the precipitates, the solid solution and work hardening (dislocations) [74,75].

The Critical Resolved Shear Stress (CRSS) is the stress necessary to initiate slip in a single grain. In order to account for the polycrystallinity of a given material, the yield stress is related to the CRSS by the Taylor factor M. Its value, of about 3 in the case of an isotropic distribution of crystal orientations, can be somewhat lower when the material possesses a strong crystallographic texture. The minimum value of 2 corresponds to all the slip systems oriented with a maximum Schmid factor with respect to the loading direction.

4.1 Solid Solution hardening

Among other interactions, the atoms in solid solution are of a different size compared to the matrix atoms and therefore induce a local distortion of the crystal structure and a resulting stress field. The interaction of the dislocations with these stress fields induces strengthening. In industrial Al-Li-Cu alloys, the number of alloying elements makes it difficult to obtain an accurate prediction of the solid solution strengthening. Based on the power law valid for a single solute species, the following expression is often used to estimate the solid solution contribution to the overall macroscopic yield strength [76,77]:

$$\sigma_{ss} = \left(\sum_j k_j C_j\right)^{2/3} \tag{1}$$

Where C_j is the concentration of the alloying element j and k_j is a factor related to this alloying element.

4.2 Work hardening

When plastic deformation is induced, dislocations travel through the material forming a so called “dislocations forest”. These dislocations act as obstacles to the other moving dislocations, which contribute to the overall strengthening of the material. This contribution is referred to as ‘work hardening’ and can be written as [78]:

$$\sigma_{wh} = M\alpha\mu b\sqrt{\rho_d} \tag{2}$$

Where α is a constant depending on the strength of dislocation junctions and is usually estimated at 0.27 [79], μ is the shear modulus for aluminium, b is the Burgers vector and ρ_d is the density of dislocations.

4.3 Precipitation hardening

4.3.1 *Hardening by spherical precipitates*

Precipitation hardening is the predominant strengthening mechanism in heat-treatable Al-alloys. When a dislocation encounters a precipitate, it will either shear it or by-pass it (Figure 19). In the case of spherical particles, a transition between those two mechanisms is generally considered depending on the radius of the particles. The precipitates are first sheared and then by-passed after reaching a critical radius, this transition corresponds to the peak in yield strength.

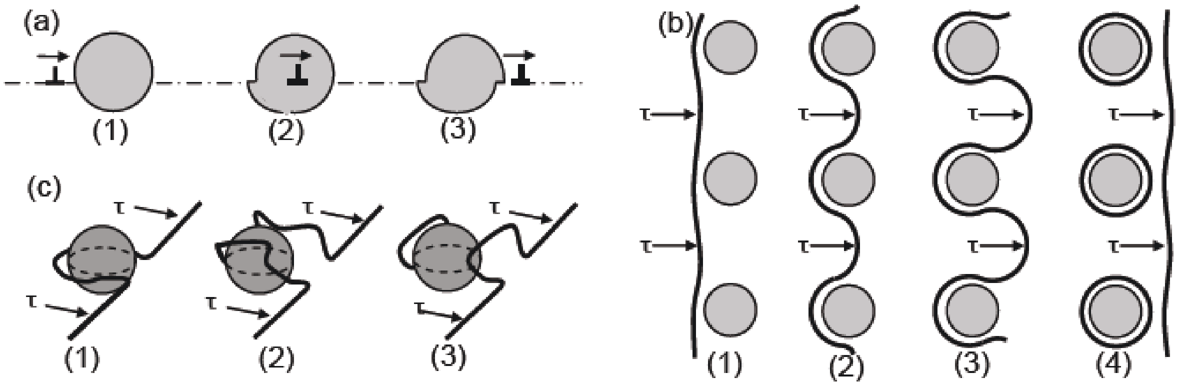

Figure 19: Scheme of the dislocation/precipitate interaction. (a) shearing, (b) by-passing by the Orowan mechanism, leaving a loop around the precipitate and (c) by-passing by the cross-slip mechanism leaving a loop in front of the precipitate [80].

A simple scheme shown on Figure 20 displays the balance of forces between a point obstacle and a moving dislocation. The force F acting from the obstacle onto the dislocation can be defined as:

$$F = 2T cos\frac{\varphi}{2} \tag{3}$$

Where T is the line tension which can be written as [81]:

$$T = \frac{1}{2}\mu b^2 \tag{4}$$

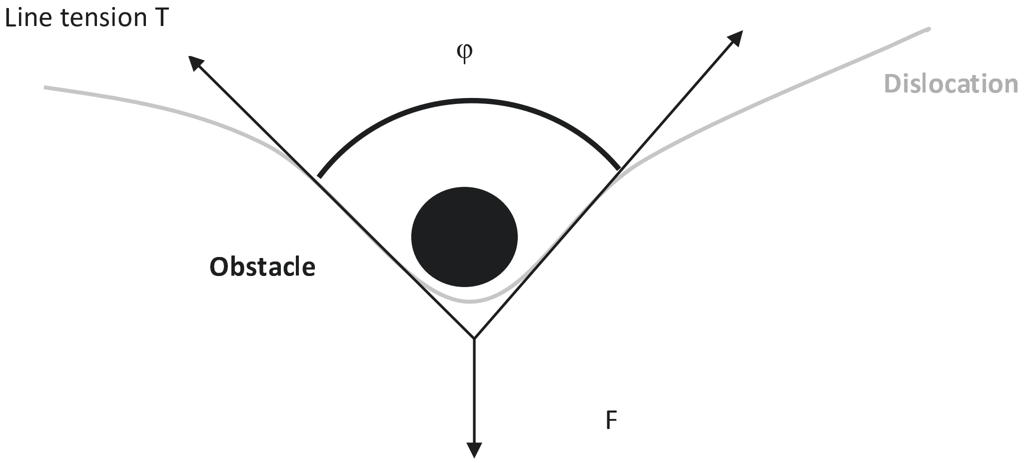

Figure 20: Force equilibrium between a dislocation and an obstacle on the gliding plane.

The value of the force to overcome an obstacle will depend on whether this obstacle is shearable or non-shearable. In the case of shearable precipitates, the dislocation bows around the precipitate until reaching a critical angle value φ_c when the precipitate is sheared. If the precipitate is by-passed by the Orowan mechanism, the dislocation bows around the precipitate until the angle φ reaches 0. When considering spherical obstacles of radius R, the value of F generally increases as a function of R until it reaches a constant value when the precipitate is by-passed. As a consequence, the following more general formula can be considered for the force acting on the dislocation when considering a spherical precipitate of radius R [82]:

$$\begin{aligned} F(R) &= k\mu b^2 R \qquad \text{if } R<R_c \\ F(R) &= k\mu b^2 R_c \qquad \text{if } R>R_c \end{aligned} \tag{5}$$

Where k is a constant that is adjusted depending on the mechanism, and R_c is the critical radius.

The obstacle force induced by a precipitate on a moving dislocation originates from a number of different mechanisms, some of which can be simultaneously operative:

- Chemical effect: This contribution is due to the creation of a new interface between the matrix and the precipitate. The energy needed to create it depends on the matrix/precipitate interfacial energy.
- Modulus strengthening: this contribution depends on the difference in shear modulus between precipitate and matrix
- Coherency strengthening: this contribution is linked to the stress field created around the precipitate when its crystal structure is coherent with the matrix.
- Order strengthening: This contribution is due to the formation of an anti-phase boundary (APB) when the precipitate is sheared by a matrix dislocation.

- ***Orowan strengthening***

A wide range of models have been developed in order to evaluate the yield strength increment associated with spherical precipitates. Most of those models use the Orowan equation as a basis. The Orowan equation that describes the CRSS increment, induced by a family of spherical non-shearable precipitates can be written as [82]:

$$\tau = \frac{\bar{F}}{b\bar{L}} \approx k\frac{\mu b}{\bar{L}} \tag{6}$$

Where $\bar{F}$ is the mean obstacle force and $\bar{L}$ is the average precipitate spacing along the dislocation line on the glide plane.

In the case of distribution of spherical precipitates of same sizes and following Fullman [83], the average precipitate spacing L along the dislocation line can be written as:

$$L = \sqrt{\frac{2\pi}{3f_v}}R \tag{7}$$

Where f_v is the volume fraction and R the mean radius of the precipitates.

The CRSS can thus be written as:

$$\tau = k\mu b\sqrt{\frac{3}{2\pi}}\frac{\sqrt{f_v}}{R} \tag{8}$$

- ***Precipitate shearing***

In the case of precipitate shearing, the following expression for the CRSS can be used [76]:

$$\tau = \frac{\mu}{\sqrt{b}}\sqrt{\frac{3}{2\pi}}k^{3/2}\sqrt{Rf_v} \tag{9}$$

The yield strength evolution is plotted as a function of the precipitate radius on Figure 21. This graph clearly highlights the transition in mechanisms that always favours the smallest flow stress.

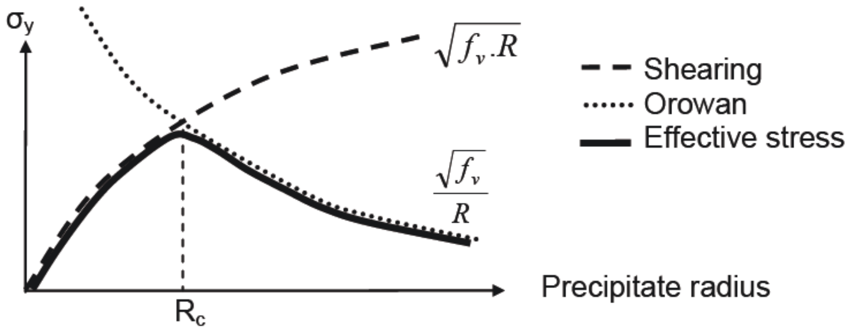

Figure 21: Graph that shows the yield strength evolution as a function of the precipitate radius (taken from Fribourg [84]).

4.3.2 *Hardening by plates: the case of the T_1 phase*

In the case of the Al-Li-Cu alloys, the strengthening T_1 precipitates have a platelet shape. Two attempts, to use modified Orowan equations, can be found in the literature. Nie et al. [85] have proposed a geometrical modification of the Orowan equation in order to be suitable for strengthening by $\{111\}_{Al}$ precipitates plates:

$$\Delta\sigma = 2 * M * \left(\frac{\mu b}{4\pi\sqrt{1-\nu}}\right) * \left(\frac{1}{0.931\sqrt{\frac{0.265\pi Dt}{f_v}} - \frac{\pi D}{8} - 0.919t}\right)(ln\frac{1.061t}{r_0}) \tag{10}$$

Where D is the diameter, t is the thickness and f_v is the volume fraction of the precipitates.

The second model by Zhu and Starke [86], is based on a simulation of the interaction of dislocations with a range of obstacles dispersed in the glide plane, similarly to the Forman and Makin simulations for point-like obstacles. The following expression is obtained:

$$\Delta\sigma = 0.12 * M * \left(\frac{\mu b}{\sqrt{Dt}}\right) * \left(\sqrt{f_v}\sqrt{\frac{0.7D}{t}f_v} + \frac{0.12D}{t}f_v^{3/2}\right)(ln\frac{0.079t}{r_0}) \tag{11}$$

These two models suffer from the fact that they both are based on the assumption that the T_1 precipitates are non-shearable. Nevertheless, a few studies using HRTEM have shown images of sheared T_1 precipitates [64,70,87,88]. Figure 22 is the first HRTEM observation of an edge-on sheared T_1 by Howe and Lee in 1988 [64].

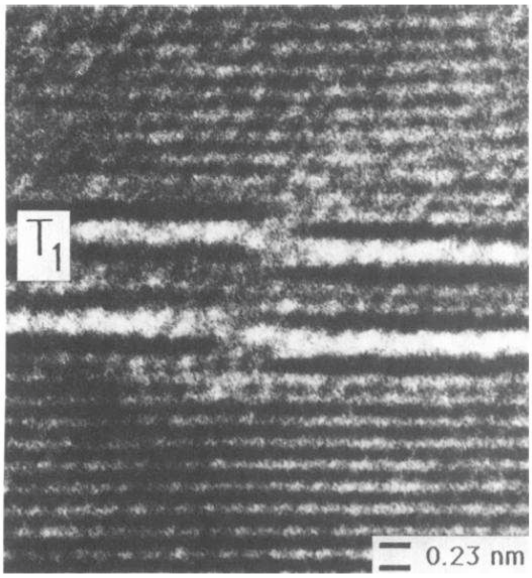

Figure 22: HRTEM image of a sheared T_1 plate observed edge-on along a <110> zone axis (taken from Howe and Lee [64])

In regards to the recent observations using HRTEM, T_1 precipitates seem to be shearable when they have the minimal thickness of one unit cell, as a consequence, the Orowan-type mechanism is not suitable to model strengthening by this type of precipitate.

The only known attempt to consider the shearing ability of the T_1 phase to model the yield strength has been made by Nie and Muddle [89] who proposed an interfacial strengthening approach. This model considers the energy needed to create a new precipitate/matrix interface when shearing a T1 precipitate:

$$\Delta\tau = \frac{1.211 D {\gamma_i}^{3/2}}{t^2}\sqrt{\frac{b f_v}{\Gamma}} \tag{12}$$

Where γ_i is the precipitate/matrix interfacial energy.

4.4 Addition rules

In order to estimate the global increment in yield strength, one has to add all the different contributions seen above. Many studies have shown, that the addition law is often more complicated than a simple linear addition. Most generally, the CRSS increment for a distribution of two types of obstacles with respective CRSS increment τ_1 and τ_2 can be written as [81,90]:

$$\tau_{tot}^k = \tau_1^k + \tau_2^k \tag{13}$$

The most classical values for k is 1 and 2 but more generally, it can be considered that $1 \leq k \leq 2$ [91].

The additivity of the solid solution contribution with another type of contribution such as precipitate strengthening has been studied recently by Dong et al. [91]. It has been demonstrated that the additive strengthening k=1 applies when the density of the precipitate is low but that k tends toward 2 with an increasing density of precipitates. As a consequence, the additivity of the strengthening contributions does not seem to be as easy as a linear or quadratic addition rule and even seems to evolve when the density of the obstacles changes.

For the sake of simplification, the following mixture law for the CRSS increment is often used [79]:

$$\tau_{tot} = \tau_0 + \tau_{SS} + \sqrt{\tau_{wh}^2 + \tau_{ppt}^2} \tag{14}$$

Where $\sigma_0 \sim 10 MPa$ is the intrinsic stress of pure aluminium.

5. Conclusion

Extensive work has been performed on precipitation in Al-Li-Cu alloys. The precipitation hardening capability of these alloys makes them natural candidates for aerospace applications. It is highlighted, in the literature, that precipitation in these systems is a complex process, which is highly dependent on composition but also on the thermo-mechanical treatment applied to the alloy. The commercial alloys, such as the AA2198, involve many types of alloying elements, and thus a wide range of precipitates could form. However, when applying pre-age stretch with a suitable heat treatment temperature, the T_1 phase has been noticed to be highly dominant in the AA2198 alloy and it is recognised as the principal actor in the overall strengthening.

Although the relationship between the precipitate microstructure in Al-Cu-Li and the resulting mechanical properties has been studied before, the state of the art in this area is not yet satisfactory. There is a need for a systematic, quantitative, database of microstructure / properties relationships to serve as a strong basis for the modelling of strengthening. Furthermore, the available models available that describe the strengthening by plate-like precipitates do not seem really suited to the strengthening of the T_1 phase.

6. References

1. The Aluminium Association: Aluminum Standards and Data.
2. Vargel, C.: Métallurgie de l'aluminium. (2010)
3. Starke Jr, E. A., Staley, J. T.: Prog. Aerospace Sci. 32, 131-172 (1996)
4. Williams, J. C., Starke Jr, E. A.: Acta Mater. 51, 5775-5799 (2003)
5. Rioja, R. J., Liu, J.: Met. and Mat. Trans. A 43A, 3325-3337 (2012)
6. Polmear, I. J.: Mat. Trans., 12-31 (1996)
7. Jata, K. V., Panchanadeeswaran, S., Vasudevan, A. K.: Mat. Sci and Eng. A 257, 37-46 (1998)
8. Blakenship Jr, C. P., Starke Jr, E. A.: Acta Metall. Mater. 42 (1994)
9. Warner, T.: Mat. Sci For. 519-521, 1271-1278 (2006)
10. Decreus, B., Deschamps, A., De Geuser, F., Donnadieu, P., Sigli, C., Weyland, M.: Acta Mat. 61, 2207-2218 (2013)
11. Sainfort, P., Dubost, B.: J. de phys. 48, 407-413 (1987)
12. Hardy, H. K., Silcock, J. M.: J.Inst. Met. 84, 423-428 (1955-56)
13. Cassada, W., Shiflet, G. J., Starke Jr., E. A.: Met. Trans. A 22A (1991)
14. Kim, J. D., Park, J. K.: Met and Mat. Trans. A 24, 2613-2621 (1993)
15. Ringer, S. P., Muddle, B. C., Polmear, I. J.: Met. and Mat. Trans. A 26A, 1659-1671 (1995)
16. Gable, B. M., Zhu, A. W., Csontos, A. A., Starke Jr., E. A.: J. of L. Met., 1-14 (2001)
17. Munoz-Morris, M. A., Morris, D. G.: Scripta Mat., 304-307 (2010)
18. Decreus, B., De Geuser, F., Donnadieu, P., Deschamps, A.: Precipitation evolution in AA2198 and AA2196 Al-Li-Cu alloys. In : PTM 2010 - International Conference on Solid-Solid Phase Transformations, Avignon (2010)
19. Cassada, W. A., Shiflet, G. J. .: J. de Phys. 48, 397-406 (1987)
20. Cassada W. A., S.: Met. Trans. A 22A, 287-297 (1991)
21. Silcock, J. M.: J. Inst. Metals 89, 203 (1960)

22. Dubost, B., Sainfort, P.: (1991)

23. Silcock, J. M., Heal, T. J., Hardy, H. K.: J. Inst. Met. 82, 239-248 (1953-54)

24. Ringer, S. P., Hono, K.: Mat. Charac. 44, 101-131 (2000)

25. Guinier, A.: Nature (1938)

26. Preston, G. D.: Roy. Soc. Pub. (1938)

27. Wang, S. C., Starink, M. J.: Int. Mater. Rev. 50, 193-215 (2005)

28. Hono, K., Satoh, T., Hirano, K. I.: Phil. Mag. A 53(4), 495-504 (1986)

29. Yoshimura, R., Konno, T. J., Abe, E., Hiraga, K.: Acta Mater. 51, 4251-4266 (2003)

30. Papazian, J. M.: Met. Trans. A 12A, 269-280 (1981)

31. Auld, J. H.: Mat. Sci. and Tech. 2, 784-787 (1986)

32. Kerry, S., Scott, V. D.: Met. Sci. 18(6), 289-294 (1984)

33. Knowles, K. M., Stobbs, W. M.: Acta Cryst. 44, 207-227 (1988)

34. Muddle, B. C., Polmear, I. J.: Acta Met. 37(3), 777-789 (1989)

35. Garg, A., Howe, J. M.: Acta Met. et Mat. 39(8), 1939-1946 (1991)

36. Flower, H. M., Gregson, P. J.: Mat. Sci. and Tech. 3, 81-90 (1987)

37. Yoshimura, R., Konno, T. J. ., Hiraga, K.: Acta Mater. 51, 2891-2903 (2003)

38. Gault, B., De Geuser, F., Bourgeois, L., Gable, B. M., Ringer, S. P., Muddle, B. C.: Ultramicroscopy 6, 683-689 (2011)

39. Gregson, P. J., Flower, H. M.: J. of Mat. Sci. Lett. 3, 829-834 (1984)

40. Ringer, S. P., Sakurai, T., Polmear, I. J.: Acta Mater. 45(9), 3731-3744 (1997)

41. Ratchev, P., Verlinden, B., De Smet, P., Van Houtte, P.: Acta Mater. 46(10), 3523-3533 (1998)

42. Starink, M. J., Gao, N., Davin, L., Yan, J., Cerezo, A.: Phil. Mag. 85(13), 1395-1417 (2005)

43. Wang, S. G., Starink, M. J., Gao, N.: Scripta Mat. 54, 287-291 (2006)

44. Tolley, A., Ferragut, R., Somoza, A.: Phil. Mag. 89(13), 1095-1110 (2009)

45. Bagaryatski: Dokl. Akad. SSSR 87, 397 (1952)

46. Reich, L., Ringer, S. P. .: Phil. Mag. Lett. 79(9), 639-648 (1999)

47. Majimel, J., Molenat, G., Danoix, F., Blavette, D., Lapasset, G., Casanove, M. J.: Mat. Sci. For. 396-402, 1025-1030 (2002)

48. Majimel, J., Molenat, G., Danoix, F., Thuillier, O., Blavette, D., Lapasset, G., Casanove, M. J.: Phil. Mag. 84(30), 3263-3280 (2004)

49. Marceau, R. K. W., Sha, G., Ferragut, R., Dupasquier, A., Ringer, S. P.: Acta Mater. 58, 4923-4939 (2010)

50. Kovarik, L., Court, S. A. .: Acta Mater. 56, 4804-4815 (2008)

51. Wolverton, C.: Acta Mater. 49, 3129-3142 (2001)

52. Zahra, A. M., Zahra, C. Y., Alfonso, C., Charai, A.: Scripta Mat. 39(11), 1553-1558 (1998)

53. Kovarik, L., Gouma, P. I., Kisielowski, C., Court, S. A. .: Acta Mater. 52, 2509-2520 (2004)

54. Parel, T. S., Wang, S. C., Starink, M. J.: Mat. and Des. 31, S2-S5 (2010)

55. Kovarik, L., Miller, M. K., Court, S. A., Mills, M. J.: Acta Mater. 54, 1731-1740 (2006)

56. Perlitz, H., Westgren, A.: Arkiv. Kemi. Min. Geol. 16B (1943)

57. Mondolfo, L. F.: (1976)

58. Gupta, A. K., Gaunt, P., Chaturvedi, M. C.: Phil. Mag. A 55(3), 375-387 (1987)

59. Boukos, N., Flouda, E., Papastaikoudis, C.: J. of Mat. Sci. 33, 3213-3218 (1998)

60. Feng, Z. Q., Yang, Y. Q., Huang, B., Luo, X., Li, M. H., Han, M., Fu, M. S.: Acta Mater. 59, 2412-2422 (2011)

61. Styles, M. J., Hutchinson, C. R., Chen, Y., Deschamps, A., Bastow, T. J.: Acta Mater. 60, 6940-6951 (2012)

62. Huang, J. C., Ardell, A. J.: Mat. Sci. and Techn. 3, 176-198 (1987)

63. Radmilovic, V., Thomas, G.: J. de phys. 48, 385-396 (1987)

64. Howe, J. M., Lee, J., Vasudevan, A. K.: Met. Trans. A 19A, 2911-2920 (1988)

65. Van Smaalen, S. ., De Boer, J.: J. of Sol. St. Chem. 85, 293-298 (1990)

66. Donnadieu, P., Shao, Y., De Geuser, F., Botton, G. A., Lazar, S., Cheynet, M., de Boissieu, M., Deschamps, A.: Acta Mater. 59, 462-472 (2011)

67. Dwyer, C., Weyland, M., Chang, L. Y., Muddle, B. C.: Appl. Phys. Lett. 98 (2011)

68. Decreus, B.: Etude de la précipitation dans les alliages Al-Li-Cu de troisième génération-Relations entre microstructures et propriétés mécaniques. Phd (2010)

69. Csontos, A. A., Starke Jr, E. A.: Met. and Mat. Trans. A 31A, 1965-1976 (2000)

70. Csontos, E. A., Starke, A. A.: Int. J. of Plast. 21, 1097-1118 (2005)

71. Kolobnev, N. I., Khokhlatova, L. B., Fridlyander, I. N.: Mat. For. 28 (2004)

72. De Geuser, F., Bley, F., Deschamps, A.: J. of App. Cryst. 45, 1208-1218 (2012)

73. Gable, B. M., Pana, M. A., Shiflet, G. J., Starke Jr., E. A.: Mat. Sci. For. 396-402, 699-704 (2002)

74. Shercliff, H. R., Ashby, M. F.: Acta Metall. Mater. 38, 1789-1802 (1990)

75. Shercliff, H. R., Ashby, M. F.: Acta Metall. Mater. 38 (1990)

76. Friedel, J.: Dislocations. Pergamon, Oxford (1964)

77. Nabarro, F. R. N.: Theory of Crystal Dislocations. University Press, Oxford (1967)

78. Kocks, U. F., Meckings, H.: Prog. Mat. Sci. 48(3), 171-273 (2003)

79. Deschamps, A., Brechet, Y.: Acta Mater. 47 (1999)

80. Guyot, P.: Phil. Mag. 24(190), 987-993 (1971)

81. Ardell, A. J.: Met. Trans. A 16A, 2131-2165 (1985)

82. Gerold, V.: Dislocations in Solids 4., Amsterdam: North-Holland (1979)

83. Fullman, R. L.: J. Metals 5, 447-452 (1953)

84. Fribourg, G.: Couplages entre précipitation et plasticité dans un alliage d'aluminium 7xxx : application à des traitements thermomécaniques de réduction des distorsions dans des composants aéronautiques. (2009)

85. Nie, J. F., Muddle, B., Polmear, I. J.: Trans Tech Publ. 217-222, 1257-1262 (1996)

86. Zhu, A. W., Starke Jr, E. A.: Acta Mater. 47, 3263-3269 (1999)

87. Nie, J. F., Muddle, B. C.: Mat. Sci. and Eng., 448-451 (2001)

88. Deschamps, A., Decreus, B., De Geuser, F., Dorin, T., Weyland, M.: Acta Mater. 61(11), 4010-4021 (2013)

89. Nie, J. F., Muddle, B. C.: J. of Phase eq. 19(6), 543-551 (1998)

90. Zhu, A. W., Csontos, A., Starke, E. A.: Acta Mater. 47(6), 1713-1721 (1999)

91. Dong, Y., Nogaret, T., Curtin, W. A.: Met. and Mat. Trans. A 41A, 1954-1960 (2010)

92. Sepehrband, P., Esmaeili, S.: Mat. Sci. and Eng. A 487, 309-315 (2008)

93. Song, M.: Mat. Sci. and Eng. A 443, 172-177 (2007)

94. Myhr, O., Grong, O., Andersen, S. J.: Acta Mater. 49, 65-75 (2001)

95. Simar, A., Bréchet, Y., De Meester, B., Denquin, A., Pardoen, T.: Acta Mater. 55, 6133-6143 (2007)

Chapter II: Material and experimental methods

In this chapter, the material that was investigated during this work, namely AA2198, will first be presented. The thermo-mechanical treatments which have been performed on the specimens in order to reach the desired microstructures will be detailed. Then, the different experimental methods that were necessary in order to carry out this work will be described. The main goal of this chapter is to place each of the techniques used into the general framework of the study. The techniques that have been employed can be classified as follows:

- Characterisation of the T_1-phase microstructure
- Characterisation of localisation of plastic strain
- Characterisation of the mechanical properties

Some of the characterisation techniques that have been used are commonly used in metallurgy and therefore the principle of the methods will not be presented in detail, such as the mechanical tests (micro-hardness and tensile tests). However, more emphasis will be placed upon other techniques such as Small-Angle X-ray Scattering (SAXS), Transmission Electron Microscopy (TEM) and High Angular Annular Scanning Transmission Electron Microscopy (HAADF-STEM), Differential Scanning Calorimetry (DSC) and Confocal Laser Scanning Microscopy (CLSM). The principle of the techniques will first be reminded and the data analysis will then be detailed when necessary.

1. Material and thermo-mechanical treatment

1.1 The AA2198 alloy

The AA2198 alloy is an age-hardenable alloy which belongs to the 2xxx aluminium alloys series. The AA2198 alloy is a recently developed alloy of optimised composition (sometimes referred to as “third generation Al-Li alloys) and it belongs to Constellium’s AIRWARE material technology [1]. Due to its high specific strength, good damage tolerance and ability to withstand great temperature variations, the AA2198 alloy is a key product of the aerospace industry. It is typically formed as rolled plate or extrusions and is utilized as fuel tanks ribs and longerons [2]. The composition of the AA2198 alloy is detailed in Table 8.

A section of the ternary Al-Li-Cu phase diagram was described by Silcock [3] and suggests that only the T_1 and θ’ phases can form for the AA2198 composition at the expense of GP-zones and δ’ (see Figure 23), due to the relatively low composition in Li. This has been confirmed by the detailed study of Decreus. Moreover, the T_1-phase has been shown to be dominant over the θ’ phase when cold working is applied prior to the final ageing treatment. The presence of Ag and Mg have also been revealed to help T_1 nucleation. The main role of Zr in this alloy is to prevent recrystallisation by the formation of the Al_3Zr dispersoids.

The AA2198 alloy was provided by the Constellium Voreppe Research Centre, as a rolled 5mm thick sheet. The sheet was provided in the T351 state that corresponds to approximately 2-4% cold-working after solution treatment and quench, followed by several months of natural ageing.

Table 8: AA2198 alloy composition ranges in wt% as given by the Constellium Voreppe Research Centre, France.

AA2198	*Cu*	*Li*	*Mg*	*Ag*	*Zr*	*Al*
Min	2.9	0.8	0.25	0.1	0.04	bal
Max	3.5	1.1	0.8	0.5	0.18	bal

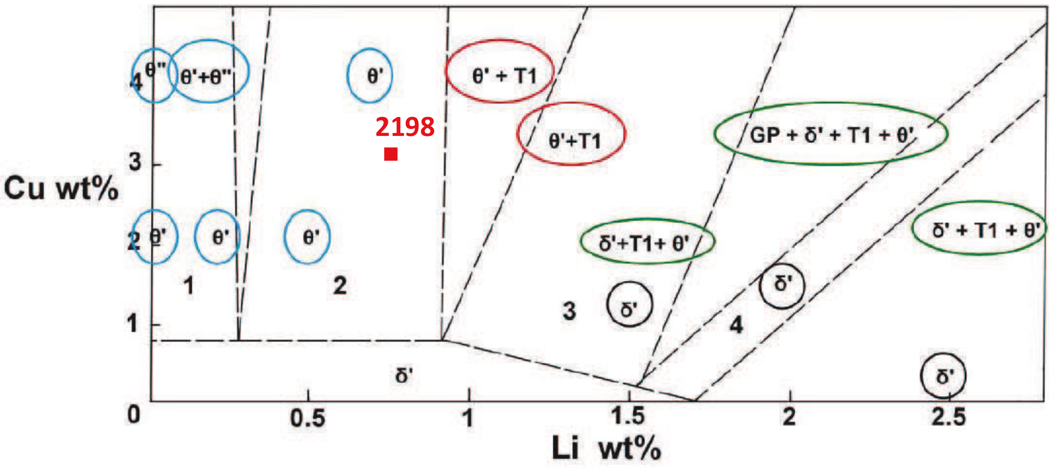

Figure 23: Isothermal section of the Al-Cu-Li ternary phase diagram by Silcock. (taken from Decreus [4])

1.2 **Thermo-mechanical treatments**

A series of thermo-mechanical processes are usually applied to most wrought Al-alloys in order to obtain the desired microstructure characteristics. Figure 2 gives a schematic view of the succession of typical industrial thermo-mechanical treatment steps applied to 2xxx alloys. The first casting step results in the formation of a cast ingot of $\sim 500mm$ in thickness. The ingot is usually cooled down to room temperature and then heated up to $\sim 500°C$ for the hot-rolling process. After a series of hot and cold rolling steps, the alloy thickness is reduced down to its final thickness of $\sim 2-6mm$. The rolling steps determine the resulting grain texture of the alloy. In the case of the AA2198, it results in an unrecrystallized grain structure with a moderate Brass texture {110}<112>. Solutionising followed by water quenching, is then performed in order to retain a Super Saturated Solid Solution (SSSS) of the α-Al matrix. The quenching step results in the presence of residual stresses in the alloy and as a consequence a stress relieving step is usually performed in order to relax these stresses. The precipitation strengthening step is the most crucial and occurs during the final natural and artificial ageing steps. The most important thermo-mechanical steps will be described in more details.

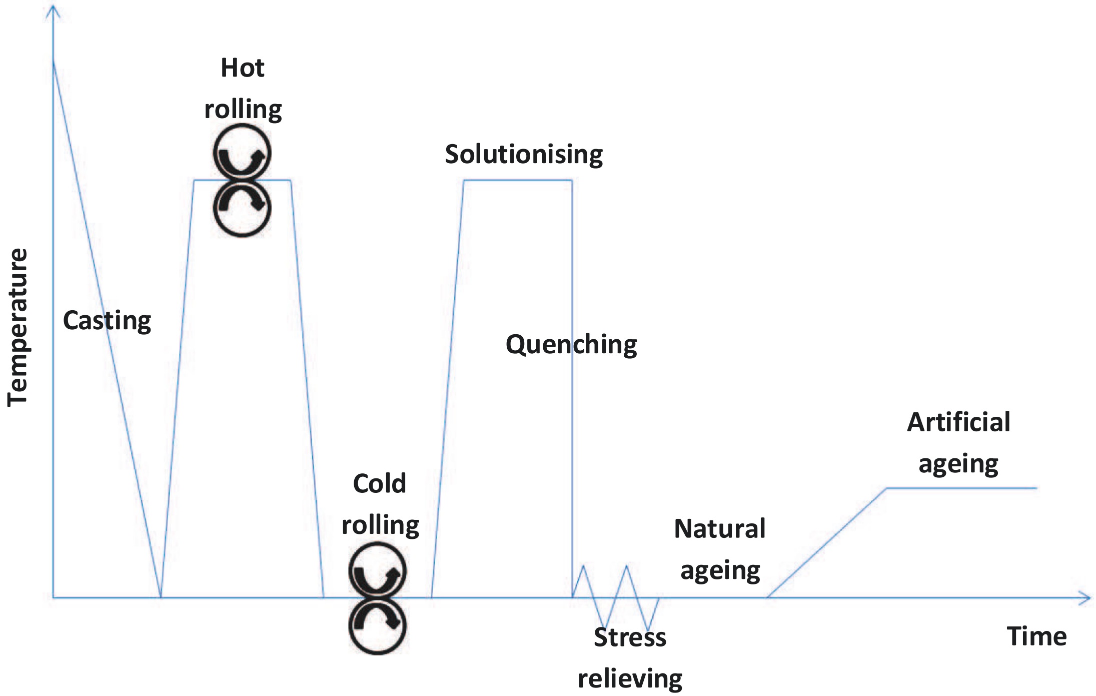

Figure 24 : Schematic of the industrial thermo-mechanical processes for 2xxx Al-alloys.

1.2.1 Solutionising and quenching

The solution treatment is realised at a temperature where all the solutes involved in precipitation hardening are in solid solution. As a consequence, the temperature must be above the solvus of the alloy and the treatment must be long enough to allow time for diffusion. During this step, the coarse precipitates, which have formed during the previous thermo-mechanical treatments, are dissolved and the solute elements are redistributed into the Al-matrix. The temperature and duration of the solutionising treatment must be chosen carefully in order to avoid undesirable effects such as local melting or solute depletion at the samples' surfaces. In the present study, the solutionising process was performed at 510°C for 30 min.

In order to create a SSSS at room temperature, the second step is to quench the alloy. This step is critical and has to be executed fast enough to avoid undesirable segregation especially at the grain boundaries, which would be detrimental to the mechanical properties. In this work, quenching was performed in cold water ($\sim 15°C$) on samples of thickness up to 3mm.

1.2.2 Residual stresses and stress relieving

Residual stresses are caused by plastic deformation during rapid cooling due to the heterogeneity of thermal contraction within the material's thickness. These stresses are highly undesirable as they can cause distortion during machining or assembly. The stress relieving method can either be thermal or mechanical. For precipitation hardening Al alloys, stress relieving is performed by applying a small plastic deformation (of the order of 2 to 4%) in the rolling direction. The alloys which have been solution treated, quenched, stress relieved and naturally aged are denominated T351.

When carried out in the laboratory, the stress relieving stage is denominated pre-deformation. In the current study we applied pre-deformation from 0 to 12% to the studied samples. The amount of pre-deformation applied is a key parameter that controls the resulting precipitation. It is notably the case for 2xxx alloys, where the strengthening particles tend to preferentially nucleate on dislocations.

1.2.3 Natural and artificial ageing

The principle of age-hardening lies in the decomposition of the SSSS into a fine dispersion of strengthening precipitates. If the alloy is maintained at room temperature directly after quenching, it will experience so-called 'natural ageing'. The SSSS starts to decompose into small clusters of particles. For instance, in binary Al-Cu alloys, precipitates called GP-zones (Guinier Preston) start to form as mono-layers of Cu, which results in an increase of the yield strength. Depending on the alloying elements, it will take more or less time for the alloy to stabilise at room temperature ranging from a few days in 2xxx alloys to a few years for 7xxx alloys.

After some of the natural ageing stage has occurred, a heat treatment is carried out, called artificial ageing. Artificial ageing is a medium temperature heat treatment, generally below 250°C, with a time of heat treatment typically between 10 to 100h. The heat treatment temperature is reached with a slow heating rate, usually below 50°C/h, which permits the dissolution of clusters that formed during natural ageing. During this heat treatment, the alloy will reach peak strength (the T8 state). When heat treated before the peak ageing state, the sample is usually denominated as "under-aged" and when heat treated longer, it is referred to as "over-aged".

Two types of heat treatments were used in this study with an initial heating ramp of 20°C/h. First a classical isothermal treatment at 155°C, and secondly a duplex ageing treatment, with a first isothermal treatment for 18h at 155°C followed by a second treatment at 190°C.

2. Characterisation of the T_1 microstructure

The T_1 phase is the main strengthening phase in Al-Li-Cu alloys. The structure of this phase has been extensively studied in the literature [5,6,7,8] and is now clearly defined. The T_1 phase forms as semi-coherent platelets along the $\{111\}_{Al}$ planes with an hexagonal structure. The particularity of these precipitates relies on their high aspect ratio with a small dimension of ~1nm (referred to as thickness) and a large dimension in the range of 100nm (referred to as diameter). Due to the small dimension and the anisotropy of this phase, a large range of techniques is necessary to reach a full characterization. As it was highlighted previously, the AA2198 alloy has a moderate rolling texture, the rolling plane is along the $\{110\}_{Al}$ planes of the matrix and the rolling direction is in the $<112>_{Al}$ direction. Such a texture is ideal for the characterisation of plate-like precipitates along the $\{111\}_{Al}$ and $\{001\}_{Al}$, seen "edge-on" (Figure 25) using scattering-based techniques such as SAXS and TEM. Two T_1 variants (out of four) and one θ' variant (out of three) are observed edge-on.

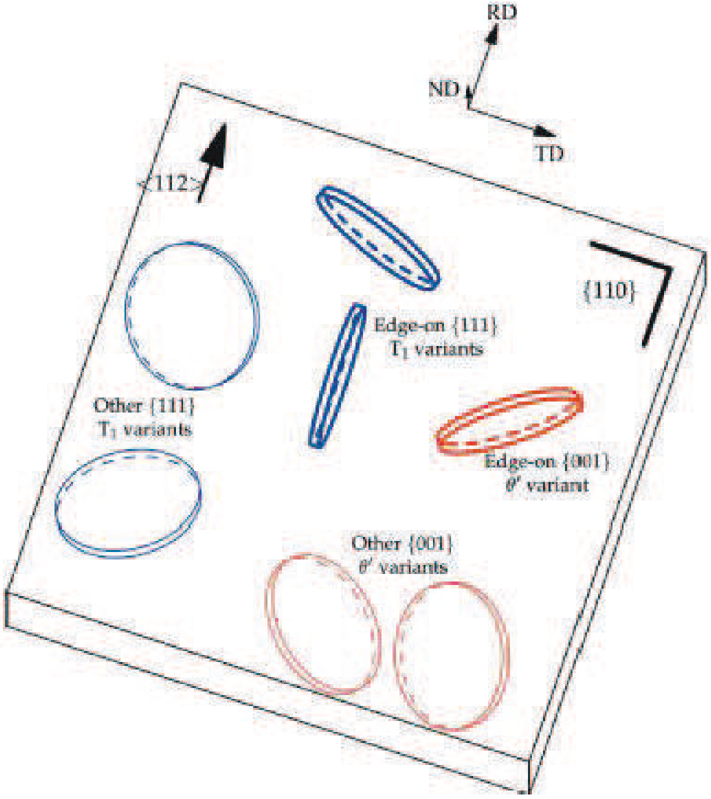

Figure 25 : Illustration of the rolling texture of the AA2198 alloy. The rolling plane corresponds to the $\{110\}_{Al}$ planes of the Al matrix and the rolling direction is $<112>_{Al}$. Two variants of the $\{111\}_{Al}$ plate-like precipitates are perpendicular to the main plane and thus generate a strong scattering signal (taken from De Geuser et al. [9]).

The T_1-phase is the most desirable phase as it provides the highest strength. As it nucleates on dislocations, cold-working prior to the ageing treatment favours the presence of the T_1 phase [10,11,12,13]. Conventional TEM is used to obtain a local measurement of the T_1 diameter. The HAADF-STEM technique permits the observation of the T_1 shearing events on deformed samples. The DSC technique allows following the T_1 precipitation evolution and we will present later, in chapter III, a new method to extract the T_1 volume fraction evolution from DSC measurements. The SAXS technique allows to obtain in-situ the evolution of the mean diameter and thickness of the T_1 precipitates. All of these techniques complement each other in order to give an accurate description of the T_1 phase morphology in terms of diameter, thickness, volume fraction and number density (refer to chapter III).

2.1 **Transmission Electron Microscopy (TEM)**

2.1.1 Equipment

The conventional TEM was performed at the SIMAP laboratory on a JEOL 3010 300kV. The HAADF-STEM has been conducted at two places:

- At the centre of microscopy of Monash University, Melbourne, Australia on a Titan^3 80-300 FEGTEM operating at 300KV with an objective aperture semi-angle of 15mrad and a detector half-collection angle of 48mrad.
- At the University of Rouen, France on a JEOL ARM 200F equipped with a Schottky field emitter and operating at 200kV with an objective aperture semi-angle of 22.5mrad and a detector half-collection angle between 40 and 150mrad.

2.1.2 Samples

The samples for TEM observations were first mechanically polished into thin foils of $\sim 100\mu\mathrm{m}$. The specimens were then punched into 3mm diameter discs that were electro-polished using a twin double jet system in a solution of 33% nitric acid in methanol at -20°C and 15V. The analysed area is usually $\sim 100\mathrm{nm}$ thick.

2.1.3 Principle of Conventional Transmission Electron Microscopy

The classic scheme of a TEM column is displayed in Figure 26a. The TEM first consists of an emission source which may either be thermoionic, Schottky or field emission. The JEOL 3010 TEM electron gun is thermoionic with a LaB_6 emission source. A succession of lenses is then used to accelerate the electrons to the desired voltage and focus the beam. It results in a mono-energetic, parallel beam of electrons that passes through the thin specimen. The interactions between the electrons and the specimen can either occur without energy loss (elastic interactions) or with energy transfers (inelastic interactions).

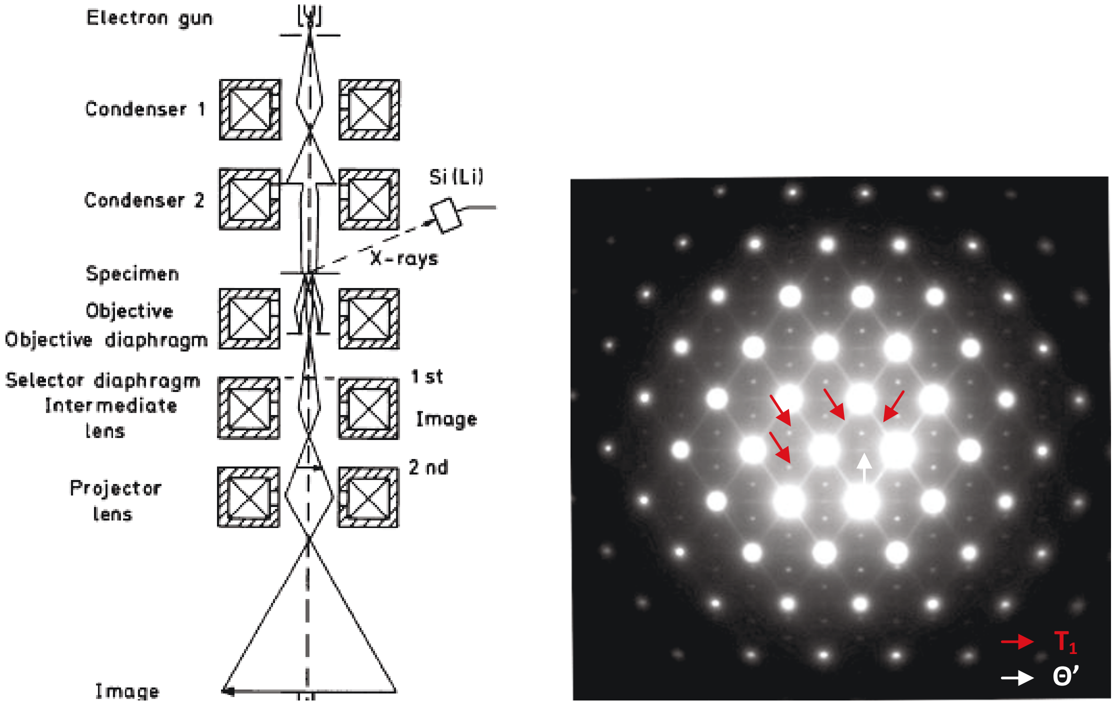

Figure 26 : (a) Schematic of a TEM column (taken from Reimer and Kohl [14]), (b) Selected Area Diffraction pattern of an AA2198 sample along the <110> zone axis.

The diffraction theory applies to elastically scattered electrons which behave as waves. The wavelength of high-energy electrons is of the same order as the atomic spacing and thus results in the diffraction of the incident electrons. Selected Area Diffraction (SAD) can be performed in order to record a section of the reciprocal space. An example of SAD Pattern obtained on an AA2198 alloy heat treated to the T8 state along the <110> zone axis is displayed in Figure 26b. The intense diffraction spots correspond to the diffraction from Al matrix planes. The sub-lattice diffraction spots and streaks correspond to the diffraction from small oriented objects in the sample. In this case the diffraction streaks come from edge-on plate-like T_1 precipitates (two variants) and θ’ precipitates (one variant) and the sub-lattice spots come from inclined plate-like T_1 precipitates (two variants).

The objective diaphragm (see Figure 26a) allows us to record an image by selecting only a part of the scattered signal. Bright Field (BF) is performed when imaging the transmitted beam only. The contrast obtained in the BF mode is referred to as ‘diffraction contrast’. Figure 27 (a) displays a BF image that was taken along the <112> zone axis, on an AA2198 sample heat treated to the T8 state. Along the <112> axis, one T_1 variant can be imaged edge-on. The dark areas correspond to objects or inhomogeneities in the sample that have diffracted the electrons. In the AA2198, the BF technique is often not desirable due to the presence of a high density of objects and microstrains that result in a high but spatially heterogeneous contrast. The Dark Field (DF) mode consists in imaging a part of the diffracted signal. This type of imaging permits a focus on the electrons diffracted by a specific type of objects. The image in Figure 27 (b) corresponds to the same area as in Figure 27 (a) imaged in DF. This image has been recorded by selecting the diffraction signal from one variant of the T_1 precipitates. The selected zone to perform the DF image is highlighted on the diffraction pattern. In our study, these two modes have commonly been used in the study of the morphology and size distributions of the T_1 precipitates. DF imaging was favoured to obtain T_1 diameter distributions.

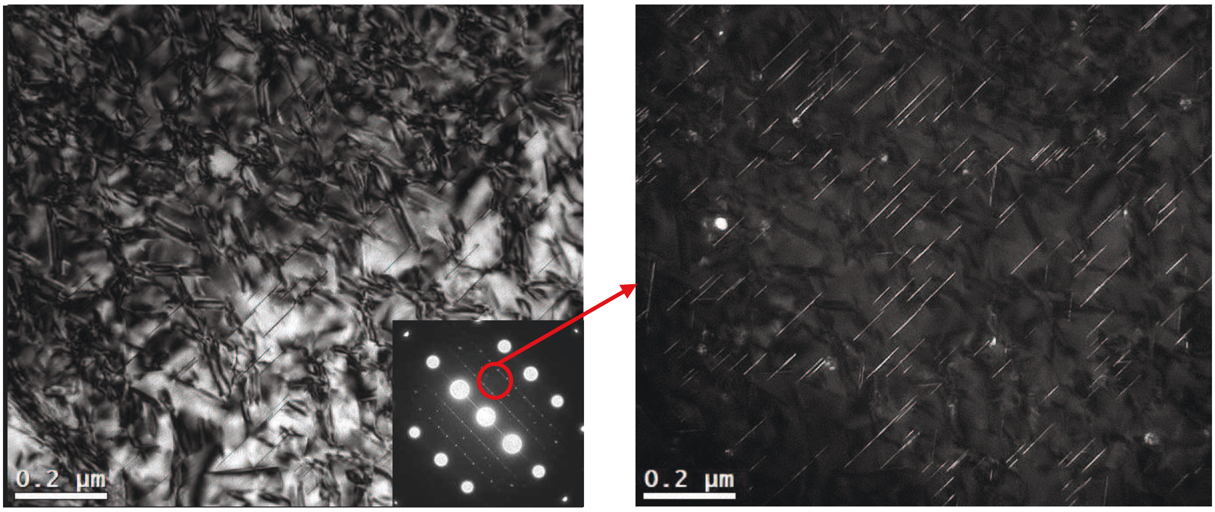

Figure 27 : (a) BF image taken along the <112> zone axis on an AA2198 specimen heat treated to the T8 state and (b) DF image of the same area.

2.1.4 Principle of High Angular Annular Dark Field Scanning Transmission Electron Microscopy (HAADF-STEM)

The HAADF-STEM technique uses a detector to collect inelastically scattered electrons at large angles. These electrons are the result of energy transfers with the atoms and thus their scattering cross-section is directly linked with the element they interacted with. As a consequence, the HAADF-STEM contrast is proportional to the square of the atomic number (Z^2). Figure 28 gives a schematic view of the observed regions in conventional TEM and in HAADF-STEM.

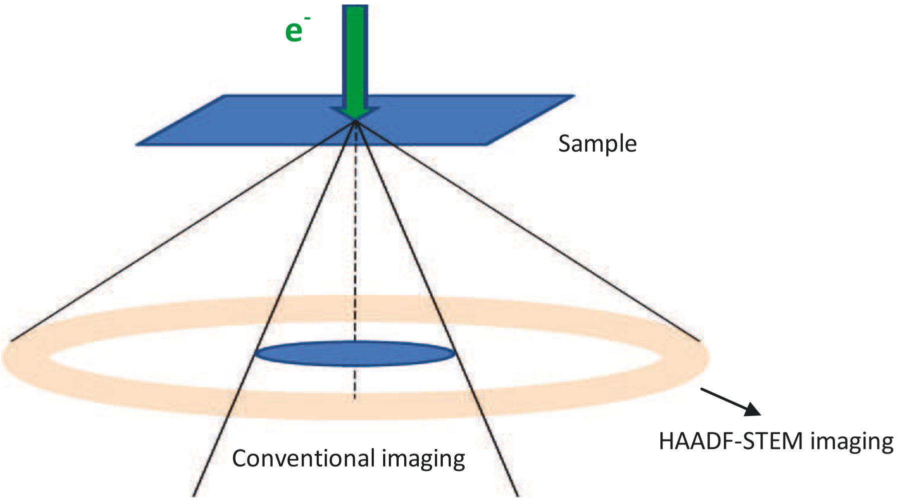

Figure 28 : Scheme that presents the differences between conventional TEM and HAADF-STEM.

HAADF-STEM was used in order to study the strengthening mechanisms involved in the presence of the T_1 phase. The samples that were analysed were heat treated in different conditions and then plastically deformed 2%. The observations of sheared T_1 were then carried out on the different samples. The Z^2 resolution of the HAADF-STEM technique makes it ideal to the observation of T_1 precipitates. Indeed, when a T_1 precipitate is observed edge-on, it is mainly composed of one Li-rich layer (dark contrast) surrounded by two Cu-rich layers (bright contrast). Figure 29 shows an image of an unsheared edge-on T_1 and of sheared edge-on T_1 taken along the <110> zone axis recorded in HAADF-STEM on an un-deformed and a deformed AA2198 sample in the T8 state.

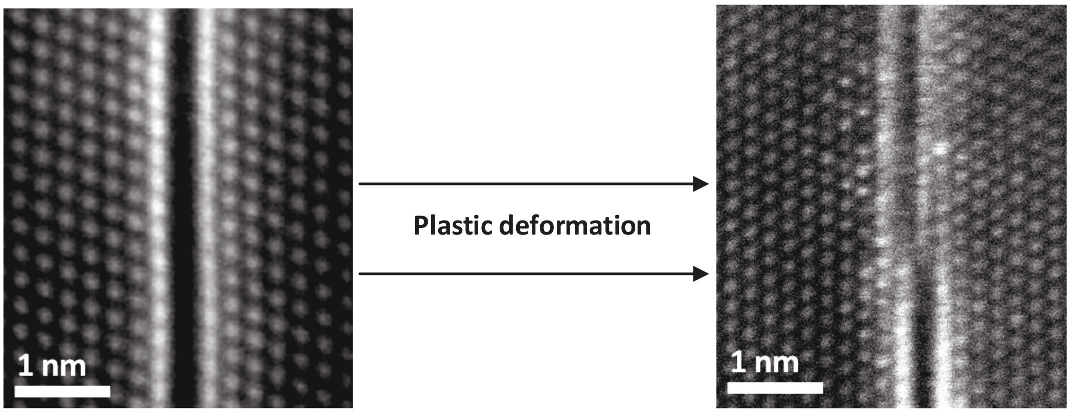

Figure 29 : Image of two edge-on single-layer T_1 precipitates (sheared and unsheared) taken in HAADF-STEM along the <110> zone axis.

2.2 **Differential Scanning Calorimetry (DSC)**

2.2.1 Equipment

DSC measurements were carried out in a Perkin Elmer Pyris Diamond apparatus.

2.2.2 Samples

The samples consisted of 0.5mm thick disks, 4mm in diameter, in order to fit in the dedicated pure aluminium crucibles. An empty crucible is used as a reference. The influence of sample preparation on the results in the case of Al-alloys has been studied by Starink et al. [15]. The impact of dislocation introduced during sample cutting and grinding can result in a significant effect on the resulting precipitation reaction. Furthermore, the impact of sample thickness on the loss of light elements (such as Li) has been observed. In order to limit the impact of these elements, the ageing treatments were always performed prior to the sample preparation. The surface roughness corresponds to a mechanical polishing down to a SiC 1200 paper. The samples studied in DSC are extracted at different times during a given heat treatment.

2.2.3 Principle

The DSC is a thermo-analytical technique that allows the measurement of the heat flow between a specimen and a reference when submitted to temperature variations. The principle scheme of a DSC is shown in Figure 30. On the Perkin-Elmer apparatus, the samples are displayed in two separated calorimeters. The heat flow that is measured corresponds to the difference in energy needed to maintain both calorimeters at the same temperature. This difference comes from the absorbed and released energy from the sample. The calorimeters are maintained under a neutral atmosphere by continuous nitrogen circulation.

In the case of Al-alloys, DSC can for instance be used to study the solid-solid transformations such as precipitation, dissolution and recrystallisation. The evolutions of the phases can be characterised; roughly speaking, the exothermic peaks correspond to precipitation peaks while endothermic peaks correspond to phase dissolution. The phase transformation temperatures, activation energies and phase volume fractions can usually be obtained from DSC measurements.

In the current study, DSC was used in order to follow the precipitation evolution on samples which were aged at different times at a given temperature. The DSC procedure consisted in a ramp in temperature from -40°C to 520°C at 50°C/min. We chose to start at an initial temperature of -40°C in order to allow enough time for the apparatus to stabilise when reaching room temperature.

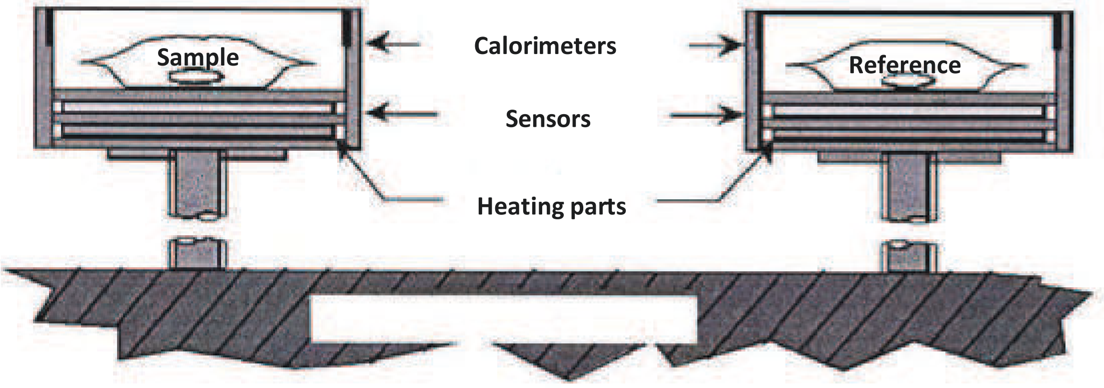

Figure 30 : Schematic of the DSC Perkin-Elmer Pyris-Diamond apparatus

2.2.4 Data analysis

During the DSC ramp, the precipitation reactions that were initiated during the artificial ageing treatment will complete and finally all the precipitates formed will dissolve. As a consequence, it is possible to follow the relative evolution of precipitation during the artificial ageing treatment and we will demonstrate later that it can be translated into the T_1 volume fraction evolution.

A systematic correction procedure of the measured heat flows has been established. From now on, the heat flows will always be displayed with the endothermic peaks facing up and the exothermic peaks facing down. The heat flows are systematically normalised from the sample mass which is always measured prior to the DSC experiment.

2.2.5 Correction procedure

The heat effects that are recorded during the DSC ramp are due to the reactions occurring in the alloy but also to numerous parasitic effects. Indeed, the presence of the crucible, the sample preparation [15], the heat capacity evolution with temperature and the instability in time of the system are some of the elements often encountered when performing DSC [16]. The baseline instability often makes it difficult to realise an accurate baseline measurement. In order to isolate the heat effects caused by the transformations occurring solely in the alloy, we developed a numerical correction method in order to overcome the unpredictable variability of the baseline. The correction steps will be detailed on a sample heat treated to the end of ramp (EoR) (20°C/h from 35°C to 155°C). The reproducibility of the correction methods will be demonstrated later in chapter III.

The first step in the correction procedure is based on the limit conditions. Indeed, if we assume that no heat effects are due to phase transformations at low temperature (<100°C) before the main precipitation occurs and above 500°C when the material is back in solid solution, one can deduce:

$$\text{For } T < 100°C \text{ and } T > 500°C \quad Q_i^{corr1}(T) = 0 \tag{15}$$

where $Q_i^{corr1}(T)$ is the heat flux as a function of temperature recorded for the sample i, after the first correction step.

As a result, the first correction lies in the subtraction of a linear contribution $Q_i^{lin}(T)$ such as:

$$Q_i^{corr1}(T) = Q_i^{measured}(T) - Q_i^{lin}(T) \tag{16}$$

where $Q_i^{lin}(T)$ is a linear fit of $Q_i^{measured}(T)$ in the following temperature range: $T < 100°C$ and $T > 500°C$. The DSC heat flow of an EoR sample, normalized by the sample mass and the corresponding linear fit are represented in Figure 31a and the heat flow after the linear correction is displayed in Figure 31b.

The second correction step is based upon the assumption that the final dissolution peak should always be the same, whatever the initial microstructure in the sample. In all the samples, the precipitation, which was initiated during the heat treatment, completes during the DSC heating ramp and thus should result in the same dissolution peak when temperature is sufficiently high so that the alloy is at thermodynamic equilibrium at all times. We stated that the final dissolution peak should be equal to a mean dissolution peak. The average signal can be written as follow:

$$\mathrm{Q_{moy}(T)} = \frac{\sum_i Q_i^{corr1}(T)}{N} \tag{17}$$

where $Q_{moy}(T)$ is the average DSC signal and N is the number of samples analysed for a given heat treatment. The average heat flow was measured on 14 samples heat treated at different times at 155°C and displayed in Figure 31c.

$Q_{moy}(T)$ is subtracted from the DSC signals such that:

$$Q_i^{'}(T) = Q_i^{corr1}(T) - Q_{moy}(T) \tag{18}$$

Our hypothesis that the dissolution peak should be the same for all the samples, can translate into the following statement when considering the final corrected signal $Q_i^{corrected}(T)$:

$$\text{For } T > 400°C,\ Q_i^{corrected}(T) = 0 \tag{19}$$

$Q_i^{'}(T)$ is thus fitted with a polynomial fit with an order of 4 and subtracted to the signal such that:

$$Q_i^{corrected}(T) = Q_i^{corr1}(T) - Q_i^{pol}(T) \tag{20}$$

The corrected DSC signals $Q_i^{corrected}(T)$ for the EoR sample is plotted in Figure 31d. In chapter III, we will demonstrate how it is possible to extract the T_1 volume fraction from a corrected DSC heat flow.

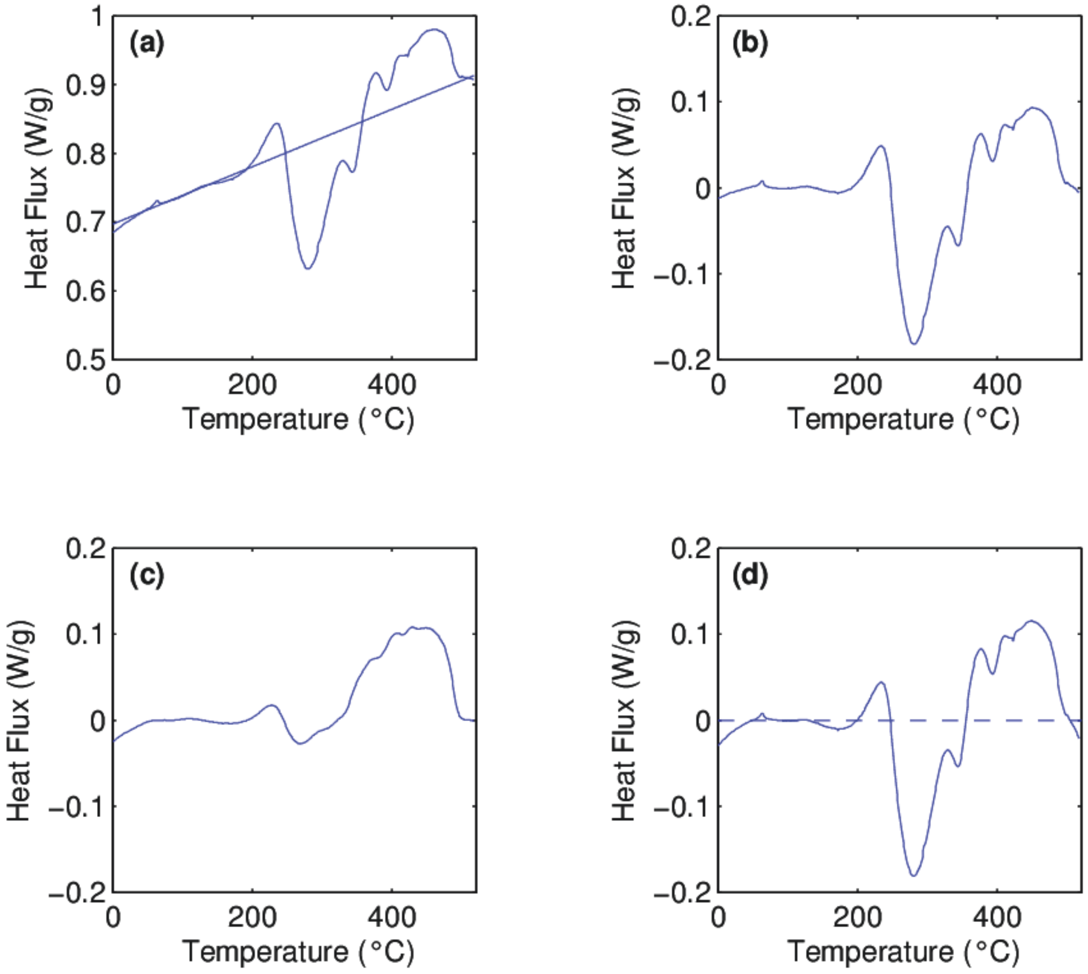

Figure 31: Different correction steps performed on the heat flow recorded in DSC on an EoR sample.

2.3 **Small Angle X-Ray Scattering (SAXS)**

2.3.1 Equipment

SAXS measurements were realised both at the BM02-D2AM beamline of the synchrotron ESRF (Grenoble) and on a laboratory rotating anode system (Cu Kα source). In this part, the SIMAP laboratory equipment will only be detailed as most of the experiments were performed on this system.

2.3.2 Samples

The main criterion to consider when preparing a sample for a SAXS experiment is to optimise the sample thickness to maximize the scattered signal. Indeed, if the sample is too thick, it would absorb most of the incident X-Ray beam while if the sample is too thin the scattered signal would not be intense enough to be exploitable. The transmission rate can be estimated thanks to the following expression:

$$tr = \frac{I_{scatt}}{I_{inc}} = \exp\left(-\left(\frac{\mu}{\rho}\right)_{alloy} * \rho_{alloy} * t\right) \qquad \textbf{(21)}$$

Where tr is the sample transmission, μ is the absorption coefficient of the material (mm^{-1}), ρ is the alloy's density and t is the sample's thickness.

$$\left(\frac{\mu}{\rho}\right)_{alloy} = \sum_i C_i \left(\frac{\mu}{\rho}\right)_i \qquad \textbf{(22)}$$

Where C_i is the mass concentration in the i element and $\left(\frac{\mu}{\rho}\right)_i$ is estimated for each element i.

In the case of the AA2198 alloy, the optimal thickness has been estimated to ~75µm. The absorption coefficients values were taken on the following website: http://www.csrri.iit.edu/mucal.html.
Prior to the measurements, the samples were mechanically grinded down to the optimal thickness and mirror polished.

2.3.3 Principle

Small-Angle Scattering and more particularly Small-Angle X-Ray Scattering are commonly used to measure precipitates sizes in the nanometre range in metallic systems. On the laboratory instrument, the X-Ray emission source is a rotating anode of power 1.2kW. The X-Rays are created by bombarding a Cu electrode with electrons generated by heating a tungsten filament. A multi-layer mirror is then used to select the correct wavelength ($\lambda = 1.5406$ Å) and successive slits are then utilized to focus and design the X-Ray beam to the optimum size. A dedicated furnace, placed in the X-Ray beam, was used for in-situ measurements which allowed having precise information on the precipitation kinetics.

2.3.4 Data analysis

Analysing a small angle scattering pattern goes back to the study of the Fourier transform of the analysed objects. In the case of a distribution of spherical particles, the scattered intensity at small angle can be approximated to a Gaussian function. In this case, the classical parameter that is extracted from the scattered intensity is the Guinier radius [17]. In the case of a distribution of spherical precipitates, there is a simple relation between the Guinier radius and the precipitate mean radius; the volume fraction and number density of particles can also be estimated.

In the case of plate-like particles, the data treatment is not as straightforward. From now on, most of the method that will be presented is based on a recent paper by De Geuser et al. [9] that explains how to extract quantitative measurements on plate-like precipitates from SAXS experimental patterns. Their protocol has been proven successful in the case of the AA2198 alloy. For more details, please refer to the actual paper.

If a plate-like precipitate is approximated by a cylinder, the Fourier transform will give rise to a streak in the reciprocal space as depicted in Figure 32. Fratzl et al. [18] examined the scattering signal of plate-like particles in the case of a single-crystal. In that case, the authors used Guinier type plots, in the direction of the streaks, in order to extract information on the precipitates sizes. However, industrial metallic systems are usually polycrystalline. If the texture is completely random, with an associated random orientation of the plates, then the scattered pattern on a 2d-detector would be isotropic and a global analysis of the intensity would be possible. However, the AA2198 alloy is polycrystalline with a moderate Brass texture. The SAXS experimental pattern of an AA2198 specimen in the T8 state is shown in Figure 33a. Due to the dominant Brass texture, two T_1 variants are perpendicular to the incident X-Ray beam, thus giving rise to scattered streaks. The angular distribution of the grains' orientations results in a symmetry in the SAXS pattern, along the rolling direction, thus resulting in three apparent streaks. Due to the symmetry of the texture and crystals' angular distribution, the streak perpendicular to the rolling direction should be weighted by a factor 2 and the two other streaks should be weighed by a factor 3.

The widths of the streaks contain information on the precipitates length (diameter) while the lengths of the streaks contain information on the precipitates thickness. In order to analyse the data from a scattering pattern such as the one in Figure 33a, the intensity is extracted in angular sector as a function of the scattering vector q (see Figure 33b). The obtained intensities can be fitted as a sum of six Lorentzian functions such as

$$I(\alpha) = Bg + \sum_i \frac{A_i}{\pi} \frac{{\sigma_i}^2}{(\alpha - {\alpha_i}^2) + {\sigma_i}^2} \tag{23}$$

Where A_i are the amplitudes, α_i the centers and σ_i the width of the six peaks (i=1 to 6). Bg is a constant that accounts for the background signal which comes from the scattering of isotropic particles such as clusters. All the Lorentzian parameters (A_i, α_i, σ_i) are extracted for the six peaks and for each value of q. They can be related to the precipitate dimensions. The thickness of the precipitates is related to the intensity along the streaks. By considering this, De Geuser et al. come down to the following expression:

$$\mathrm{A_i \sigma_i q^2} \propto \frac{\sin\left({}^{qt}/_{2}\right)}{{}^{qt}/_{2}} \tag{24}$$

Where $\mathrm{A_i}$ and $\mathrm{\sigma_i}$ are the amplitudes and widths for peak i (i=1 to 6) and t is the mean T_1 thickness. A fitting procedure using the ${}^{\sin(x)}/_{x}$ function can then be performed to calculate the thickness t.

In order to determine the precipitates mean diameter, the following expression can be used:

$$\frac{\kappa}{\mathrm{\sigma_i q}} = \frac{R}{1 + f_{rot}(q)} \tag{25}$$

Where κ is a constant, R is the precipitates mean radius and $f_{rot}(q)$ is a function that accounts for the texture rotation distribution which affects the apparent widths of the streaks. The latter function can be described as a second order polynomial function such as $f_{rot}(q) = aq^2 + bq$. A value of $\kappa = 2$ was used in this work. The mean precipitate radius R can be found as the extrapolation to q=0 of the fit of ${}^{\kappa}/_{\sigma_{\mathrm{i}}\mathrm{q}}$ as a function of q.

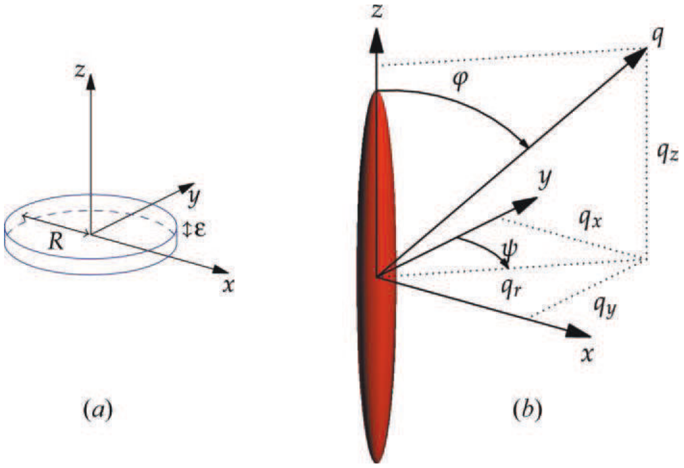

Figure 32: Flat particle associated to a cylinder (a) in the direct space and (b) in the reciprocal space. (taken from De Geuser et al. [9])

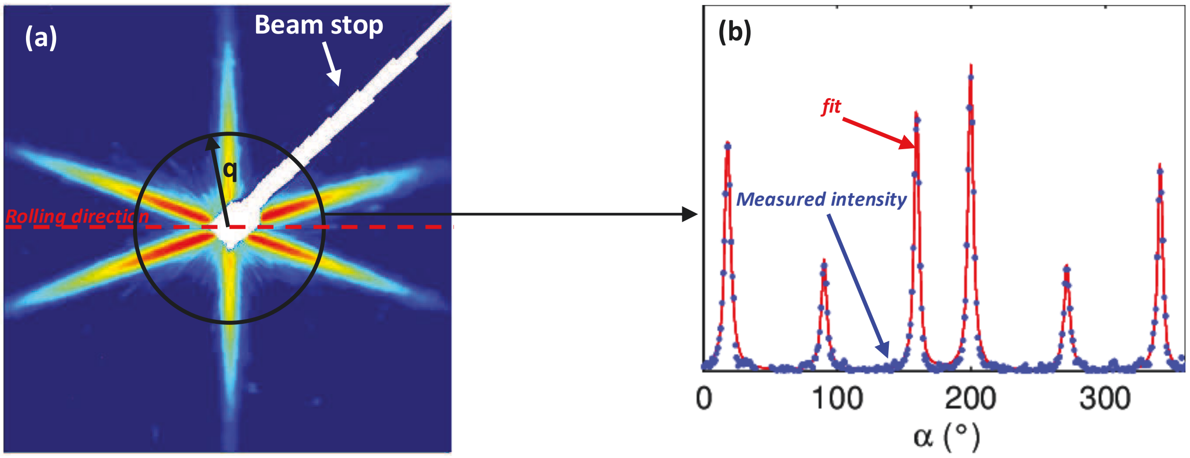

Figure 33: (a) SAXS experimental pattern recorded from an AA2198 specimen heat treated to the T8 state and (b) angular section of the SAXS intensity at one scattering vector q.

3. Characterisation of the plastic strain localization

The study of plastic strain localization was carried out in order to get a better understanding of the strengthening mechanisms involved in the presence of the T_1 phase. Indeed, the plasticity behaviour of a metallic system highly depends on the deformation properties of its strengthening particles. A good way to study the localization of plasticity is to study the evolution of shear bands. Two techniques have been used to observe shear banding on the samples' surfaces. Nomarski type Optical microscopy was used in order to get a macroscopical view of the shear bands density. To get a finer description of the shear bands, Confocal Laser Scanning Microscopy (CLSM) has also been carried out.

The tensile samples are heat treated to different conditions, then mirror polished and strained up to 2% plastic deformation. Special care has to be taken not to damage the samples surfaces when strained. The observations are then carried out directly on the samples' surfaces. The same samples are used for optical microscopy and CLSM observations.

3.1 Nomarski Optical Microscopy

3.1.1 Equipment and use

The Nomarski type observations give a differential interference contrast which permits the observation of small topographic details on a sample's surface [19]. Figure 34 shows an example of image, in Nomarski contrast, taken on an AA2198 sample heat treated to the T8 state and then deformed plastically 2%. The presence of shear bands is highlighted on the sample's surface. One can notice that the orientation of the shear bands depends on the grain's orientation.

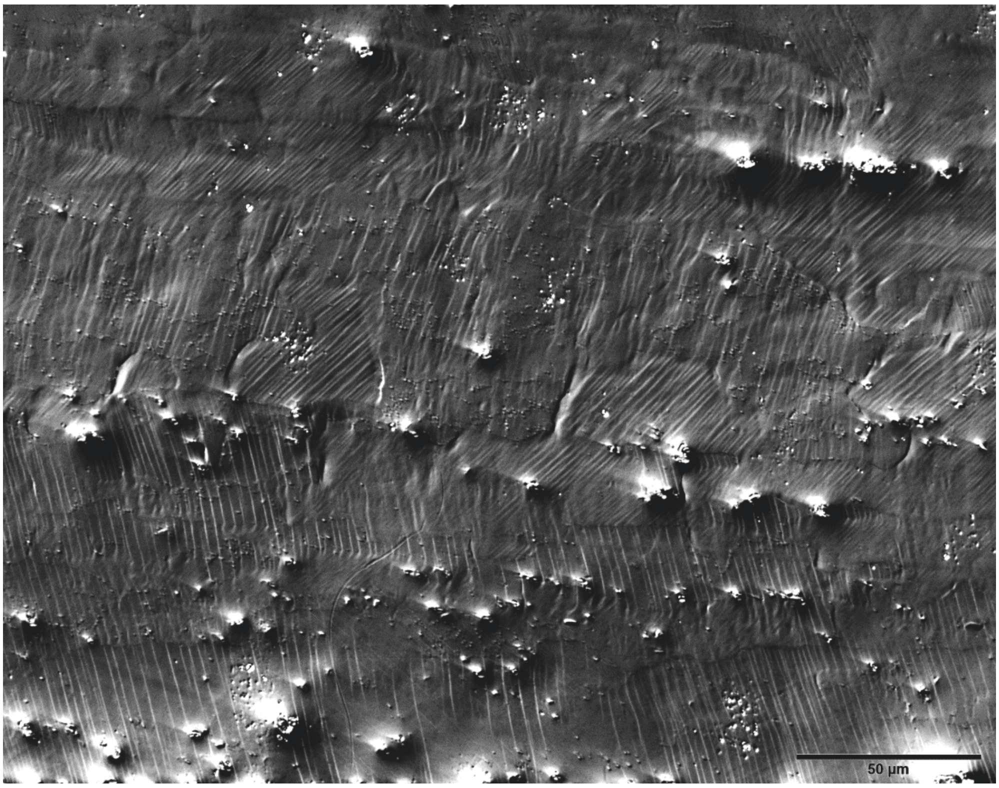

Figure 34: Image taken in the Nomarski contrast of an AA2198 sample's surface after 2% plastic deformation.

3.2 Confocal Laser Scanning Microscopy (CLSM)

3.2.1 Equipment

The experiments were conducted at the University of Poitiers on a Talysurf CCI 6000 microscope.

3.2.2 Principle

The main interest of a CLSM as compared to an optical microscope is to perform imaging with a high resolution in depth (typically $\sim 1nm$). The x and y resolutions however are of the same order as for the optical microscope ($\sim 1\mu m$). The principle of a CLSM is depicted in Figure 35. A monochromatic light emission source is used. The principle of this technique relies on optical interferometry; a semi-reflecting mirror reflects part of the incident light while the rest of the light goes through and is reflected by the sample, those two beams will then interfere. Optical interferometry happens when two waves of same frequency superimpose. The sample points which reflect the maximum intensity are situated in the focal point of the reference mirror. As a consequence, the height z of these points is determined. The microscope conducts a series of images in a given range in height z with highly precise movement governed by a piezo-electric actuator. The heights are then indexed step by step and a three dimensional representation of the sample surface is obtained by computer reconstruction.

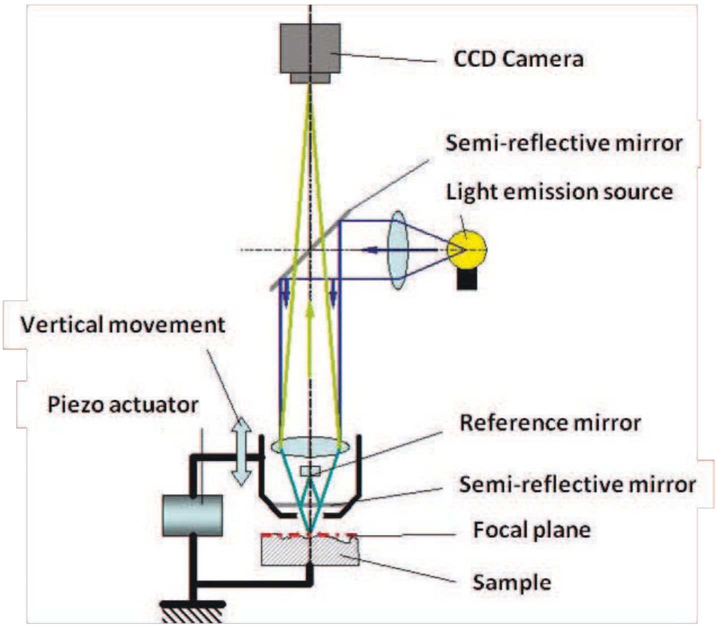

Figure 35 : Schematic of the Talysurf CCI 6000 CLSM.

3.2.3 Data analysis

The results are obtained on the form of a 3d mapping of the sample's surface. Figure 36a shows an image of a sample's surface heat treated to the T8 state and then deformed plastically 2%. The variations on the surface are due to the shear bands but also to parasitic variations that have larger wavelengths than the shear bands. These variations come from mechanical grinding, impurities or intermetallics at the sample's surface. A Gaussian-type filter can be used in order to cut-off these oscillations. The result of the Gaussian filter is represented in Figure 36b. The Gaussian filter is subtracted from the initial mapping in order to only keep the shear bands' oscillations (Figure 36c). A precise description, in terms of shear bands height and inter-band spacing can be obtained.

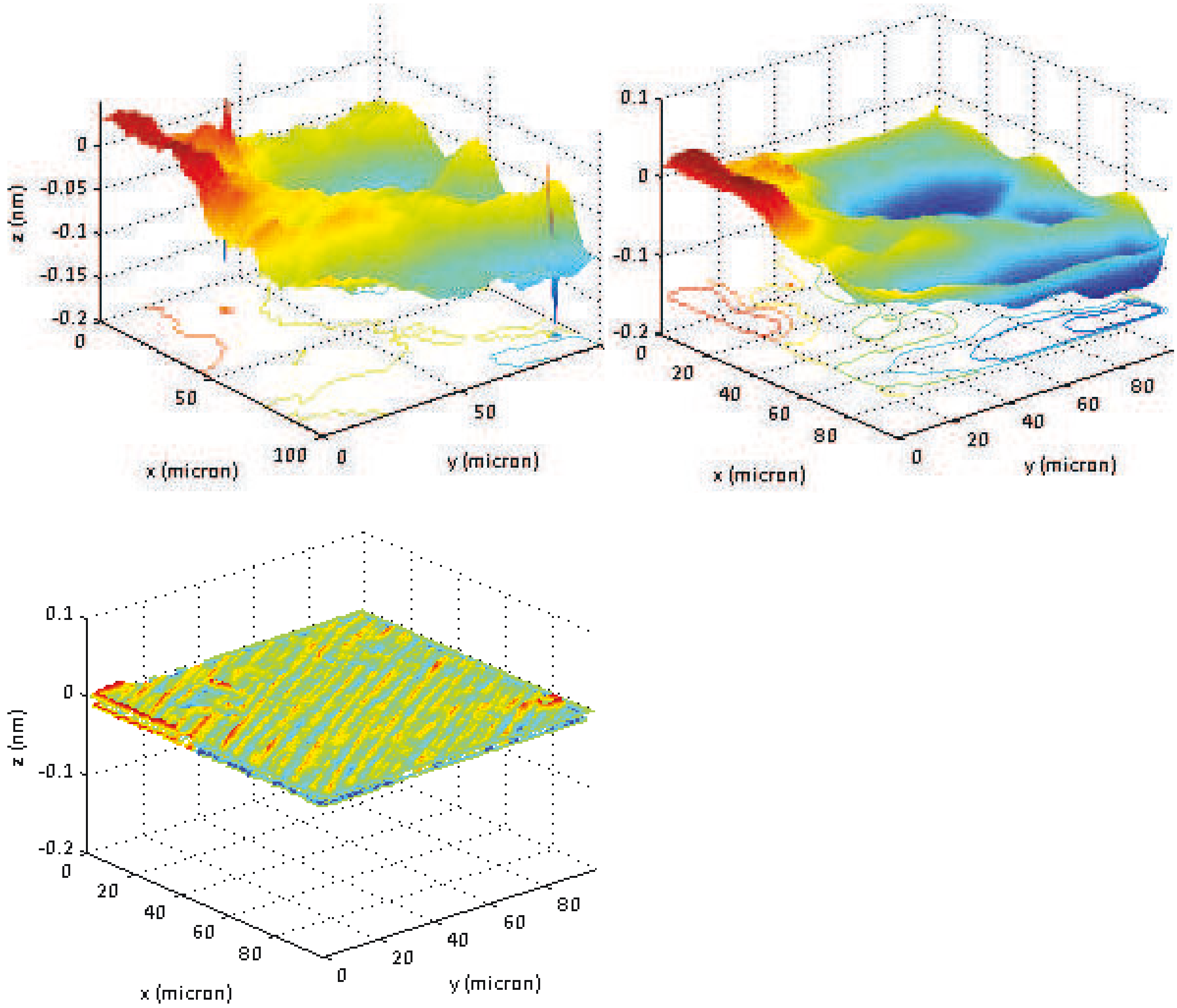

Figure 36 : (a) 3d mapping of a sample's surface that was heat treated to the T8 state and then deformed plastically 2%, (b) 3d mapping of the Gaussian filter that is applied to variations of large wavelengths and (c) 3d mapping of the sample's surface after correction revealing the shear bands.

4. Characterization of the mechanical properties

4.1 Micro-hardness measurements

The samples for micro-hardness measurements were systematically mirror polished. The use of micro-hardness is a quick and effective way of estimating the mechanical properties of a specimen. As a consequence, this technique was systematically used for preliminary experiments, but for more accurate estimation of the yield strength, tensile tests were always performed on selected conditions.

4.2 Tensile tests

4.2.1 Equipment

All the tensile measurements were carried out on an Instron apparatus with a load cell of 30kN.

4.2.2 Samples and use

The tensile tests were used for two purposes, either to measure the tensile behaviour of a sample or to apply a pre-deformation to the sample prior to the ageing treatment. Special samples, with a section gradient have been designed in order to apply a pre-deformation gradient (Figure 37). In that case, Digital Image Correlation was used in order to record accurately the deformation. Further details will be given in chapter III on this method.

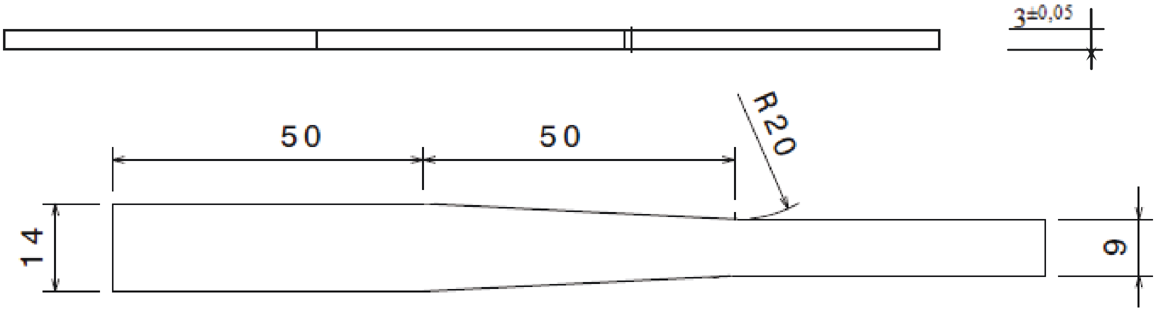

Figure 37: Special tensile sample design with a section gradient.

The classical uniaxial tensile tests were performed on normalised samples (Figure 38) at different duration of heat treatments. The yield strength evolution as a function of time of heat treatment was extracted. These tests were also used to study the strain hardening behaviour and its evolution as a function of time of heat treatment. The yield strength and strain hardening evolutions were used to investigate the evolution of the strengthening mechanisms in relation to the T_1 phase, in terms of interaction mechanisms between dislocations and precipitates. The tensile tests were always carried out along the rolling direction of the AA2198 alloy. The strain rate was 10^{-3} s^{-1}.

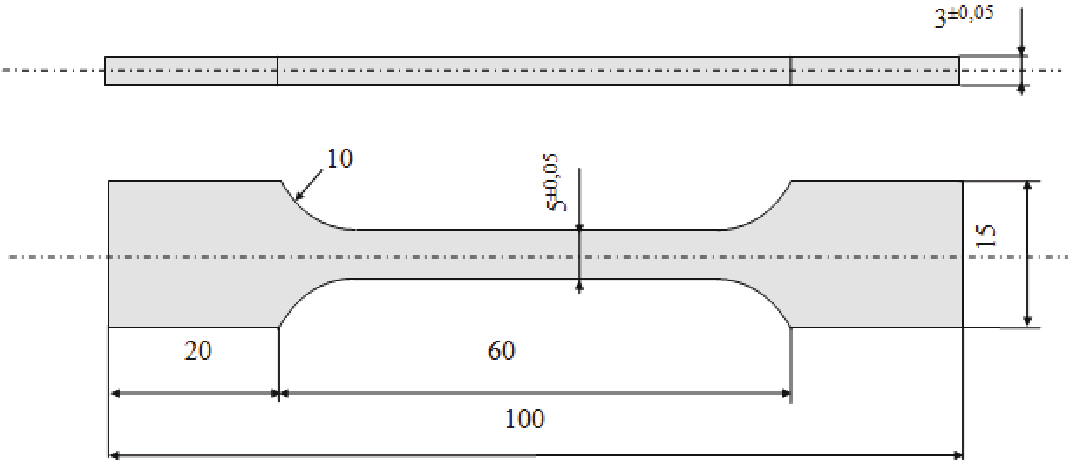

Figure 38: Normalized tensile sample.

4.3 **Bauschinger tests**

4.3.1 Equipment

The Bauschinger tests have been carried out on a Servo-hydraulic MTS.

4.3.2 Samples and use

The design of the Bauschinger samples is presented in Figure 39. A Bauschinger test corresponds to the first tension/compression cycle of an oligo-cyclic fatigue test. This type of technique permits the study of the slip reversibility and of the evolution of internal stresses. The results, obtained with this technique, are highly dependent on the interaction mechanisms between dislocations and precipitates. As a consequence, Bauschinger tests will be used in order to study the evolution of the strengthening mechanisms associated to the T_1 phase.

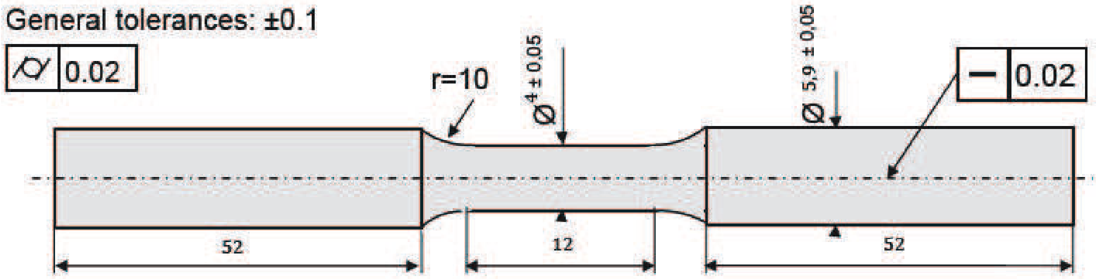

Figure 39: Bauschinger Cylindrical sample.

5. Conclusion

This chapter first permitted to detail the thermo-mechanical treatments that are applied to the AA2198 alloy with emphasis on the industrial and laboratory scales treatments. The critical aspect of these treatments on microstructural and macrostructural properties has been highlighted.
We then gave an overview of all the experimental techniques that were necessary to conduct the present study. It was emphasized that a wide range of techniques were necessary to characterise the T_1-phase accurately. The use of numerous techniques permitted to characterise numerous determining properties at different scales. The precipitation characteristics, mechanical properties and plasticity mechanisms were regarded. We will see later in this work that the results obtained in these different domains often cross and complement each other. The present study is multi-scale and multi-disciplinary and thus permits a global understanding of the microstructure impact on strength and plasticity.

6. References

1. Daniélou, A., Ronxin, J. P., Nardin, C., Ehstrom, J. C.: Proceedings of the 13th international conference on aluminium alloys, Pittsburgh, PA: TMS, Warrendale, PA. (2012)
2. Constellium: Space Key Products. In: http://www.constellium.com/markets/aerospace/space/space-key-products. (Accessed 2013) Available at: http://www.constellium.com/markets/aerospace/space/space-key-products
3. Silcock, J. M.: J. Inst. Metals 89, 203 (1960)
4. Decreus, B.: Etude de la précipitation dans les alliages Al-Li-Cu de troisième génération-Relations entre microstructures et propriétés mécaniques. Phd (2010)
5. Huang, J. C., Ardell, A. J.: Mat. Sci. and Techn. 3, 176-198 (1987)
6. Van Smaalen, S. .: J. of sol. st. chem. 85, 293-298 (1990)
7. Dwyer, C., Weyland, M., Chang, L. Y., Muddle, B. C.: Appl. Phys. Lett. 98 (2011)
8. Donnadieu, P., Shao, Y., De Geuser, F., Botton, G. A., Lazar, S., Cheynet, M., de Boissieu, M., Deschamps, A.: Act. Mater. 59, 462-472 (2011)
9. De Geuser, F., Bley, F., Deschamps, A.: J. of Appl. Crystal. 45, 1208-1218 (2012)
10. Cassada, W., Shiflet, G. J., Starke Jr., E. A.: Met. Trans. A 22A (1991)
11. Kim, J. D.: Met. and Mat. Trans. A 24
12. Ringer, S. P., Muddle, B. C., Polmear, I. J.: Met. and Mat. Trans. A 26A, 1659-1671 (1995)
13. Gable, B. M., Zhu, A. W., Csontos, A. A., Starke Jr., E. A.: J. of L. Met., 1-14 (2001)
14. Reimer, L., Kohl, H.: Springer (2008)
15. Starink M.J., H.: Scripta Mater. 34(11), 1711-1716 (1996)
16. Starink, M. J.: Int. Mat. Rev. 49, 191-226 (2004)
17. Guinier, A., Fournet, G.: Small-angle scattering of X-Rays. (1955)
18. Fratzl, P., Langmayr, F., Paris, O.: J. Appl. Cryst. 26, 820-826 (1993)
19. Allen, R. D., David, G. B., Nomarski, G.: Z. fur Wiss. Mikro. und Mikro. Tech. 69(4), 193-221 (1969)

Chapter III: Set-up a characterisation method adapted to the T_1 phase

This PhD study focuses on the T_1-Al_2CuLi phase and this chapter will present the characterisation procedure that we developed to describe this phase. As a consequence, this chapter is critical to the rest of the study. The set of microstructural parameters of importance to describe the T_1 platelets are the morphological parameters (diameter and thickness) but also the volume fraction of the phase. In order to characterise accurately those parameters, we used existing methods but also developed new practices. A method to describe the T_1 average diameter and thickness evolution using in-situ SAXS was developed recently by De Geuser et al.. We applied this method and also combined it with TEM in order to calibrate the diameter evolution. Due to the strong anisotropy of the T_1 phase, the estimation of its volume fraction is not straight forward. We developed a new technique that is based on the global analysis of a DSC heat flow. The HAADF-STEM technique is also used to calibrate the volume fraction evolution. We will see that this combination of techniques permits the accurate evaluation of all the parameters that are characteristic to the T_1 phase.

Quantitative description of the T_1 formation kinetics in an Al-Cu-Li alloy using Differential Scanning Calorimetry, Small Angle X-Ray Scattering and Transmission Electron Microscopy

Thomas Dorin[1,2], Frédéric De Geuser[2], Williams Lefebvre[3], Christophe Sigli[1], Alexis Deschamps[2]

[1]Constellium, Voreppe Research Centre, BP 27, 38341 Voreppe Cedex, France
[2]SIMAP, INP Grenoble – CNRS – UJF, BP 75, 38402 St Martin d'Hères Cedex, France
[3] Groupe de Physique des Matériaux – CNRS – University of Rouen, 76 801 St Etienne du Rouvray Cedex, France

Abstract

The object of the present study is to design a methodology to follow the kinetics of T_1 precipitation, in an AA2198 alloy, in terms of precipitate size, morphology (thickness, diameter) and volume fraction, during a two-temperature isothermal heat treatment. We used in-situ small angle X-Ray scattering (SAXS) as a way to measure the evolution of the T_1 mean thickness and diameter during the heat treatment. Transmission electron microscopy (TEM) was then performed in order to calibrate these evolutions. Furthermore, we demonstrate that the volume fraction evolution can be described successfully using a simple analysis of the differential scanning calorimetry (DSC) thermograms. The latter was calibrated by selected observations in high angular annular dark field scanning transmission electron microscopy (HAADF-STEM). Microstructure evolution during DSC heating ramps was analysed using in-situ SAXS: The T_1 phase transformation is found to consist in a two step thickening process explained by two consecutive diffusion mechanisms. The enthalpy of formation of the T_1 phase is deduced from the DSC measurements.

1. Introduction

New generation of Al-Cu-Li based alloys, offering a good combination of properties such as low density, high strength, good damage tolerance and very long time property stability, have been developed in the last decade particularly for aerospace applications [1,2,3,4]; they can be found for instance under the commercial name AIRWARE® [5]. They are currently the subject of active research on processing, microstructure development and associated properties [6,7,8]. These alloys are subject to major precipitation strengthening, which is stimulated by cold deformation prior to ageing and small addition elements such as Mg and Ag [9]. The phases from the following systems can be potentially formed: the binary Al-Cu (GP-zones, θ') and Al-Li (δ', δ) systems but also the ternary Al-Cu-Mg (GPB-zones, S') and Al-Li-Cu (T_1, T_B) systems [10,11,12,13,14,15]. The T_1-AL_2CuLi phase is usually the most desirable as it provides the highest strength [6,8], and has been shown to dominate the microstructure in artificially aged tempers for some alloy compositions such as that of the AA2198 alloy [8]. This phase is strongly non-isotropic, which makes it difficult to apply current models to accurately predict the ageing kinetics and the corresponding strengthening behaviour. In order to improve the understanding of precipitation kinetics in this system, to optimise the microstructure/properties relationships and to provide data for future models, a methodology is needed to quantitatively characterize the precipitate microstructures in terms of size, geometry and volume fraction of the precipitate phase.

Small angle X-ray scattering (SAXS) can be used in order to extract quantitative information on plate-like particles such as the T_1 phase [16]. The evolution of the diameter and thickness of the T_1 phase during an in-situ SAXS experiment at 155°C has been described successfully by De Geuser et al. [16]. Although it gives a good description of the precipitate size and morphology, this technique is not suited to give an absolute evaluation of the anisotropic precipitates volume fraction [8]. As a consequence, a reliable method to measure the volume fraction of such precipitates is yet to be developed. The volume fraction of nanometre-size precipitates can be measured from Transmission Electron Microscopy observations [17,18,19,20,21] by measuring the projected image of precipitates present in the thin foil and the foil thickness by different methods such as electron energy loss spectroscopy [22,23]. Correction methods have been derived in order to evaluate the volume fraction of plate-like particles from such TEM imaging [21]. However, such volume fraction measurements remain extremely tedious, and therefore are ill adapted to a systematic study of precipitation kinetics. Moreover they become difficult to apply when precipitation is not uniform in the microstructure, and in the first stages of precipitation where the characterized objects are very small.

Differential scanning calorimetry (DSC) has been used for more than 50 years in order to study phase transformations in Al-alloys [24,25,26,27,28,29,30,31,32,33],[34,35,36,37]. Many methods have been derived in order to estimate the kinetic parameters of these phase transformations such as their activation energy [31,38,39]. A review of all these methods and recommended use has been established by Starink recently [40]. The use of DSC for extracting a relative evolution of the volume fraction of phase formed has also been attempted in Al systems [36,40]. These methods are all based on the assumption that every peak recorded in the DSC thermogram corresponds to the precipitation or dissolution of only one phase. As a consequence, they have proved to be accurate in simple systems governed by a single precipitation sequence such as Al-Li [28], Al-Si [36] or Al-Cu-Mg [30] but they become more delicate to use in the case of multi-sequences systems such as the commercial Al-Cu-Li alloys. In multiple phase transformation, the overlapping of successive peaks often makes it difficult to obtain quantitative data on a specific phase [35,40] from DSC measurements only. Therefore, Transmission Electron Microscopy (TEM) has been used in parallel to DSC in order to relate the DSC peaks to the different phases [25,29,33]. The limit of this approach is that the TEM observations can only be made ex-situ observations, which hinders the accurate determination of the relationship between the precipitation sequence and the DSC signal.

In this paper, we will present a methodology for the combination of experimental techniques, which makes it possible to fully characterize the precipitation kinetics of the T_1 phase (namely the evolution with time of thickness, diameter and volume fraction). This method will be illustrated on a two step ageing treatment (155°C followed by 190°C) applied to the AA2198 Al-Cu-Li-(Mg, Ag) alloy. SAXS will be used to extract the T_1 thickness and diameter evolution in-situ during the ageing treatment. DSC measurements, where particular care will be taken for baseline subtraction, will be used to obtain systematically the heat of transformation associated with precipitation along the heat treatment. These measurements will be calibrated to absolute precipitate volume fractions by High Angular

Annular Dark Field Scanning Transmission Electron Microscopy (HAADF-STEM) observations on two selected samples. In addition, in-situ SAXS measurements will be presented in parallel to the DSC experiments in order to relate directly the DSC heat effects to the phase transformations involved. We will discuss the implications of the volume fraction evolution in terms of the T_1 growth kinetics and associated diffusion mechanisms.

2. Material and experimental procedures

The AA2198 alloy was provided by the Constellium Voreppe Research Centre, France, as rolled 5mm thick sheets with a fully unrecrystallised grain structure. Table 1 gives the composition range for the AA2198 alloy. The same thermo-mechanical treatment was applied to all samples. The samples were first solution treated for 30min at 510°C and water quenched. Right after quenching, the samples were pre-deformed to a plastic strain of 2.5%. Pre-deformation prior to the precipitation treatment is known to greatly promote the precipitation of the T_1 phase, which nucleates on dislocations [6,12,20,41]. The samples were then naturally aged for seven days. For all ex-situ experiments, the artificial ageing treatment was performed in an oil bath, starting with a heating ramp of 20 $K.h^{-1}$ to 155°C, followed by an isothermal hold of 18h at 155°C and by a second isothermal treatment at 190°C (temperature reached in approximately 5 min). The samples were quenched into cold water at different times during the heat treatment and then analysed. In-situ SAXS experiments were performed using exactly the same temperature schedule in a dedicated furnace.

SAXS measurements were realised both at the BM02-D2AM beamline of the synchrotron ESRF (Grenoble) and on a laboratory rotating anode (Cu Kα source). Prior to the measurements, the samples were mechanically grinded down to approximately 70μm and mirror polished. Synchrotron measurements were used for emulating the DSC heating ramps at 50 $K.min^{-1}$, where a good time resolution was required. The beam size at the ESRF was about 200 μm^2 and the photon energy was 7.7keV. The distance between the sample and the two-dimensional CCD detector was 446mm. For these experiments, SAXS patterns were recorded every 4s. The two step isothermal ageing at 155°C and 190°C, which was much longer, was realised on the laboratory set-up. For this system, the beam size was approximately $1mm^2$ and SAXS patterns were recorded every 512s. In this setup, the distance between the sample and the two-dimensional CCD detector was 351mm. SAXS patterns were corrected for flat field and geometrical distortions, background noise, and then normalized using a glassy carbon as secondary absolute calibration sample [42].

DSC measurements were carried out in a Perkin Elmer Pyris Diamond apparatus. The experiments were conducted under a high purity nitrogen flux. The heating ramp rate was 50 $K.min^{-1}$ from -40°C to 520°C. We chose to start at an initial temperature of -40°C in order to allow enough time for the apparatus to stabilise when reaching room temperature. The samples consisted of 0.5mm thick disks 4mm in diameter in order to fit in the dedicated pure aluminium crucibles. Prior to each DSC measurement, the sample weight was systematically measured for normalisation (range of sample weights: 50-100mg).

The samples for TEM observation were first mechanically polished into thin foils of $\sim 100 \mu m$ and then electro-polished using a twin double jet system in a solution of 33% nitric acid in methanol at -20°C and 15V. Observations in conventional mode were carried out in a JEOL 3010 instrument operating at an accelerating voltage of 300kV. HAADF-STEM observations were performed in a JEOL

ARM 200F equipped with a Schottky field emitter and operating at 200kV. This instrument was also equipped with a spherical aberration Cs-probe corrector. The following parameters were used: probe diameter of 0.1nm, an objective aperture semi-angle of 22.5mrad, detector half-collection angle between 40 and 150mrad.

Table 9: AA2198 alloy composition ranges in wt% as given by the Constellium Voreppe Research Centre, France.

AA2198	*Cu*	*Li*	*Mg*	*Ag*	*Zr*	*Al*
Min	2.9	0.8	0.25	0.1	0.04	bal
Max	3.5	1.1	0.8	0.5	0.18	bal

3. Results

3.1 In-situ SAXS: Following the evolution of the T_1 precipitates morphology during artificial ageing

An in-situ SAXS experiment was carried out in order to record the precipitation evolution during the two-step artificial ageing treatment. From now on, the sample at end of the heating ramp to 155°C will be considered as the time of reference (0h of treatment) and named EoR. Earlier work by Decreus et al. [8] revealed that a heat treatment at 155°C for comparable times as the present 18h, results in a distribution of T_1 precipitates with the thickness corresponding to only one unit cell. The thickness for such single-layer T_1 embedded in the Al-matrix corresponds approximately to the spacing of 5 {111} matrix planes, which corresponds to ~1.15nm [43,44]. We have used a duplex ageing in order to form single-layer T_1 precipitates at 155°C and then achieve thickening of the T_1 distribution at a higher temperature of 190°C [45,46]. Figure 40 shows SAXS images taken at different times during the heat treatment. The corresponding Selected Area Diffraction (SAD) patterns recorded in TEM are also displayed in Figure 40 for the same ageing times. The strong brass texture of the alloy with a dominant <110> zone axis allows the observation of two {111} variants edge-on when looking perpendicularly to the rolling plane [47]. These two variants of T_1 result in the characteristic diffraction signal along the <111> direction on the SAD patterns [47], and to the streaks observed in SAXS [16]. The method developed by De Geuser et al. [16] was applied in order to extract the T_1 diameter and thickness evolution during the heat treatment (Figure 41). The non isotropic scattering of the T_1 precipitates allows measuring their characteristics independently of the possible presence of isotropic scattering that would be due to minor phases such as dispersoids. T_1 precipitation starts after approximately 3h at 155°C; this was already reported by Decreus et al. [8]. It then grows to a distribution of single-layer T_1 precipitates after 18h at 155°C, as shown by the constant thickness of 1.3 nm. The difference with the expected 1.15nm value is most likely to be due to the variation in electronic density inside the T_1 precipitates which impacts the scattered signal and thus results in an apparent thickness of 1.3nm in SAXS. Thickening of the T_1 distribution starts immediately when the temperature is increased to 190°C and the thickness reaches a second plateau after 70h at 190°C around 2nm. The value of this second plateau does not mean that all the T_1 have grown to the same thickness of 2nm; in reality the thickness of T_1 precipitates ranges between single-layer to multi-layer precipitates and stabilises around this average value. Figure 42 shows a HAADF-STEM image of a sample heat treated 18h at 155°C and 70h at 190°C. On this image, four T_1 plates can be observed edge-on with four different thicknesses corresponding to 1, 2, 3 and 4 layers.

Complementary observations in conventional TEM at different holding times were used in order to validate the SAXS measurements of the T_1 diameters and the evolution was found to be very similar (see Figure 41 where the TEM measurements are reported in red). Figure 43 illustrates the microstructures obtained after 3 and 18h at 155°C.

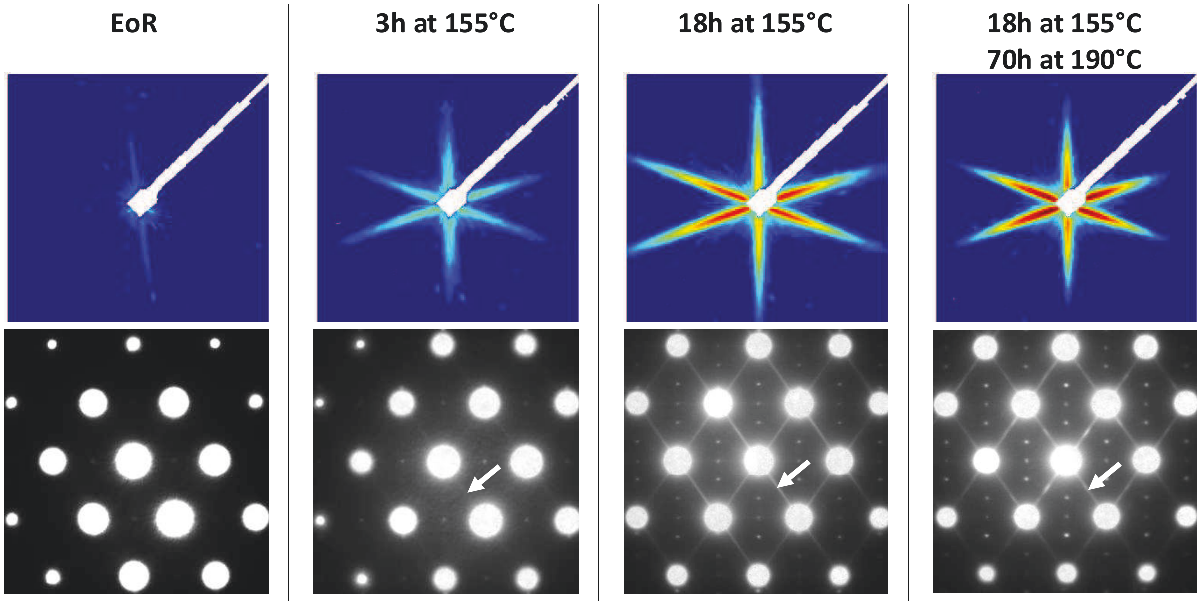
EoR

3h at 155°C

18h at 155°C

18h at 155°C 70h at 190°C

Figure 40: SAXS images and corresponding TEM SAD patterns taken along the <110> zone axis on samples heat treated at different times. Characteristic streaking caused by the T_1 precipitates along the <111> directions start to appear after 3h at 155°C and it becomes more intense as the heat treatment progresses.

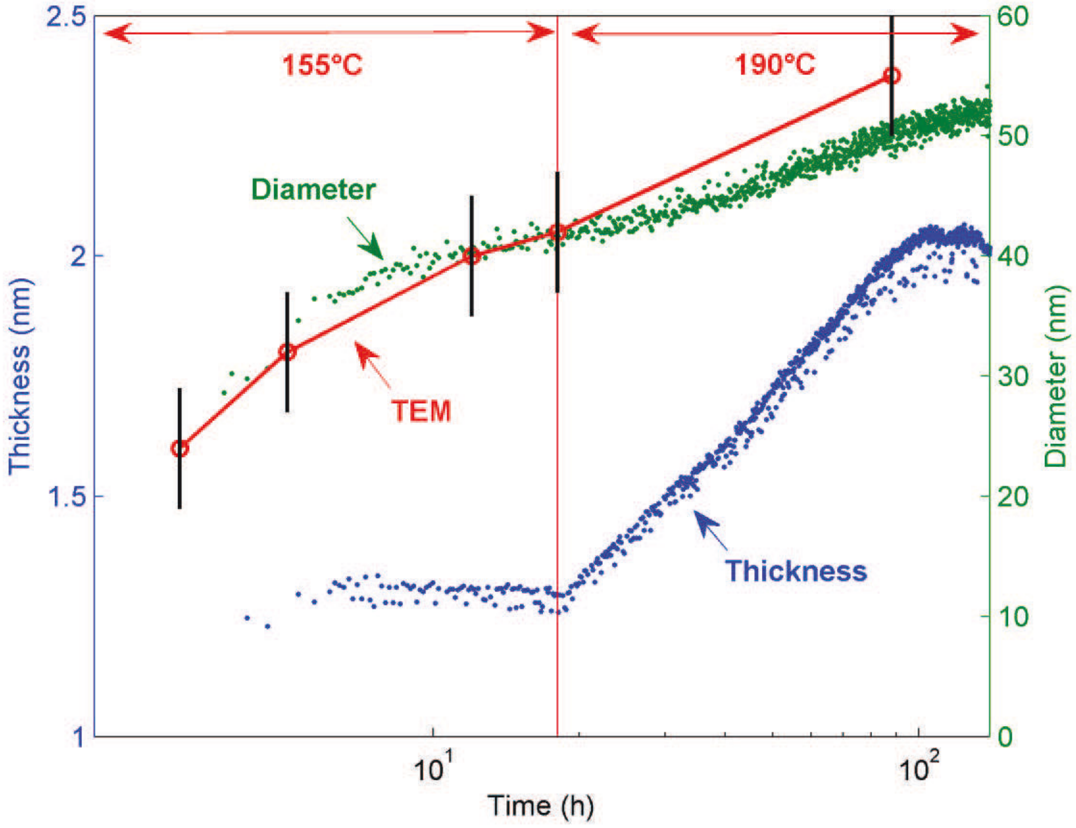

Figure 41: T_1 average diameter and thickness evolution, during the duplex heat treatment, as calculated from the in-situ SAXS images and T_1 diameter as measured from TEM observations.

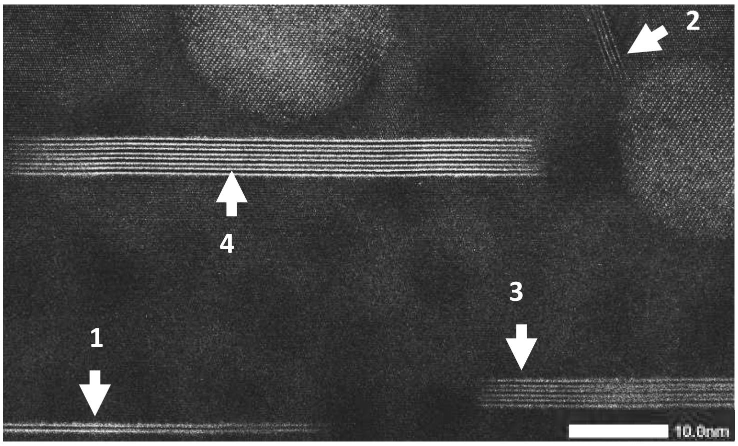

Figure 42: HAADF-STEM image along the <110> zone axis of a sample that was heat treated 18h at 155°C and 70h at 190°C. Two T_1 variants are observed edge-on. The T_1 precipitates (1 to 4) have one to four layers, respectively. The two spherical particles are β'-Al3Zr dispersoids whose main role is to prevent recrystallisation.

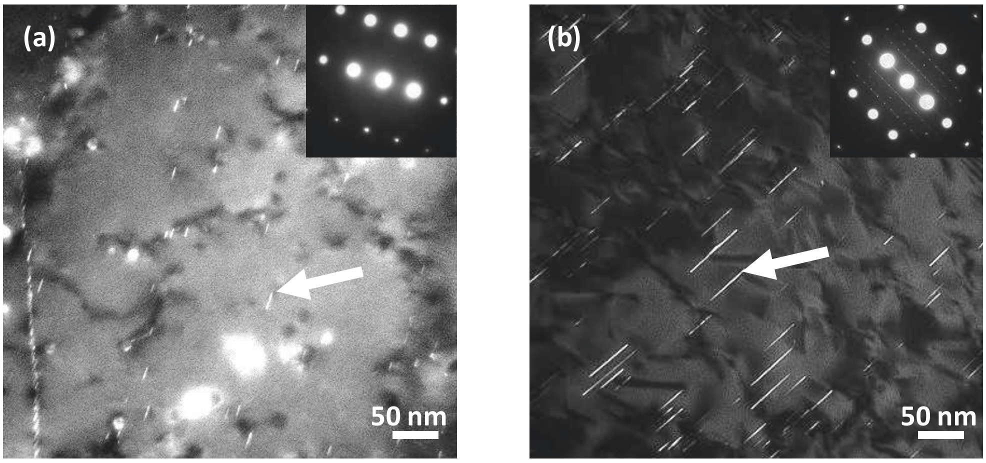

Figure 43: Dark field images in TEM taken on samples extracted at different times during the heat treatment and observed along the <112> zone axis. One T_1 variant (out of 4) is observed edge-on, (a) sample extracted after 3h at 155°C and (b) after 18h at 155°C.

3.2 DSC experiments: A correction method of the raw data

The samples for DSC experiments were taken at different holding times. The heat effects recorded during the DSC ramp are due to the reactions occurring in the alloy but also to the instrument's baseline as well as the evolution of the sample heat capacity with temperature [40]. Depending on the instrument stability and the signal-to-baseline ratio, the baseline stability may not be sufficiently reliable to enable a simple subtraction from the signal measured with a sample of interest. In order to isolate the heat effects caused by the transformations occurring solely in the alloy, we developed a specific correction method. Note that all heat flows considered here are normalized by the sample mass.

The classical assumption made to perform a correction of the DSC signal, lies on the boundary conditions [30]. It consists in assuming that no heat is released by phase transformation when diffusivity is too low nor above the (dynamic) solvus temperature. In our case, we can assume that below 100°C and above 500°C, the measured signal is composed from the baseline only. As the shape of the baseline may be highly nonlinear, we have extended the region in which the baseline may be evaluated by assuming that the final dissolution peak (above 400°C) should always be the same for every sample along the heat treatment. Indeed, the precipitation, which was initiated during the heat treatment, completes during the DSC heating ramp and thus after a given temperature one can assume that the DSC signal is governed only by the thermodynamics of the alloy, and results in the same peak, or collection of peaks, characteristic of the precipitate dissolution. The choice of the temperature of 400°C is justified a posteriori on the corrected DSC thermograms for all samples along the heat treatment (see Figure 6), where the signal is almost identical above this temperature. The baseline subtraction method then consists in the following steps. First, the average signal of all DSC scans on all heat treatments is subtracted from the scan of interest. In the ideal case of a perfect baseline and of a reproducible signal above 400°C for all samples, this subtraction should be equal to zero in the temperature range T<100°C and T>400°C. A polynomial fit to this signal thus provides the measurement of the baseline for this sample. This baseline is then subtracted to the initial DSC scan to provide the corrected thermogram.

The reproducibility of the DSC measurement and correction method has been assessed by performing several measurements on samples subjected to identical heat treatments. Figure 44 shows the corrected thermograms for two samples after EoR and after 18h at 155°C. The remaining deviations will be considered as indication of the experimental dispersion and used in the calculation of error bars when performing the analysis of the DSC data. The DSC thermograms from all samples along the heat treatment are depicted in Figure 45.

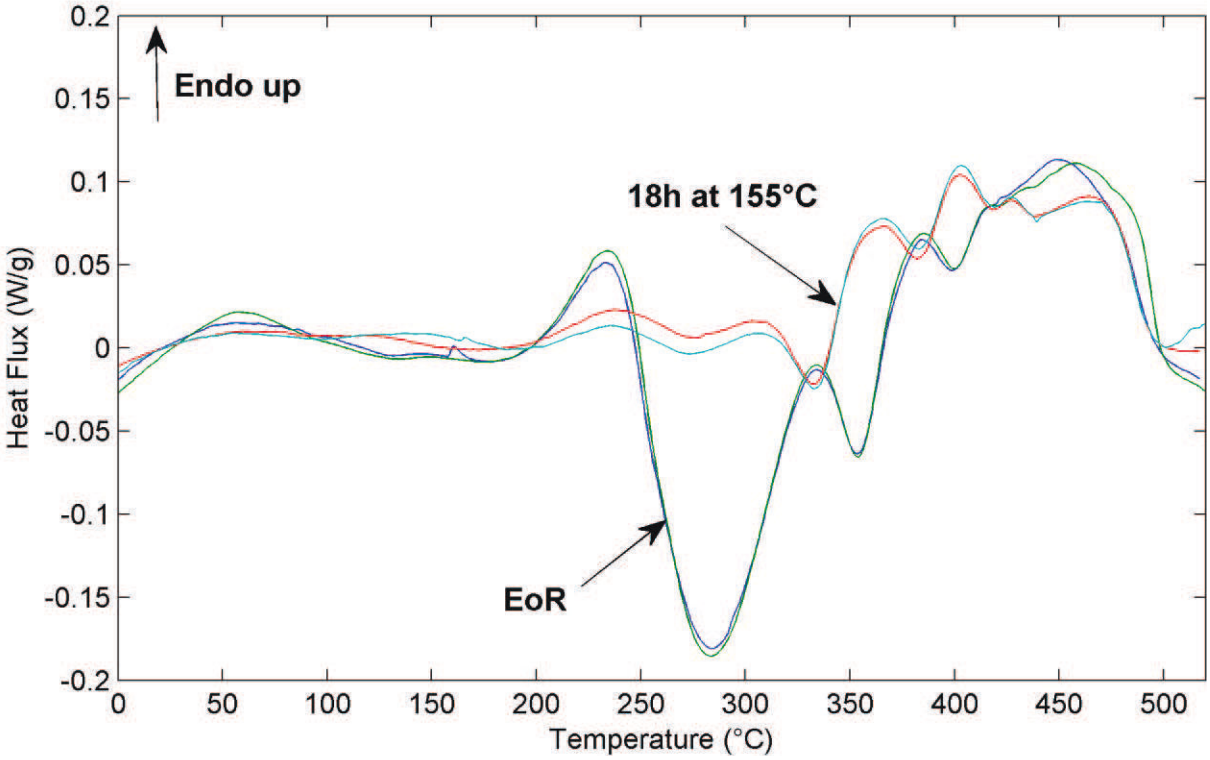

Figure 44: Corrected heat flows for two EoR and two 18 at 155°C samples.

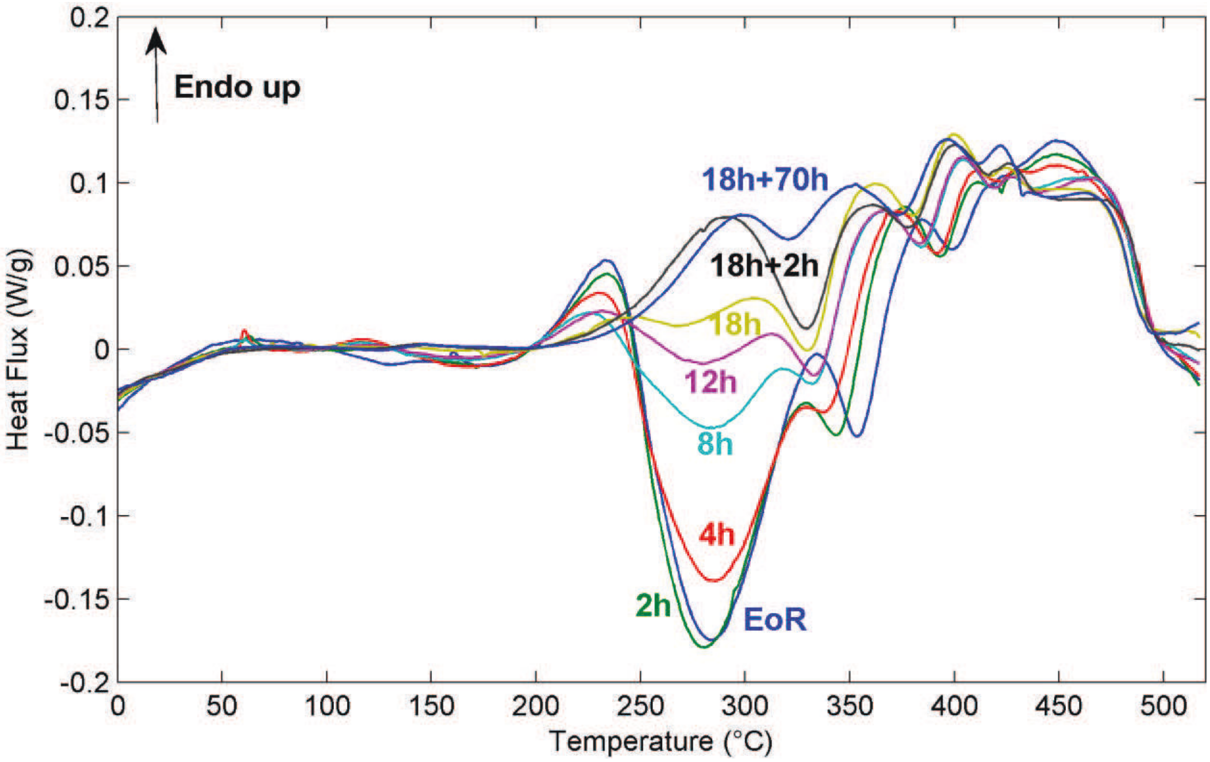

Figure 45: Corrected DSC heat flows for samples extracted at different times during the heat treatment from the EoR to 18h at 155°C + 70h at 190°C.

3.3 In-situ SAXS: Relating the phase transformations with the DSC heat effects

While the T_1 phase is considered to dominate the precipitation sequence, the DSC thermograms of Figure 45 are composed of many well resolved peaks. Before analysing systematically the DSC thermograms in the objective of calculating the T_1 precipitate volume fraction present initially in these different samples, it is of interest to investigate the phase transformations that occur during the DSC ramp to identify to which mechanism and/or phase these peaks are related. This was achieved by performing in-situ SAXS measurements during a heat treatment identical to that of the DSC ramp, using a synchrotron X-ray beam in order to obtain a sufficient temporal resolution. Three states of ageing were investigated, namely EoR, 18h at 155°C, and 18h at 155°C + 70h at 190°C.

First we consider the EoR sample. As discussed before, the microstructure of such a sample is mostly free from precipitates (Figure 40). As a consequence, the entire precipitation process should occur during the DSC ramp. The corrected DSC heat flow for this sample is displayed in Figure 46a. The significant endothermic and exothermic peaks during the DSC ramp are marked A to E. Figure 47 shows a selection of SAXS images at characteristic temperatures during the DSC ramp. The SAXS images reveal that T_1 starts to form around 250°C and that T_1 dissolution ends around 500°C. The length of the streaking in the SAXS images is inversely related to the thickness of the precipitates, so that the fact that the streaking appears to disappear on the 395°C image is in fact a combined effect of the thickening of the precipitates (shortening of the streak) and dissolution (lowering of intensity).

In addition, the evolution of the average thickness of T_1 precipitates is displayed in Figure 46b. The endothermic peak (A) at approximately 230°C corresponds to the dissolution of small precipitates that were already present in the sample at room temperature. It is quite similar to the signal corresponding, in naturally aged samples, to the dissolution of solute clusters formed at room temperature [8]. The presence of these solute clusters in the EoR sample will be discussed in more details in part 4. The main exothermic peak (B) at 280°C can be identified from the SAXS images as originating from the precipitation of the T_1 phase, as only streaks corresponding to this phase are observed, and no sign of other phases such as θ' or S can be detected (as identified by the orientation of the streaks, characteristic of their habit plane). An important point is that during all this exothermic peak the thickness of the T_1 precipitates remains at 1.3 nm, corresponding to single-layer precipitates, similarly to what happens during isothermal heat treatment at 155°C.

During the next exothermic peak (C), no sign of other phases is recorded on the SAXS patterns, which indicates again that only the T_1 phase is significantly present in the microstructure. Thus, it may seem surprising that the thermogram contains a distinct peak. This peak can be associated with a thickening of the T_1 precipitates. At this stage we postulate that the precipitation of T_1 occurs via two successive mechanisms: one rapid plate growth at constant thickness (single layer), and a second slower mechanism involving precipitate thickening. The interruption of the DSC signal, corresponding to a stabilization of the T_1 volume fraction, would correspond to the temperature interval where the first mechanism is completed and the second not yet significantly activated.

Above 370°C, the signal becomes overall endothermic, signalling essentially precipitate dissolution. However, new streaks, characteristic of the formation of plate-like particles in the {001} planes, most likely θ'-AlCu precipitates [16], start to appear around 375°C (peak (D)). Therefore the present results indicate first that θ' precipitates form later than T_1 in the precipitation process, second that they were not involved in lower temperature thermal events, and third that they can form concurrently with the dissolution of T_1. The final endothermic peak (E) between 400 and 500°C involves only precipitate dissolution which justifies the previous choice of temperature range for the polynomial fitting (see part 3.2).

Further indications of the relationship between the different peaks in the DSC thermograms and associated phase transformations can be obtained from the study of the samples aged 18h at 155°C and 18h at 155°C + 70h at 190°C. The three DSC thermograms (including the previously shown EoR sample) are shown together in Figure 48. The sample aged 18h at 155°C contains essentially single layer precipitates, whose average thickness is 1.3 nm, and whose growth is essentially completed (see Figure 41). The exothermic (B) peak has disappeared in this sample, which confirms in accordance with our interpretation proposed above that it was associated to the formation of the single layer T_1. Moreover, the exothermic peaks (C) and (D) that we have respectively associated to the thickening of T_1 precipitates and to the formation of θ', are still present in this sample. Now if we consider the sample aged 18h at 155°C + 70h at 190°C, we can see that both peaks (B) and (C) have now mostly disappeared, which is consistent with the fact that this sample already contains thick T_1 precipitates (see Figure 41) and further validates our interpretation of the nature of the thermal events. In this last sample the peak (D), corresponding to the formation of θ', is still present.

A selection of SAXS images for this last sample is displayed in Figure 49. They confirm that from room temperature to 375°C the microstructure is completely dominated by the T_1 phase and that around 400°C the θ' phase is also observed. The signal from the T_1 precipitates initially present is visually stable until about 300°C and then changes due to size increase and dissolution. This temperature range is again consistent with the DSC signal.

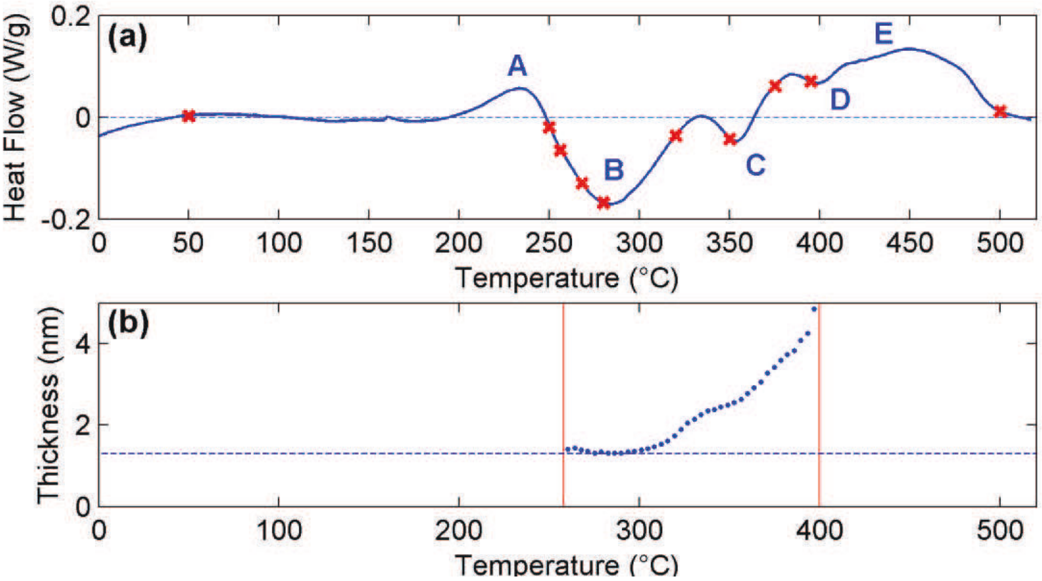

Figure 46: (a) Heat flow recorded in DSC during a heating ramp of 50 K.min^{-1} from 0°C to 520°C. Red crosses highlight the temperatures where SAXS images have been recorded (see Figure 47). (b) T_1 thickness evolution during the DSC heating ramp.

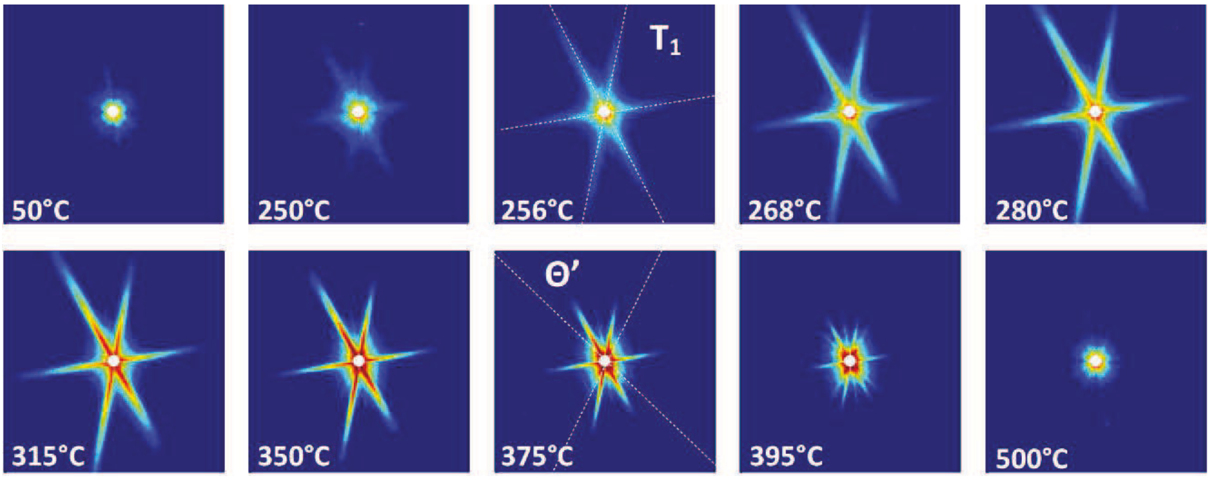

Figure 47: SAXS images recorded during an in-situ ramp from 50°C to 500°C at a speed of 50 K.min^{-1}, starting from an EoR sample.

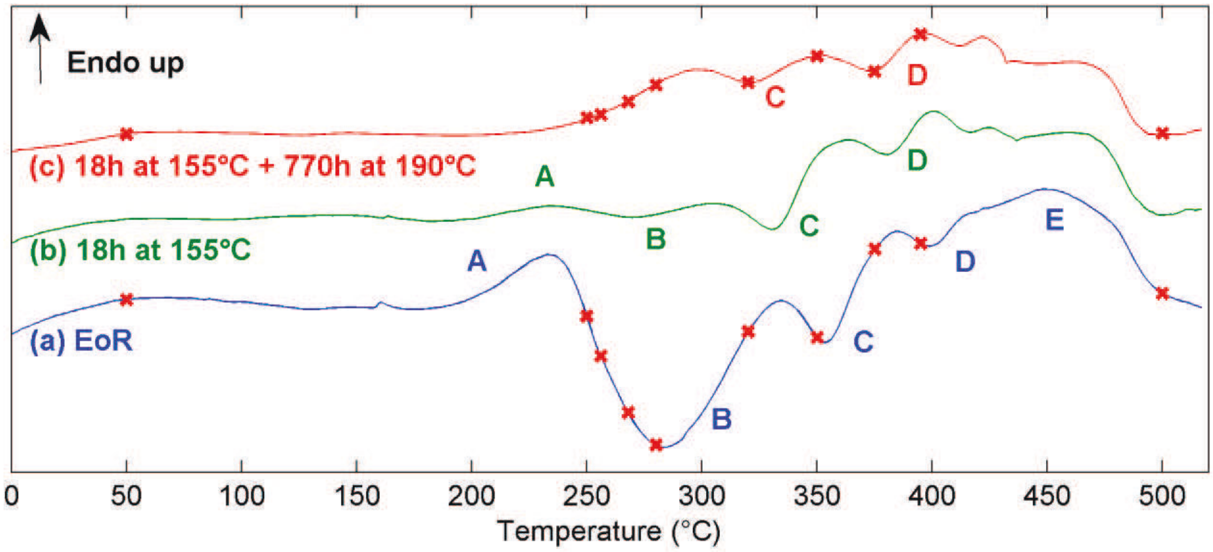

Figure 48: DSC heat flows for 3 samples previously heat treated (a) at the EoR, (b) 18h at 155°C and (c) 18h at 155°C and 70h at 190°C.

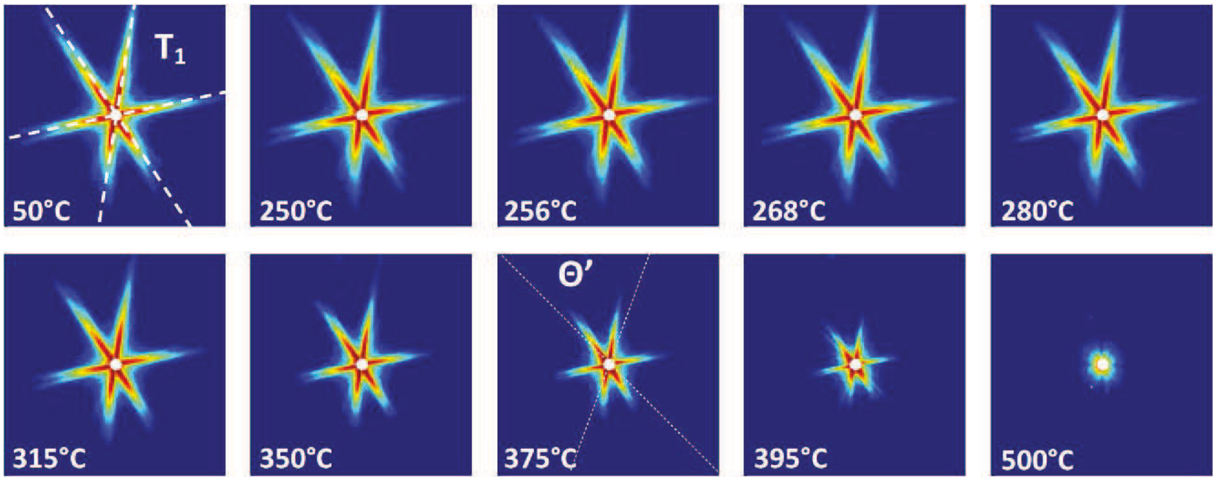

Figure 49: SAXS images recorded during an in-situ ramp from 50°C to 500°C at a speed of 50 K.min^{-1}, starting from an 18h at 155°C and 70h at 190°C sample.

3.4 DSC and HAADF-STEM: Extracting a quantitative evolution of the T_1 volume fraction during artificial ageing

From the SAXS results in part 3.1, it is established that in all the samples heat treated at 155°C and 190°C, the microstructure is dominated by the T_1 phase. During the DSC heating ramp, we have determined that the T_1 precipitates continue to grow and then dissolve, and to a lesser extent the θ' phase may form and dissolve. However, notwithstanding the complexity of the thermal events and associated phase transformations, which occur during the DSC ramp, the integral of the thermal signal between the initial state until the full solid solution must be proportional to the volume fraction of the precipitates initially present, namely T_1:

$$\Delta\mathrm{H} = \beta \int_{100°\mathrm{C}}^{520°\mathrm{C}} \mathrm{Q_i}\,(\mathrm{T})\mathrm{dT} \propto \mathrm{f_v^{initial}} \tag{26}$$

where β is the heating rate. We chose 100°C as the initial temperature because no significant heat effects due to phase transformations occur below this temperature during the heating ramp. However, determining the proportionality factor between the enthalpy and the volume fraction of precipitates is not straightforward [40] and a procedure to calibrate the volume fraction is still necessary.

The normalised enthalpy (in J/g), which can be associated to the precipitate relative volume fraction, is calculated from the corrected DSC heat flows (shown in Figure 45) and plotted in Figure 50 as a function of time of heat treatment. We can note that the volume fraction reaches a first plateau after 18h at 155°C but increases significantly again when the temperature is increased to 190°C. The evolution of volume fraction is easily fitted with two JMAK type curves [40]. In order to calibrate the relationship between this enthalpy and volume fraction of precipitates, the two samples corresponding to 18h at 155°C and 18h at 155°C + 70h at 190°C were observed in HAADF-STEM. An area of 700 nm^2 was evaluated in both cases. The area studied in the case of the latter is shown in Figure 51. This image was taken along a <110> zone axis which enables the observation of two T_1 variants edge-on. Along this axis, one θ' variant is also visible edge-on, but in this area, only one θ' precipitate (highlighted in the figure) is present. This further justifies that the T_1 phase is highly predominant in this alloy in the investigated conditions. In order to always discriminate between the different T_1 thicknesses, we performed higher magnification images. The area corresponding to one of these images, shown previously in Figure 42, is highlighted with a white box in Figure 51.

In these areas, the projected length of each T_1 precipitate was measured. Their number of layers was converted to thickness by considering that a single layer precipitate has a thickness of 1.15 nm, and that the addition of one layer to the thickness adds the equivalent of four {111} matrix planes, which converts to 0.92 nm. Therefore the precipitates of (1, 2, 3, 4, …) layers have a thickness of (1.15 ,2.07 ,2.99 ,3.91, …) (all in nm).

The difficulty with TEM imaging to obtain quantitative volume fraction measurements is that it only provides a projection of the real microstructure which could result in an over-estimation of the volume fraction [48]. The importance of this overestimation is highly dependent on the sample thickness. As a result, in parallel to the HAADF-STEM imaging, a thickness map of the measured area was recorded using energy-loss spectroscopy. The latter technique gives access to t/λ where t is the sample thickness and λ is the mean free path for inelastic scattering [23]. λ can be expressed such that [23]:

$$\lambda = \frac{106F({}^{E_0}/_{E_m})}{\ln\,(2\beta\,{}^{E_0}/_{E_m})} \tag{27}$$

where $E_0 = 200\,keV$ corresponds to the incident energy, E_m is the mean energy loss ($E_m \approx 19.14\,eV$ for Al-alloys), β is the collection semiangle and F is a relativistic factor ($F = 0.618$ at 200keV). For large β values, the mean free path saturates and in this case, a reasonable approximation is obtained by using $\beta = 15\,mrad$ instead [23]. In these conditions, the mean free path is found to be equal to 119nm, which corresponds to a sample thickness around 30nm. The sample thickness is rather small as compared to the precipitate diameters that can go up to 100nm.

In order to obtain the real T_1 length distribution from the projected lengths, we used a method inspired by Jensen [21]. This method considers simple geometrical corrections and is based on the probability for a plate-like particle to intersect with the edges of the TEM sample.

A T_1 volume fraction of approximately 3.6% was found in the case of the sample at the end of the heat treatment (18h at 155°C + 70h at 190°C). The same correction procedure was applied for the sample aged 18h at 155°C and a volume fraction of 2.6% has been found. The ratio between these two values of volume fraction is in perfect agreement with the evolution found using the DSC evaluation method (see Figure 50). From these two values, a calibration factor can be used to re-plot Figure 50a directly as a volume fraction (see Figure 50b). The calibration factor can be expressed in kJ/mol and if we consider the bulk composition of the T_1 phase [49], it reads ~ 57.9 kJ.mol^{-1} by considering the Cu and Li atoms in solid solution as a reference. Although this value really encompasses different mechanisms, it can be approximated as the enthalpy of formation of the T_1 phase and has the correct order of magnitude as compared to formation enthalpies of other phases in Al-alloys [50].

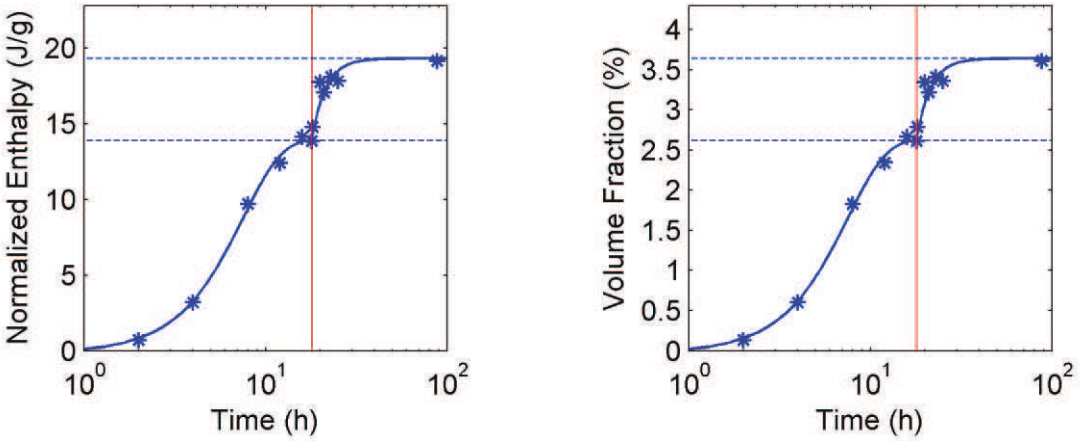

Figure 50: (a) Normalized enthalpy evolution in J/g as a function of time, deduced from the DSC measurements, during the duplex heat treatment and (b) T_1 volume fraction evolution in % after calibration with HAADF-STEM measurements. The transition in temperature after 18h is highlighted with a vertical red line.

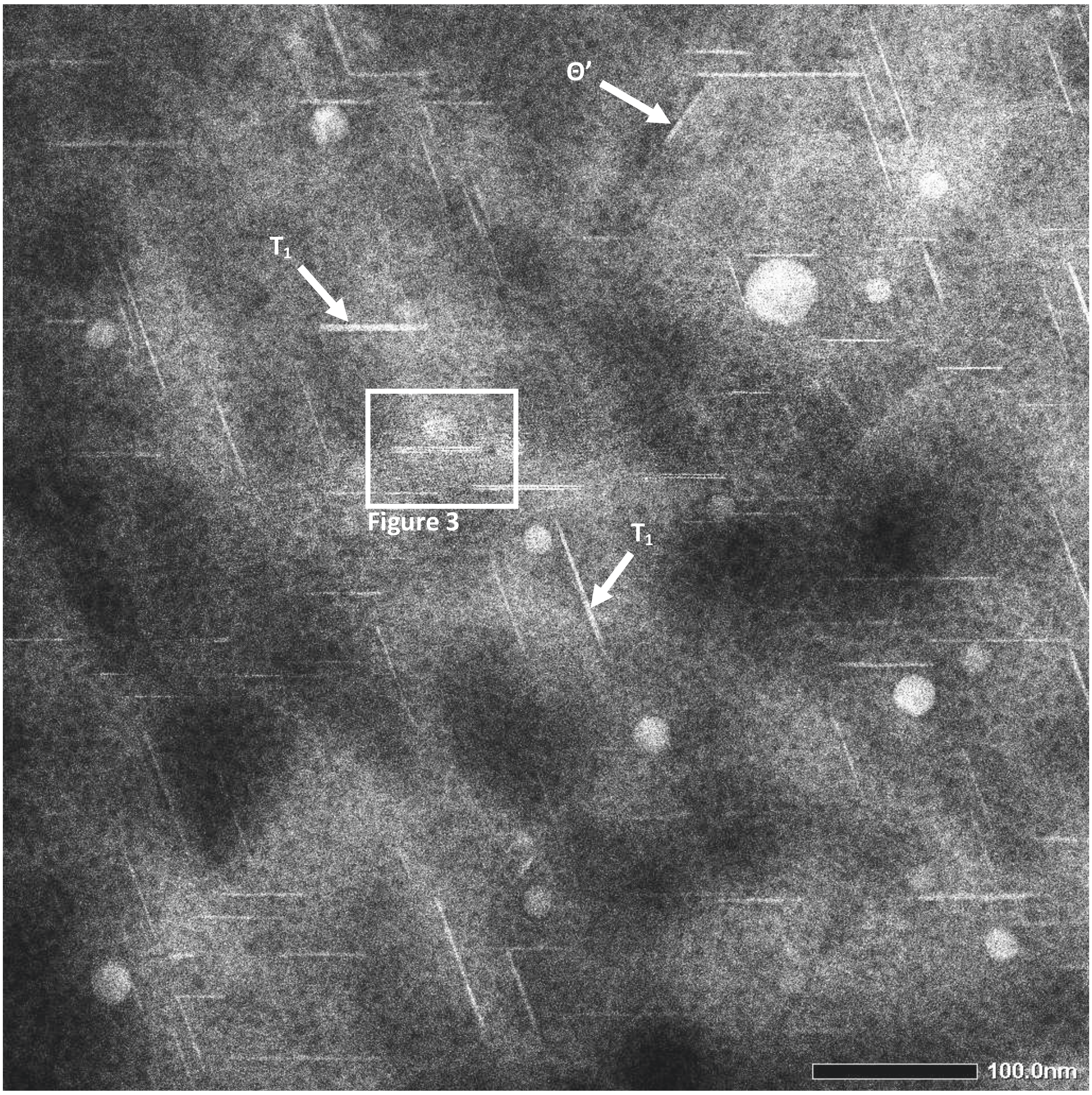

Figure 51: Dark Field image along the <110> zone axis taken in the HAADF-STEM mode, of a sample heat treated 18h at 155°C and 70h at 190°C. Two T_1 variants and one θ' variant are observed edge-on. The spherical particles are β'-Al_3Zr dispersoids.

4. Discussion

In the different studies using DSC on Al-Cu-Li alloys that can be found in the literature [8,12,25,26,29,32,33,34,40,51],[52,53,54]; discrepancies can be found when it comes to relate DSC heat effects to phase transformations. These differences are partly due to the complexity of the precipitation sequence and its dependence on alloy composition but are also due to the lack of means to relate accurately the DSC peaks to the phase transformations involved. Most commonly, each exothermic or endothermic peak is considered to be the result of the formation or dissolution of a single different phase. Combining DSC and SAXS along identical heating ramps makes it possible to follow in-situ the precipitation sequence during the ramp and to clarify the microstructure evolution associated with the thermal events of the DSC thermogram.

The first endothermic peak (A) (Figure 46) at low temperature has previously been attributed to GP-zones dissolution [12]. This first dissolution peak is present for samples at early ageing times, but fades away as soon as T_1 precipitation occurs (see Figure 45). As a consequence, this dissolution event is consistent with the presence of solute clusters in the EoR sample, probably similar to the clusters present in the naturally aged material [8].

Previous publications on similar alloys [8,34] already revealed that the main precipitation peak around 280°C (peak (B) in Figure 48) was due to T_1 precipitation but the subsequent exothermic event (peak (C) in Figure 48) was not associated to this phase in previous reports. In the present study we have shown that these two exothermic peaks both correspond to precipitation of the T_1 phase, which is subject to an interruption around 325°C. Such interruption of precipitate evolution has been observed before for precipitate dissolution during ramp heating [55,56]. It was successfully modelled by considering the competition between the evolution of critical radius and average radius with the changes in temperature and microstructure. It is not clear if such a mechanism can be operative during precipitation (contrarily to precipitate dissolution). However in our case we show that this two-stage precipitation process can be related to the evolution of the thickness of T_1 precipitates.

In another study on a similar alloy, Ringer and co-workers [12] interpreted the three consecutive exothermic peaks arising in DSC as the successive precipitation of T_1, θ' and S' phases. Instead, our interpretation revealed that the second exothermic peak is likely to be due to T_1 plates thickening and the third exothermic peak could instead be due to θ' formation. The 8090 alloy (Al-2.34Li-1.25Cu-1.04Mg-0.11Zr) has been studied extensively using DSC [31,33,34,40,51,52,53]. Due to the important differences in Li and Cu contents, the precipitation sequence in this system presents significant differences from precipitation in the AA2198 alloy (particularly in terms of δ' precipitation). Nevertheless, the main precipitation peak, for similar heating rates as the one we used, occurs around 280°C and has often been attributed to the formation of the S' phase only. Ghosh et al. [34] suggested recently that this main exothermic peak, in the 8090 alloy, could be the result of combined formation of S', T_1, T_2 and δ phases. The subsequent exothermic peak arising in this system was often attributed to the formation of T_2 phase. In the light of our observations, we can propose that the thickening of the T_1 precipitates should also be considered when interpreting the DSC heat effects in alloys where T_1 is known to form.

Previous attempts for extracting a relative evolution of the volume fraction using DSC have been performed in Al systems [37,40], but these attempts were always based on the independent study of each peak and considered proportionality between the enthalpy of formation and the volume fraction of phase formed. In the case of the AA2198 alloy, we demonstrated the efficiency of a global approach that uses the integration of the signal over the complete thermal ramp. The constraint of this method is to require a high precision in the baseline correction; however its result depends only on the microstructure initially present in the material before the DSC scan, and not on the complexity of the heat effects occurring during the ramp. Its applicability is of course limited to microstructures consisting in one dominating precipitated phase.

The AA2198 alloy is known to reach peak strength after approximately 18h at 155°C when starting from the T351 temper [8]. Moreover, the dominating phase in this condition, namely T_1, is the equilibrium phase. Therefore, it could be expected that in this condition the volume fraction of this phase should be close to the equilibrium one at 155°C, and therefore that it should decrease when the temperature is increased to 190°C because of an increased solubility of the solute in the Al matrix. However, the evolution of T_1 volume fraction extracted from DSC results (Figure 50) reveals that the precipitation sequence occurs in two steps and that it increases significantly when the temperature is increased to 190°C, which may seem counterintuitive with respect to solubility. This evolution was confirmed by HAADF-STEM calibration observations. After 18h at 155°C and 70h at 190°C, the T_1 volume fraction was found to stabilize around 3.6%. In order to assess the reliability of this measurement, a simple estimation of the expected value for the equilibrium volume fraction for T_1 precipitates can first be made by considering that the alloy contains a strong excess of Li with respect to the precipitate stoichiometry Al_2CuLi. Therefore, at equilibrium one can expect the residual Cu content to be negligibly small and thus an upper bound for the equilibrium volume fraction is about 5%, calculated on the basis of the total Cu solute content and on the T_1 phase stoichiometry. This value was confirmed by FactSage calculations performed with internal Constellium databases. The gap between this upper bound and our measurement can first be due to a residual Cu content in solid solution. Actually, recent work using atom probe tomography on an Al-Cu-Li alloy with excess Li found matrix concentrations of Cu of 0.7 at% after 5h of ageing at 200°C [57]. Similar results have been obtained also on the AA2198 alloy [58]. Such solute contents show that the alloy is likely to be still highly out-of-equilibrium in the conditions investigated here. Moreover, we know that the alloy contains a limited amount of other Cu-containing phases (θ’ and S), which further reduces the available solute for T_1 precipitation. Thus, we believe that our estimate of the volume fraction is in a reasonable range, although it remains challenging to assess precisely the degree of precision of our calibration procedure.

The two steps precipitation process that is observed actually correlates with the two stages observed when considering the sequence of T_1 precipitation during the heating ramp as observed by DSC and SAXS. This two-step precipitation kinetics can be interpreted as originating from the activation of two consecutive diffusion phenomena. We propose a simple explanation in order to explain that solute remains available even after 18h at 155°C. At 155°C, the T_1 plates grow as single-layers precipitates, and thus the solute enrichment occurs by diffusion at the plates’ tips only, thus limiting the accessible solute domain (see Figure 52a). When the temperature is increased to 190°C, the thickening process is activated and remaining solute thus becomes accessible through a lateral diffusion process (see Figure 52b), which explains the late increase of precipitate volume fraction and is coherent with the previous statement that Cu remains available in solid solution even after long ageing time.

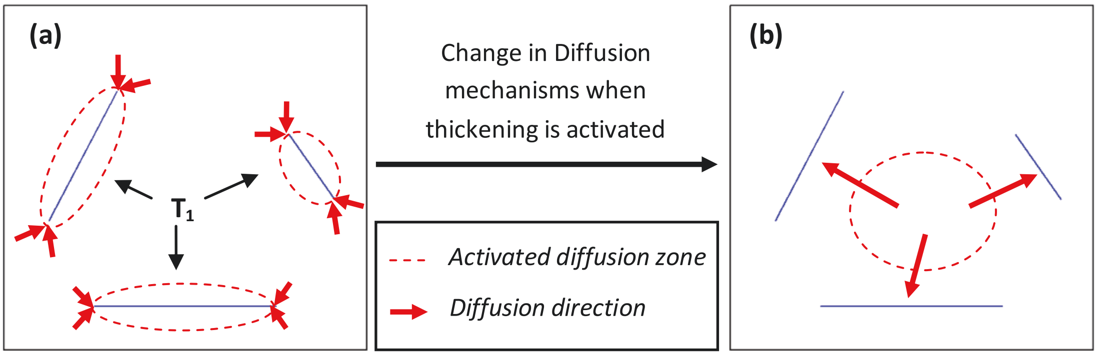

Figure 52: Two steps diffusion mechanisms (a) Growing of single-layer T_1 precipitates by solute diffusion at the plate tips and (b) Activation of a second diffusion mechanism when thickening of the T_1 precipitates is activated.

The combination of SAXS, DSC and TEM has proven to be a successful way of describing the entire precipitation process of the T_1 phase. One interesting outcome of this full characterization is to calculate the evolution of precipitate number density during the heat treatment:

$$N \propto \frac{4 * f_V}{\pi * t * D^2} \tag{28}$$

where f_V is the volume fraction, t the thickness and D the diameter of the T_1 precipitates. The number density is represented in Figure 53 together with the other previously determined parameters. The number of T_1 precipitates is shown to increase throughout the heat treatment at 155°C and then stabilise at the end of this heat treatment. When the temperature is increased to 190°C, the number density is observed to remain stable during a few hours and then decrease steadily, showing the initiation of a coarsening stage.

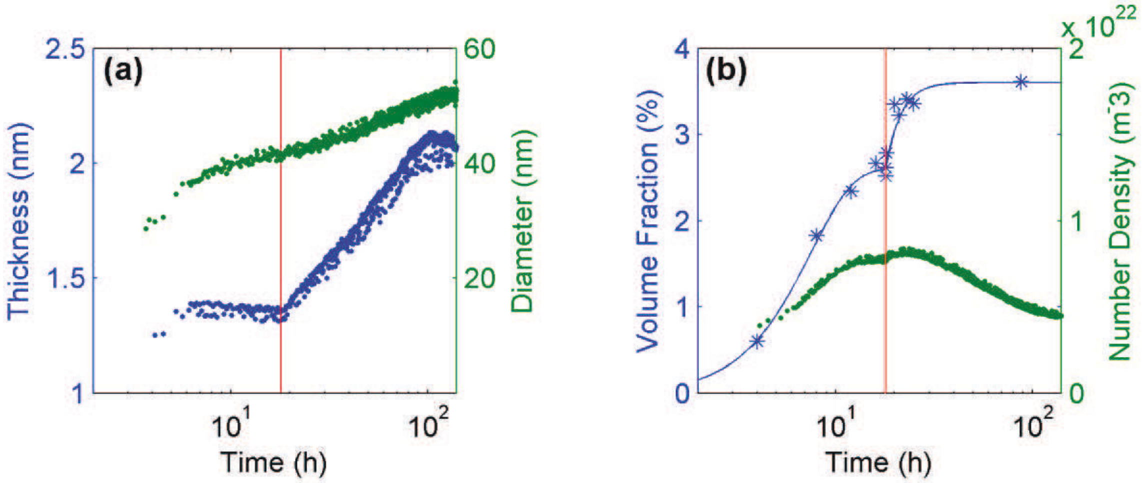

Figure 53: Plots of the evolution of characteristics parameters of the T_1 phase during a duplex heat treatment at 155°C (for 18h) and then at 190°C. (a) Evolution of the mean thickness and diameter (in nm) of the T_1 plates and (b) evolution of the volume fraction (in %) and normalized number density (in m^{-3}) of the T_1 precipitates.

5. Conclusion

1) Using a combination of differential scanning calorimetry (DSC), small-angle X-ray scattering (SAXS) and transmission electron microscopy (TEM), we present a method to quantitatively characterize the evolution of all parameters of T_1 precipitates in Al-Cu-Li alloys along a heat treatment, namely their average thickness, diameter and volume fraction. This method has been applied to a duplex ageing treatment at 155°C and 190°C.
2) The evolution of microstructure during the DSC ramps, and particularly the events associated with the observed exothermic and endothermic peaks, has been directly evaluated by in-situ synchrotron SAXS measurements. Precipitation of the T_1 phase during heating ramp has been shown to proceed in two consecutive steps, the first one being associated to the growth of single layer T_1 precipitates and the second to the activation of precipitate thickening. Such two-stage precipitation kinetics has also been evidenced during the two-step isothermal heat treatment and has been interpreted in a similar manner.
3) In the AA2198 alloy, within the studied heat treatment conditions, the T_1 phase has been shown to dominate the precipitation process. The θ' phase has been significantly observed only at high temperature during the heating ramps.

Acknowledgements

We are very grateful for the help and support we received from the technical staff of beamline BM02-D2AM of ESRF. We would like to express our appreciation to Dr. P. Donnadieu for fruitful discussions; her expertise in TEM has been of great benefit to the present work. We also convey special thanks to G. Renou for conducting some of the TEM experiments.

6. References

1. Williams, J. C., Starke Jr, E. A.: Acta Mater. 51, 5775-5799 (2003)

2. Warner, T.: Mat. Sci For. 519-521, 1271-1278 (2006)

3. Rioja, R. J., Liu, J.: Met. and Mat. Trans. A 43A, 3325-3337 (2012)

4. Tchitembo Goma, F. A., Larouche, D., Bois-Brochu, A., Blais, C., Boselli, J., Brochu, M.: Proceedings of the 13th international conference on aluminium alloys, Pittsburgh, PA: TMS, Warrendale, PA. (2012)

5. Daniélou, A., Ronxin, J. P., Nardin, C., Ehstrom, J. C.: Proceedings of the 13th international conference on aluminium alloys, Pittsburgh, PA: TMS, Warrendale, PA. (2012)

6. Gable, B. M., Zhu, A. W., Csontos, A. A., Starke Jr., E. A.: J. of L. Met. 1, 1-14 (2001)

7. Lequeu, P., Smith, K. P., Danielou, A.: J. of Mat. Ang. and Perf. 19, 841-847 (2010)

8. Decreus, B., Deschamps, A., De Geuser, F., Donnadieu, P., Sigli, C., Weyland, M.: Acta Mater. 61, 2207-2218 (2013)

9. Khan, A. K., Robinson, J. S.: Mat. Sci. and Tech. 9, 1369-1377 (2008)

10. Hardy, H. K., Silcock, J. M.: J.Inst. Met. 84, 423-428 (1955-56)

11. Sainfort, P., Dubost, B.: J. de phys. 48, 407-413 (1987)

12. Ringer, S. P., Muddle, B. C., Polmear, I. J.: Met. and Mat. Trans. A 26A, 1659-1671 (1995)

13. Yoshimura, R., Konno, T. J. ., Hiraga, K.: Acta Mater. 51, 2891-2903 (2003)

14. Yoshimura, R., Konno, T. J., Abe, E., Hiraga, K.: Acta Mater. 51, 4251-4266 (2003)

15. Wang, S. C., Starink, M. J.: Int. Mater. Rev. 50, 193-215 (2005)

16. De Geuser, F., Bley, F., Deschamps, A.: J. of App. Cryst. 45, 1208-1218 (2012)

17. Schwartz, H. A.: Met. All. 5, 139 (1934)

18. Hilliard, J. E.: Trans. Met. Soc. AIME, 906 (1962)

19. Crompton, J. M. G., Waghorne, R. M., Brook, G. B.: Brit. J; Appl. Phys. 17, 1301-1305 (1966)

20. Cassada, W., Shiflet, G. J., Starke Jr., E. A.: Met. Trans. A 22A (1991)

21. Jensen, D. G.: J. Phys. D.: App. Phys. 28, 549-558 (1995)

22. Raether, H.: Excitation of plasmons and interband transitions by electrons. Springer-Verlag (1980)

23. Egerton, R. F.: Electron energy-loss spectroscopy in the electron microscope - SECOND EDITION. Plenum Press, New York (1996)

24. Thompson, D. S.: Ther. Anal. V2: Inorg. Mat. and Phys. Chem. 2, 1147-1170 (1969)

25. Papazian, J. M.: Met. Trans. A 12A, 269-280 (1981)

26. Papazian, J. M.: Met. Trans. A 13A, 761-769 (1982)

27. Lloyd, D. J., Chaturvedi, M. C.: J. of Mat. Sci. 17, 1819-1925 (1982)

28. Balmuth, E. S.: Scripta Met. 18, 301-304 (1984)

29. Abis, S., Evangelista, E., Mengucci, P., Riontino, G.: J. de Phys. 48, 447-453 (1987)

30. Jena, A. K., Gupta, A. K., Chatuverdi, M. C.: Acta Met. 37, 885-895 (1989)

31. Luo, A., Lloyd, D. J., Gupta, A., Youdelis, W. V.: Acta Met. Mat. 41(3), 769-776 (1993)

32. De Macedo, M. C., Avillez, R. R., Solorzano, I. G.: Scripta Met. et Mat. 31(12), 1701-1704 (1994)

33. Starink, M. J., Gregson, P. J.: Mat. Sci. and Eng. A, 54-65 (1996)

34. Ghosh, K. S., Das, K., Chatterjee, U. K.: Met. and Mat. Trans. A 38A, 1965-1975 (2007)

35. Ghosh, K. S., Gao, N.: Trans. Nonferrous Met. Soc. China 21, 1199-1209 (2011)

36. Van Rooyen, M., Mittemeijer, E. J.: Met. Trans. A 20A, 1207-1214 (1989)

37. Esmaeili, S., Wang, X., Lloyd, D. J., Poole, W. J.: Met. and Mat. Trans. A 34A, 751-763 (2003)

38. Kissinger, H. E.: Anal. Chem. 29(11), 1702-1706 (1957)

39. Ozawa, T.: J. of Therm. Anal. 2, 301-324 (1970)

40. Starink, M. J.: Int. Mat. Rev. 49, 191-226 (2004)

41. Decreus, B.: Etude de la précipitation dans les alliages Al-Li-Cu de troisième génération-Relations entre microstructures et propriétés mécaniques. Phd (2010)

42. Zhang, F., Ilavsky, J., Long, G. G., Quintana, J. P. G., Allen, A. J., Jemian, P. R.: Met. and Mat. Trans. A 41A, 1151-1158 (2010)

43. Donnadieu, P., Shao, Y., De Geuser, F., Botton, G. A., Lazar, S., Cheynet, M., de Boissieu, M., Deschamps, A.: Act. Mat. 59, 462-472 (2011)

44. Dwyer, C., Weyland, M., Chang, L. Y., Muddle, B. C.: Appl. Phys. Lett. 98 (2011)

45. Csontos, A. A., Starke Jr, E. A.: Met. and Mat. Trans. A 31A, 1965-1976 (2000)

46. Csontos, E. A., Starke, A. A.: Int. J. of Plast. 21, 1097-1118 (2005)

47. Huang, J. C., Ardell, A. J.: Mat. Sci. and Techn. 3, 176-198 (1987)

48. Donnadieu, P., Roux-Michollet, M., Chastagnier, V.: Phil. Mag. A 79(6), 1347-1366 (1999)

49. Van Smaalen, S., Meetsma, A., De Boer, J.: J. of Sol. St. Chem. 85, 293-298 (1990)

50. Wolverton, C.: Acta Mater. 49, 3129-3142 (2001)

51. Starink, M. J., Hobson, A. J., Gregson, P. J.: Scripta Mat. 34(11), 1711-1716 (1996)

52. Starink, M. J., Gregson, P. J.: Scripta Met. Mat. 33, 893-900 (1995)

53. Gao, N., Starink, M. J. ., Cerezo, A., Wang, S. C., Gregson, P. J.: Mat. Sci. and Tech. 21, 1010-1018 (2005)

54. Ahmadi, S., Arabi, H., Nouri, S., Shokuhfar, A.: Ir. J; of Mat. Sci. and Eng. 6(3), 15-20 (2009)

55. Nicolas, M., Deschamps, A.: Acta Mat. 51, 6077-6094 (2003)

56. Marlaud, T., Deschamps, A., Bley, F., Lefebvre, W., Baroux, B.: Acta Mat. 58, 4814-4826 (2010)

57. Gault, B., De Geuser, F., Bourgeois, L., Gable, B. M., Ringer, S. P., Muddle, B. C.: Ultramicroscopy 6, 683-689 (2011)

58. Araullo-Peters, V., Gault, B., De Geuser, F., Deschamps, A., Cairney, J. M.: Acta Mater. in press. (2013)

Chapter IV: Quantifying and modelling the microstructure/ strength relationship

The aim of this chapter is to understand the relationship between the T_1-microstructure and the strength variations. The precedent chapter gave us the basis of a characterisation procedure of the T_1 phase that will now be used in the rest of the study. The approach to understand, quantify and model the microstructure/strength relationship can be divided in two steps:

- Explore a wide range of T_1 microstructures by varying the thermo-mechanical treatment parameters while measuring the yield strength. This step is essential as it serves the creation of a strong experimental data base that can then be used to test and improve the existing yield strength models.
- Apply the existing models to see their ability to predict the yield strength evolution. Three existing models are tested and improved in order to predict accurately the yield strength evolution.

The implications of the experimental and modelling results on the strengthening mechanisms associated to the T_1 phase are finally discussed.

Quantifying and modelling the microstructure/ strength relationship by tailoring the morphological parameters of the T$_1$ phase in an Al-Cu-Li alloy.

Thomas Dorin[1,2], Alexis Deschamps[1], Frédéric De Geuser[1], Christophe Sigli[2]

[1]SIMAP, INP Grenoble – CNRS – UJF, BP 75, 38402 St Martin d'Hères Cedex, France
[2]Constellium, Voreppe Research Centre, CS 10027, 38341 Voreppe Cedex, France

Abstract

We present a detailed study of the relationship between precipitate microstructures in an Al-Cu-Li alloy and resulting yield strength. By varying the thermo-mechanical ageing treatments applied to the AA2198 alloy (pre-deformation, heat treatment temperature and duration), T$_1$ microstructural parameters (thickness, diameter and volume fraction) are varied on a large range, and the corresponding yield strength is determined. The resulting database of microstructure-strength relationships is used to establish a strengthening model based on interfacial and anti-phase boundary strengthening. This model successfully describes the strength evolution from under-aged to over-aged conditions without the need for a transition from precipitate shearing to by-passing.

1. Introduction

The high specific strength, good damage tolerance and excellent property stability of Al-Cu-Li alloys makes them highly attractive for aerospace applications [1,2,3]. Recently developed Al-Cu-Li alloys can be found, for instance, under the name AIRWARE® [4]. A complex precipitation sequence that strongly depends on the thermo-mechanical treatment is involved in these alloys [5,6]. However, cold working prior to the final ageing treatment, has been shown to promote the precipitation of the T$_1$-Al$_2$LiCu phase at the expense of other phases [7,8,9,10]. The T$_1$ phase is known to provide the highest strength [9,11]; it forms as semi-coherent platelets along the $\{111\}_{Al}$ planes and exhibits an hexagonal structure [12,13].

The strengthening response associated to the formation of precipitates in Al-alloys has been widely studied in the literature. In the case of shear-resistant spherical precipitates, the yield strength increment is usually expressed by Orowan equation [14]:

$$\Delta\tau = \frac{F}{bL} \tag{29}$$

where $\Delta\tau$ is the Critical Resolved Shear Stress (CRSS) increment, F is the obstacle strength, b is the Burgers' vector and L is the inter-particle spacing. The T$_1$ plates were originally thought to be shear-resistant [15] and thus attempts have been made to use modified versions of the Orowan equation to model the yield strength increment associated to the T$_1$ phase [16,17]. The applicability of these early attempts is however questionable as T_1 precipitates are now recognised as being shearable for wide ranges of heat treatments [18,19,20,21]. An interfacial strengthening model, considering the energy required to create a new precipitate/matrix interface when shearing a T_1 plate, has been developed by Nie and Muddle [22]. This model has been only once compared to microstructural data [22]. Therefore there is a shortage of quantitative microstructure data available to critically discuss the applicability of the different strengthening models, their robustness and domain of validity. We present in this report a systematic study where a wide range of T_1 microstructures are generated by varying the parameters of the thermo-mechanical treatment, in order to generate a complete database of microstructure – strength relationships. This database will be used to evaluate and to improve the existing strengthening models.

The choice of the thermo-mechanical treatment parameters has been already shown to be decisive on the resulting precipitation microstructure in Al-Cu-Li alloys [7,8,9,10,23,20,24]. The thermo-mechanical parameters that strongly influence precipitation are: the pre-age stretch, the heat treatment temperature and the heat treatment duration. Varying these parameters is a suitable approach to reach a large variety of T_1 microstructures and provides a strategy for varying the parameters of the precipitate microstructure independently. The heat treatment temperature has recently been shown to be a key parameter that controls the activation of the T_1 thickening process [24]. Namely, it was shown that at 155°C the thickness of T_1 precipitates remains constant for very long ageing times at the minimum value of 1.3 nm, and that when temperature is increased from 155°C to 190°C T_1 thickening is quickly activated. In addition, a pre-deformation increase leads to a greater density of smaller precipitates [9] as T_1 nucleates on dislocations. The influence of pre-deformation on the competitive precipitation of T_1, θ' and δ' has been addressed by Gable et al. [9]. They revealed that the same strength of 450MPa could be reached for different pre-deformations (0%, 2%, 4% and 6%) that result in significantly different T_1 microstructures: the mean T_1 diameter was found to range from 40nm to 160nm, highlighting that the relationship between the T_1 morphological parameters and the yield strength in not straightforward. However, in the alloy studied by Gable et al., θ' and δ' were also present in considerable amounts, making the analysis complex. We will show in the present study that with an appropriate choice of alloy composition and thermo-mechanical treatment, the microstructure becomes dominated by T_1 precipitates only.

We recently developed a method to characterise the T_1 phase quantitatively in terms of morphological parameters and volume fraction [24]. This method first uses Small Angle X-Ray Scattering (SAXS) to measure the mean diameter and thickness of T_1 precipitates. SAXS can be carried out in-situ during the heat treatments, giving access to the precipitation kinetics [25]. Secondly, this method uses Differential Scanning Calorimetry (DSC) to measure the volume fraction of T_1 precipitates. It will be applied systematically in the present investigation to record the T_1 microstructures for a wide range of thermo-mechanical treatments. In parallel, the yield strength will also be measured in all the studied heat treatment conditions. The resulting microstructure-strength characterisation will be then used to challenge the existing models for platelet strengthening; a modified approach to T_1 strengthening will then be proposed.

2. Material and experimental procedure

The AA2198 alloy, whose composition range is given in Table 10, was provided by the Constellium Voreppe Research Centre, France, as rolled 5mm thick sheets with a fully unrecrystallised grain structure. The samples were first solution treated and water quenched. Directly after quenching, the samples were pre-deformed to a plastic strain ranging from 0% to 12%. The samples were then naturally aged for seven days. The artificial ageing treatment was executed in an oil bath, starting with a heating ramp of 20 K.h^{-1} to 155°C, followed by an isothermal at 155°C or by a duplex ageing treatment for 18h at 155°C followed by ageing at 190°C (temperature reached within approximately 5 minutes). The samples were quenched in cold water at different times during the ageing and then analysed. In-situ SAXS experiments were performed using exactly the same temperature schedules in a dedicated furnace.

SAXS measurements were carried out on a laboratory rotating anode system (Cu Kα source). Prior to the measurements, the samples were mechanically ground down to approximately 70µm and mirror polished. The beam size was approximately 1mm^2 and SAXS patterns were recorded every 512s. The distance between the sample and the two-dimensional CCD detector was 351mm. SAXS patterns were corrected for flat field and geometrical distortions, background noise, and then normalised using a glassy carbon as secondary absolute calibration sample [26].

DSC measurements were carried out in a Perkin-Elmer Pyris Diamond apparatus. The experiments were conducted under a high purity nitrogen flux. The heating ramp rate was 50 K.min^{-1} from -40°C to 520°C. We chose to start at an initial temperature of -40°C in order to allow enough time for the apparatus to stabilise when reaching room temperature. The samples consisted of 0.5mm thick disks 4mm in diameter in order to fit in the dedicated pure aluminium crucibles. Prior to each DSC measurement, the sample weight was systematically measured for normalisation (range of sample weights: 50-100mg).

Tensile measurements were carried out using a screw-driven Instron machine with a 30kN load cell. Special tensile samples with a section gradient were used for preliminary experiments (more details will be given in part 3.1). Classical tensile samples, with a cross-section of 3mm*5mm and gauge length of 60mm, were also used. The extensometer gauge length was 10mm and the strain rate was 10^{-3} s^{-1}.

Table 10: Composition of AA2198 alloy given in wt%

AA2198	*Cu*	*Li*	*Mg*	*Ag*	*Zr*	*Al*
Min	2.9	0.8	0.25	0.1	0.04	bal
Max	3.5	1.1	0.8	0.5	0.18	bal

3. Experimental results

3.1 Preliminary study: impact of pre-deformation on hardness

Because T_1 nucleates on dislocations, it is well established that pre-deformation prior to ageing greatly enhances T_1 precipitation kinetics at the expense of other phases such as θ' or S. The impact of pre-deformation on competitive precipitation and resulting strength increment has been already reported [7,8,9,10]. Pre-deformation directly influences the dislocation density and thus is expected to determine the final T_1 number density. In order to explore the role of pre-deformation in a continuous way, we designed tensile samples of variable section (see Figure 54a) that provide a deformation gradient along the sample during uniaxial stretching. This deformation gradient was characterised accurately using Digital Image Correlation (DIC) [27]. The mean plastic strain along the sample is calculated from the deformation map and plotted as a function of position on the sample (see Figure 54b). In order to cover the entire pre-deformation range with enough precision, we chose appropriate section gradients and used three individual samples. The three samples were subjected to a common ageing treatment, consisting in a seven-day natural ageing at room temperature followed by artificial ageing for 18h at 155°C. The impact of pre-deformation on strengthening was evaluated through a series of hardness measurements along the three aged samples (Figure 54c). For this particular ageing time, the results show a continuous increase in strength as a function of pre-deformation, so that changing this parameter can effectively control the precipitation kinetics. For the purpose of our study, we needed additionally to restrict the range of pre-deformations to values where the T_1 phase dominates the microstructure. The distribution of precipitates has been evaluated by ex-situ SAXS measurements on four samples respectively pre-deformed 0%, 0.5%, 2.5% and 12% (see Figure 55). These measurements make it possible to separate the presence of T_1, θ' and S phases [25]. The presence of the θ' and S phases appears to be significant only in the non-pre-deformed sample (highlighted in Figure 55), so that pre-deformation is revealed to be a necessary, but sufficient condition for T_1 to dominate the precipitate microstructure in AA2198. In the following paragraph, T_1 precipitation kinetics and related strengthening will be studied in detail for the 0.5%, 2.5% and 12% pre-deformations.

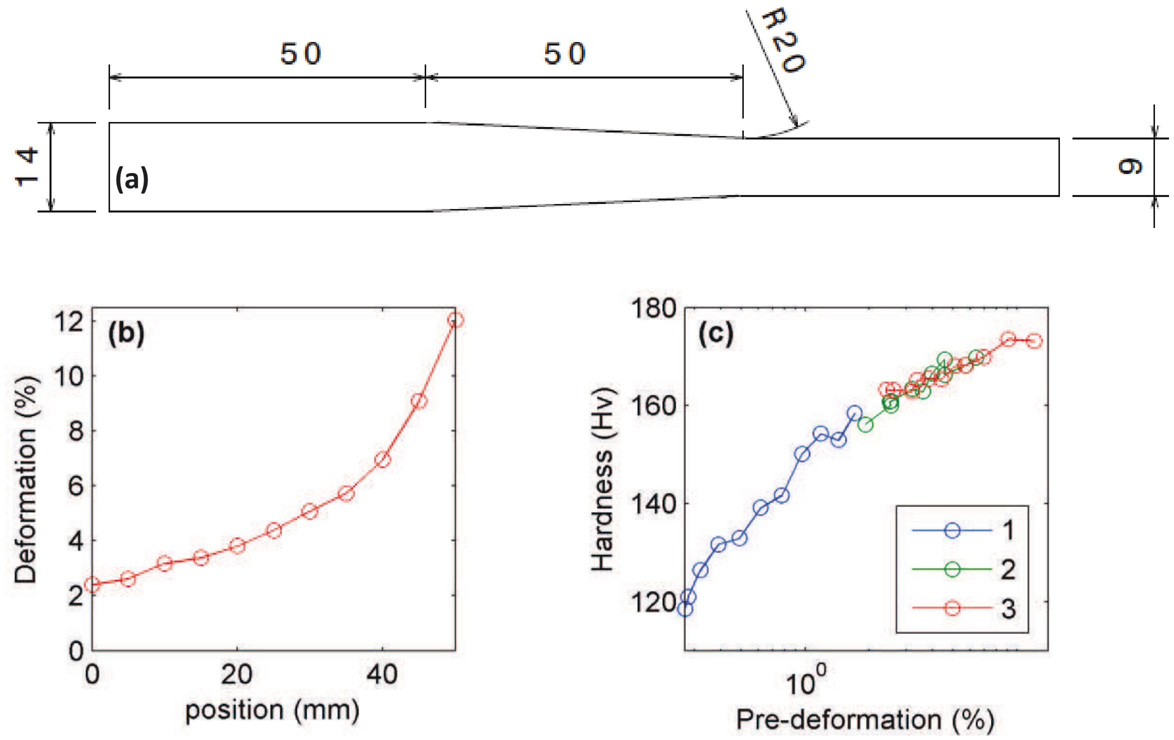

Figure 54: (a) uniaxial tensile sample with a section gradient, (b) mean deformation as a function of position along one gradient sample and (c) Hardness measurements plotted as a function of pre-deformation for the three pre-deformed samples covering the complete pre-deformation range and heat treated 18h at 155°C.

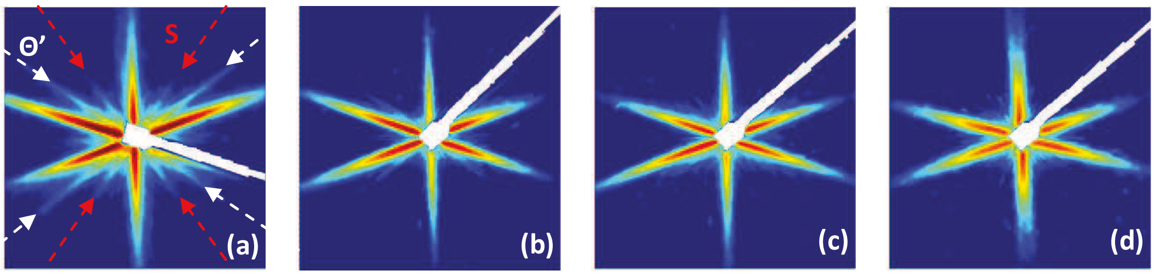

Figure 55: SAXS images recorded on four samples heat treated for 18h at 155°C. The pre-deformations applied prior to the heat treatment were respectively (a) 0%, (b) 0.5%, (c) 2.5% and (d) 12%.

3.2 Microstructure and strength evolution during ageing at constant T_1 thickness

In this section the precipitation kinetics and related strengthening during ageing at 155°C will be presented for the three selected levels of pre-deformation, namely 0.5%, 2.5% and 12%. The T_1 precipitation kinetics was followed in-situ in SAXS for these three conditions. Snapshots of the continuous recording of SAXS images are shown in Figure 56 for the three deformation levels and selected ageing times. Clearly, increasing the level of pre-deformation results in a faster precipitation kinetics, both in terms of the apparition of characteristic streaks for platelet precipitates and subsequent increase of SAXS intensity. Following the method developed by De Geuser et al. [25], the mean diameter and thickness of the T_1 precipitates were extracted from the SAXS images and are plotted in Figure 57. As expected, a higher pre-deformation (and therefore a higher density of nucleation sites) results in a faster kinetics and smaller mean T_1 diameter at the end of the heat treatment. Additionally, one can notice that the mean T_1 thickness remains highly stable around 1.3nm in the three conditions, which reveals precipitation of only single-layer T_1 precipitates [24]. Figure 57c displays the evolution of T_1 volume fraction extracted from DSC thermograms following the method detailed in [24]. Finally, the information on diameter, thickness and volume fraction makes it possible to evaluate the number density N of precipitates per unit volume:

$$N = \frac{4f_v}{\pi t D^2} \tag{30}$$

where t and D are the T_1 mean thickness and diameter and f_v is the volume fraction of T_1 precipitates (the fitted function shown in Figure 57c is used to estimate the volume fraction at each ageing time). Figure 57a-d emphasise that a stable microstructure is reached in all the conditions after approximately 150h at 155°C. The three resulting microstructures differ in precipitate number density by almost an order of magnitude and thus in mean T_1 diameter while keeping a constant T_1 thickness and similar volume fraction.

The evolution of yield strength during ageing for the three levels of pre-deformation is shown in Figure 58 for the same ageing times as those chosen for the measurements of volume fraction. The continuous curves are JMAK type fits [28] applied to the data. One can notice that a similar yield strength is reached at the end of the heat treatment for the three conditions. The volume fraction and yield strength evolutions during the heat treatment were found to be very similar in the investigated conditions and within experimental uncertainty a linear relationship is observed between these two parameters (see Figure 58b).

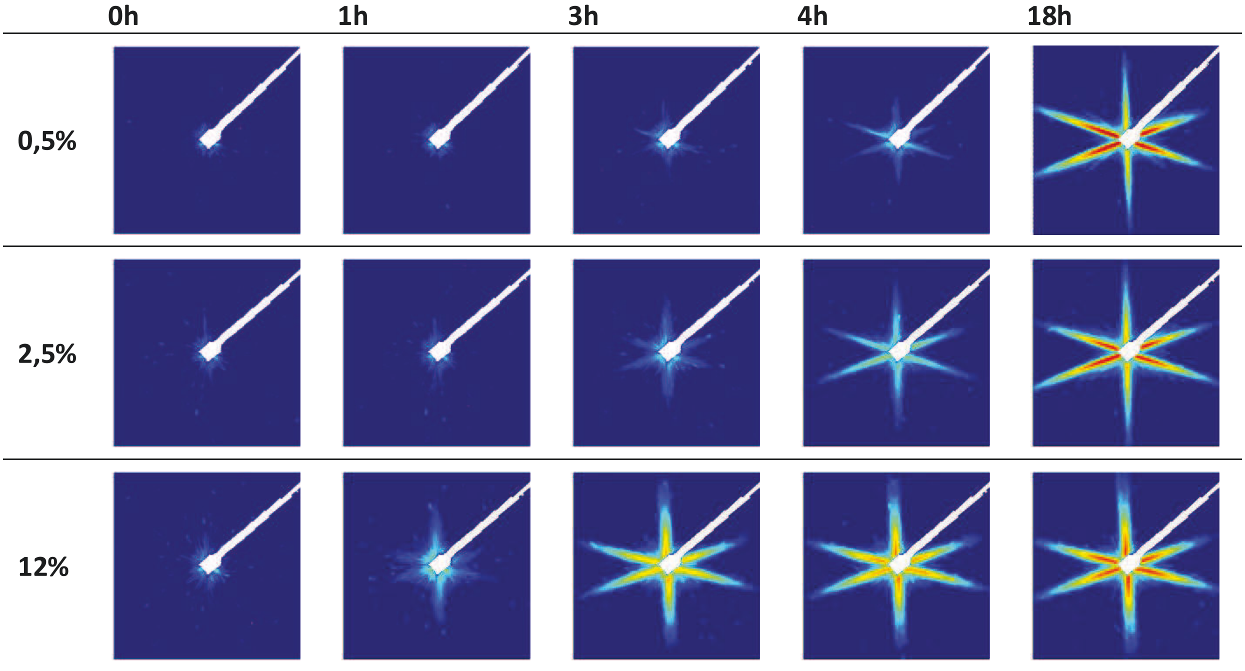

Figure 56: SAXS images recorded at various times during in-situ heat treatment at 155°C for three different pre-deformations: 0.5%, 2.5% and 12%.

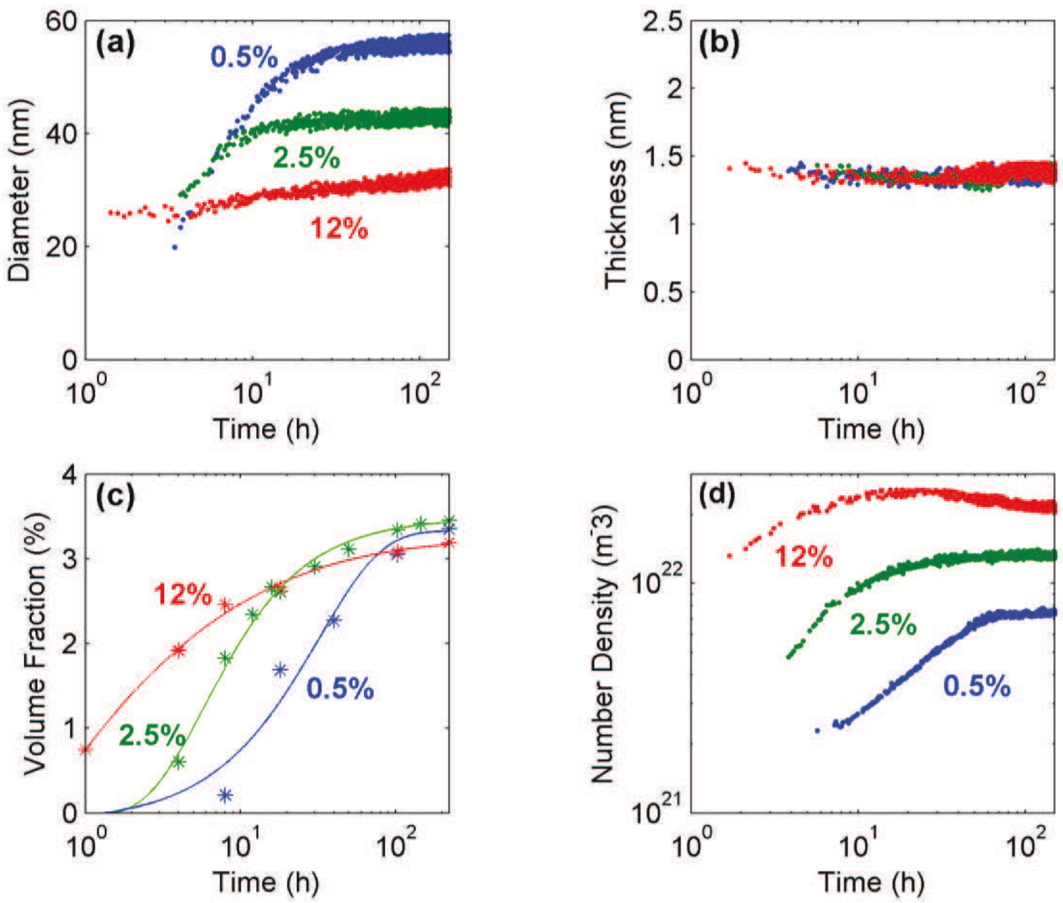

Figure 57: Evolution of the mean T_1 (a) diameter and (b) thickness extracted from images recorded in-situ in SAXS for three pre-deformations (0.5%, 2.5% and 12%). (c) T_1 volume fraction evolution extracted from DSC measurements and (d) T_1 number density evolution re-calculated from data of a), b) and c).

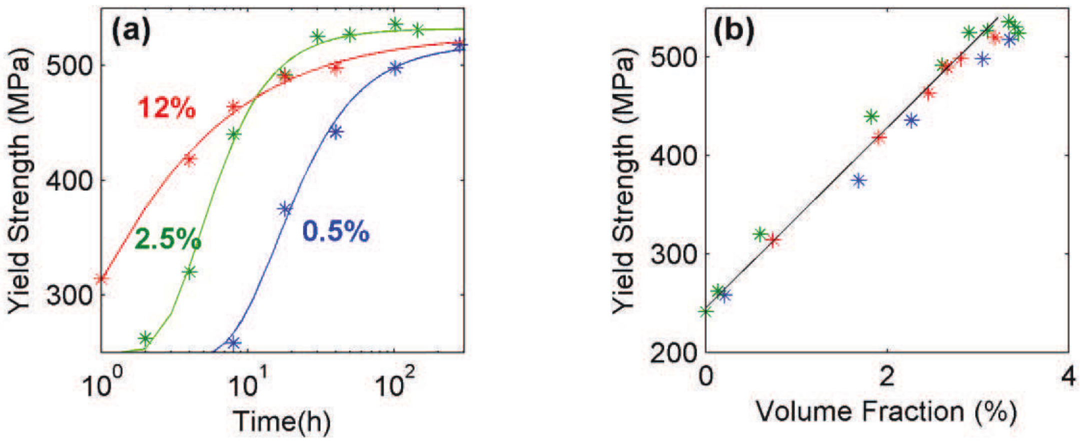

Figure 58: (a) Yield strength evolution as a function of ageing time at 155°C and (b) yield strength evolution as a function of T_1 volume fraction for the same heat treatment for three pre-deformations: 0.5%, 2.5% and 12%.

3.3 Microstructure and strength during ageing with evolution of T_1 thickness

We suggested, in a previous study, that T_1 precipitation occurs in two steps corresponding to two distinct diffusion stages [24], and resulting for the first stage in a precipitate growth at constant thickness and for the second stage in an increase of precipitate thickness by a ledge mechanism. The use of a duplex ageing strategy at 155°C followed by 190°C has proved to be efficient in successively activating these two diffusion stages. In this section, we compare the precipitate microstructures during duplex ageing to the formerly presented single isothermal treatment starting from a sample pre-deformed 2.5%. Figure 59 shows snapshots of the recorded SAXS images during the two ageing treatments. A significant shortening of the characteristic streaks for the platelet precipitates is observed during ageing at 190°C (contrarily to 155°C), which can be related to the increase in precipitate thickness. This qualitative view is confirmed by the quantitative evaluation of the SAXS data. The mean T_1 thickness experiences a significant increase from 1.3nm to 2nm at 190°C while the mean diameter increases from 40nm to 55nm (Figure 60a and Figure 60b). The volume fraction evolutions, as extracted from DSC measurements, are displayed in Figure 60c. A significant increase in volume fraction occurs when going to 190°C but one can notice that the heat treatment at 155°C eventually reaches a similar volume fraction after long enough ageing times. The T_1 number density evolutions are evaluated and plotted in Figure 60d. The increase of both the thickness and the diameter at 190°C results in a significant drop of precipitate number density despite the increase in volume fraction.

Figure 61a shows the evolution of yield strength during the duplex ageing treatment at 155°C and 190°C. At 190°C, the strength is first constant for a few hours and then significantly drops. At the end of the heat treatment the strength has decreased from a peak strength of more than 500 MPa to about 350 MPa. This result highlights the fact that the precipitate thickness seems to play a significant role in the strengthening mechanism of T_1. Figure 61b shows the yield strength represented as a function of the T_1 volume fraction along the duplex ageing treatment. The monotonous linear relationship between yield strength and precipitate volume fraction that was observed in the case of a distribution of single-layer precipitates no longer applies when the T_1 thickness starts to increase.

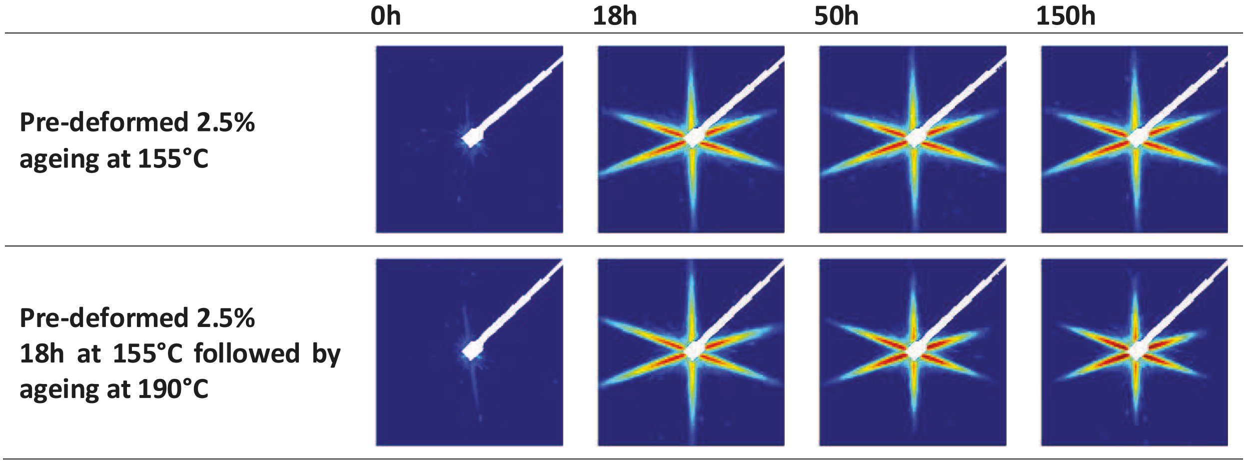

Figure 59: SAXS images recorded in-situ from a sample pre-deformed 2.5%, (a) at 155°C and (b) 18h at 155°C and then at 190°C.

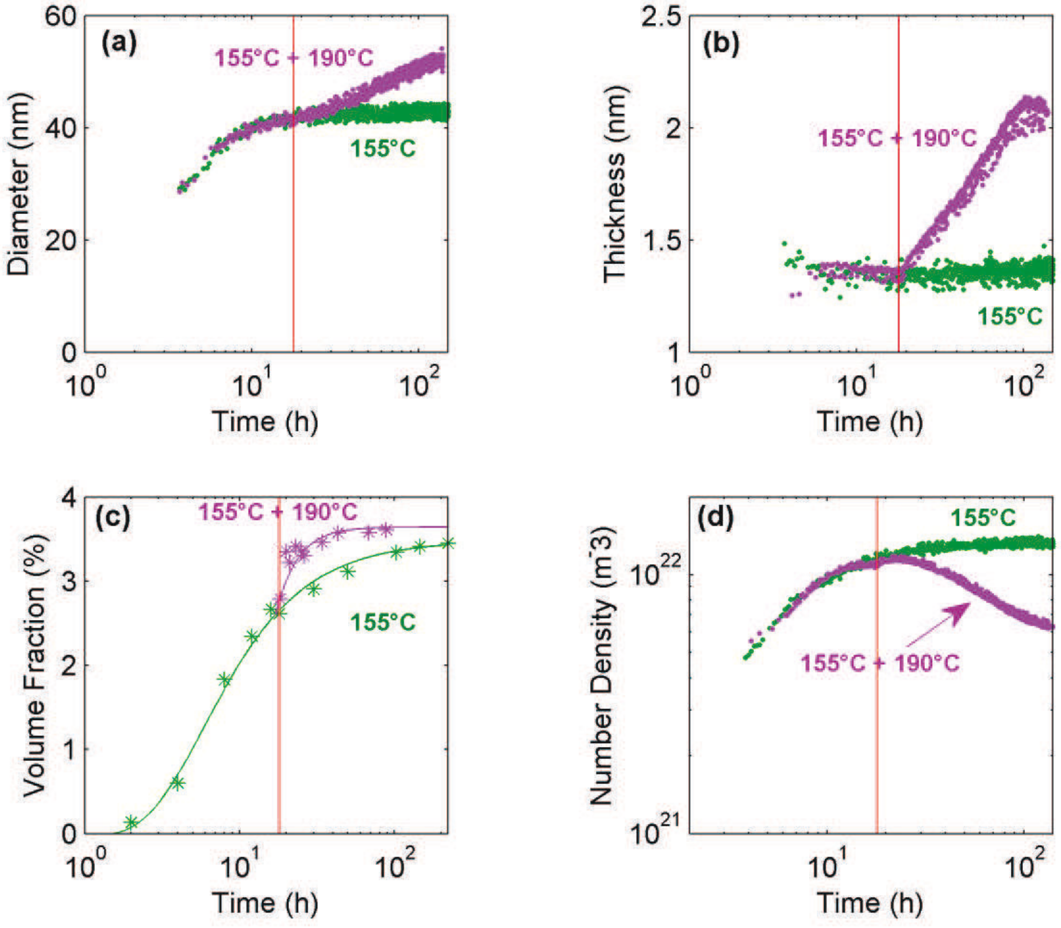

Figure 60: Evolution of the T_1 precipitate characteristics during ageing of the 2.5% pre-deformed sample at 155°C (green symbols) and duplex ageing 18h at 155°C followed by ageing at 190°C (purple symbols): (a) T_1 mean diameter and (b) thickness, (c) T_1 volume fraction evolution and (d) T_1 Number density.

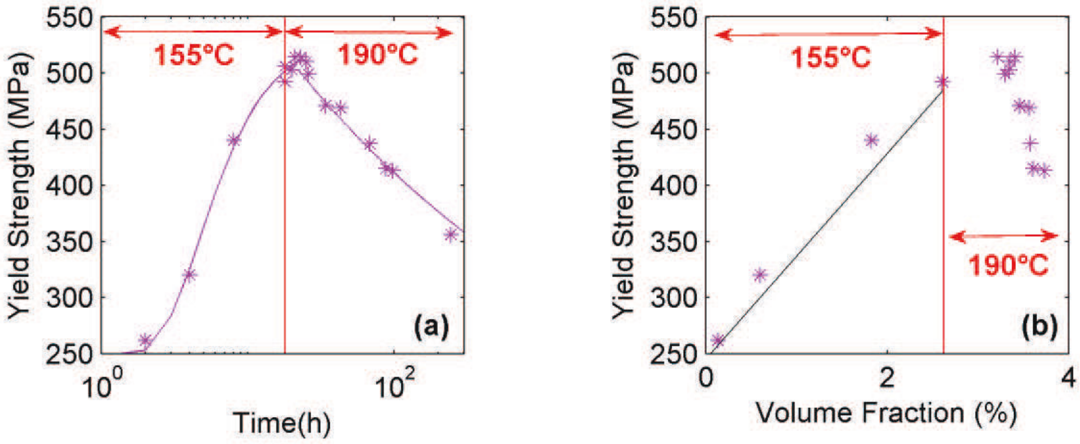

Figure 61: (a) Yield strength plotted as a function of ageing time and (b) yield strength evolution as a function of T_1 volume fraction during a duplex ageing treatment for 18h at 155°C and then at 190°C from a sample pre-deformed 2.5%.

3.4 Summary of the experimental results

Challenging efficiently the strengthening models to assess their robustness, validity domain and limitations requires obtaining microstructure-strength characterisation in a range as wide as possible of microstructural conditions. Platelet precipitates such as the T_1 phase are characterised by three independent parameters out of the four presented here (thickness, diameter, number density and volume fraction). Our study aims at covering wide ranges of variations of all of these parameters, in order to determine as independently as possible the effect of each of them on the alloy's strength. The range of precipitate microstructures obtained is summarised for all investigated conditions in Figure 62. We can see that precipitate number densities cover a range of nearly two orders of magnitude. Precipitate diameters range between 20 and 55 nm, and volume fraction between 0.3 and 2.5%. At constant volume fraction, microstructures with a two-fold difference in precipitate diameter have been generated. At constant diameter, microstructures with a three-fold difference in volume fraction have been characterised. In addition, the thickness of precipitates has been varied by almost a factor of 2 while keeping a comparable precipitate diameter and volume fraction. This experimental database will now be used to test the ability of the existing yield strength models to predict the yield strength evolutions.

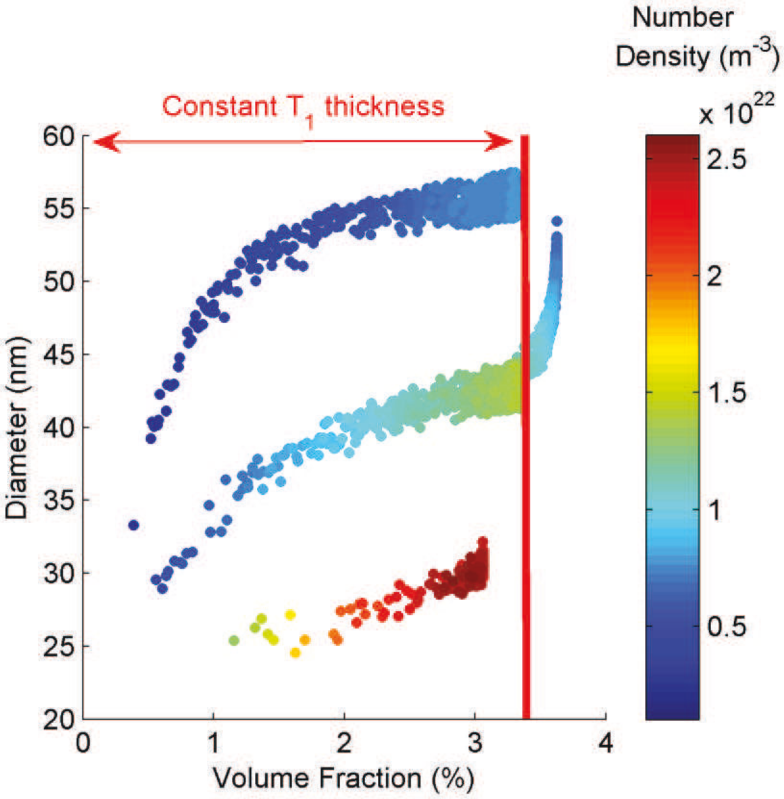

Figure 62: Map of the T_1 microstructure domain that was explored during the present investigation.

4. Yield strength modelling

4.1 Models based on the Orowan by-passing mechanism

Modified versions of the Orowan equation have been proposed in the literature to describe the strengthening associated with the presence of semi-coherent anisotropic plate-like precipitates. Based on simple geometrical considerations, the following modified Orowan equation has been suggested by Nie et al. [16] for aluminium containing precipitate plates lying on {111} matrix planes:

$$\Delta\tau = 2\frac{Gb}{4\pi\sqrt{1-\nu}}\frac{1}{0.931\sqrt{\frac{0.265\pi Dt}{f_v}}-\frac{\pi D}{8}-0.919t}\ln\left(\frac{1.061t}{b}\right) \tag{31}$$

where $\Delta\tau$ is the critical resolved shear stress (CRSS) increment, ν=0.36 is the Poisson's ratio for Aluminium.

In an alternative study, Zhu and Starke [17] proposed another modified Orowan equation by using computer simulations to examine the dislocation slip process in a random distribution of rectangular obstacles. As a result of these simulations, they proposed the following expression for the CRSS increment of plate-like precipitates lying on {111} matrix planes:

$$\Delta\tau = 0.12G\frac{b}{\sqrt{Dt}}\left(\sqrt{f_v} + 0.7\sqrt{\frac{D}{t}f_v} + 0.12\frac{D}{t}f_v^{\;3/2}\right)\ln\left(\frac{0.079D}{b}\right) \tag{32}$$

The applicability of equation (31) and (32) to T_1 strengthening is nowadays questionable as they do not consider the shearable nature of T_1 precipitates. Nevertheless, we will test the ability of these two models to predict the yield strength evolutions during the duplex ageing treatment at 155°C and 190°C (described in part 3.3). In order to convert the CRSS increment into yield strength, the following expression is usually applied:

$$\Delta\sigma = M\Delta\tau + \sigma_0 \tag{33}$$

where M~3 is the Taylor factor [29], σ_0 is the strength factor including all the other contributions to strengthening (Peierls stress, grain and sub-grain strengthening, solute and dislocation strengthening). For the 2.5% pre-deformed sample, we will approximate σ_0 as the yield strength of a sample at the end of the ramp (free from precipitates), which is approximately 250 MPa. Figure 63 displays the predicted and measured yield strength evolutions. As expected, the predictions from these two Orowan-like models are not satisfying. As a consequence, we will rule out these models for the prediction of strengthening by the T_1-phase.

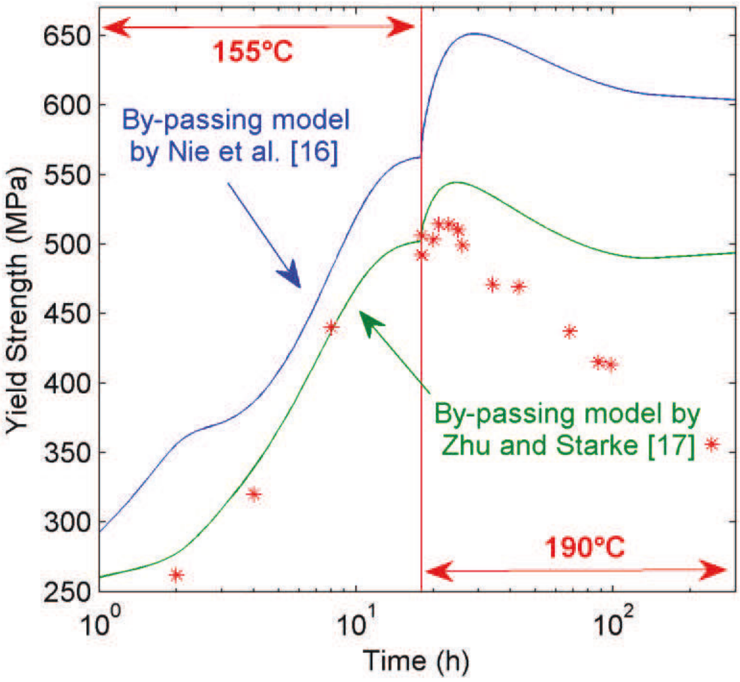

Figure 63: Experimentally measured yield strength during the duplex ageing treatment (symbols), and predictions by the two models based on the by-passing mechanism (lines).

4.2 Models based on the shearing mechanism

In order to model accurately the yield strength evolution, the shearable feature of the T_1 phase has to be accounted for. Shearing a T_1 leads to the creation of a new precipitate/matrix interface and of an anti-phase boundary (APB) as depicted in Figure 64a.

Nie and Muddle [22] proposed a model describing the effect of the creation of a precipitate/matrix interface on strengthening. They established the following expression for interfacial strengthening for Al alloys containing regular triangular arrays of shearable $\{111\}_{Al}$ plates:

$$\Delta\tau = \frac{1.211 D \gamma_i^{3/2}}{t^2} \sqrt{\frac{b f_v}{\Gamma}} \tag{34}$$

where γ_i is the precipitate/matrix interfacial energy. However, this model does not include the influence of the formation of an APB on the slip plane within the precipitate, which should be considered when regarding the T_1 shearing process (Figure 64). We will now propose a modified version of Nie and Muddle's interfacial strengthening model in order to consider both the new interface and APB contributions to strengthening.

In the approximation of weak obstacles, the contribution of shearable precipitates to the strength increment has been described by Guyot [30] as:

$$\Delta\tau = \alpha^{3/2} \left(\frac{\Gamma}{\sqrt{2} b L} \right) \tag{35}$$

where $\alpha = {}^{F}/_{\Gamma}$ is a parameter that characterises the precipitate's resistance to dislocation glide $(0 < \alpha < 2)$ and Γ is the dislocation line tension in the Al matrix which can be approximated as:

$$\Gamma = \frac{1}{2} G b^2 \tag{36}$$

where G=25GPa is the shear modulus of aluminium, b=0.286nm is the Burgers' vector.

Defining the obstacle strength in the case of shearable particles is delicate as many contributions are often involved in the particle shearing mechanism. For the sake of simplicity, we will approximate the T_1 plates to square plates of width D and thickness t (Figure 64a). The T_1 shearing mechanism has been recently revealed to only occur by single-steps [21] (Figure 64b). The length of a shearing step is $b * \sin(\alpha)$, where $b \sim 0.286 nm$ is the Burger's vector and $\alpha = 60°$ is the angle between the slip direction and the sheared plate.

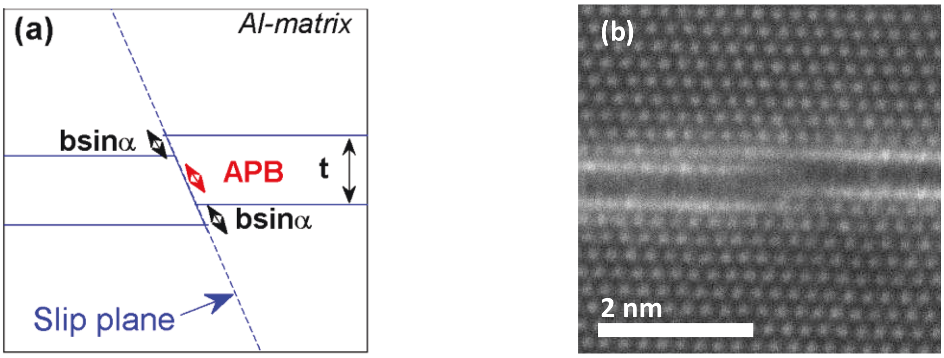

Figure 64: (a) scheme of a sheared plate observed edge-on revealing the creation of a new precipitate/matrix interface and the creation of an anti-phase boundary. (b) Image of a sheared T_1 taken in HAADF-STEM along the <110> zone axis.

The area of the new matrix/precipitate interface is $A_i = 2b\sin(\alpha)D$ and the area of the APB is $A_{APB} = D(t/\sin(\theta) - b\sin(\alpha))$ where θ=70.53° is the angle between two $\{111\}_{Al}$ planes. The energies related to the formation of these new interfaces are:

$$\begin{gathered} E_i = A_i\gamma_i = 2b\sin(\alpha)D\gamma_i \\ E_{APB} = A_{APB}\gamma_{APB} = D(t/\sin(\theta) - b\sin(\alpha))\gamma_{APB} \end{gathered} \tag{37}$$

Where γ_{APB} is the interfacial energy corresponding to the created APB.

The strength of a shearable precipitate plate F can thus be written as:

$$F = F_i + F_{APB} = \frac{E_i + E_{APB}}{t/\sin(\theta)} = \frac{2b\sin(\alpha)D\gamma_i + D(t/\sin(\theta) - b\sin(\alpha))\gamma_{APB}}{t/\sin(\theta)} \tag{38}$$

The mean planar centre-to-centre precipitate spacing L has been expressed by Nie and Muddle [16] considering triangular arrays distribution of $\{111\}_{AL}$ plates:

$$L = 0.931\sqrt{\frac{0.265\pi D t}{f_v}} \tag{39}$$

By combining equations (35), (36), (38) and (39), we can deduce the following expression for the CRSS increment attributed to shearable $\{111\}_{Al}$ plate-like precipitates:

$$\begin{gathered} \Delta\tau_{T1} = \frac{0.762 D\gamma_{eff}^{\,3/2}}{t^2}\sqrt{\frac{bf_v}{\Gamma}} \\ \text{With } \gamma_{eff} = 2\sin(\alpha)\gamma_i + \left(\frac{t}{b\sin(\theta)} - \sin(\alpha)\right)\gamma_{APB} \end{gathered} \tag{40}$$

This expression is a modified version of equation (35), which accounts for the creation of both the new interface and the APB. The yield strength evolutions, as predicted by equation (35) and (40), are plotted together in Figure 65 for the duplex ageing treatment, where the interfacial energies (only γ_i for the original model, γ_i and γ_{APB} for the modified model) are fitting parameters. The predictions at constant T_1 thickness are necessarily the same for both models (although for a different value of γ_i).

However, one can notice that the predictions differ when the T_1 precipitates are thickening. The contribution of the APB to the yield strength becomes more important for thicker plates, which results in a higher predicted yield strength when the precipitates are thickening.

In the case of Nie and Muddle's model the fitted interfacial energy is $\gamma_i = 0.107$ J/m^2. For the modified interfacial strengthening model, the following interfacial energies are found: $\gamma_i = 0.07$ J/m^2 and $\gamma_{APB} = 0.007$ J/m^2. These energies are in the range of classical interfacial energy values for semi-coherent precipitates. However, one can notice a significant difference between the interfacial and APB energies. The high amount of energy required to create a new interface is related to the difference in precipitate and matrix structures which results in a high strain field at the new created interface. The presence of this high strain field gives rise to a blurry contrast in HAADF-STEM around the sheared region (see Figure 64b). For the Ω phase in Aluminium alloys, Lie and Wawner [31] revealed that the interfacial energy for the new interface increases dramatically with multiple shearing events, which makes multiple shearing highly unfavourable, as confirmed recently for the T_1 phase by the observations of Deschamps et al. [21]. However, the creation of an APB, which is internal to the precipitate, may result in a smaller mismatch and thus requires less energy. This result highlights that the contribution of the APB creation is only minor in the shearing process as it requires much less energy than the creation of a new precipitate/matrix interface. It thus explains why Nie and Muddle's interfacial strengthening model is able to predict accurately the yield strength evolution by only considering the creation of the new precipitate/matrix interface while neglecting the APB creation. However, we believe that the modified interfacial strengthening model is physically more correct and applies better to late ageing times and we will thus use it in the following.

One important observation resulting from the fit of the modified model to the experimental data is that it describes very accurately the first stages of the ageing treatment at 190°C, where all parameters vary very quickly (namely diameter, volume fraction and thickness). It is also capable of describing a large part of the strength decrease during over-ageing at 190°C, confirming that it is not necessary to invoke a precipitate by-passing mechanism even at these late stages of ageing. Actually sheared T_1 precipitates thicker than one unit cell have been reported in literature [19]. However, at very late ageing times (last point at 250h of ageing) the model prediction strongly deviates from the experimental data. This deviation could be related to a change in the precipitate-dislocation interaction mechanism.

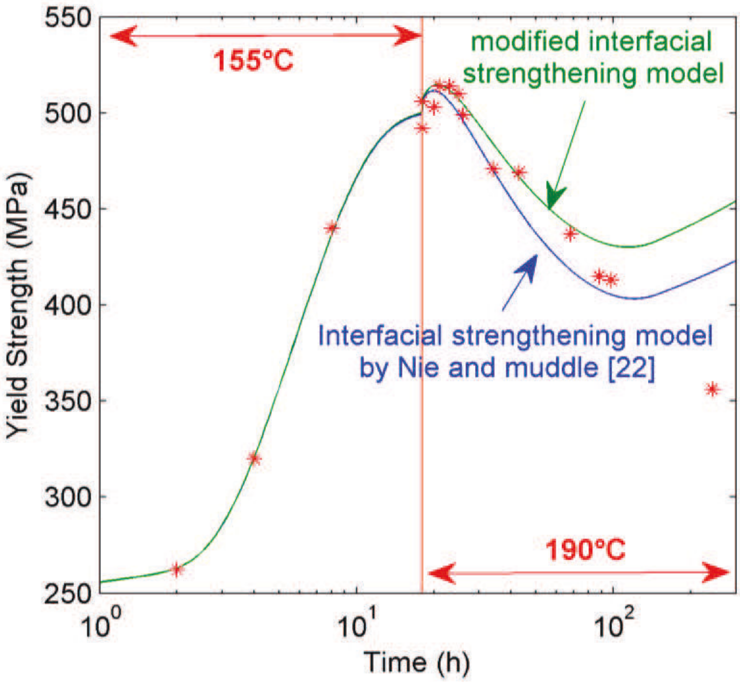

Figure 65: Experimentally measured yield strength during the duplex ageing treatment (symbols), and predictions by the two models based on the shearing mechanism (lines). The interfacial strengthening by Nie and Muddle corresponds to equation (35) and the modified interfacial strengthening curve corresponds to equation (40).

4.3 Applicability of the modified interfacial strengthening model to the different T_1 kinetics

The preceding section showed that the modified interfacial strengthening model (equation (40)) is suitable to describe the yield strength evolution in the presence of T_1 precipitates. In order to test the robustness of this model, we calculated the yield strength evolutions for the ageing treatments with different pre-deformations studied in part 3.2, using the measured microstructural parameters for the T_1 precipitates. As shown in Figure 13, the model can be successfully applied to this data, provided that the base strength in the absence of precipitates σ_0 is adjusted depending on the pre-deformation value. σ_0 was respectively adjusted to 152MPa, 250MPa and 310MPa for the 0.5%, 2.5% and 12% pre-deformations. The signification of this adjustment will be discussed in the next section.

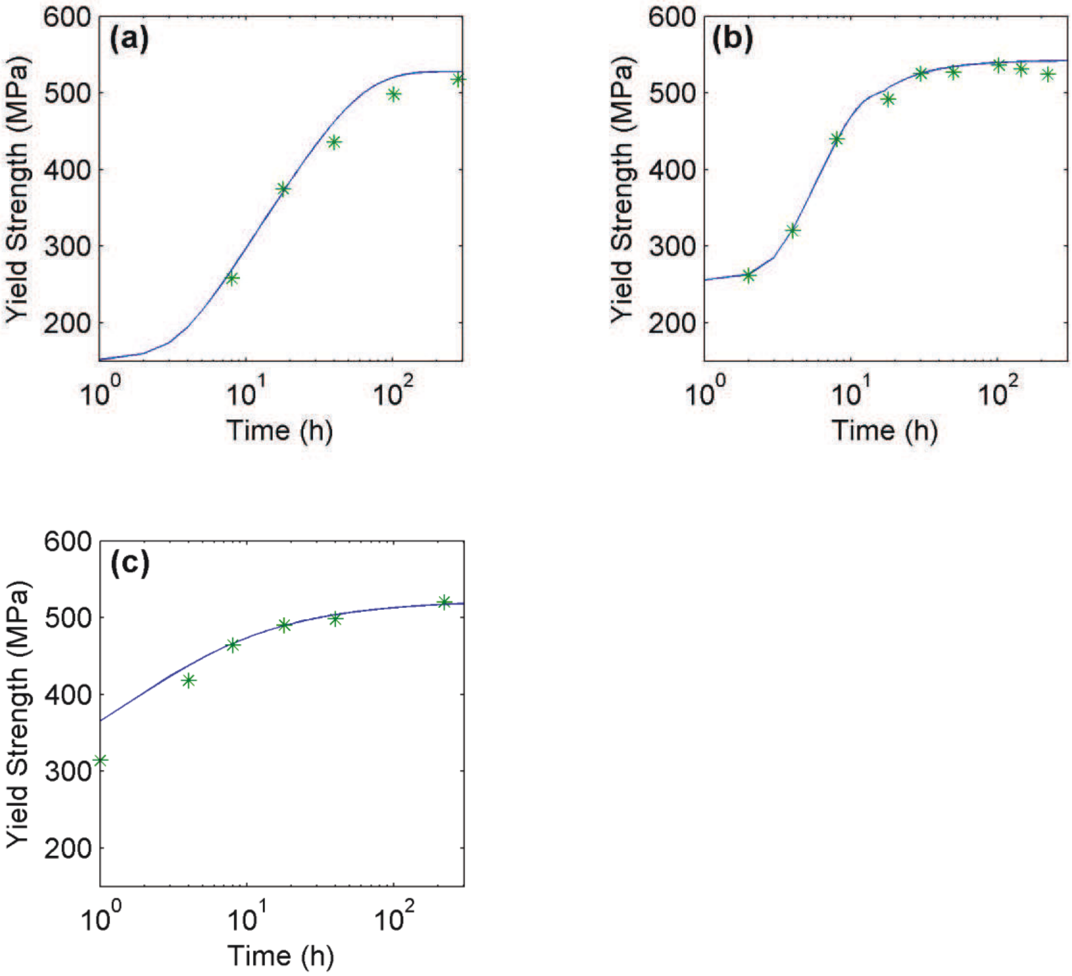

Figure 66: Experimental yield strength measurements (symbols) and evolutions as predicted from equation (40) (lines) as a function of ageing time during a heat treatment at 155°C and different pre-deformation; (a) 0.5%, (b) 2.5% and (c) 12%.

5. Discussion

The experimental database of microstructure-strength relationships that we generated makes it possible to test the possibility of precipitation strengthening models to describe the effect of precipitation of T_1 on yield strength. We have shown that models based on the by-passing mechanism were unsuccessful in describing our experimental results, consistently with the now widely accepted shearable nature of the T_1 precipitates. On the other hand, Nie and Muddle's model for interfacial strengthening by platelet precipitates [22] has been shown to provide a good agreement with experimental data. A modified version of this model has been shown to successfully describe a wide range of experimental data, including the transition on each side of the peak-aged state. This agreement strongly suggests that the peak ageing state is not related in this case to a change of precipitate-dislocation mechanism from precipitate shearing to precipitate by-passing as is commonly observed in some aluminium alloys such as Al-Zn-Mg-Cu alloys [32,33]. Instead, the experimental data and the model agree in attributing the strength decrease after peak ageing to an increase in precipitate thickness ($\Delta\tau \propto t^{-2}$). However for very long over-ageing the model predictions deviate strongly form the experimental data, suggesting a change in strengthening mechanism. When T_1 precipitates reach a sufficient thickness and when their number density becomes sufficiently small so that their spacing increases, it seems reasonable that the by-passing mechanism should be activated. However, it can be noted that the models based on the by-passing mechanism do not predict the good range of strengthening for these overaged conditions either. The influence of precipitate microstructures on this possible change in strengthening mechanism requires a more detailed study of the alloy's plasticity that will be reported in a separate paper.

The modified interfacial strengthening model has been shown to be applicable to all the investigated thermo-mechanical treatment, including the ageing treatments where the pre-deformation had been varied, resulting in a wide range of precipitate number densities. However, this applicability required to choose different base strengths σ_0 depending on the initial pre-deformation. This difference can naturally reflect the influence of pre-deformation on dislocation strengthening. In fact, the flow stress during the tensile test used for stretching is approximately 100 MPa, 150 MPa and 300 MPa for, respectively, the 0.5, 2.5 and 12% pre-deformations. The remaining difference could be due to the presence on the dislocations of other phases such as Mg-rich precipitates that have been shown to form together with the T_1 precipitates [34]. This can explain the relatively high strength of the sample at the end of the heating ramp to 155°C when no significant T_1 precipitates are present (250 MPa for the 2.5% pre-deformed material).

Assuming that this description of T_1 strengthening is correct, it has a number of interesting consequences. Firstly, it implies that the linear relationship, independent of pre-deformation, that was experimentally observed between yield strength and T_1 precipitate volume fraction (Figure 58b) is not supported by our model. In fact, it results from a compensation of the change in precipitation strengthening by a change in base strength with pre-deformation. Equation 12 of our model can be written as $\Delta\tau \propto f_v N^{-1/2} t^{-5/2}$, meaning that the linear relationship between volume fraction and strengthening increment holds for a constant precipitate thickness and number density. The constant precipitate thickness is a valid assumption during ageing at 155°C (Figure 57b), however the precipitate density changes moderately during the ageing treatment after a given pre-deformation, and strongly from one pre-deformation to another. This change in precipitate density explains the necessary compensation of a loss of strengthening by an increased base strength to describe the entire range of studied microstructures.

It may seem at first sight counter-intuitive that the precipitate strength should decrease when the precipitate number density becomes higher, at constant volume fraction and thickness. Such a dependence to precipitate number density is opposite to what happens with strengthening by spherical precipitates. However it can be better understood if equation 12 of our model is re-organised in yet another way as $\Delta\tau \propto D^2 N^{1/2} t^{-3/2}$ where the volume fraction does not appear explicitly. This form of the equation shows that both the contributions of precipitate number density and precipitate diameter are positive to the strengthening increment; however the diameter has a much stronger contribution, because increasing the precipitate diameter has a large effect on the precipitate strength. Consequently, increasing the precipitate number density at constant volume fraction and thickness (such as is achieved by increasing the pre-deformation), which necessarily results in a decrease of their diameter, induces a decrease of the strength increment.

6. Conclusion

1) By combining the effect of pre-deformation, ageing time and ageing temperature, a wide range of T_1 microstructures have been obtained. The parameters of the T_1 precipitate distributions have been systematically characterised in terms of precipitate thickness, diameter, volume fraction and the resulting number density has been calculated. The yield strengths corresponding to these microstructures have been systematically measured, resulting in a large database of microstructure – strength relationships.

2) The yield strength evolution, in the case of strengthening by T_1 precipitates, has been successfully described using a model for precipitate shearing considering the combination of interfacial and anti-phase boundary strengthening. The transition at peak strength and subsequent decrease in yield strength are successfully represented without accounting for a shearing-to-by-passing transition.

3) The interfacial strengthening model overestimates the yield strength for highly over-aged samples. This result suggests that a transition in strengthening mechanisms occurs in the late stages of precipitation. An alternative model is necessary to predict the yield strength for these conditions.

7. References

1. Williams, J. C., Starke Jr, E. A.: Acta Mater. 51, 5775-5799 (2003)

2. Warner, T.: Mat. Sci For. 519-521, 1271-1278 (2006)

3. Rioja, R. J., Liu, J.: Met. and Mat. Trans. A 43A, 3325-3337 (2012)

4. Daniélou, A., Ronxin, J. P., Nardin, C., Ehstrom, J. C.: Proceedings of the 13th international conference on aluminium alloys, Pittsburgh, PA: TMS, Warrendale, PA, 511-516 (2012)

5. Hardy, H. K., Silcock, J. M.: J.Inst. Met. 84, 423-428 (1955-56)

6. Sainfort, P., Dubost, B.: J. de phys. 48, 407-413 (1987)

7. Cassada, W., Shiflet, G. J., Starke Jr., E. A.: Met. Trans. A 22A, 299-306 (1991)

8. Ringer, S. P., Muddle, B. C., Polmear, I. J.: Met. and Mat. Trans. A 26A, 1659-1671 (1995)

9. Gable, B., Zhu, A. W., Csontos, A. A., E.A., S.: J. of Light Met. 1, 1-14 (2001)

10. Decreus, B.: Etude de la précipitation dans les alliages Al-Li-Cu de troisième génération-Relations entre microstructures et propriétés mécaniques. Phd Thesis. Institut Polytechnique de Grenoble, France (2010)

11. Decreus, B., Deschamps, A., De Geuser, F., Donnadieu, P., Sigli, C., Weyland, M.: Acta Mater. 61, 2207-2218 (2013)

12. Donnadieu, P., Shao, Y., De Geuser, F., Botton, G. A., Lazar, S., Cheynet, M., de Boissieu, M., Deschamps, A.: Act. Mater. 59, 462-472 (2011)

13. Dwyer, C., Weyland, M., Chang, L. Y., Muddle, B. C.: Appl. Phys. Lett. 98 (2011)

14. Orowan, E.: , Londres, p.451 (1948)

15. Huang, J. C., Ardell, A. J.: J. Phys. 48, 373-383 (1987)

16. Nie, J. F., Muddle, B., Polmear, I. J.: Trans Tech Publ. 217-222, 1257-1262 (1996)

17. Zhu, A. W., Starke, E. A.: Acta Metall. 47(11), 3262-3269 (1999)

18. Howe, J. M., Lee, J., Vasudevan, A. K.: Met. Trans. A 19A, 2911-2920 (1988)

19. Nie, J. F., Muddle, B. C.: Mat. Sci. and Eng., 448-451 (2001)

20. Csontos, E. A., Starke, A. A.: Int. J. of Plast. 21, 1097-1118 (2005)

21. Deschamps, A., Decreus, B., De Geuser, F., Dorin, T., Weyland, M.: Acta Mater. 61(11), 4010-4021 (2013)

22. Nie, J. F., Muddle, B. C.: J. of Phase eq. 19(6), 543-551 (1998)

23. Csontos, A. A., Starke Jr, E. A.: Met. and Mat. Trans. A 31A, 1965-1976 (2000)

24. Dorin, T., De Geuser, F., Lefebvre, W., Sigli, C., Deschamps, A.: Phil Mag. in press (2013)

25. De Geuser, F., Bley, F., Deschamps, A.: J. of App. Cryst. 45, 1208-1218 (2012)

26. Zhang, F., Ilavsky, J., Long, G. G., Quintana, J. P. G., Allen, A. J., Jemian, P. R.: Met. and Mat. Trans. A 41A, 1151-1158 (2010)

27. Chu, T. C., Ranson, W. F., Sutton, M. A., Peters, W. H.: Exp. Mech. 25(3), 232-244 (1985)

28. Avrami, M.: J. Chem. Phys. 7, 1103-1112 (1939)

29. Tayron, W., Crooks, R., Domack, M., Wagner, J.: Experimental Mechanics 50, 135-143 (2010)

30. Guyot, P.: Interactions des dislocations avec des impuretés fixes. In : Dislocations et déformation plastique, Yravals, pp.185-197 (1979)

31. Li, B. Q., Wawner, F. E.: Acta Mater. 46(15), 5483-5490 (1998)

32. Guyot, P., Cottignies, L.: Acta Mater. 44, 61-67 (1996)

33. Fribourg, G., Bréchet, Y., Deschamps, A., Simar, A.: Acta Mater. 59, 3621-3635 (2011)

34. Araullo-Peters, V., Gault, B., De Geuser, F., Deschamps, A., Cairney, J. M.: Acta Mater. in press. (2013)

Chapter V: Investigation on the strengthening mechanisms of the T_1 precipitates and influence on the plasticity behaviour

The aim of this chapter is to get a better understanding of the strengthening mechanisms in terms of interactions between the dislocations and the T_1 precipitates. In the precedent chapter, we managed to model the yield strength by using a model based on shearing only. The model failed to predict the yield strength only in the case of heavily over-aged conditions suggesting a transition from shearing to by passing that would occur long after the peak strength. We will see that the observation of the plasticity behaviour and evolution as a function of the T_1 kinetics is a strong tool to get information on the strengthening mechanisms.

Strengthening mechanisms of T_1 precipitates and their influence on the plasticity of an Al-Cu-Li alloy

Thomas Dorin[1,2], Frédéric De Geuser[1], Williams Lefebvre[3], Christophe Sigli[2], Alexis Deschamps[1]

[1]SIMAP, INP Grenoble – CNRS – UJF, BP 75, 38402 St Martin d'Hères Cedex, France
[2]Constellium, Voreppe Research Centre, CS 10027, 38341 Voreppe Cedex, France
[3] Groupe de Physique des Matériaux – CNRS – University of Rouen, 76 801 St Etienne du Rouvray Cedex, France

1. Introduction

Al-Cu-Li alloys exhibit a good combination of properties such as high strength, low weight and good damage tolerance, which makes them well suited for aerospace applications [1,2,3]. In the recently developed Al-Cu-Li alloys, the main contribution to strengthening is provided by the precipitation of the T_1 phase, which forms as platelets on the {111}Al planes [4,5]. During the first stages of ageing at 155°C until peak strength, T_1 precipitates have a constant thickness of one unit cell (1.3 nm, called single-layer T_1) [5,6]. For very long ageing times and/or higher temperatures, the thickness of T_1 precipitates progressively increases, together with a decrease of yield strength [7].

The strengthening mechanisms associated to the presence of T_1 precipitates and the associated precipitate-dislocation interactions have been the subject of a number of reports in literature. In early studies, T_1 precipitates were described as strong unshearable particles similarly to the θ' phase [8,9,10,11,12]. However, the development of high-resolution electron microscopy (HREM) made it possible to observe sheared precipitates in deformed samples. Thin T_1 precipitates, whose thickness consist in only one unit cell (that can be called "single layer T_1"), have now been observed sheared by dislocations in numerous studies [13,14,15,16,17]. Deschamps et al. [17] recently observed more than 70 shearing events of single-layer T_1 precipitates on an AA2198 alloy in the peak-aged condition deformed at 2% plastic strain. The observation of a thicker sheared T_1 precipitate (three-layer) has only been reported once in a study by Nie and Muddle [15], so that it remains unclear if another mechanism such as precipitate by-passing takes over when T_1 precipitates coarsen.

A recent work studied the relationship between yield strength and T_1 precipitate microstructures on AA2198 alloy, ranging from under-aged to heavily over-aged [7]. In all conditions but the longest over-ageing times, the evolution of yield strength was successfully described by a shearing mechanism model based on Nie and Muddle's work [18]. The yield strength was shown to increase at constant T_1 thickness as a function of T_1 volume fraction and to decrease when the T_1 plates are thickening [7]. The transition in yield strength from under-ageing to over-ageing was solely explained by invoking the shearing mechanism based on interfacial strengthening. This model was only found to overestimate the yield strength for only long over-ageing times, suggesting a change in precipitate-dislocation interaction mechanism.

The mode of interaction between dislocations and precipitates strongly influences the plasticity behaviour. Precipitate by-passing usually results in a homogenisation of plasticity while precipitate shearing is commonly considered to result in the localisation of plasticity [19]. In Al-Cu-Li alloys, the shearing of δ' actually results in significant plastic localisation and thus in a degraded ductility [20,21,22]. Csontos and Starke [16] observed that the shearing mechanism of the T_1 phase also results in the formation of intense shear bands. However, Deschamps et al. [17] proposed that single-layer T_1 precipitates could only be sheared once in the same place, thus preventing catastrophic planar slip. As a consequence, it seems that the presence of single-layer T_1 precipitates prevents a localisation of plasticity on a microscopic scale although it may still result in the localisation of plasticity at a macroscopic scale (formation of slip lines).

The aim of the present paper is to clarify the influence of T_1 precipitate microstructure, and particularly the effect of plate thickness, on the plasticity of Al-Cu-Li alloys. For this purpose, the precipitate-dislocation mechanisms and the associated alloy's plasticity will be studied in situations where the T_1 precipitate microstructure is varied in a wide range, ranging from under-aged tempers of precipitation (growing single-layer precipitates) to heavily over-aged tempers (multiple layer precipitates). The microstructure characterisation along a duplex ageing treatment at 155°C and 190°C is based on a recently published paper [6]. Deformed samples are observed using high resolution scanning transmission electron microscopy (STEM) in the high angle annular dark field mode (HAADF) in order to observe at the microscopic scale the precipitate-dislocation interactions. The strain hardening evolution will then be analysed using uniaxial tensile tests and Bauschinger tests. Finally, the plastic strain localisation at the macroscopic scale is evaluated using optical microscopy with Nomarski contrast and Confocal Laser Scanning Microscopy (CLSM) observations.

2. Material and experimental procedure

The AA2198 alloy was provided by the Constellium Voreppe Research Centre, France, as rolled 5mm thick sheets with a fully unrecrystallised grain structure. Table 11 gives the composition range for AA2198 alloy. The samples were first solution treated and water quenched. Right after quenching, the samples were pre-deformed to a plastic strain of 2.5%. The samples were naturally aged for seven days and then aged in an oil bath, starting with a heating ramp of 20 $K.h^{-1}$ to 155°C, followed by a duplex ageing treatment for 18h at 155°C and then 190°C (temperature reached in approximately 5 min). The samples were quenched into cold water at different times during the heat treatment and analysed.

The samples for HAADF-STEM observations were first mechanically polished into thin foils of $\sim 100\mu\text{m}$ and then electro-polished using a twin double jet system in a solution of 33% nitric acid in methanol at -20°C and 15V. The observations were performed in a JEOL ARM 200F equipped with a Schottky field emitter and operating at 200kV. This instrument was also equipped with a spherical aberration Cs-probe corrector. The following parameters were used: probe diameter of 0.1nm, an objective aperture semi-angle of 22.5mrad, detector half-collection angle between 40 and 150mrad.

The samples for optical microscopy and CLSM were mirror polished then deformed up to 2% plastic strain, in uniaxial tension, with special care not to damage the polished area. Optical microscopy observations were carried out on a BX60M Olympus microscope equipped with a Nomarski prism. The CLSM experiments were carried out on a Talysurf CCI 6000 microscope at the Pprime Institute in Poitiers, France.

Tensile measurements were carried out using a screw-driven Instron machine with a 30kN load cell. Normalised tensile samples, with a cross-section of 3mm*5mm and gauge length of 60mm, were used. The extensometer gauge length was 10mm. The strain rate was 10^{-3} s^{-1}.

Bauschinger tests were conducted on a servo-hydraulic MTS machine with hydraulic wedge grips to hold the specimen. The gauge section was 4mm in diameter and the gauge length was 12mm. The extensometer gauge length was 10mm. The strain rate was 10^{-3} s^{-1}.

Table 11: Composition of AA2198 alloy given in wt%

AA2198	*Cu*	*Li*	*Mg*	*Ag*	*Zr*	*Al*
Min	2.9	0.8	0.25	0.1	0.04	bal
Max	3.5	1.1	0.8	0.5	0.18	bal

3. Results

3.1 Precipitate microstructure evolution during the duplex ageing treatment

The quantitative description of the T_1 kinetics during the duplex ageing treatment (18h at 155°C and then 190°C) has been the subject of a recent paper [6]. The evolution of the morphological parameters and volume fraction of the T_1 phase was investigated using in-situ Small-Angle X-Ray Scattering (SAXS), Differential Scanning Calorimetry (DSC) and HAADF-STEM. In this section, we will briefly summarise the main outcome of this previous study. The evolutions of the average thickness and diameter, volume fraction and number density of the T_1 precipitates are reported in Figure 67 as a function of ageing time. The precipitate thickness is constant at 1.3nm during the 18h at 155°C that correspond to the growth of single-layer precipitates only. Precipitate thickening is activated when temperature is raised to 190°C and an average thickness of 2nm is reached after approximately 70h at 190°C. During ageing at 155°C, the volume fraction first stabilises around 2%, corresponding to the saturation of the growth of single-layer precipitates. Increasing the temperature to 190°C activates precipitate thickening, which enables the remaining solute to join the precipitates [6] and the volume fraction reaches a saturation value of 2.5%. It has previously been observed that the average thickness of 2nm measured after 18h at 155°C + 70h at 190°C actually consists of a distribution of T_1 thickness from single layer to multi-layer precipitates [6].

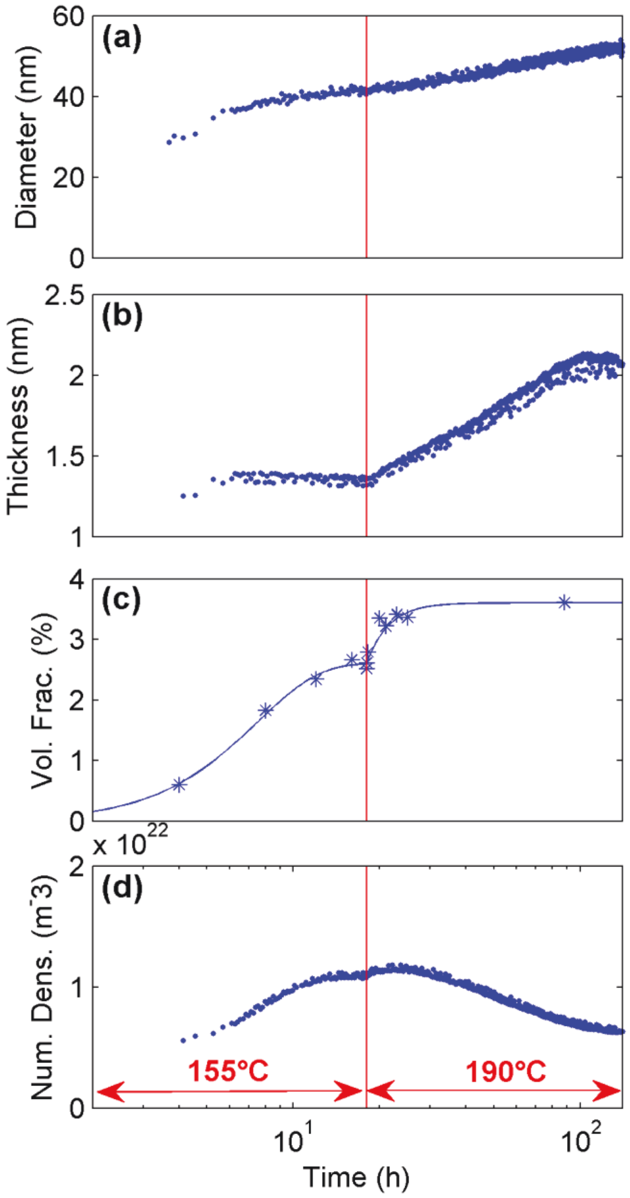

Figure 67: Plots of the evolution of the characteristic parameters of the T_1 phase during a duplex heat treatment at 155°C (for 18h) and then at 190°C. (a) Evolution of the mean diameter (in nm), (b) of the mean thickness (in nm), (c) of the volume fraction (in %) and (d) of the number density (in m^{-3}) of the T_1 precipitates (results taken from [6]).

3.2 HAADF-STEM observations of the shearing events

The HAADF-STEM technique provides an atomic resolution with a contrast in atomic number (Z) approximately proportional to Z^2 [23], which makes it suitable to observe the T_1-Al_2CuLi precipitates that have a strong contrast with respect to the Al matrix. Indeed, when viewed edge-on such as on a <110> or <112> matrix zone axis, the contrast arises from the bright Cu-rich layers in the T1 precipitate which surround a dark Li-rich layer (Figure 68a) [24,25]. We conducted HAADF-STEM observations on an AA2198 sample aged for 18h at 155°C and 70h at 190°C and then deformed plastically 2%. The observations were carried out along the <110> matrix zone axis (Figure 68a and e) and along the <112> matrix zone axis (Figure 68b, c and d). Shearing events were observed on single-layer, two and three-layer precipitates (see Figure 68a to 2d), but no evidence was found for the shearing of T_1 precipitates consisting of 4 layers or more: all such precipitates were observed unsheared (see Figure 68e). However, it is not possible using STEM-HAADF observations to conclude on the existence of a by-passing mechanism for such precipitates and this possibility will be evaluated by the study of plasticity further in this paper.

Similarly to what had been observed in [17] for single-layer precipitates, the extent of the shearing events was always found to be of one Burgers' vector only, irrespective of the thickness of the sheared precipitates. This suggests that it is energetically more favourable for a gliding dislocation to cross-slip and shear the precipitate in a different location than shear it again on the same plane (see Figure 68c).

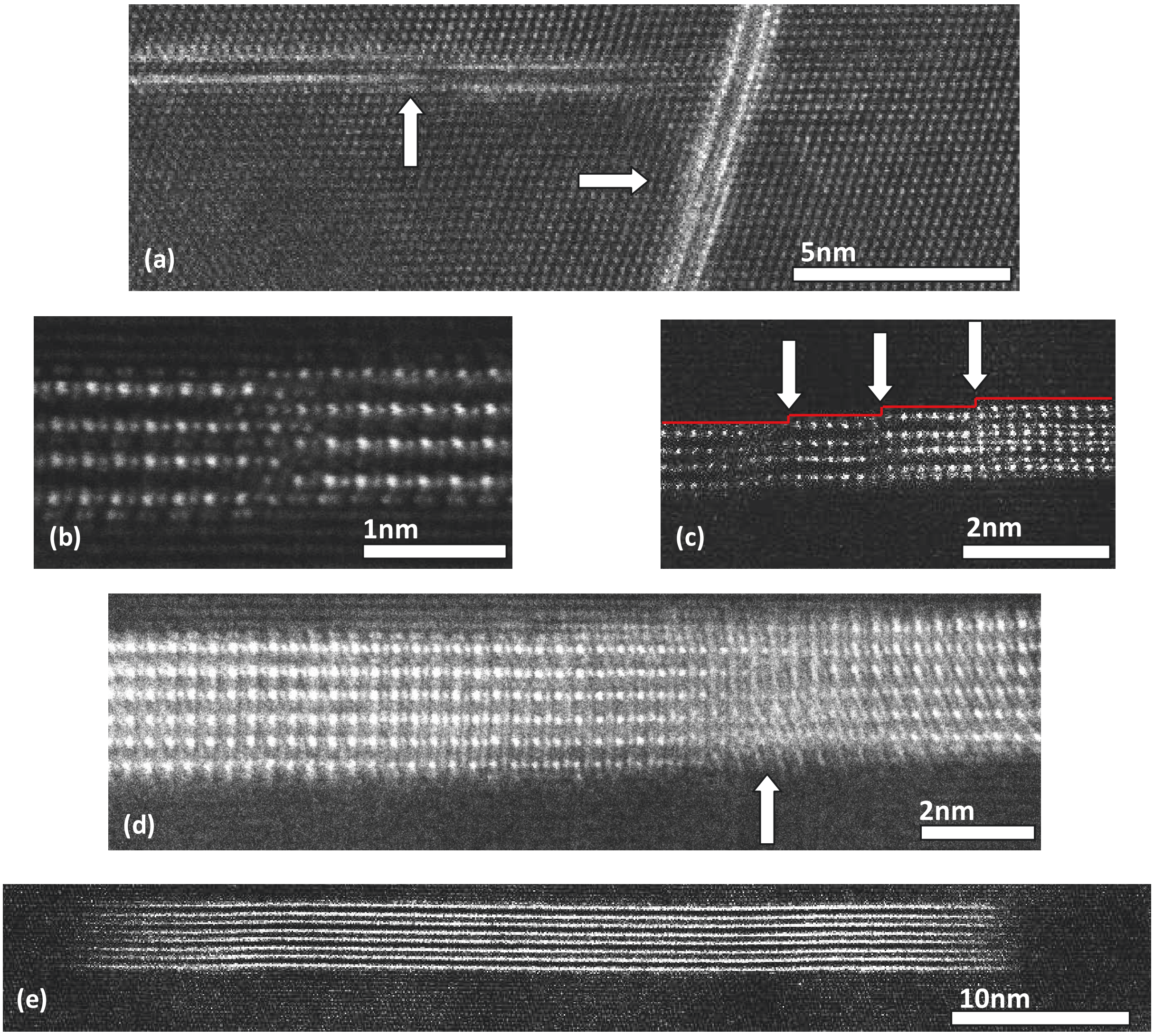

Figure 68: HAADF-STEM images taken on a sample aged 18h at 155°C and 70h at 190°C and then deformed plastically 2%, (a) to (d) Single to three-layer T_1 precipitates that have all been sheared and (e) a four-layer T_1 precipitate that has not been sheared.

3.3 **Mechanical tests: investigation of the strain hardening behaviour**

3.3.1 Tensile tests

The strain hardening capability of metals can be impacted by many factors such as the presence of solute elements or precipitates [26]. The influence of precipitates on the strain hardening capability highly depends on the dislocation/precipitate interaction [19]. Precipitate shearing prevents additional dislocation storage, which results in a low strain hardening rate. Additionally, if precipitates become completely sheared by a series of dislocations, massive dislocation movement can occur, resulting in early ductile failure [20]. On the contrary, precipitate by-passing induces the storage of dislocations in the form of Orowan loops, which results in a high strain hardening rate, at least for small plastic strains before the recovery of stored dislocations becomes significant. The plastic flow is homogenised due to the stress exerted on incoming dislocations by the Orowan loops, which favours their cross-slip.

The yield strength and ultimate tensile strength (UTS) are plotted in Figure 69a for samples along the entire heat treatment. The yield strength rapidly increases until the transition in temperature; in parallel the UTS also increases but more slowly, indicating a decreasing strain hardening capability. When the temperature is raised to 190°C, the yield strength first continues to increase slightly and then rapidly decreases. The UTS follows the same tendency, and only for long over-ageing times it is observed that the strain hardening capability increases again. Tensile stress-strain curves are represented in Figure 69b at different characteristic stages of over-ageing after the transition in temperature from the peak-aged state (18h at 155°C). It is observed that the stress-strain curves first remain almost parallel and progressively the strain hardening rate at small strains is observed to increase.

In order to observe this transition in more detail, the strain hardening rate $\theta = \frac{d\sigma}{d\varepsilon}$ is calculated and plotted as a function of $\sigma - \sigma_y$ in Figure 70a (so-called Kocks-Mecking plots). The strain hardening rate is observed to gradually increase with holding time at 190°C, which is well correlated with the increase of T_1 thickness. The early strain hardening rate is frequently described by the initial strain hardening rate θ_0 [27,28,29], where this value is obtained by extrapolation of the linear part of the Kocks-Mecking plot to $\sigma = \sigma_y$ (Figure 70b). The initial hardening rate is first observed to decrease from 2100 MPa to a minimum of 1500 MPa at peak strength (18h at 155°C). This value of the strain hardening rate at peak strength is close to that of pure aluminium [17,29], which is consistent with the absence of additional dislocation storage associated with the presence of the precipitates when they are sheared by dislocations. After peak strength, θ_0 is found to increase gradually to a maximum of about 4700 MPa after 225h at 190°C. This increase in θ_0 is classically attributed to a shearing-to-by-passing transition and has been observed in 7000 and 6000 series Aluminium alloys [29,30].

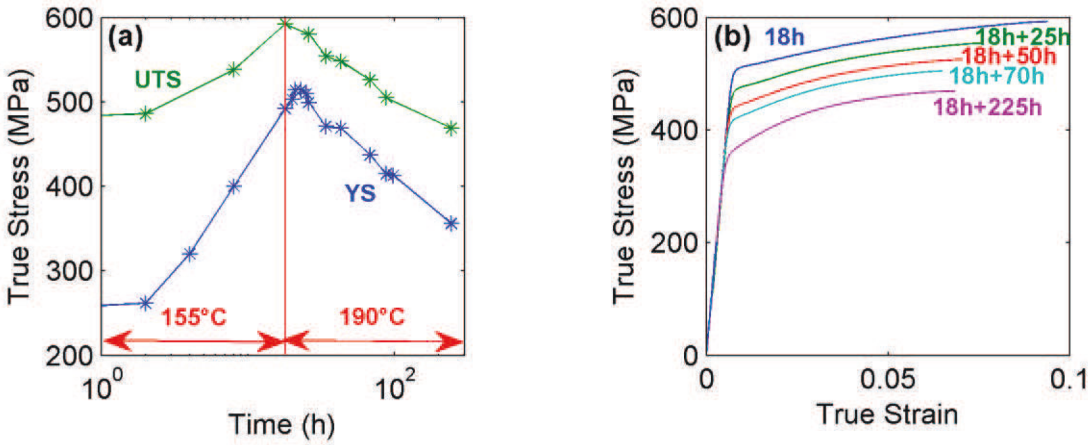

Figure 69: (a) Stress-strain curves for different ageing times during the duplex ageing treatment and (b) Yield strength and ultimate tensile strength evolutions during the duplex ageing treatment.

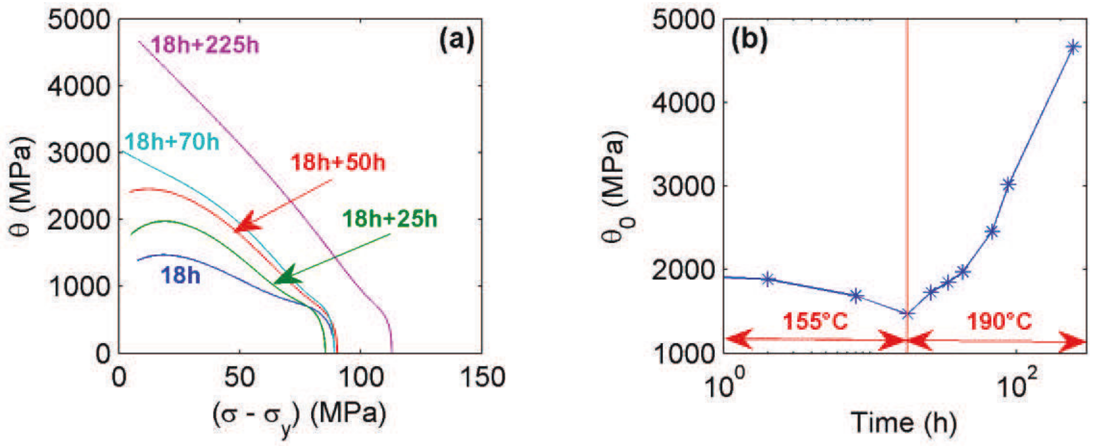

Figure 70: (a) Strain hardening rate for different ageing times during the duplex ageing treatment and (b) evolution of the initial strain hardening rate θ_0.

3.3.2 Bauschinger tests

Strain reversal tests, or Bauschinger tests, are classically used to evaluate the kinematic contribution of strain hardening [29]. More precisely, the magnitude of the difference in flow stress during monotonic loading and strain reversal is characteristic of the presence of internal stresses in the material, and a high value is often related to the presence of impenetrable obstacles to dislocations, such as non-shearable precipitates [31]. However is has been shown recently that the situation could be more complicated since the Bauschinger stress can be high, at least for small reverse strains, in cases where precipitates are sheared but the strain path is highly reversible [17].

We performed Bauschinger tests in three selected conditions that are representative of three important stages before and during the T_1 thickening process (18h at 155°C, 18h at 155°C + 25h at 190°C and 18h at 155°C + 70h at 190°C) and show different strain hardening behaviours. The samples were first deformed in tension up to ~1% plastic strain and then deformed back in compression up to ~2.5%. The forward and reverse stress-strain curves are represented, in absolute value of flow stress, in Figure 71a, for these three conditions. The curves in the case of monotonic tensile deformation are also represented (dashed lines). A strong Bauschinger effect for small reverse plastic strains is revealed and is increasing as a function of ageing time. However, the Bauschinger effect rapidly disappears and the compression curve in absolute value reaches similar values as for the classical tensile curve after a reverse plastic strain of approximately 1%. When over-ageing proceeds, two evolutions are observed. First, the magnitude of the Bauschinger stress for a given strain increases, and secondly the shape of the reversal curve changes, from a rapid increase of reversal stress (monotonically decreasing strain hardening rate) in the first sample to a more progressive one (sigmoidal) in the third sample. The first behaviour was already observed by Deschamps and co-workers in microstructures containing shearable T_1 precipitates [17] while the second behaviour is typical of the Orowan-helped reverse by-passing mechanism in the case of non-shearable precipitates which has been observed several times in different studies [29,32].

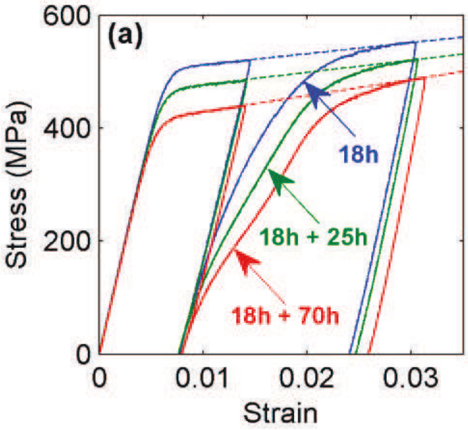

Figure 71: tension-compression Bauschinger tests represented in absolute values of flow stress for three samples heat treated (18h at 155°C), (18h at 155°C + 25h at 190°C) and (18h at 155°C + 70h at 190°C).

3.4 Plastic strain localisation into shear bands

The presence of single-layer T_1 precipitates in a peak-aged sample has been shown to result in a homogeneous plasticity at a microscopic scale (i.e., no catastrophic shearing of precipitates by avalanches of dislocations), together with a plastic strain localisation at a macroscopic scale (presence of slip lines) [16,17]. Recently [17], confocal microscopy observations of slightly over-aged AA2198 samples (250h at 155°C) revealed a reduced magnitude of the localisation of plasticity into slip lines. In order to evaluate the impact of T_1 microstructure, and particularly its thickness, on plastic localisation at the macroscopic scale, we selected 4 different conditions: 18h at 155°C, 18h + 25h at 190°C, 18h + 50h at 190°C and 18h + 70h at 190°C. The samples were deformed 2%. The presence of slip lines on the surface was first observed qualitatively using optical microscopy with the Nomarski contrast [33] (Figure 72). On the peak-aged sample that contains solely single-layer T_1 plates, intense slip lines are observed on the sample's surface. The number density and intensity of the slip lines seem to fade away as a function of ageing time. In the 18h at 155°C + 70h at 190°C sample, the slip lines have totally disappeared from the sample's surface showing a complete homogenisation of plasticity at a macroscopic scale. In order to quantify the slip line activity, we performed confocal laser scanning microscopy (CLSM). Examples of two images obtained in CLSM for the two extreme cases (peak-aged 18h at 155°C and over-aged 18h at 155°C + 70h at 190°C) are shown in Figure 73. Once more, the presence of intense slip lines is revealed on the peak aged state and no slip lines are observed in the over-aged state. CLSM gives a precision up to 1nm in depth, thus permitting to measure, precisely, the height of the slip lines on several samples aged at different times, provided that their spacing is compatible with the lateral resolution of an optical microscope. The evolution of the average slip lines' height is displayed in Figure 74. The height reaches a maximum at peak strength and drops quickly when temperature is increased to 190°C. For samples aged 18h at 155°C + 50h at 190°C and more, the slip lines cannot be laterally resolved and it was thus not possible to perform any quantitative measurement.

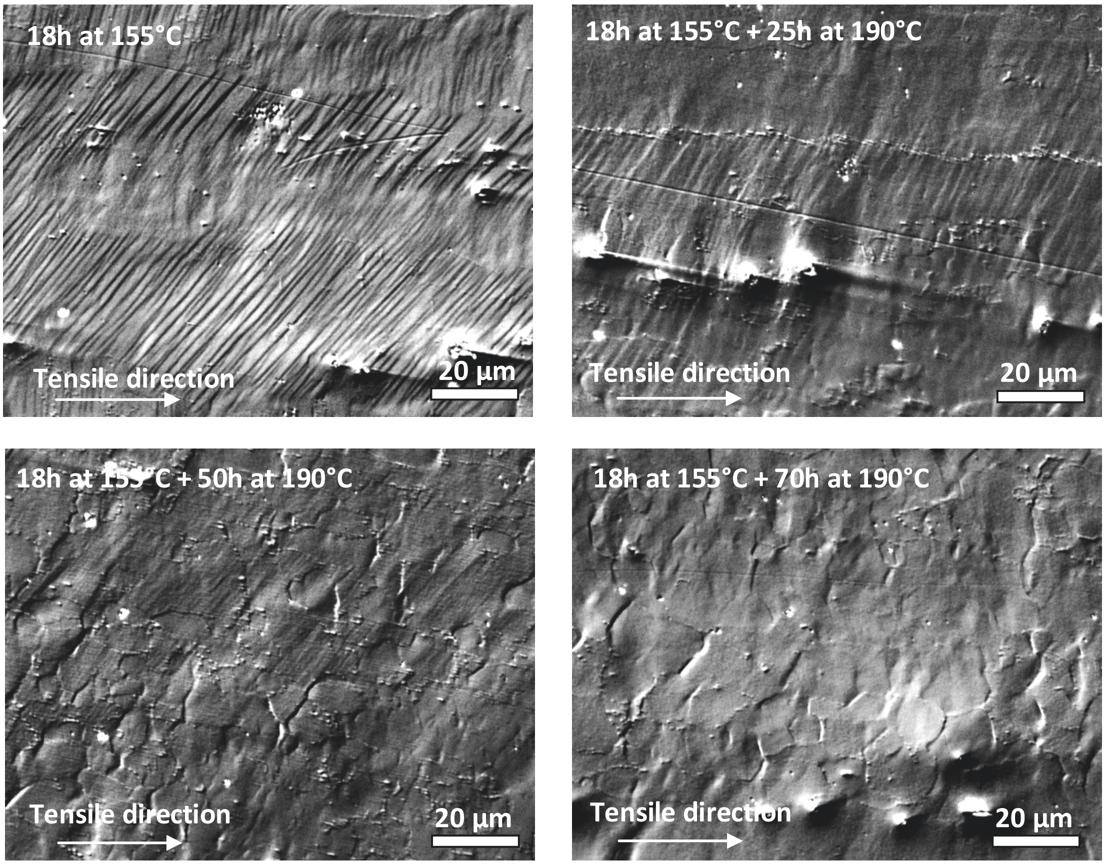

Figure 72: Images taken under the optical microscope in the Nomarski mode, the samples were deformed plastically 2% after being heat treated (a) for 18h at 155°C and (b) for 18h at 155°C and 70h at 190°C.

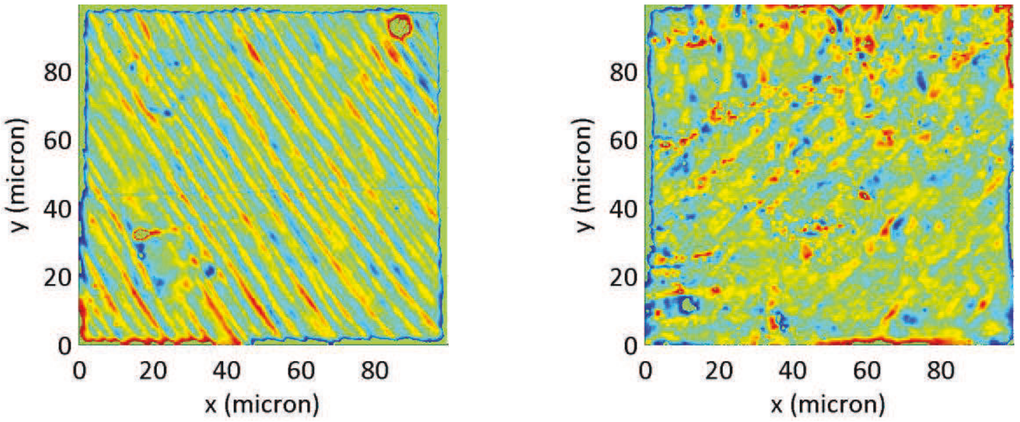

Figure 73: Images of shear bands, obtained in CLSM, on the surface of samples deformed plastically 2%. (a) Sample heat treated 18h at 155°C and (b) sample heat treated 18h at 155°C and 70h at 190°C.

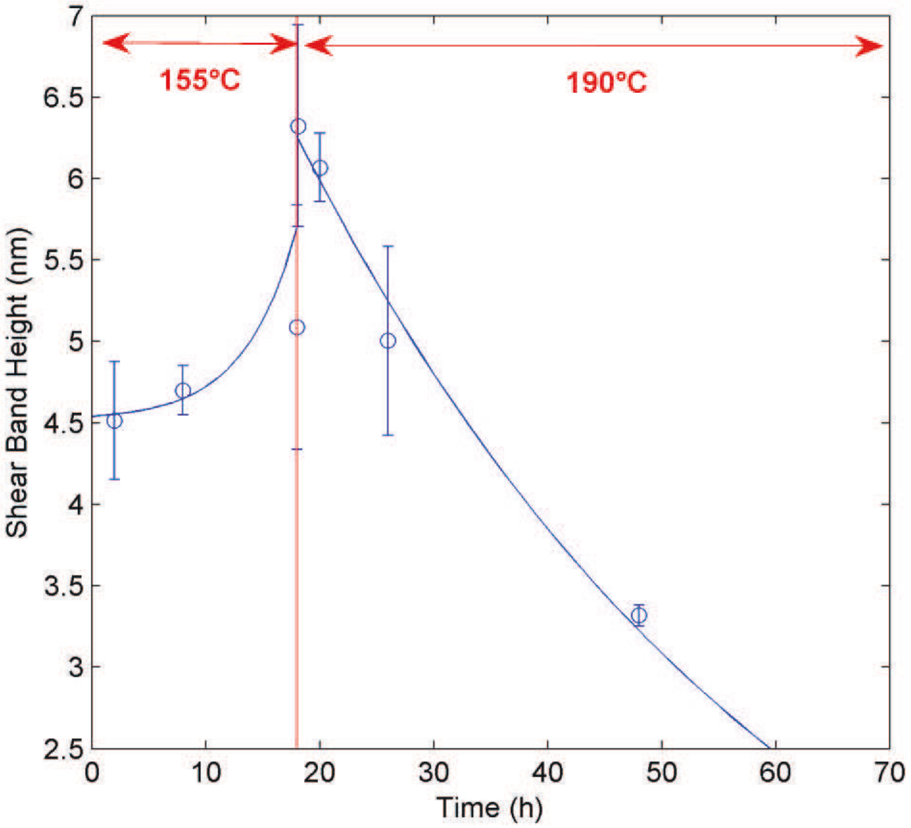

Figure 74: Evolution of the average shear bands' height as a function of ageing time during the duplex ageing treatment. The shear bands' heights were estimated from CLSM observations.

4. Summary and discussion

The strengthening mechanisms and associated dislocation/T_1-precipitate interactions have been discussed in several studies **[11,12,13,15,16,17].** The T_1 phase was first thought to be a strong unshearable phase similar to θ' [8,9,10,11,12]. However, several studies demonstrated the shearable feature of the T_1 phase, at least when it is sufficiently thin [13,14,15,16,17]. The peak-aged state of recent Al-Li-Cu alloys such as the AA2198 alloy consists in a distribution of single-layer precipitates and in this situation the shearing mechanism was shown to be dominant [17]. In the present study we investigated both similar cases (single-layer precipitates leading to peak strength at 155°C) and what happens during over-ageing at higher temperature (190°C) where the thickness of T_1 precipitates is observed to increase together with a decrease in yield strength.

Before considering the behaviour during over-ageing, we can first discuss the current results obtained after ageing 18h at 155°C. In this condition all precipitates have a thickness of one unit cell, and based on [17] these precipitates are shearable by dislocations. The associated strain hardening rate behaviour (see Figure 4) is consistent with this mechanism, since the initial strain hardening rate is similar to that of pure aluminium. At a microscopic scale, this precipitate shearing has been shown not to result in catastrophic shear localisation by separation of the precipitates [17], which has been attributed to the shearing of precipitates only by single events on a given slip plane, because a multiple shearing event would involve a too high cost in energy. However we show in the present study that at a more macroscopic scale intense slip banding occurs in this condition. Such slip banding is actually consistent with the absence of build up of internal stresses during the interaction between precipitates and dislocations, and should be regarded as a characteristic feature of precipitate shearing. Finally, in agreement with the earlier study on the same alloy [17], in this state a strong Bauschinger effect is observed at small reversal strains. Therefore a strong Bauschinger stress cannot be considered as characteristic of precipitate by-passing and we share the interpretation of this effect by the reversal of some of the precipitate shearing events during strain reversal [17], which requires a low resolved shear stress. This Bauschinger stress is however observed to recover extremely quickly (in fractions of % of plastic strain), which can be understood as a fast decrease of the probability of a dislocation to follow exactly the same path during forward strain and strain reversal, which is the necessary condition for this mechanism to operate.

For over-aged states, we can first consider the sample aged 18h at 155°C and 70h at 190°C. In this sample, the yield strength is already significantly smaller than in the peak aged temper. However, the T_1 plates are still quite thin on average (less than 2 nm), and a yield strength model based on precipitate shearing is still successful to describe the value of yield strength [7]. Our STEM-HAADF observations show that in this condition many precipitates are sheared, including those with thickness larger than one unit cell. Actually only precipitates equal or larger than 4 unit cells were not observed sheared, although it is difficult from limited observations to ascertain that this value defines a transition between shearing and by-passing. However, our other observations are consistent with a partial transition of the precipitate-dislocation interaction mechanism to by-passing. First, the strain hardening rate at low strains (illustrated by the initial strain hardening rate) has significantly increased, reflecting an additional dislocation storage mechanism with respect to that in the peak-aged state. Secondly, the plasticity is observed to become much more homogeneous at a macroscopic scale: no shear bands can be observed at the scale probed by optical microscopy (CLSM or Normarski contrast). Such homogenisation of plasticity is consistent with the build-up of internal stresses by Orowan looping of precipitates (or groups of precipitates), resulting in the deviation of subsequent dislocations on different slip planes. The interpretation of the Bauschinger test is more complicated, since we have seen above that a high value of Bauschinger stress was not necessarily related to the activation of precipitate by-passing. However, the behaviour of the strain reversal test is qualitatively different in this sample as compared to the case where only precipitate shearing occurs. Namely, the recovery of Bauschinger stress is much slower, which is illustrated by a sigmoidal reversal stress-strain curve. Following the interpretation of the strong Bauschinger stress in an alloy containing non-shearable precipitates [29,32], as resulting from the interaction between reversal dislocations and stored Orowan loops (mechanism called Orowan-Helped Reverse By-passing or OHRB), the length of the “plateau” of Bauschinger stress observed during strain reversal is characteristic of the number of dislocation loops that can be recovered. The value of this parameter is unclear, but it must be related to the forward strain (number of stored loops) and to the distance between precipitates (distance between recovered loops during strain reversal). Such sigmoidal shape of the strain reversal behaviour was actually observed in all of Fribourg’s experiments where precipitates were non-shearable.

When moving to a higher degree of over-ageing, namely the sample aged 225h at 190°C, the initial strain hardening rate takes very high values, very close actually to those observed in 7000 series alloys containing non-shearable precipitates of large radius [29]. In addition, it has been shown in [7] that in this condition the strengthening model based on precipitate shearing was not applicable. Therefore it can be safely stated that with this microstructure, T_1 precipitates are mostly by-passed by dislocations.

The effect of plasticity homogenisation on a macroscopic scale when going from shearable particles only to a combination of shearable and un-shearable particles has been observed before in Al-Li systems. For example, Cassada et al. [22] observed the same effect when going from a microstructure of shearable δ’ precipitates only (in an Al-2Li alloy) to a microstructure of combined δ’ and unshearable Ge particles (in an Al-2Li-0.2Ge alloy). The presence of these un-shearable particles was effective in homogenising dislocation slip. However one must recall that there is strong evidence that the effect of δ’ and shearable T_1 plates on plasticity is very different [17].

The localisation of plasticity has been studied in an AA8090 alloy during a duplex ageing treatment by Blankenship and Starke [34]. The authors observed intense shear bands in the T8 state (32h at 170°C). The coarse planar slip was attributed to the shearable δ’ phase that dominates the microstructure. Starting from the T8 temper they applied a second isothermal treatment at 300°C and observed a homogenisation of plasticity with a disappearance of the shear bands. The second isothermal treatment resulted in the partial dissolution of the δ’ phase that was replaced by the S’ and T_1 phase. The homogenisation of plasticity was only attributed to the apparition of the strong S’ phase. However, the authors observed a significant number of T_1 precipitates in TEM. Based on our observations, we can propose that the microstructure consisted of a distribution of strong multi-layers T_1 precipitates (because the high temperature promoted rapid thickening of the precipitates). As a consequence, the presence of such T_1 shear-resistant precipitates probably played a significant role in the homogenisation of plasticity in this system as it does in the AA2198 system.

The effect of the T_1 precipitates on the homogeneity of plasticity has also been investigated by Kim and Lee in an Al-Li-Cu AA2090 alloy [35]. The presence of a high density of T_1 precipitates in the activated slip planes has been observed to effectively homogenise slip at the macroscopic scale (disappearance of the shear bands). The thermo-mechanical treatment that was performed consisted of a reversion treatment at high temperature (265°C) to dissolve the δ’ precipitates. Such a reversion treatment probably favoured an extensive thickening of the T_1 precipitates. As was observed in the present work, the homogenisation of plasticity observed by Kim and Lee was probably a consequence of T_1 thickening.

We can see that the different strengthening mechanisms linked to the T_1 phase evidenced in the present study, namely a transition from shearing to by-passing depending on the state of ageing, can explain the plasticity behaviour in a wide range of studies. However, the T_1 microstructural parameters that control the transition from shearing-to-by-passing are yet to be established. Due to the high coherency of the broad face of a T_1 precipitate, the thickness of a T_1 precipitate was often proposed as the critical dimension that controls the transition from shearing to by-passing [11]. However, due to the high aspect ratio of the T_1 plates, it seems over-simplifying to only consider the T_1 thickness as critical, as the spacing between precipitates is likely to play a key role as well, and certainly evolves together with precipitate thickening. Furthermore, we demonstrated that multi-layers T_1 plates could also be sheared, although there may be a limit to the thickness that can be sheared by dislocations. As a consequence, the shearing to by passing transition may be more complex than previously thought and further work is needed to evaluate the energy required to shear T_1 plates of different diameters and thicknesses.

5. Conclusion

1) A shearing to by passing transition in the dislocation/T_1 interaction has been unravelled by coupling microscopic and macroscopic observations of plasticity and investigation of the plasticity behaviour.
2) When T_1 precipitates are sheared, this process always occurs by single step shearing events even for multi-layers precipitates.
3) Activation of the by-passing mechanism favours homogenisation of the plasticity up to the macroscopic scale, as well as a high strain hardening rate.
4) Both in the case of precipitate shearing and by-passing, the material shows a strong Bauschinger effect. However the stress-strain curves upon strain reversal are qualitatively different in both cases and we propose that the associated mechanism is different.
5) The transition between shearing and by-passing is progressive. It occurs later than the peak ageing condition, and is correlated to the coarsening of the precipitate microstructure, and particularly to the increase of the T_1 plate thickness.

6. References

1. Williams, J. C., Starke Jr, E. A.: Acta Mater. 51, 5775-5799 (2003)
2. Warner, T.: Mat. Sci For. 519-521, 1271-1278 (2006)
3. Rioja, R. J., Liu, J.: Met. and Mat. Trans. A 43A, 3325-3337 (2012)
4. Gable, B. M., Zhu, A. W., Csontos, A. A., Starke Jr., E. A.: J. of L. Met., 1-14 (2001)
5. Decreus, B., Deschamps, A., De Geuser, F., Donnadieu, P., Sigli, C., Weyland, M.: Acta Mater. 61, 2207-2218 (2013)
6. Dorin, T., De Geuser, F., Lefebvre, W., Sigli, C., Deschamps, A.: Phil. Mag. in press (2013)
7. Dorin, T., Deschamps, A., De Geuser, F., Sigli, C.: to be submitted (2013)
8. Sainfort, P., Guyot, P.: Aluminium-Lithium alloys III. edited by C. Barker, P.J. Gregson, S.J. Harris and C.J. Peels (Inst. of metals, London), pp. 420, 1986
9. Huang, J. C., Ardell, A. J.: Acta Metall. 36(11), 2995-3006 (1988)
10. Blakenship, C. P., Starke, E. A.: Scripta Met. et Mat. 26(11), 1719-1722 (1992)
11. Blankenship Jr., C. P., Hornbogen, E., Starke Jr., E. A.: Mat. Sci. and Eng. A 169, 33-41 (1993)
12. Nie, J. F., Muddle, B., Polmear, I. J.: Trans Tech Publ. 217-222, 1257-1262 (1996)
13. Howe, J. M., Lee, J., Vasudevan, A. K.: Met. Trans. A 19A, 2911-2920 (1988)
14. Csontos, A. A., Starke Jr, E. A.: Met. and Mat. Trans. A 31A, 1965-1976 (2000)
15. Nie, J. F., Muddle, B. C.: Mat. Sci. and Eng., 448-451 (2001)
16. Csontos, E. A., Starke, A. A.: Int. J. of Plast. 21, 1097-1118 (2005)
17. Deschamps, A., Decreus, B., De Geuser, F., Dorin, T., Weyland, M.: Acta Mater. 61(11), 4010-4021 (2013)
18. Nie, J. F., Muddle, B. C.: J. of Phase eq. 19(6), 543-551 (1998)
19. De, P. S., Mishra, R. S., Baumann, J. A.: Acta Mater. 59, 5946-5960 (2011)
20. Sanders, T. H., Starke Jr., E. A.: Acta Metall. 30(5), 927-939 (1982)
21. Furukawa, M., Miura, Y., Nemoto, M.: Japan Inst. Metals 26(4), 230-235 (1985)
22. Cassada, W. A., Shiflet, G. J., Starke Jr., E. A.: Acta Metall. 34, 367-378 (1986)

23. Nellist, P. D., Pennycook, S. J.: Ultramicroscopy 78, 111-124 (1999)

24. Dwyer, C., Weyland, M., Chang, L. Y., Muddle, B. C.: Appl. Phys. Lett. 98 (2011)

25. Donnadieu, P., Shao, Y., De Geuser, F., Botton, G. A., Lazar, S., Cheynet, M., de Boissieu, M., Deschamps, A.: Acta Mater. 59, 462-472 (2011)

26. Guyot, P.: Interactions des dislocations avec des impuretés fixes. In : Dislocations et déformation plastique, Yravals, pp.185-197 (1979)

27. Cheng, L. M., Poole, W. J., Embury, J. D., Lloyd, D. J.: Met. and Mat. Trans. A 34A, 2473-2481 (2003)

28. Westermann, I., Hopperstad, O. S., K., M., Holmedal, B.: Mat. Sci. and Eng. A 524, 151-157 (2009)

29. Fribourg, G., Bréchet, Y., Deschamps, A., Simar, A.: Acta Mater. 59, 3621-3635 (2011)

30. Simar, A., Bréchet, Y., De Meester, B., Denquin, A., Pardoen, T.: Acta Mater. 55, 6133-6143 (2007)

31. Stoltz, R. E., Pelloux, R. M.: Met. Trans. A 7A, 1295-1306 (1976)

32. Gould, D., Hirsh, P. B., Humphreys, F. J.: Phil. Mag. 30(6), 1353-1377 (1974)

33. Allen, R. D., David, G. B., Nomarski, G.: Z. fur Wiss. Mikr. und Mikr. Tech. 69(4), 193-221 (1969)

34. Blankenship Jr., C. P., Starke Jr., E. A.: Met. Trans. A 24A, 833-841 (1993)

35. Kim, N. J., Lee, E. W.: Acta Metall. Mater. 41(3), 941-948 (1993)

Discussion and prospects

The aim of this part is to conduct a general discussion linking the different chapters, to point out the possible limitations of approach and results and to propose possible directions for future work.

- ***Characterisation procedure for quantitative, systematic precipitate characterization***

The first step of our study was to propose a characterisation procedure for the T_1 phase that permits the estimation of the morphological parameters (diameter and thickness) and of the T_1 volume fraction. The validity of this characterisation procedure is critical as most of the experimental and modelling results presented in this thesis are highly dependent on this first step. The evaluation of the diameter and thickness was performed by using a method developed by De Geuser et al.; this method has already proven successful in previous studies. However the consistency of the results obtained as a function of the different parameters of the thermo-mechanical treatments investigated greatly increases the confidence of the validity of this procedure. The real innovation, in the method proposed, is on the estimation of the volume fraction. Contrarily to the case of isotropic spherical particles, using the SAXS technique to measure the T_1 volume fraction is extremely difficult due to the anisotropy of the signal arising from the strong texture of the AA2198 alloy. The estimation of the volume fraction of anisotropic plate like precipitates has always been proven difficult. As a result, we proposed a novel global approach which uses the heat flow obtained during a thermal ramp in DSC. The method consists in the integration of the signal over the complete thermal ramp to extract the T_1 volume fraction. Even if this technique is subject to a number of uncertainties (discussed in chapter III), we believe that it gives a fair estimation of the volume fraction evolution. However, this technique only gives access to a relative evolution and thus requires an alternative estimation for calibration. Furthermore, it only permits a discontinuous evaluation of the volume fraction evolution. Alternative techniques could be used to confirm the evolution as obtained in DSC. For instance, preliminary results in X-Ray diffraction (XRD) have revealed that the T_1 phase results in a measurable peak close to that of the {111} matrix planes that evolves as a function of time of heat treatment. Such measurements could be performed in-situ during heat treatments. The apparition of the T_1-phase has also been observed during dilatometry experiments, probably linked to the change in lattice constant in the direction normal to the precipitate habit planes. Dilatometry is inherently an in-situ technique, although it is mostly limited to isothermal heat treatments due to the difficulty to account precisely for the sample dilatation during temperature changes. These techniques could bring complementary information and confirm the evolution obtained in DSC. However, these techniques are mostly qualitative and would require a careful validation procedure by complementary techniques. The evolution of the volume fraction could probably be followed by SAXS (and therefore during in-situ measurements) in the case of a completely random distribution of the T_1 plates (powder like samples). The elaboration of a sample of random texture, with a grain size much smaller than the beam size, would then result in an isotropic signal in SAXS, easier to analyse in terms of volume fraction.

The characterisation procedure that we set up permits an estimation of the average T_1 microstructural parameters, which are sufficient for the model that we developed. However, this method does not provide information on the spatial distribution of the precipitates. The heterogeneous nucleation of T_1 precipitates on dislocations is likely to result in an inhomogeneous spatial distribution, which could play a role in the determination of the mechanical behaviour. The only method to evaluate the spatial distribution of precipitates is by performing complementary observations in electron microscopy. TEM remains the method of choice, although the last generation of scanning electron microscopes do show some ability to characterise such fine precipitates in an easier way (albeit with less precision). An example of heterogeneous distribution is given in Figure 75 which shows a TEM image of an AA2198 sample aged 18h at 155°C. The localisation of nucleation, presumably on a sub-grain boundary, leaves a precipitate free zone due to the local depletion in solute elements.

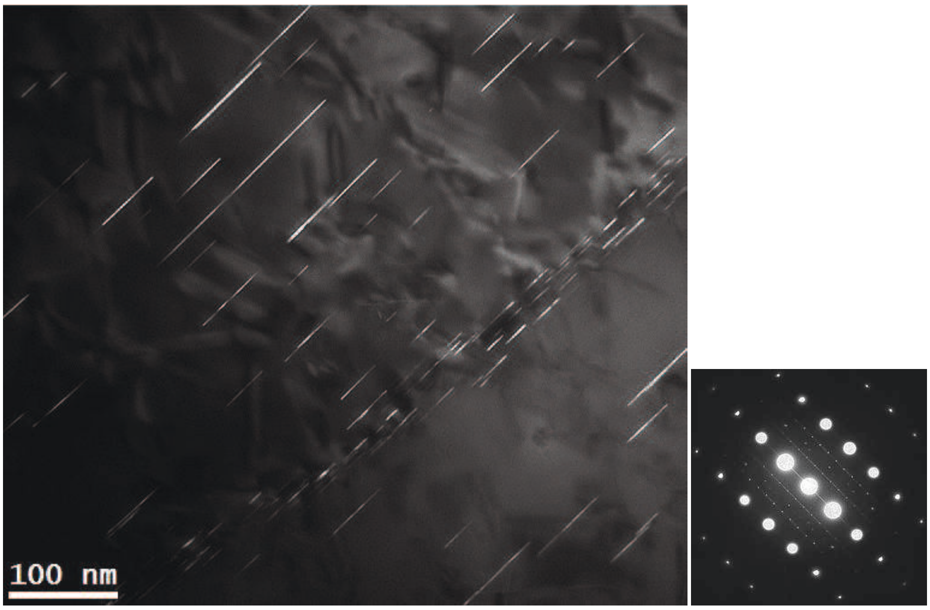

Figure 75: TEM image along the <112> zone axis revealing the high density of precipitates along a sub-grain boundary leaving precipitate free zones (PFZ) in the neighbourhood of the dislocation.

- ***Domination of the T_1 phase***

The T_1-phase has been shown to dominate the precipitation microstructure in our alloy when sufficient cold working is applied. However, other phases such as θ’ and S’ might also form in minor quantities, especially for low pre-deformation values. A TEM image of an AA2198 sample pre-deformed 0.5% along the <100> zone axis is displayed in Figure 76. It highlights the presence of the θ’ and S’ phases. These two phases precipitate respectively as plates and rods resulting in similar 2D projections. However, the spots on the image are the result of the projection of S’ rods only. The impact of the minor phases on the T_1 precipitation is poorly known. An on-going atom-probe study has revealed the presence of Mg-rich phases at the dislocations that are believed to play a major role as they might act as precursor to the T_1 phase [1]. A PhD work is on progress at the SIMAP laboratory and focuses on the impact of minor elements on the nucleation behaviour of the T_1 phase. In order to model accurately the yield strength evolution related to the T_1 phase, we had to choose different σ_0 values (base strength in the absence of T_1 precipitates) depending on the initial pre-deformation. These different values might be a sign of the presence of such phases associated to the dislocations from the beginning of the heat treatment, which would act as significant contributors to strengthening.

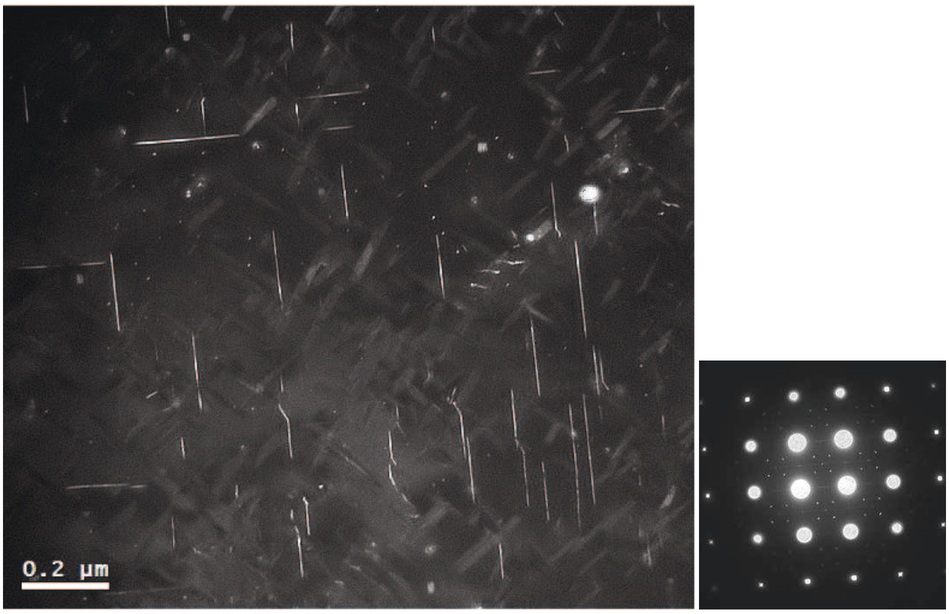

Figure 76: TEM image along a <110> zone axis of a sample pre-deformed 0.5% and aged for 18h at 155°C highlighting the presence of θ' and S' phases.

- ***Yield strength modelling and strengthening mechanisms***

The coupled experimental and modelling investigation permitted to get a better understanding of the strengthening mechanisms related to the T_1 phase and their evolution during the heat treatment. We highlighted that the shearing mechanism remains dominant after peak strength and that the by-passing mechanism only dominates for heavily over-aged conditions. The yield strength evolution has been successfully described using a model for precipitate shearing. This model considers the creation of a new precipitate/matrix interface and of an anti-phase boundary during the shearing process. The model used was initially proposed by Friedel who described the geometry of a dislocation glide through a distribution of discrete obstacles. The underlying hypothesis in the way the equation was proposed is that the inter-precipitate distance should be much larger than the average obstacle size. However, the T_1 phase results in large objects in projection in the glide plane probably of the same order of magnitude of the inter-precipitate distance as revealed on many TEM observations. As a consequence, even if the Friedel equation seems to predict accurately the yield strength evolution associated to the T_1 phase, it should be kept in mind that the T_1 phase does not verify the hypothesis which served to the establishment of the initial model. In order to further improve the model, it seems inevitable to use modelling approaches describing explicitly the distribution of precipitates in the glide plane. Phase field models are being developed which enable the description of the precipitate-dislocation interactions. They have already given promising results in the case of the by-passed θ' phase and could also be applied to shearable precipitates such as the T_1 phase. However, a pre-requisite of the application of such a model to the shearing mechanism is a more precise description of the precipitate shearing, both in terms of geometry of the process (shear plane in the precipitate) and related energetics (critical strength or more generally gamma-surfaces during the shearing event). Now that the structure of T_1 has been ascertained, ab initio calculations could be carried out to provide such information.

The existing models based on by-passing failed to predict the yield strength even for long over-ageing times where the by-passing is thought to dominate. The reasons for this prediction failure are unknown and should be investigated further. Again, in this case it is probably necessary to consider models capable of taking into account explicitly the spatial distribution of precipitates.

Both the experimental and modelling results go in favour of a shearing-to-by-passing transition for heavily over-aged conditions. Indeed, the transition at peak strength and subsequent decrease in yield strength were successfully represented by the yield strength model without accounting for a shearing-to-by-passing transition but the model fails in predicting highly over-aged conditions. The evolution of the plasticity mechanisms were also in favour of such a transition for long over-ageing times with a homogenisation of plasticity related to the apparition of by-passing. However, the critical microstructural T_1 parameters that control this transition are still poorly understood. The two main parameters that can be invoked to control this transition are the precipitate thickness (controlling the precipitate strength) and the precipitate spacing (controlling the stress required to curve the dislocations to the by-passing configuration). However, the respective roles of these two parameters are difficult to separate. Again, modelling methods that allow taking into account the energetics of the interaction between precipitates and dislocations and the precipitate distribution should be developed to reach a better understanding.

The impact of the T_1 phase on the localisation of plasticity has permitted to investigate the transition in strengthening mechanisms. However, the influence of the T_1 shearing on the multi-scale plasticity mechanisms is still poorly understood. Indeed, we concluded from our observations that the shearing process only occurs by single-step (only one Burgers’ vector). The implication of this mechanism is that plasticity does not localise at the micro-scale although we observed intense shear banding at the macro-scale. This difference between micro and macro-scale behaviours is still to be elucidated with further experimental investigations.

- ***Strengthening mechanisms and modelling of more complex microstructures***

This work has been on purpose restricted to an alloy with a comparatively simple microstructure where the strengthening precipitates consisted almost exclusively of the T_1 phase. However many alloys of the same family show more complex microstructures, including phases such as δ’ and θ’ as was revealed in many studies. Understanding the additivity of the contributions arising from each of the phases present is a challenge for further research investigations.

General Conclusions

During this PhD work, we have gone through a set of experimental and modelling results with the aim of acquiring a better understanding of the strengthening mechanisms involved in the presence of a highly anisotropic precipitate, the T_1 phase, and related impact on the strength increment. In order to do so, we carried out a specific strategy. This strategy has been described in the general introduction at the beginning of the manuscript through the definition of thesis objectives. We will now detail how each of these objectives has been fulfilled.

- ***Set-up a characterization procedure of the T_1 phase***

The first step has been the set-up of a reliable quantitative characterisation method of the T_1 phase based on the joint use of SAXS, DSC, TEM and HAADF-STEM. This procedure has proven successful to characterise the T_1 phase quantitatively in terms of morphological parameters and volume fraction. The combined use of SAXS and TEM permitted to extract the average diameter and thickness of the T_1 precipitates. The combined use of DSC and HAADF-STEM permitted the access to the T_1 volume fraction.

- ***Explore a wide range of T_1 microstructures***

After an efficient characterisation method has been set-up, we were then able to explore a wide range of T_1 microstructures by varying the thermo-mechanical treatment parameters (pre-age stretch, heat treatment temperature and heat treatment duration). This systematic work resulted in the generation of a robust database of microstructure-strength relationships.

- ***Test and improve the existing yield strength models***

This database was then used to test the ability of the existing models to predict the yield strength evolution in the case of the T_1 phase. The yield strength models based on by-passing were proven ineffective in modelling the yield strength evolution. However, the yield strength evolution has been successfully described using a model for precipitate shearing considering the combination of interfacial and anti-phase boundary strengthening. The transition at peak strength and subsequent decrease in yield strength were successfully represented without accounting for a shearing-to-by-passing transition. However, the model failed in predicting highly over-aged conditions suggesting a late transition in strengthening mechanisms.

- ***Understand the strengthening mechanisms in terms of dislocation/precipitate interaction***

The study of the plasticity behaviour confirmed that a transition from shearing to by-passing occurs for long over-ageing times. This transition was shown to influence strongly the homogeneity of plasticity, which was studied both at the microscopic and the macroscopic scale. It was shown to also influence the reversibility of plasticity (as evidenced by Bauschinger tests) and the strain hardening behaviour.

Appendix I: Relationship between the grain texture and the spatial dispersion of hardness during ageing

The effect of the grain texture on the age-hardening behaviour is investigated on both a recrystallized and an unrecrystallized AA2198 alloy. The grain texture is probed with Electron Back Scattered Diffraction (EBSD) imaging and the elastic properties are investigated locally by performing Vickers micro-hardness measurements. The micro-hardness kinetics is first examined and a combined EBSD and Micro-hardness mapping is then performed on a selected state in order to relate the crystalline orientations to the local strength. A significantly more pronounced heterogeneity of the micro-hardness distribution is observed on the recrystallized specimen as compared to the unrecrystallized specimen. The heterogeneity in mechanical properties is discussed in terms of inhomogeneity of precipitation resulting from the pre-stretch step in the thermo-mechanical treatment.

1. Introduction

The thermo-mechanical treatment that is usually applied to industrial Al-Li-Cu alloys involves a succession of rolling steps that result in highly textured metal sheets with long elongated grains (see chapter II). This specific texture has been shown to result in an anisotropy of the mechanical properties measured in the rolling plane as a function of the angle to the rolling direction. A minimum of yield strength is usually found at about 60° from the rolling direction; this behaviour can be referred to as in-plane anisotropy [1]. The angular variation of yield strength in the plane of textured metal plates has been theoretically correlated to the grain texture by Davies et al. [2]. The yield strength of such alloys is also strongly related to the microstructure and more particularly to the T_1 phase that forms in the $\{111\}_{Al}$ planes. The T_1 precipitation is promoted by applying cold working prior to the age-hardening treatment. The impact of both the grain texture and the precipitate microstructure on the angular anisotropy has been studied by Kim and Lee in an AA2090 alloy [3]. These authors observed the effect of specimen orientation in under-aged samples (without T_1, effect of texture only) and peak-aged samples (presence of T_1, combined effect of texture and T_1). The angular yield strength variations were successfully related to the crystallographic texture. They also highlighted anisotropy in the fracture behaviour which was attributed to an inhomogeneous distribution of the T_1 nucleation sites. Indeed, they found that during pre-stretching, two out of the four {111} slip planes were preferentially activated resulting in a higher dislocations' density in those two planes. However, the distribution of grain orientations in the material not only affects the number of activated slip planes in each grain, but may also influence the spatial distribution of plastic strain (hence of resulting dislocation density), particularly when small plastic strains are applied like during pre-stretch operation (typically between 2 and 3%). Because T_1 precipitates nucleate on dislocations, a heterogeneous distribution of plastic strain can result in a heterogeneous distribution of strength. In chapter IV, we have in fact shown that changing the amount of pre-strain changed significantly the kinetics of hardening in the alloy, and not the end strength after long ageing times at 155°C.

The aim of this chapter is to evaluate the effect of texture on spatial dispersion of strength. We combine micro-hardness measurements with EBSD on both recrystallized and unrecrystallized AA2198 specimens. The heterogeneous distribution of micro-hardness is then discussed as a function of the crystallographic texture and inhomogeneous presence of the T_1 precipitates.

2. Material and experimental procedure

Two sheets of AA2198 alloy were provided by the Constellium Voreppe Research Centre. The first sheet was 5mm thick with a fully unrecrystallised grain structure and the second sheet was 1.4mm thick with a fully recrystallized grain structure. The samples were first solution treated for 30 min at 510°C and water quenched. Right after quenching, the samples were pre-deformed to a macroscopic tensile plastic strain of 2.5%. The samples were then naturally aged for seven days. The artificial ageing treatment was then executed in an oil bath, starting with a heating ramp of 20 $K.h^{-1}$ to 155°C, followed by an isothermal treatment at 155°C. The samples were quenched into cold water at different times during the heat treatment and then analysed. The samples were then mirror polished prior to the EBSD and micro-hardness measurements.

The Vickers micro-hardness measurements were performed on a Wilson hardness Tukon 1102 fully automatic apparatus. A mass of 100g was used for the indentations.

The Electron Back Scattered Diffraction (EBSD) measurements were conducted on a SEM-FEG ZEISS Ultra 55 apparatus. A scanning step of 1µm was used for the EBSD acquisition.

3. Micro-hardness evolution during ageing treatment

The Vickers micro-hardness evolution was recorded during the isothermal heat treatment at 155°C on both sheets. Twenty indents were performed for each ageing time in order to calculate a standard deviation of the measurements. The average micro-hardness is plotted as a function of ageing time for both the unrecrystallized and recrystallized samples in Figure 77a. The micro-hardness evolution is similar for both alloys, although the recrystallized samples reach a slightly higher micro-hardness after 20h at 155°C. The drop in micro-hardness during the heating ramp has previously been attributed to the dissolution of clusters [4]. The evolution of the standard deviation is plotted as a function of ageing time in Figure 77b. For early ageing times, the standard deviation is found to be similar for both specimens but rapidly differ after a few hours at 155°C. The standard deviation for the unrecrystallized specimen remains constant to ~1.5Hv. The standard deviation for the recrystallized sample is significantly higher; it first increases and reaches a maximum of ~12Hv after 7h at 155°C and then decreases when reaching the end of the heat treatment. After 7h at 155°C, the standard deviation for the recrystallized and un-recrystallized specimens respectively corresponds to ~10% (~12Hv) and ~1% (~1.4Hv) of the average micro-hardness value (~130Hv). As a consequence, we will perform a combined EBSD and micro-hardness mapping after 7h at 155°C in both texture conditions in order to investigate further the relationship between the crystal orientation and the local micro-hardness.

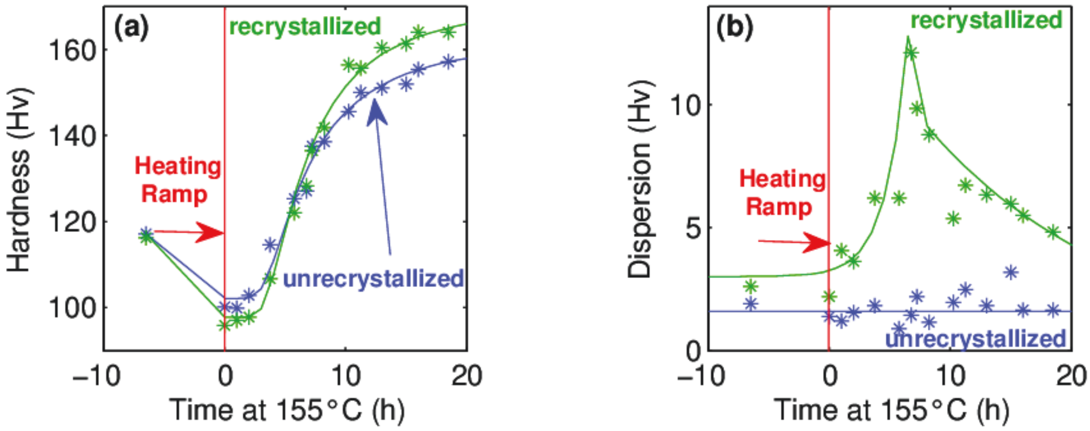

Figure 77: (a) Vickers micro-hardness evolution as a function of ageing time at 155°C for both the unrecrystallized and recrystallized AA2198 sheets and (b) Evolution of the dispersion of the micro-hardness measurements for both sheets.

4. EBSD and Micro-hardness mapping

The samples' surfaces were mirror polished and a 4mm^2 area was identified with 4 micro-hardness indents. EBSD mapping was first performed on both samples (Figure 78a and b). The unrecrystallised sample exhibits long elongated grains. In the recrystallized sample, the grain distribution is more equiaxed and grain sizes ranging from ~20µm to ~500µm with an average grain size of ~150µm. A micro-hardness map, consisting in 20 lines of 24 indents (480 indents in total) was then realised on both specimens on the same areas, the indents were regularly spaced every 100µm and a load of 100g was used. The distance between the indents was large enough to avoid un-desired interactions between the indents' strain fields (the diagonal d of the indents was always <40µm, corresponding to an inter-indent distance of at least $2.5 * d$). The micro-hardness maps, for the two specimens, are displayed in Figure 79. The average hardness (~130Hv) was found to be the same as was previously reported in figure 1. However, one can notice that the micro-hardness span is much wider for the recrystallized sample (105Hv to 150Hv) as compared to the unrecrystallized sample (125Hv-145Hv). Furthermore, the micro-hardness mapping reveals the presence of "soft" and "hard" zones. The characteristic size of these zones is observed to be of same order of magnitude as the grain size showing a strong correlation between the grain texture and the micro-hardness measurements. In the case of the unrecrystallized sample, the "soft" and "hard" zones are long and elongated similarly to the grain shape, while they are isotropic in the recrystallized sample. However, if we superimpose the EBSD and micro-hardness maps, it is difficult to directly attribute a specific crystal orientation to a micro-hardness value. Indeed, when indenting a grain, a number of factors are involved and influence the resulting hardness such as the distance to the grain boundary, the presence of intermetallic particles at the surface or grains lying below the surface and probed by the indenter. However, we can clearly see a direct qualitative influence of the local crystal orientation on the mechanical properties.

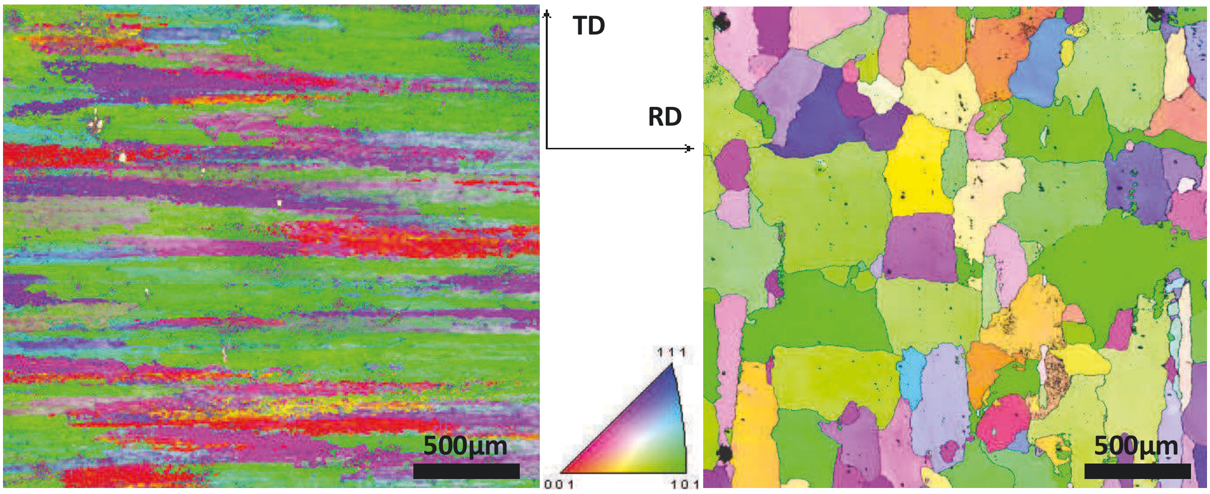

Figure 78: EBSD images of an AA2198 alloy with (a) an unrecrystallized texture and (b) with a recrystallized texture.

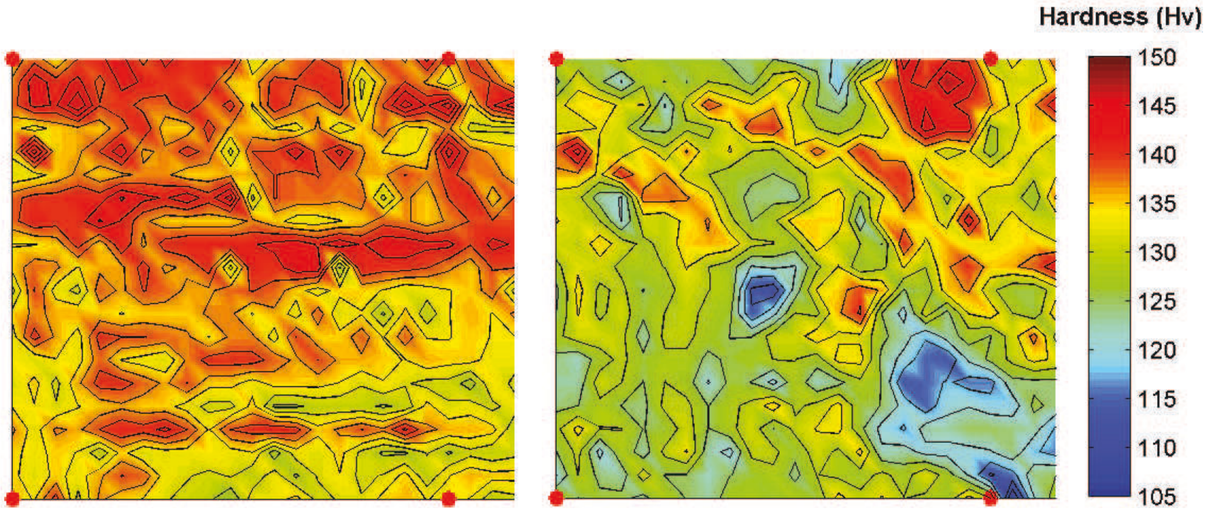

Figure 79: Vickers micro-hardness mapping of (a) an unrecrystallized AA2198 specimen and (b) a recrystallized AA2198 specimen. The red dots, on both maps, highlight the four indents which were used to select the studied area.

5. Discussion

The heterogeneity of hardness revealed in the case of the recrystallized specimen indicates the presence of weaker and stronger grains after 7h at 155°C. However, as it was shown in Figure 77b, this heterogeneity was not present for very early ageing times where no T_1 precipitate is present, and tends to vanish at very long ageing times. Therefore our observations strongly suggest a difference in the T_1 precipitation kinetics in the different grains, which is directly related to the crystal orientation. The influence of pre-stretching on the T_1 precipitation kinetics is well-established and the kinetics is known to be enhanced for higher pre-deformation values. We know from observations by Kim and Lee that the dislocations' density is more important in two out of four {111} variants in the case of a textured material. In the case of a random texture, we can easily imagine that the amount of pre-stretching differs from one grain to another depending on the activated slip planes. As a consequence, the distribution of pre-stretching is likely to be highly inhomogeneous from one grain to another, inducing differences in the T_1 precipitation kinetics. In agreement with our study of the effect of pre-strain on the strengthening kinetics by T_1 (chapter IV), the grains subjected to the highest level of pre-strain are expected to experience faster hardening than those where a lower dislocation density is stored. In chapter IV we have shown that the strength contrast as a function of pre-strain was maximum between 5h and 15h of ageing approximately, which corresponds to the time span where the standard deviation of the recrystallized material is much larger than that of the unrecrystallized material. For shorter ageing times the effect of pre-strain on hardness is only moderate, so that the distribution of hardness in the material is relatively homogeneous (yet the standard deviation is still slightly higher in the recrystallized material). For longer ageing times, the precipitation reaction reaches completion regardless of the pre-strain value (provided that it is larger than approximately 0.5%), and the resulting strength was observed to be independent on pre-strain, so that the distribution of hardness becomes spatially uniform again. The fact that the unrecrystallized material does not show such a development of strength heterogeneity can be related to its stronger texture. With a strong rolling texture, it can be expected that the distribution of Schmid factors with respect to the tensile direction of the pre-stretch is very uniform through the grains, resulting in a homogeneous distribution of the dislocation density and hence of the precipitate distribution.

Using samples of varying cross-section (see chapter IV) it is possible to estimate more quantitatively the influence of pre-strain on the distribution of hardness for a given heat treatment time. In chapter IV we showed this evolution after 18h at 155°C (the fitted curve is represented in Figure 80). If we consider the experimentally measured standard deviation of 5 HV measured for this ageing time on the recrystallized material, an average strain contrast of 2.55% can be estimated. A similar estimation on the unrecrystallized material with a standard deviation of 1.5 HV gives an estimation of the strain contrast of about 0.7%.

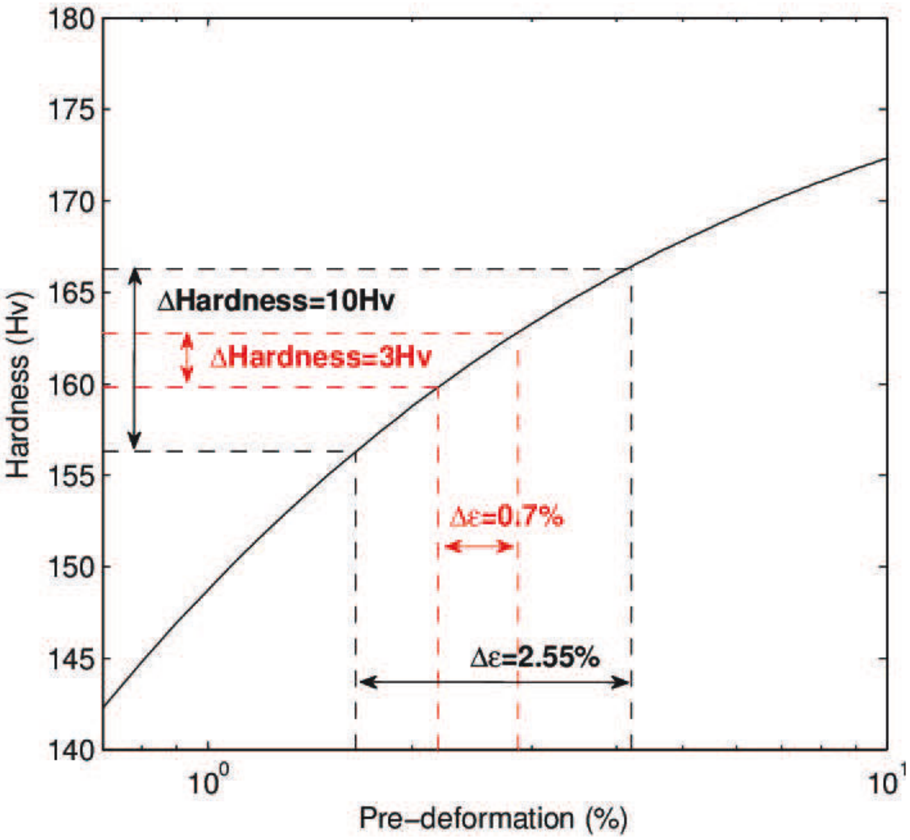

Figure 80: Hardness as a function of pre-deformation after 18h at 155°C.

6. Conclusion

We used micro-hardness mapping combined with EBSD in order to study the local relationship between the strength and the crystal orientation. The age-hardening condition (7h at 155°C) which exhibited the highest dispersion in micro-hardness measurements was chosen for the analysis. The dispersion of the hardness measurements was observed to be strongly related to the grain texture. We highlighted a difference in the T_1 precipitation kinetics in the different grains, which is directly related to an inhomogeneous distribution of the pre-stretching between the different grains. Estimation of the Schmid factors with respect to the direction of pre-stretching are in progress to relate more quantitatively the grain orientation to the strength distribution after ageing.

7. References

1. Jata, K. V., Hopkins, A. K., Rioja, R. J.: Mat. Sci. For. 217-222, 647-652 (1996)

2. Davies, G. J., Goodwill, D. J., Kallend, J. S.: Met. Trans. 3, 1627-1631 (1972)

3. Kim, N. J., Lee, E. W.: Acta Metall. Mater. 41(3), 941-948 (1993)

4. Decreus, B., Deschamps, A., De Geuser, F., Donnadieu, P., Sigli, C., Weyland, M.: Acta Mater. 61, 2207-2218 (2013)

Appendix II: The influence of precipitation on plastic deformation of Al-Cu-Li alloys

The article, which is displayed in this appendix, was published in Acta Materialia, Volume 61, Issue 11, June 2013, Pages 4010–4021.

The influence of precipitation on the plastic behaviour in two Al-Li-Cu alloys with different Li/Cu ratio is investigated. The impact of the δ’ and T_1 precipitates on plasticity is discussed in terms of dislocation/precipitate interaction mechanisms. This article was not included in the core of the manuscript as the main author is Alexis Deschamps and most of the results used come from a recent PhD work at the SIMAP laboratory by B. Decreus. However, the HAADF-STEM observations were executed as a part of this PhD.

The influence of precipitation on plastic deformation of Al-Cu-Li alloys

A. Deschamps[1], B. Decreus[1,2], F. De Geuser[1], T. Dorin[1], M. Weyland[3]

[1]SIMAP, INP Grenoble – CNRS – UJF, BP 75, 38402 St Martin d'Hères Cedex, France

[2]Constellium CRV, Voreppe Research Center, BP 27, 38341 Voreppe Cedex, France

[3]Department of Materials Engineering & Monash Centre for Electron Microscopy, Monash University, Victoria 3800, Australia

Abstract

The plastic behaviour of two recently developed Al-Cu-Li alloys of different Cu/Li ratio, AA2198 and AA2196, has been studied as a function of precipitation state by tensile tests, strain hardening rate analysis, Bauschinger tests, slip line imaging and atomic scale characterisation of precipitate shearing by advanced electron microscopy. For early ageing times where δ' and/or solute clusters are present, plasticity occurs heterogeneously, strain hardening rate is high and the Bauschinger effect is moderate. When T_1 precipitates are present plasticity becomes more homogeneous and the strain hardening rate shows a slower decrease as compared to other aluminium alloys containing shearable precipitates. In addition these ageing conditions show a high reversibility of plastic strain, and it is observed that precipitates are sheared only by single steps. The possibility of a specific shearing mechanism of the T_1 phase is discussed in light of these results.

Keywords: Aluminium alloys; precipitation; plasticity

1. Introduction

Precipitation hardening alloys based on the Al-Cu-Li system are experiencing currently a strong interest in the framework of the development of new alloys, particularly for aerospace components [1–3]. Their optimised compositions make it possible to overcome some of the limitations that had hindered the application range of former available alloys [4]. These alloys, where the main solute elements Cu and Li are often supplemented with minor additions of Mg and Ag, can show a complex precipitation sequence, including phases from the binary Al-Li or Al-Cu diagrams, and from the ternary Al-Cu-Li and Al-Cu-Mg diagrams. However, it is recognised that the main strengthening precipitate in this system is the T_1 phase of nominal composition Al_2CuLi that forms very thin platelets of high aspect ratio on the {111} planes of the Al matrix [5]. The structure of this phase, when present as thin platelets in the Al matrix, has been unravelled recently [6,7]. Decreus et al. [8] have studied in detail the influence of alloy chemistry on the precipitation sequence of two recently developed alloys of the AIRWARE^{TM} family, AA2198 and AA2196. It has been shown that the precipitation behaviour of the AA2198 alloy, which is relatively Li-lean (of the order of 1wt%), is dominated by a precipitation sequence involving Cu-rich solute clusters and GP zones after natural ageing, which dissolve during the heating ramp to the artificial ageing temperature of 155°C, and are later replaced by the T_1 precipitates accompanied in smaller proportions by Cu-rich GP zones or θ′ phases. The AA2196 alloy, which has a larger Li content, presents a precipitation sequence where the δ' phase Al_3Li is present from the natural ageing up to overaged states in volume fractions from 5 to 10%. In parallel to the presence of this phase, a microstructure similar to that of the AA2198 alloy develops, namely consisting of T_1 and θ′ platelets finely dispersed in the Al matrix.

The plastic deformation of earlier alloys of the Al-Cu-Li family has been the object of a number of investigations. In many cases they have been shown to be prone to anisotropy and localisation of plastic strain, resulting in relatively poor ductility [9]. In particular, the presence of the ordered δ' phase – Al_3Li is well known to result in planar slip [9,10]. During fatigue of binary Al-Li alloys very intense localisation of plastic flow occurs [11,12] and results in the dissolution of the precipitates, leaving precipitate free channels that favour further localisation and fracture. The shearing of the δ' phase has been thought to be at least partially responsible for the poor ductility and susceptibility to intergranular fracture of Al-Cu-Li alloys containing close to 2 wt%Li where the δ' volume fraction is very high [9,10]. Conversely, it has been proposed that the presence of T_1 precipitates homogenises plastic flow when compared to the presence of δ' particles [10,12]. This effect has been sometimes attributed to the fact that this precipitate is “hardly shearable” [12]; however it is now firmly established that T_1 precipitates can be sheared by dislocations [9,13–15]. Csontos and co-workers [9] have shown that the shearing of T_1 precipitates was accompanied by a localised plasticity in the matrix (shear bands). Some differences of plastic localisation and related ductility between the two alloys studied in their work were also attributed to other factors such as the presence of θ′ precipitates or differences in grain structure. Thus, it seems that despite the shearable nature of the T_1 phase, its influence on the distribution of plasticity in the Al-Cu-Li alloys is very different from that of δ', even though this difference is until now unexplained.

Therefore, obtaining a clear picture of the interaction between plasticity and precipitation in Al-Cu-Li alloys still requires a better understanding of the respective roles of T_1 and δ' precipitates. The present paper, following the detailed study of the microstructure of two Al-Cu-Li alloys by Decreus et al. [8], aims at evaluating the effect of these microstructures on the plastic behaviour of the alloys. The two alloys present a similar grain and precipitation microstructure along the ageing heat treatments, except for the presence of the δ' phase, which exists in the AA2196 alloy but not in the AA2198 alloy (except as a very thin wetting layer on the θ′ precipitates). Thus the specific role of this phase on the plastic behaviour will be evaluated by comparing the two alloy’s mechanical behaviour. First, tensile data will be presented for an overall evaluation of the strength and ductility evolution during the ageing treatments. This tensile data will then be evaluated in more detail through an analysis of the strain hardening rate, which is known to be very sensitive to the details of the precipitate-dislocations interactions and has provided insight into the plasticity mechanisms of other alloy series in the recent past [16–19]. Then we will present results of Bauschinger tests, which provide information on the build-up of internal stresses during plastic straining and reversal, and are therefore very informative as well on the plasticity mechanisms operating in precipitate containing alloys [20]. The sensitivity of the alloys to localisation of plastic flow has been studied by confocal microscopy realised on plastically deformed samples containing different precipitate microstructures. Finally, to gain some more detailed insight on the interaction of dislocations with the precipitates in this system, aberration corrected scanning transmission electron microscopy in high angle annular dark field mode (STEM-HAADF) observations have been carried out on the AA2198 alloy plastically deformed after a near-peak ageing treatment.

2. Materials and experimental methods

Two alloys of the AIRWARE™ family were used in this study. AA2198 and AA2196 alloys have the composition ranges indicated in Table 1. They were provided by Constellium – Voreppe Research Centre, France, as rolled sheets of 6 mm thickness with a fully fibrous grain structure. The sheets showed a strong Brass texture (<112> {110}).

The same precipitation route was studied for both alloys. Initially the samples were solution treated, water quenched; a predeformation step of 2% plastic strain was then applied. The resulting introduction of dislocations into the material is known to greatly help the nucleation of the strengthening T_1 phase; this particular amount of pre-deformation is close to industrial practice and it was found in a preliminary study that it was sufficient to obtain an efficient T_1 phase nucleation [21]. This plastic deformation step was followed by a natural ageing step of several months at room temperature, leading to a so-called T351 temper. The precipitation treatment on the two alloys consisted in a ramp heating at 20 $K.h^{-1}$ followed by an isothermal heat treatment at 155°C.

Samples for transmission electron microscopy were prepared by electropolishing in a twin-jet apparatus, using a 1/3 nitric acid – 2/3 methanol solution at -20°C under 15V. Aberration corrected HAADF STEM imaging was carried out using a FEI Titan^3 80-300 FEGTEM fitted with dual CEOS aberration correctors. The probe forming convergence (semi) angle of the illumination was 15 mrad, corresponding to Gaussian probe size of ~0.12 nm. A HAADF detector an inner collection (semi) angle of 48 mrad was used.

Tensile tests were carried out on a screw-driven machine at a strain rate of 10^{-4} s^{-1}. All samples were machined in the rolling direction. The sample cross-section was 5x2 mm^2 for the AA2198 alloy and 5x2 mm^2 for the AA2196 alloy. The sample gage length was 60 mm. The Bauschinger data presented here was extracted from strain-controlled low cycle fatigue tests performed on flat tensile samples with a maximum total strain of 1% at a frequency of 0.3 Hz.

Table 12: Alloy constituents by wt %, as provided by the manufacturer specification. Note the Zr content of both alloys forms large grain refining dispersoids and takes no role in further precipitation.

Alloy	Cu	Li	Mg	Ag	Zr
AA2198	2.9-3.5	0.8-1.1	0.25-0.8	0.1-0.5	0.04-0.18
AA2196	2.5-3.3	1.4-2.1	0.25-0.8	0.25-0.6	0.04-0.18

For the confocal microscopy observations, flat tensile samples were mirror polished and then deformed plastically for 10 cycles of low cycle fatigue (in the same conditions as for the Bauschinger tests). They were then observed in a Confocal laser Scanning Microscope Talysurf CCI 5000 apparatus at University of Poitiers, France.

3. Precipitate microstructures along the heat treatments

The details of the microstructure evolution of the two alloys from the naturally aged T351 state to the different stages of the ageing treatment at 155°C have been given elsewhere [8]. However it is worth summarizing the main outcomes for the purpose of the current study. The main clustering / precipitate features are summarized in Table 2. In the T351 state the microstructures of the two alloys are very different: the AA2198 alloy microstructure contains very small Cu-rich clusters and GP zones, while the AA2196 alloy contains fine δ’ precipitates. At the end of the heating ramp to 155°C and during the first hours at this temperature, the clusters have dissolved in the AA2198 alloy, while only a partial dissolution of δ’ has occurred in the AA2196 alloy. Subsequently the T_1 phase appears along with a small amount of Cu-rich phases (GPI, GPII and θ’) in the two alloys. In both alloys the thickness of the T_1 phase has mostly its minimal value of 1.3 nm while its diameter quickly grows to more than 40 nm. Two main differences have been found between the two alloys during the 155°C ageing treatment: precipitation of T_1 occurs more rapidly in the AA2198 alloy, and this alloy does not present δ’ phase at any time while the AA2196 continuously does (note that the δ’ phase continues to coarsen along with the precipitation of T_1). As a consequence, the microstructures in the near-peak-aged states (16h at 155°C for the AA2198 alloy and 48h at 155°C for the AA2196 alloy) consist mostly in T_1 phase with some GPI/II / θ’ phases for the AA2198 alloy (illustrated in Figure 1 by a STEM-HAADF micrograph), and T_1 phase along with δ’ with some GPI/II / θ’ phases for the AA2196 alloy.

Table 13: Summary of the main features of the precipitate microstructures in the AA2198 and AA2196 alloys along the heat treatment at 155°C, summarised from the data of ref. [8].

	AA2198		AA2196	
Heat treatment	Microstructure	Time range	Microstructure	Time range
T351	Cu-rich clusters	N/A	δ’	N/A
End of ramp (EOR) & first hours at 155°C	Clusters dissolved → essentially solid solution	EOR → 2h	50% surviving δ’	EOR → 5h
Underaged	Nucleation and growth of T_1 & some θ’	2h → 16h	Nucleation and growth of T_1 & some θ’ δ’ coarsens	5h → 48h
Peak to overaged	Majority of T_1 & some θ’	16h onwards	Majority of T_1 & δ’ some θ’	48h onwards

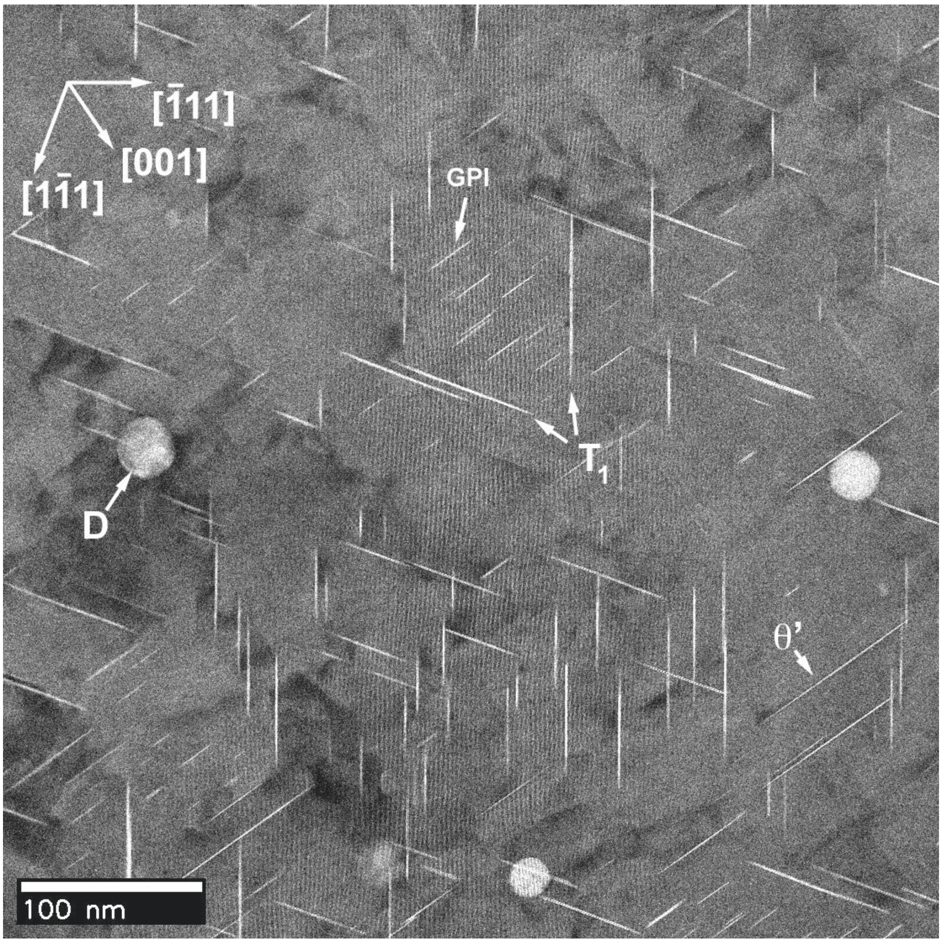

Figure 81: Low resolution STEM-HAADF micrograph of the AA2198 alloy after 16h at 155°C showing T1 precipitates (lying on the {111} matrix planes and θ' / GP zones (lying on the {100} matrix planes). Larger precipitates of spherical shape (noted "D") are Zr-containing dispersoids.

4. Tensile results and work hardening rate analysis

Figure 2 summarizes the tensile test data for different ageing conditions along the heat treatment at 155°C for the AA2198 alloy. The T351 state presents a relatively high yield stress of 330 MPa, a strong work hardening rate and does not present any serrations corresponding to a Portevin – le – Châtelier effect. This mechanical behaviour is consistent with the presence of stable clusters that trap sufficient solute to suppress the plastic instabilities and increase the material's yield strength. Similar effects (including the strong work hardening rate in the naturally aged condition) have been observed in many other Aluminium alloys e.g. from the 6000 or the 7000 series [18,22–24]. When the material is heated to 155°C (end of ramp or EOR sample) the yield stress drops, reflecting the dissolution of the clusters. Along with this decrease in yield stress serrations appear on the tensile curve, consistently with the cluster dissolution. The work hardening rate is similar to that of the T351 state. However the yield stress in the EOR sample is still quite high as compared to classical values of alloys in solid solution. As a comparison the as-quenched tensile curve has been added to the graph. The yield stress of the reverted T351 state (EOR) should be compared to the flow stress of the as-quenched sample after 2% plastic strain since the T351 alloy has been stretched to this amount prior to natural ageing. However this flow stress is still substantially lower than the yield stress in the reverted material (EOR), notwithstanding the fact that some recovery of the dislocations could have happened during the heating ramp that should have decreased further the yield stress. Thus one can conclude that despite the apparent complete dissolution of the clusters during the heating ramp, some solute segregation must remain at the dislocations, which could explain the higher than expected value of the yield strength observed in this condition and the change in the nature of the serrations during straining.

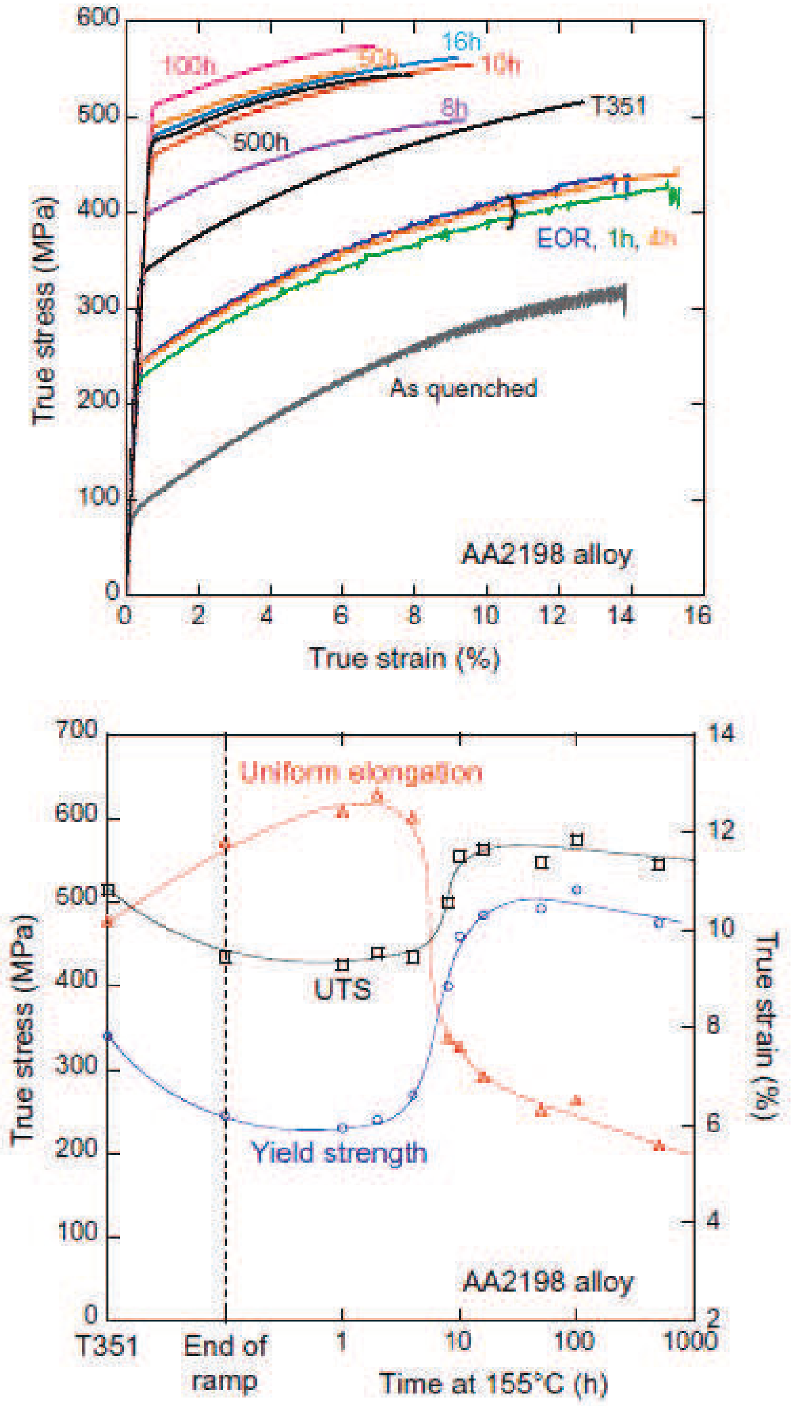

Figure 82: (a) Tensile curves of the AA2198 alloy in different ageing conditions along a heat treatment at 155°C; (b) associated yield strength, ultimate tensile strength (UTS) and uniform elongation.

During the first hours at 155°C, the tensile behaviour remains stable, which is consistent with the observed lack of any significant evolution of the microstructure [8]. After T_1 nucleation has occurred, the yield strength rapidly increases to reach about 500 MPa. Subsequently it remains stable and only slightly decreases after 500h at 155°C. This very high stability of the yield strength with ageing time can be related to the resistance to thickening of the T_1 precipitates that remain at their minimal thickness for very long times. In parallel with the increase in yield strength, the uniform elongation decreases rapidly to reach values of about 6% for long ageing times. As soon as the yield strength increases substantially, the work hardening rate is also observed to shift to much lower values. Subsequently the stress-strain curves appear to be roughly parallel.

Figure 3 present in a similar way the tensile tests results for the AA2196 alloy. When the T351 material is heated to the end of the ramp (EOR sample), the yield strength is observed to decrease, yet to a smaller extent as compare to the AA2198 alloy. This can be related to the only partial dissolution of the δ' precipitates that occurs during the heating ramp. Then the yield strength slowly increases up to 9h at 155°C, although no sign of T_1 precipitation is detected at this stage [8]. Moreover, the stress-strain curves in this ageing time range remain parallel to that of the T351 material and the same serrations are observed, suggesting a similar microstructure. Actually, it has been shown that during these early ageing times the δ' precipitates increased in volume fraction and size due to coarsening of the reverted microstructure present at the end of the heating ramp [8]. Thus the yield strength at this stage seems to be still controlled by the δ' microstructure. The situation starts to change from 24h onwards, corresponding to the observation of T_1 nucleation. Similarly to the AA2198 alloy, several features are observed simultaneously: a sharp increase in yield strength (less pronounced in the AA2196 alloy because the base strength is higher due to the δ' contribution), disappearance of the serrations and decrease of work hardening rate. For longer ageing times a plateau in yield strength is reached at almost 550 MPa, with almost constant work hardening rate as well.

By comparing the behaviour of the two alloys, it appears that the AA2196 alloy has a higher strength and a lower uniform elongation. However it is interesting to evaluate if there is any intrinsic difference between the two alloys in terms of the relationship between these two properties. Figure 4 shows this relationship in the two alloys. As usual, a clear inverse relationship is observed. However, this relationship is markedly different in the two alloys, namely for a given strength the AA2198 alloy has a higher level of uniform elongation as compared to the AA2196 alloy. This point will be addressed during the discussion.

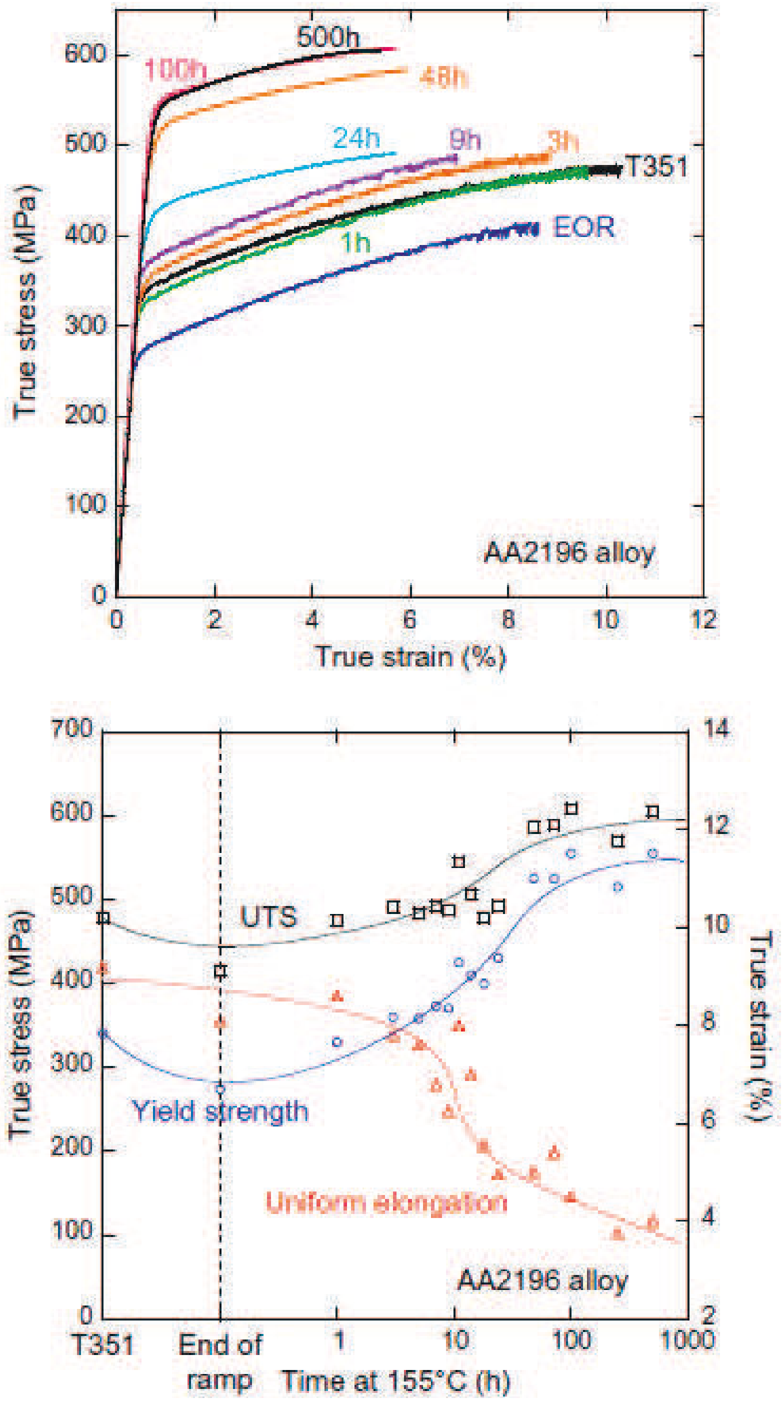

Figure 83: (a) Tensile curves of the AA2196 alloy in different ageing conditions along a heat treatment at 155°C; (b) associated yield strength, ultimate tensile strength (UTS) and uniform elongation.

In a next step it is of interest to evaluate more precisely the evolution of strain hardening as a function of the state of precipitation and alloy, as it can provide interesting information on the dislocation / precipitate interactions [25]. Figure 5 shows the Kocks-Mecking plots [26,27] (work hardening rate $\theta = d\sigma/d\varepsilon$ as a function of reduced stress σ-σ_y) for the two alloys. Both materials show qualitatively the same behaviour, namely:

- for early ageing times (materials that do not contain T_1 precipitates) the work hardening rate behaviour resembles that of other Al alloys when tested in supersaturated solid solution or in a microstructure consisting of solute clusters or GP zones. The initial work hardening rate is high (between 2500 and 3000 MPa, more than twice that of pure Aluminium), as well as the saturation stress (extrapolation of the straight line to zero work hardening rate). Such high strain hardening rate values have received several explanations in the literature, including dynamic precipitation during the tensile test [24] or increased strength of the dislocation / dislocation junctions due to high solute contents [28], resulting in an increased efficiency of dislocation storage. It is worthwhile to note that the AA2196 alloy in these early ageing conditions presents globally a lower strain hardening rate and related saturation stress as compared to the AA2198 alloy, suggesting a detrimental effect of the δ' particles on this property.
- As soon as the T_1 phase appears in significant fraction (10h for the AA2198 alloy and 24h for the AA2186 alloy), the work hardening rate behaviour suddenly shifts to much lower values, and then remains essentially stable. Such a shift is similar to what is observed when precipitating shearable phases such as the η' phase in Al-Zn-Mg-(Cu) alloys [18] or the β'' phase in Al-Mg-Si alloys [23,29]. In these conditions the initial work hardening rate is of similar magnitude as in pure aluminium (namely closer to $\mu/20$ = 1250 MPa).
- When reaching overaged states (particularly the 500h sample) the behaviour is observed to start changing, namely the work hardening rate shows a maximum with respect to the evolution of flow stress. Such behaviour has been numerously observed during overageing of other alloy series [16,18,30]. It may be an indication of a change in precipitate-dislocation interactions. However the magnitude of the increase in early stage work hardening rate is still very small (as compared to what is observed during overageing of Al-Zn-Mg-Cu alloys for instance), so that one can safely conclude that the precipitates remain mostly shearable in these metallurgical states.
- Figure 6 shows the comparison between the two alloys in three metallurgical states: naturally aged (T351), near peak aged and slightly overaged. In all three cases the initial work hardening rate is observed to be somewhat higher in the AA2196 alloy, but as it decreases faster, the saturation stress is lower. This behaviour is consistent with a lower uniform elongation under Considere's criterion.

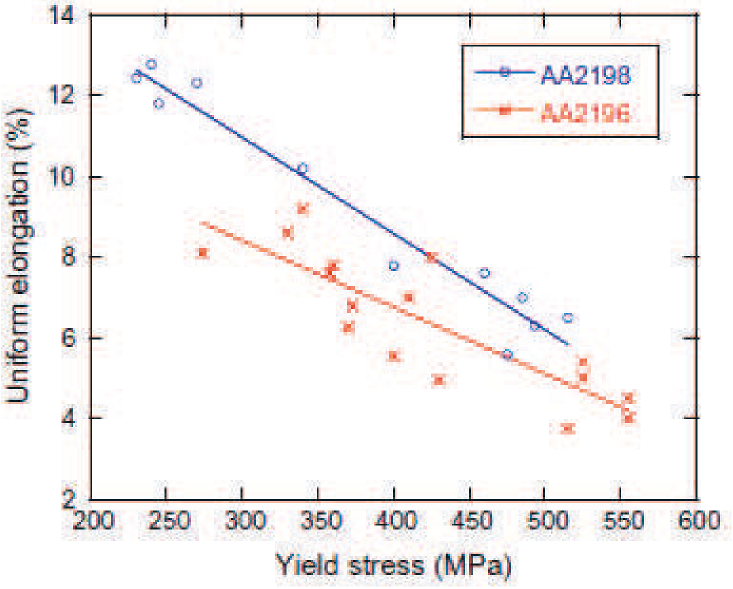

Figure 84: Correlation between uniform elongation and yield stress for the two alloys (data includes all results from figures 2 and 3)

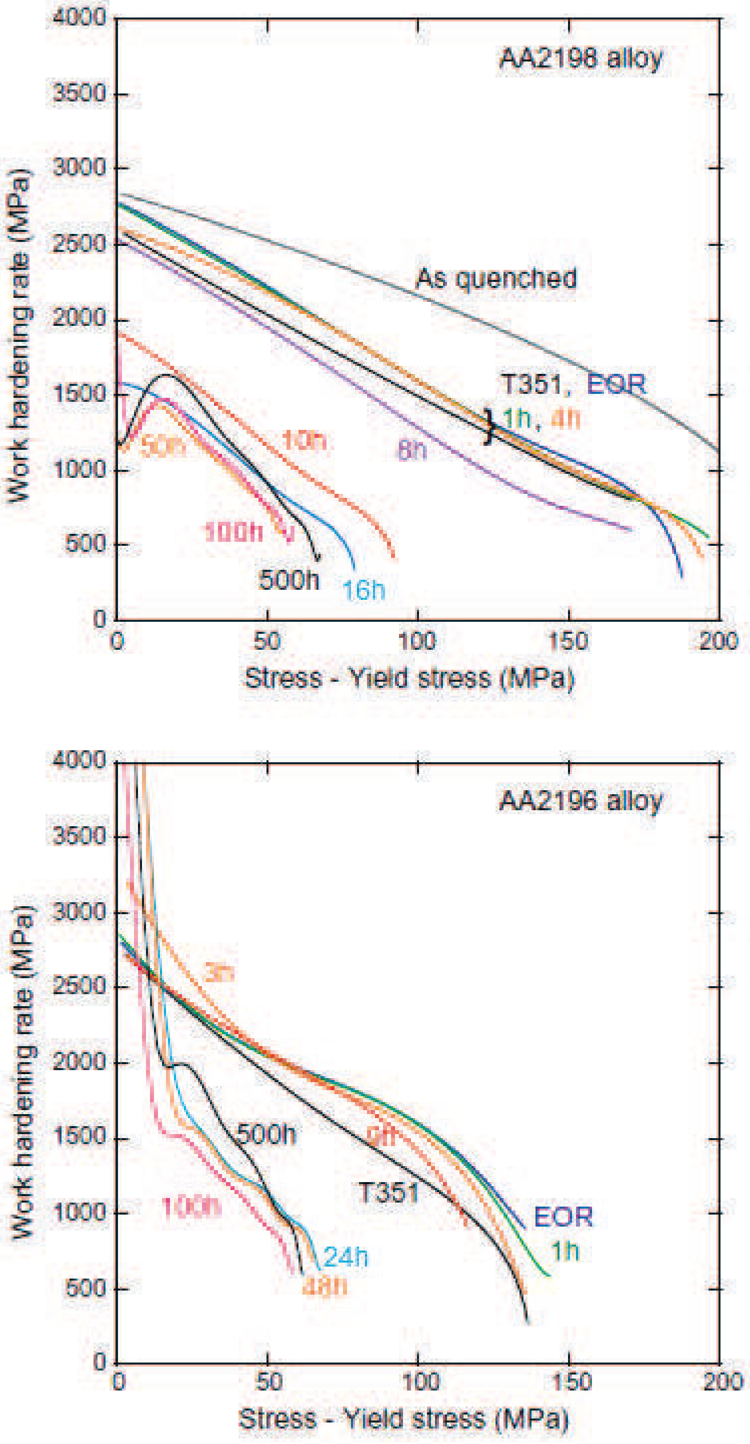

Figure 85: Work hardening rate plots for (a) the AA2198 alloy and (b) the AA2196 alloy in different ageing conditions along the heat treatment at 155°C

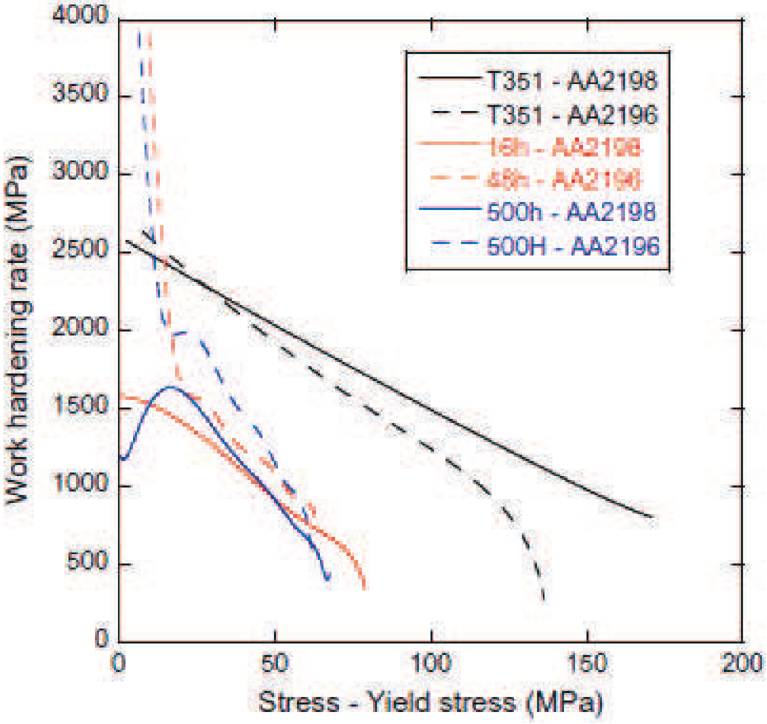

Figure 86: Comparison of the work hardening behaviour of the AA2198 and AA2196 alloys in three ageing conditions: naturally aged (T351), near-peak-aged (16h and 48h respectively) and overaged (500h).

5. Bauschinger tests

For a better understanding of the precipitate-dislocations interactions as a function of precipitate state, Bauschinger tests have been performed on four different metallurgical states: T351, underaged (intermediate T_1 precipitation), near-peak aged and slightly overaged. The samples were strained in tension between 1 and 2% of plastic strain, and then strained back in compression up to about 2% plastic strain. Figures 7 and 8 show the results of these tests (shown in absolute value of flow stress) for the AA2198 and AA2196 alloys, along with the corresponding curves for monotonic tensile deformation. The two alloys show qualitatively the same behaviour. In the T351 state, the Bauschinger effect at the onset of reverse plastic straining is moderate, however when the reverse straining increases some of this Bauschinger effect remains. All other conditions containing T_1 precipitates show a very strong Bauschinger effect at small reverse plastic strains (the yield strength in reversed compression is almost zero), which rapidly disappears after a reverse plastic strain of the order of 1%.

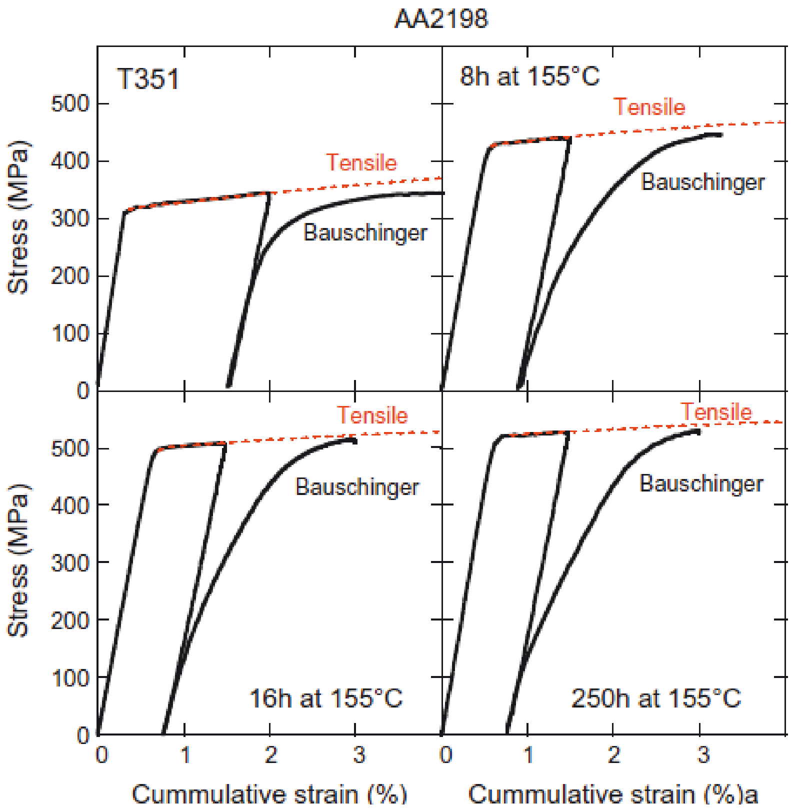

Figure 87: Bauschinger test results for the AA2198 alloy in four ageing conditions, namely naturally aged (T351), underaged (8h at 166°C), near-peak-aged (16h at 155°C) and slightly overaged (250h at 155°C).

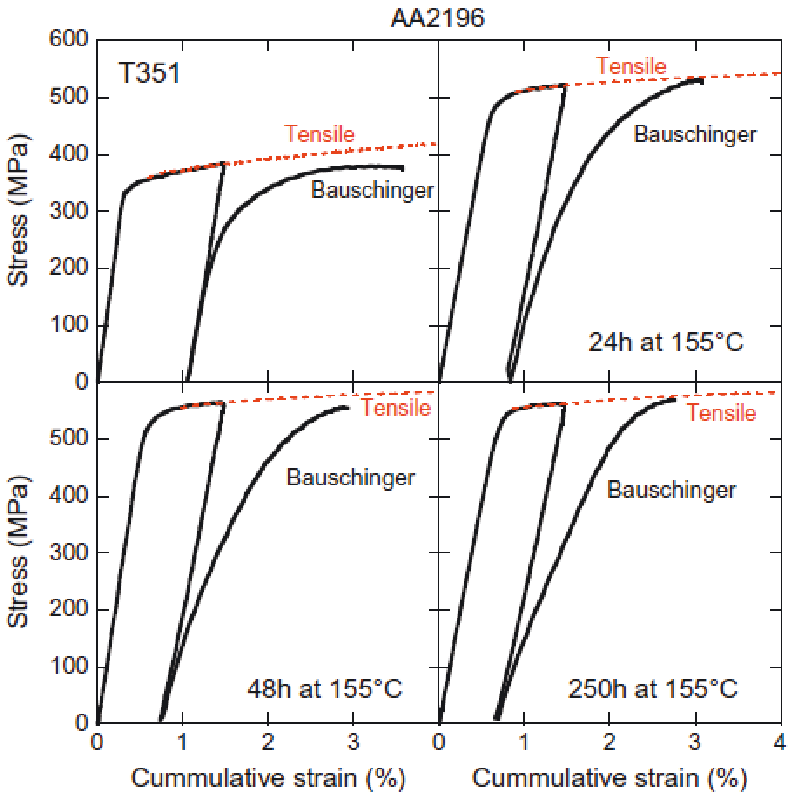

Figure 88: Bauschinger test results for the AA2196 alloy in four ageing conditions, namely naturally aged (T351), underaged (24h at 166°C), near-peak-aged (48h at 155°C) and slightly overaged (250h at 155°C).

This change in the evolution of the Bauschinger effect during reverse straining can be further evaluated by plotting a normalised Bauschinger stress:

$$\sigma_{B,n}(\varepsilon_{rev}) = \frac{\sigma_{tensile}(\varepsilon_{tot}) - |\sigma_{rev}(\varepsilon_{rev})|}{2\ \sigma_{tensile}(\varepsilon_{tot})} \tag{41}$$

where σ_{rev} is the strain of the reverse compression test and ε_{tot} is the total strain. Figure 9 shows the evolution of this normalised Bauschinger stress as a function of reverse strain for the two alloys and the four ageing conditions. As discussed above, in the T351 state the normalised Bauschinger stress is of the order of 20% at the onset of reverse plastic strain, compared to 40% when T_1 precipitates are present. After 1.5% of plastic strain the situation is reversed, with about 4% remaining in the T351 state and no Bauschinger effect left in the other conditions.

The two alloys show a very similar Bauschinger effect. However, the difference of Bauschinger stress in the AA2196 alloy between the T351 state and the states including T_1 precipitates is somewhat smaller as compared to the AA218 alloy.

Schematically, these results mean that the T351 material shows a relatively low tendency to reversible deformation at small strains. This tendency is somewhat larger in the 2196 alloy, possibly related to the presence of δ' precipitates. The Bauschinger effect in the T351 samples at larger reverse strains is less clear. It could be related to the build up of internal stresses due to grain incompatibility, or to unshearable particles such as the dispersoids.

In the ageing conditions where T_1 precipitates are present, the very high value of the initial Bauschinger stress is the sign of a highly reversible strain path. When the reverse strain becomes equal to that of the initial tensile stress, this effect of reversible deformation is cancelled and the flow stress becomes equal to that of a monotonic test of identical total plastic deformation. We will see in section 7 how this behaviour can be related to the details of the precipitate shearing mechanism.

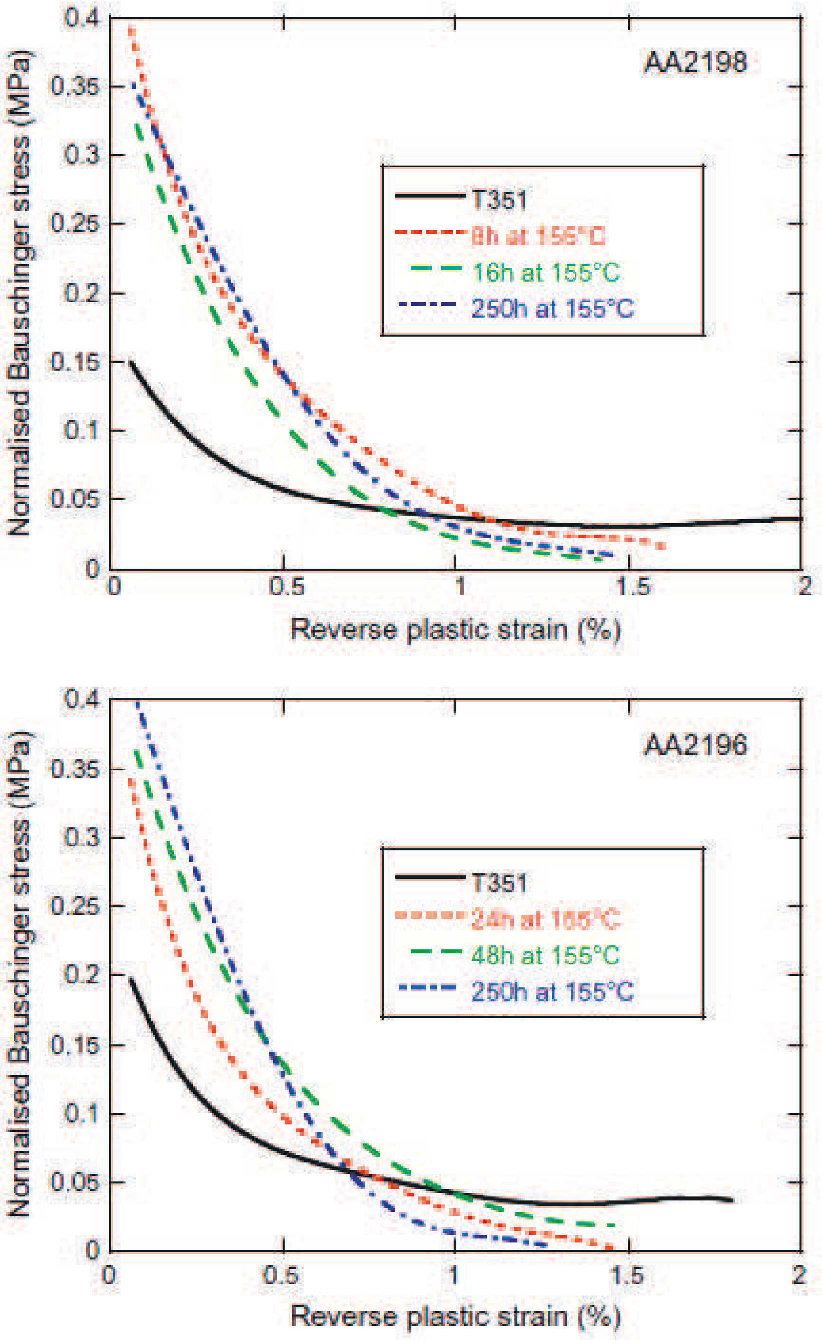

Figure 89: Evolution of the normalised Bauschinger stress (see text for definition) with strain for the two alloys and four ageing conditions presented in Figures 7 and 8.

6. Plastic strain localisation during monotonic deformation

The localisation of plasticity is strongly dependent on the details of the precipitate-microstructure interactions, and it has been proposed before that the tendency for the localisation of plasticity in Al-Cu-Li alloys had a pronounced effect on ductility [9]. Figures 10 and 11 present three dimensional images of the surface of polished samples subjected to 2% plastic strain, obtained by optical confocal microscopy, respectively for the AA2198 and AA2196 alloys in the same four ageing states as for the Bauschinger tests.

In both alloys, the strongest plastic localisation is observed in the T351 states of both alloys, in the form of widely spaced slip lines of large height. When T_1 precipitates are present, the plastic deformation becomes much more homogeneous. The density of slip lines increases and thus their height decreases. This is particularly obvious in the AA2198 alloy, whereas the AA2196 alloy remains with a comparatively more localised deformation until the peak ageing condition. In both cases, however, the most homogeneous deformation is observed in the slightly overaged material.

AA2198

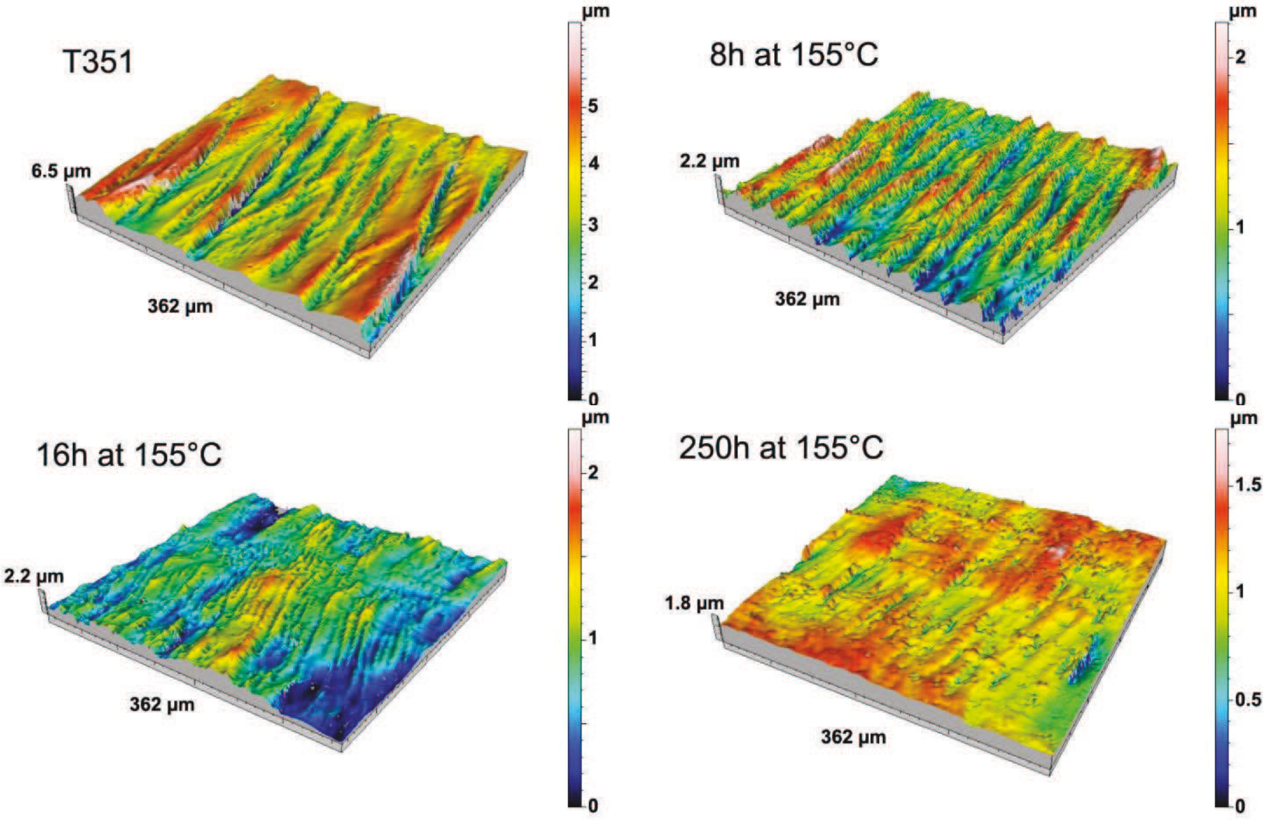

Figure 90: Confocal microscopy images of the sample surface after 10 cycles of low cycle fatigue of the AA2198 alloy in the same four ageing conditions as for the Bauschinger tests

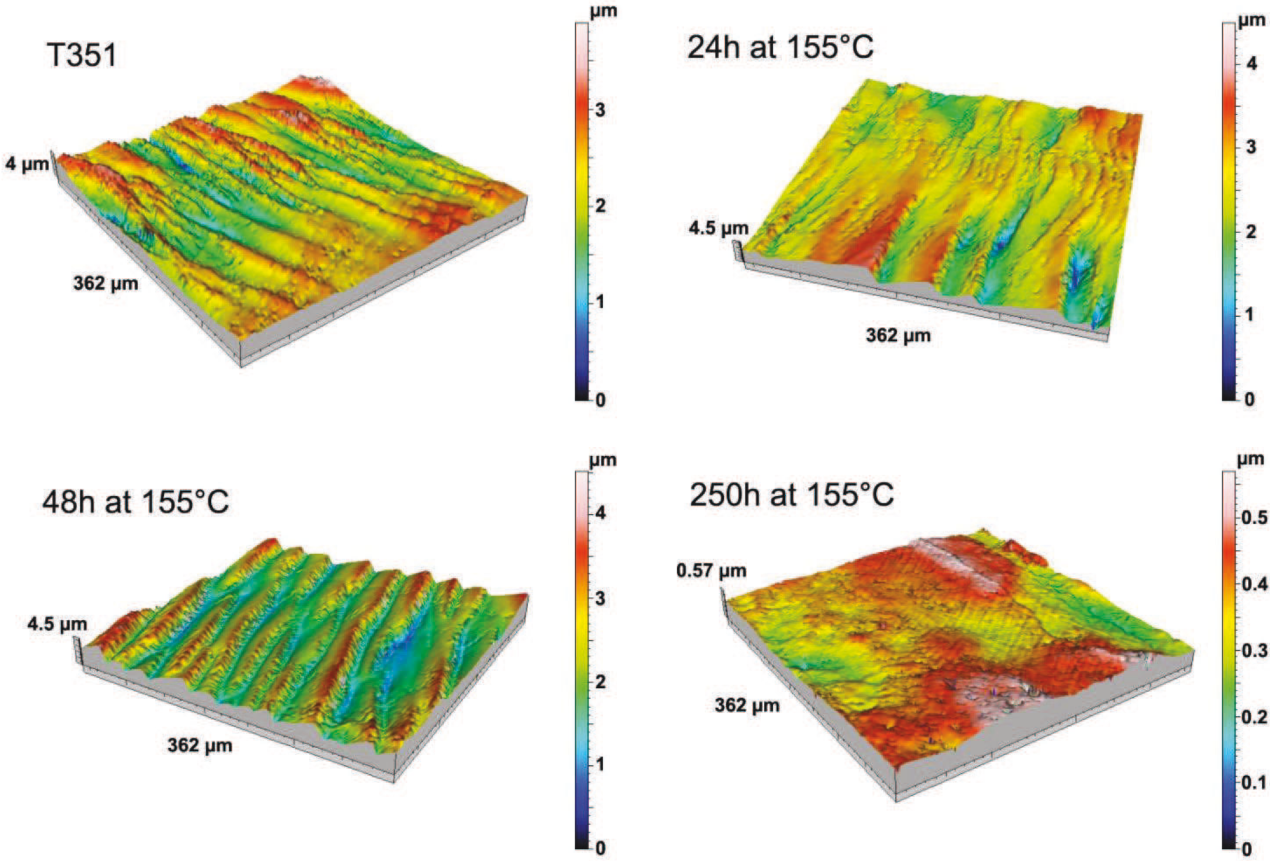

Figure 91: Confocal microscopy images of the sample surface after 10 cycles of low cycle fatigue of the AA2196 alloy in the same four ageing conditions as for the Bauschinger tests

7. Precipitate shearing mechanism

Atomic resolution STEM-HAADF observations have been carried out on the AA2198 alloy aged 16h and subsequently plastically strained 2%, in order to observe the shearing mechanisms of T_1 precipitates. The material was observed both in the <110> and the <112> zone axis. The first axis enables the edge-on observation of two of the four variants of the T_1 precipitates lying on the {111} matrix planes, and in addition makes it possible to observe one of the three families of {100} matrix planes where Cu-rich GP zones and θ' precipitates can be observed. The <112> axis only gives access to one T_1 variant edge-on but gives a better defined view of the structure of this precipitate. In total, more than seventy shearing events of precipitates have been recorded, some of which are shown in Figure 12 (shearing events are shown with a yellow arrow): two images of T_1 precipitates in a <110> axis, two in a <112> axis, and one GP zone sheared in a <100> axis.

In all occurrences, without exception, the shear events were only of one matrix Burgers vector. No multiple shearing events were observed, and no separated precipitates were observed, which would have resulted from their shearing by an avalanche of dislocations.

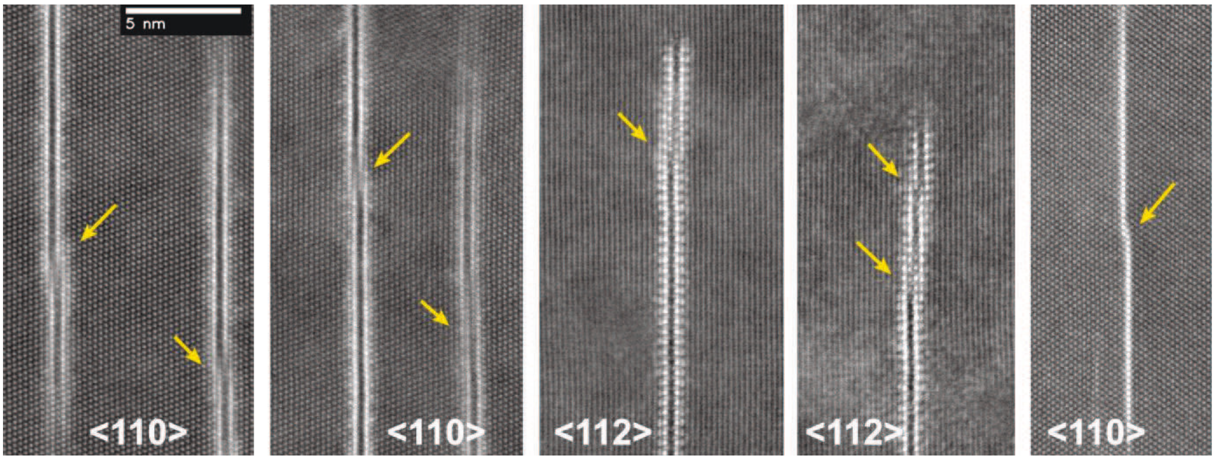

Figure 92: Atomic resolution STEM-HAADF images of sheared T1 (first 4 images) and GP zone (last image to the right) on the AA2198 alloy aged 16h at 155°C and plastically strained 2%. Images taken along <110> or <112> matrix zone axis.

8. Discussion

The results presented above give a complete picture of the effect of precipitation in Al-Cu-Li alloys on the plastic behaviour. Clearly, plasticity in these alloys depends at first order on the presence of T_1 precipitates. On all the phenomena studied here (strain hardening rate, Bauschinger effect, slip localisation), T_1-containnig and T_1-free samples show clearly distinct behaviours. The role of the other main precipitate of this system, namely η', is more to alter the behaviour within a group than to change drastically the plasticity behaviour. The δ' and T_1 precipitates seem to have a different effect on the plasticity of the studied alloys. δ' precipitates have been known for a long time to favour localisation of plastic flow, shear banding and early fracture. Actually, the δ' containing alloy (AA2196) shows a lower ductility at constant yield strength (indicated by uniform elongation) as compared to the δ' free alloy (AA2198). This loss of ductility has been shown to be directly related to a lower strain hardening rate, which can be explained by the tendency of Al_3Li to induce local work softening.

It is now clearly established in the literature that similarly to δ', T_1 is a shearable precipitate, and this has been confirmed by our own observations. However, as opposed to δ', its presence does not result in a tendency to strain localisation. Actually, as soon as T_1 precipitates are formed, plasticity becomes much more homogeneous (as shown by the change in slip line density) than in the cluster- or δ'-containing microstructures. In addition the following features can be related to the presence of T_1 precipitates within the microstructure:

- a strain hardening rate behaviour distinct from that of the other microstructures, but which does not depend on the T_1 characteristics except when overaged
- a very high Bauschinger effect at small reverse strains, which falls down to zero after about 1.5% reverse strain

Thus, T_1 precipitates appear to change the plastic behaviour of the alloys in a very different way as compared to the δ' precipitates. The STEM-HAADF observations made on the AA2198 alloy after 2% plastic strain on the near-peak aged material provide the evidence that the shearing of T_1 plates happens only as single shearing steps. These observations must imply that shearing a T_1 plate again on the same plane would cost more energy as compared to the first shearing event. It is not possible at this stage to know if this energy increment is due to the formation of a very costly atomic arrangement at the interface between the two unsheared halves of the T_1 plate, or to the creation of a highly energetic step at the T_1/matrix interface. If this interpretation is correct, it has numerous implications that explain particularly well our macroscopic observations:

- If multiple shearing events are energetically too costly, shearing happens mostly by single steps and therefore plasticity is homogenised on numerous slip systems. This is compatible with the observations by confocal microscopy that the slip is homogenised when T_1 precipitates are present.
- When reversing the strain (during a Bauschinger test), the single shearing steps can be “repaired” by a reverse motion of the dislocations, if the energy required to heal the shearing step is small as compared to shearing a new step on the precipitate. This would explain the occurrence of plasticity at very small stress during strain reversal, which shows that T_1 precipitates are not strong obstacles to dislocation motion in these conditions. Of course, once a reverse strain comparable to the forward strain is applied, the T_1 precipitates become strong obstacles again and the flow stress comes back to that of monotonic deformation.
- T_1 precipitates, being sheared, are not capable of storing dislocations like non-shearable precipitates would. However, the homogeneity of plastic flow induced by the particular dislocation-precipitate interaction prevents a catastrophic local work softening. As a result, the strain hardening capacity of the peak-aged Al-Cu-Li alloys investigated here is relatively high for a high strength material containing shearable precipitates. Figure 13 shows the strain hardening behaviour in a Kocks-Mecking plot and the stress-strain curve following the yield stress for the AA2198 alloy in the near-peak aged condition and in an AA7449 alloy (Al-Zn-Mg-Cu) in a similar condition (data extracted from [18]), except that the shearable precipitate in this alloy is η' instead of T_1. The yield stress in the AA7449 is somewhat higher than in the AA2198 but still of similar value. Despite a longer elasto-plastic transition in the AA7449 alloy, its overall strain hardening capability is much lower than that of the AA2198 alloy. Particularly, the rate of decrease of the strain hardening rate with either increasing strain or stress is particularly fast, resulting in early fracture and suggesting, in this case, a strong tendency for strain localisation related to massive precipitate shearing. This comparison further validates the interpretation of our results on the T_1 containing materials as a particular case of “only once” shearable precipitate.

A few more points still deserve some discussion. The first is the behaviour of underaged materials, and particularly the naturally aged states. The two alloys in the naturally aged conditions present very different microstructures, either consisting of Cu-rich clusters for the AA2198 alloy or of δ' precipitates in the AA2196 alloy. However these two materials present a similar plastic behaviour, namely a high strain hardening capability (consistently with most naturally aged precipitate-forming Aluminium alloys), a strongly localised plasticity (as evidenced by the confocal microscopy observations) and a mild Bauschinger effect, which however survives to larger reverse strains than in the T_1-containing microstructures. The localised plasticity is to be expected from the presence of small, ordered precipitates, which can be sheared multiple times by dislocations and eventually dissolved (as has been numerously evidenced during fatigue of Al-Li alloys). According to Gerold [31], cluster forming alloys present the same tendency to localised planar slip as compared to alloys presenting short range order or ordered precipitates. It is therefore not surprising to see a similar behaviour in the two alloys in the naturally aged condition. This tendency to localised planar slip is certainly compatible with a moderate Bauschinger effect, since the strain path must be less reversible when plasticity is strongly localised, and with the persistence of this Bauschinger effect to relatively large reverse strains, which can be the signature of grain-to-grain internal stresses caused by incompatibilities of localised strain. When a detailed comparison is made between the two alloys, it appears that the δ'-containing microstructure shows a lower capability of strain hardening. This suggests, not surprisingly, that δ' brings overall a higher sensitivity to strain localisation.

Similarly, one finds this effect of δ' precipitates on strain hardening and, as a consequence, on ductility throughout the ageing conditions tested in this study. Namely, the AA2196 material containing δ' precipitates (regardless of the presence of T_1 precipitates) always presents a lower strain hardening capacity as compared to the AA2198 material that does not contain these particles. And although the AA2196 alloy is capable of reaching a higher yield strength, the compromise between yield strength and ductility is better in the AA2198 alloy. Thus it appears that the presence of the δ' phase, even in conjunction with the T_1 phase that improves the homogeneity of strain, changes the plasticity of the alloy unfavourably.

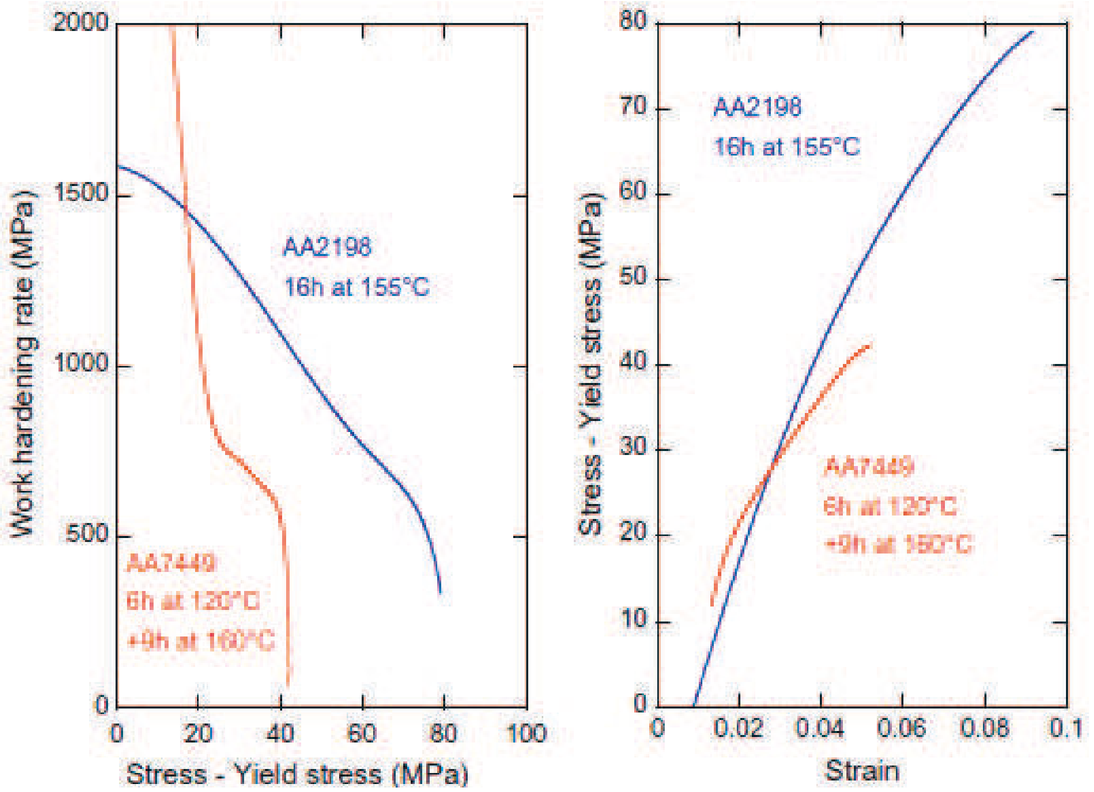

Figure 93: Comparison between (a) the strain hardening behaviour and (b) the stress-strain curve after yield stress, of the AA2198 alloy in the near-peak aged condition and of an AA7449 alloy in the near-peak aged condition containing mostly δ' precipitates.

Finally, the study of strain hardening in the overaged materials suggests that an evolution of the precipitate-dislocation interactions is starting to occur. The increase of the initial strain hardening rate and the appearance of a maximum in the Kocks-Mecking plots is similar to what is observed in other Aluminium alloy series when a transition to non-shearable precipitates occurs (7000 or 6000 series). However here the effect is very small, especially when compared to heavily overaged 7000 series alloys. Thus one can expect that the precipitates, even in these slightly overeaged states, are still mostly shearable, and that the change in dislocation-precipitate interaction occurs only for a limited fraction of the precipitates, possibly those whose thickness has most increased. However, there does not seem to be a simple relationship between an increase of precipitate thickness and a change in dislocation / precipitate interaction mechanism, as sheared T_1 of relatively large thickness (several nm) have been observed in the literature before [14].

9. Conclusion

In this work the plastic behaviour of two Al-Cu-Li alloys has been systematically investigated for a wide variety of microstructures containing a combination of solute clusters, δ' ordered precipitates and T_1 platelet precipitates. The plastic behaviour of these alloys can be divided in two groups of samples, T_1-containing and T_1-free. The presence of δ' precipitates has a significant yet secondary effect. The main conclusions are summarized below:

- Samples containing clusters or δ' precipitates, but no T_1 precipitates, show a high strain hardening rate, a strong tendency to strain localisation, and a moderate Bauschinger effect. The high strain hardening rate is attributed to the high solute content of these alloys, and the localisation of plasticity as well as the Bauschinger effect can be interpreted in terms of the presence of ordered precipitates or clusters in the microstructure.
- Samples containing T_1 precipitates show a lower strain hardening rate, yet much larger than in other Aluminium alloys with shearable precipitates. Plasticity in these materials is much more homogeneous, and they present a very high Bauschinger effect at the onset of reverse plasticity, sign of a highly reversible plasticity.
- From the atomic scale observation of the shearing mechanisms of the T_1 precipitates, it is proposed that the shearing of T_1 precipitates occurs by single shearing events, supposedly related to a high energy cost of a second shear on the same slip plane. This peculiar feature of the precipitate shearing explains all the mechanical tests results, and particularly the good plastic properties of these alloys near peak strength.
- When δ' precipitates are present concurrently to the T_1 precipitates, the plastic properties are somewhat degraded: the material presents a lower strain hardening rate, related ductility and a higher tendency to strain localisation.

Acknowledgements

Dr. J.C. Ehrström and Dr. C. Sigli are thanked for continued support and discussions during this project. Pr. P. Guyot is thanked for fruitful discussions. The French research agency (ANR) is thanked for financial support under the project ALICANTDE. The European Research Council is thanked for financial support in the framework of the NEMOLight Marie Curie International Outgoing Fellowship within the 7th European Community Framework Programme. M.W. wishes to acknowledge the use of the facilities in the Monash Centre for Electron Microscopy (MCEM) and financial support of the Australian Research Council (LE0454166) for funding for the Titan^3 instrument. Dr. S. Richard is thanked for helping with the confocal microscopy experiments.

10. References

[1] Lequeu P, Smith KP, Danielou A. J. Mater. Eng. Perform. 2010;19:841-847.

[2] Danielou A, Ronxin JP, Nardin C, Ehrström JC. In: Proceedings of the 13th International Conference on Aluminium Alloys. Pittsburgh, PA: TMS, Warrendale, USA, 2012. p. 511-516.

[3] Boselli J, Bray G, Rioja RJ, Mooy D, Venema G, Feyen G, Wang W. In: Proceedings of the 13th International Conference on Aluminium Alloys. Pittsburgh, PA: TMS, Warrendale, USA, 2012. p. 581-586.

[4] Warner T, Ehrström JC, Chenal B, Eberl F. Light Metals Age 2009;67:3-5.

[5] Gable BM, Zhu AW, Csontos AA, Starke EAJ. J. Light Met. 2001;1:1-14.

[6] Donnadieu P, Shao Y, De Geuser F, Botton GA, Lazar S, Cheynet M, De Boissieu M, Deschamps A. Acta Mater. 2011;59:462-472.

[7] Dwyer C, Weyland M, Chang LY, Muddle BC. Appl. Phys. Lett. 2011;98:201909.

[8] Decreus B, Deschamps A, De Geuser F, Donnadieu P, Sigli C, Weyland M. Acta Mater. 2013;61:2207-2218.

[9] Csontos AA, Starke EA. Int. Journal of Plasticity 2005;21:1097-1118.

[10] De PS, Mishra RS, Baumann JA. Acta Mater. 2011;59:5946-5960.

[11] Brechet Y, Louchet F, Magnin T. J. Mater. Sci. 1990;25:3053-3060.

[12] Lewandowska M, Mizera J, Wyrzykowski JW. Mat. Charact. 2000;45:195-202.

[13] Howe JM, Lee J, Vasudévan AK. Metall. Trans. A 1988;19A:2911-2920.

[14] Nie JF, Muddle BC. Mat. Sci. Eng A 2001;319-321:448-451.

[15] Dorin T, Deschamps A, De Geuser F, Weyland M. In: Proceedings of the 13th International Conference on Aluminium Alloys. Pittsburgh, PA: TMS, Warrendale, USA, 2012. p. 1155-1160.

[16] Simar A, Brechet Y, De Meester B, Denquin A, Paerdoen T. Acta Mater. 2007;55:6133-6143.

[17] Myhr OR, Grong Ø, Pedersen KO. Met. Mater. Trans. A 2010;41:2276-2289.

[18] Fribourg G, Bréchet Y, Deschamps, A., Simar A. Acta Mater. 2011;59:3621-3635.

[19] Da Costa Teixeira J, Bourgeois L, Sinclair CW, Hutchinson CR. Acta Mater. 2009;57:6075-6089.

[20] Proudhon H, Poole WJ, Wang X, Brechet Y. Phil. Mag. 2008;88:621-640.

[21] Decreus B. PhD thesis, Institut Polytechnique de Grenoble, France, 2010.

[22] Deschamps A, Esmaeili S, Poole WJ, Militzer M. J. de Phys. IV 2000;10:151-156.

[23] Esmaeili S, Cheng LM, Deschamps A, Lloyd DJ, Poole WJ. Mat. Sci. Eng. A 2001;319-321:461-465.

[24] Deschamps A, Bley F, Livet F, Fabregue D, David L. Phil. Mag. 2003;83:677-692.

[25] Embury JD, Poole WJ, Lloyd DJ. Mat. Sci. Forum 2006;519-521:71-78.

[26] Kocks UF. J. of Eng. Mater. and Techn. 1976;98:76-85.

[27] Kocks UF, Mecking H. Prog. Mater. Sci. 2003;48:171-273.

[28] Da Costa Texeira J, Brechet Y, Estrin Y, Hutchinson C. In: Proceedings of the 12th International Conference on Aluminium Alloys. Yokohama, Japan: Japan Institute of Light Metals, 2010. p. 536-541.

[29] Poole WJ, Wang X, Lloyd DJ, Embury JD. Phil. Mag. 2005;85:3113-3135.

[30] Fazeli F, Poole W, Sinclair C. Acta Mater. 2008;56:1909-1918.

[31] Gerold V, Karnthaler HP. Acta Metall. 1989;37:2177-2183.

Appendix III: Estimation of the T_1 size distribution and the T_1 volume fraction from TEM measurements

In this PhD work, Transmission Electron Microscopy (TEM) has been used as a tool to quantitatively measure the T_1 average size and validate measurements obtained with other techniques such as Small Angle X-ray Scattering (SAXS). However, the TEM technique suffers from a number of limitations that should be accounted for in order to correct the raw data. Indeed, a TEM image corresponds to a 2D projection of a 3D structure and thus it may give a false impression of the actual precipitate morphology. Furthermore, the sample thickness has a direct influence on the observed projections and therefore biases the size distribution. As a consequence, we have established a systematic correction procedure of the T_1 size distribution in the AA2198 alloy, in order to account for the limitations inherent to TEM observations. The T_1 volume fraction can then be estimated from the corrected size distribution.

The correction steps will be detailed for two different samples, a peak-aged sample (18h at 155°C) and an over-aged sample (18h at 155°C + 70h at 190°C). The observations were performed in a High-Angular Annular Dark Field Microscope (HAADF-STEM) and Energy-loss spectroscopy was used to estimate the sample thickness.

The Atom Probe Tomography (APT) technique was also used as an alternative way to estimate the T_1 volume fraction.

1. Introduction

Many correction methods have been proposed in order to correct the size distribution of spherical particles when observed in projection on a plane surface [1,2,3]. A complete review of these different methods has been proposed by Underwood [4]. Most correction methods that apply to spherical particles also apply to disc-like particles that are perpendicular to the TEM sample [5] and this is the case of the T_1 plates when observed in the suitable zone axis. The existing correction methods are all based on the same principles. The diameter of a particle as observed in projection on a TEM image is the result of either a particle whose centre is located outside the TEM sample (particle 2 and 3 in Figure 94) or from a particle whose centre is located inside the sample (particle 1 in Figure 94). When the centre of the particle is inside the sample, the projected diameter corresponds to the 'real' diameter of the precipitate and when the centre is outside, the projection differs from the real diameter of the precipitate. The principle of the correction method, presented in this paper, is to identify the particles whose centres are located inside the sample in order to obtain a 'real' diameter distribution. First, the sizes that are measured in projection are divided into a number of classes of size Δ. The initial assumption is to consider that the larger particles have their full diameter visible in projection. For classes of smaller particle sizes, the projection can also result from a slicing effect coming from larger particles. In order for the correction to be accurate, Jensen [5] highlighted that the number of size classes should ideally be more than seven, and at minimum five.

We will first detail the correction method and then apply it to two HAADF-STEM images taken on two different AA2198 samples heat treated respectively 18h at 155°C and 18h at 155°C + 70h at 190°C. We will then show how to estimate the T_1 volume fraction from the corrected size distributions. The influence of the number of size classes on the correction procedure will then be discussed. Finally Atom Probe Tomography (APT) will be used as an alternative way to evaluate the T_1 volume fractions on the two same samples.

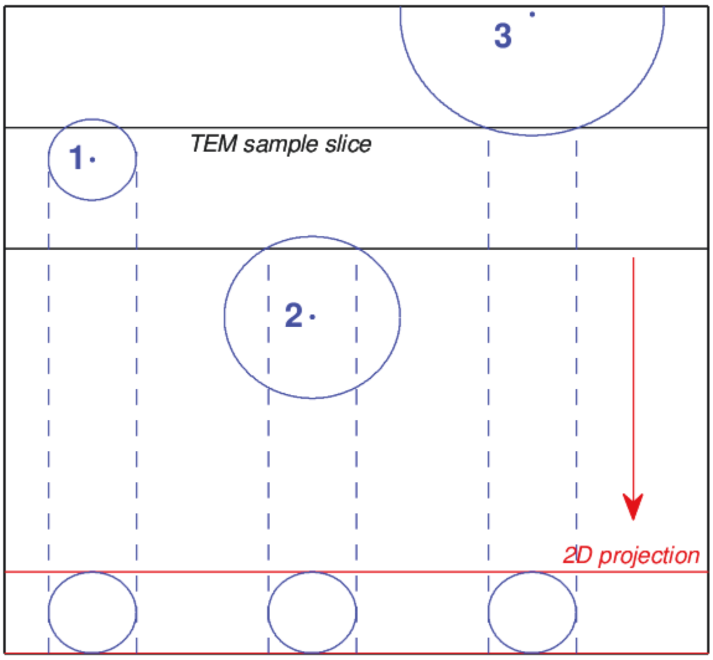

Figure 94: Three spherical particles have different diameters but exhibit a similar diameter in projection due to the intersection effect with the TEM sample. This figure highlights the necessity of applying a correction method to the size distribution obtained with TEM observations.

2. Correction method

The important parameters that are used in this part are defined in the following nomenclature:

k: Number of classes

Δ: Width of a size class (in nm)

t: TEM sample's thickness

D_i: Average diameter of the size class i, $D_i = i * \Delta$

i_{max}: Largest size class

P_j^i: Probability of a particle of diameter D_j to result in a projected diameter D_i

${N_m}^i$: Number of precipitates in a the size class i as measured on the TEM image

${N_c}^i$: Number of precipitates in a the size class i after correction

The measured size distribution can be divided into a number of size classes, k. The width of a class can be determined as follows:

$$\Delta = \frac{d_{max} - d_{min}}{k} \tag{42}$$

where d_{max} is the largest measured length and d_{min} is the smallest measured length.

The initial assumption for the correction procedure is to consider that the largest class of precipitates have their centre located inside the sample and cannot result from an intersection effect. As a consequence, we can write:

$$\text{for } i = i_{max} \quad {N_c}^{i_{max}} = {N_m}^{i_{max}} \tag{43}$$

Precipitates in smaller classes result either from a precipitate that is actually inside the sample or from an intersection effect from a larger precipitate (see Figure 95a). As a consequence, the smaller classes should be corrected from the intersection effect coming from larger size classes. The corrected number of precipitates in the size class i can be estimated as follows:

$$\text{for } i < i_{max} \quad {N_c}^{i} = {N_m}^{i} - \sum_{j>i} ({N_c}^{j} * P_{ij}) \tag{44}$$

As a result, the present method consists in taking away, from the size distribution, the precipitates whose centres are located outside the TEM sample.

In order to simplify the calculations, equation (44) can be re-arranged easily into the following matrix form:

$$\begin{pmatrix} {N_m}^1 \\ \vdots \\ {N_m}^i \end{pmatrix} = \begin{pmatrix} 1 & P_{12} & \dots \\ 0 & 1 & P_{ij} \\ 0 & 0 & 1 \end{pmatrix} * \begin{pmatrix} {N_c}^1 \\ \vdots \\ {N_c}^i \end{pmatrix} \tag{45}$$

Where $N_m = \begin{pmatrix} {N_m}^1 \\ \vdots \\ {N_m}^i \end{pmatrix}$ and $N_c = \begin{pmatrix} {N_c}^1 \\ \vdots \\ {N_c}^i \end{pmatrix}$ are the vectors of the measured and corrected number of precipitates in each class and $P = \begin{pmatrix} 1 & P_{12} & \dots \\ 0 & 1 & P_{ij} \\ 0 & 0 & 1 \end{pmatrix}$ is the probability matrix.

The corrected number of precipitates can thus be deduced such as:

$$N_c = P^{-1} \times N_m \tag{46}$$

We will now explain how to calculate the probability matrix. The probability factor can be defined into two terms such that:

$$P_{ij} = T_j * Q_{ij} \tag{47}$$

The first term, T_j, is the probability that the precipitate's centre is located outside of the TEM sample. Indeed, only a precipitate with the centre located inside a region of width $D_j + t$ can be seen in projection. The probability that the centre is located outside the sample can be written as:

$$T_j = \frac{D_j}{D_j + t} = \frac{\Delta j}{\Delta j + t} \tag{48}$$

The second term in equation (49), Q_{ij}, is the probability that a precipitate in the class j results in a projected diameter in the class i when intersecting a surface (j>i):

$$Q_{ij} = \frac{(h_{i-1} - h_i)}{D_j/2} \tag{49}$$

The h factors can easily be written as (see Figure 95b):

$$\begin{aligned} h_i &= \frac{\Delta}{2}\sqrt{j^2 - i^2} \\ h_{i-1} &= \frac{\Delta}{2}\sqrt{j^2 - (i-1)^2} \end{aligned} \tag{50}$$

As a result, the combination of equation (49) with equations (48) and (50) leads to:

$$P_{ij} = \frac{\Delta j}{\Delta j + t} \frac{(\sqrt{j^2 - (i-1)^2} - \sqrt{j^2 - i^2})}{j} \tag{51}$$

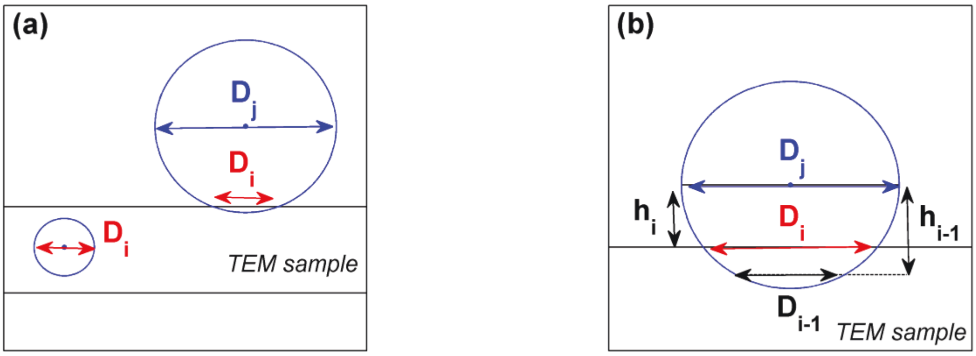

Figure 95: (a) precipitates belonging to the size classes i and j which result in precipitates of the same diameter when projected and (b) zoom on a precipitate of in the j-class which gives a projection in the i-class.

3. Experimental results

3.1 Correction of the size distributions on two AA2198 samples

In order to evaluate the impact of the correction procedure on the size distribution of disc-like particles, we carried out HAADF-STEM observations on two AA2198 samples with different ageing conditions (peak-aged: 18h at 155°C and over-aged: 18h at 155°C+70h at 190°C) (see Figure 96). The observations were carried out in the <110> zone axis where two T_1 variants can be seen edge-on.

Thickness maps were also produced for the same areas, using energy-loss spectroscopy. This technique permits the measurement of t/λ where t is the sample's thickness and λ is the mean free path for inelastic scattering [6]. λ can be expressed such that [6]:

$$\lambda = \frac{106F({}^{E_0}/_{E_m})}{\ln\,(2\beta\,{}^{E_0}/_{E_m})} \tag{52}$$

where $E_0 = 200\ keV$ corresponds to the incident energy, E_m is the mean energy loss ($E_m \approx 19.14\ eV$ for Al-alloys), β is the collection semi-angle and F is a relativistic factor ($F = 0.618$ at 200keV). For large β values, the mean free path saturates and in this case, a reasonable approximation is obtained by using $\beta = 15\ mrad$ instead [6]. In these conditions, the mean free path is found to be equal to 119nm. The sample thickness is found to be around 30nm for both samples. This value is considerably small as compared to the larger precipitates, which can go up to 100nm. However, this value compares to that of the dominant precipitate class. The size histograms, as measured on the TEM images for both samples, are represented in Figure 98. We chose to use 10 size classes. We will justify this choice in part 3.2.

The thickness of the precipitates is also measured. In the case of the sample heat treated for 18h at 155°C, all the T_1 precipitates observed consisted of one unit cell only (single-layer precipitates). However, a distribution in the precipitates' thicknesses was observed in the over-aged sample (single-layer to four-layer precipitates). We define the R_i vector which gives the ratio of precipitates having one to four layers in a given class i:

$$R_i = \begin{pmatrix} {}^{N_{1layer}}/_{N_m{}^i} \\ \vdots \\ {}^{N_{4layers}}/_{N_m{}^i} \end{pmatrix} \tag{53}$$

Where $N_{xlayers}$ is the number of precipitates having x layers. This ratio vector will be used in the next section to estimate the T_1 volume fraction.

The size distributions were corrected following the method described in part 2 and plotted in Figure 99. We can notice that the correction procedure only affects moderately the size distributions. Before and after the correction step, the average T_1 diameter goes from 39.2nm to 41.6nm for the sample heat treated 18h at 155°C and from 42.2nm to 45nm for the sample heat treated 18h at 155°C+70h at 190°C.

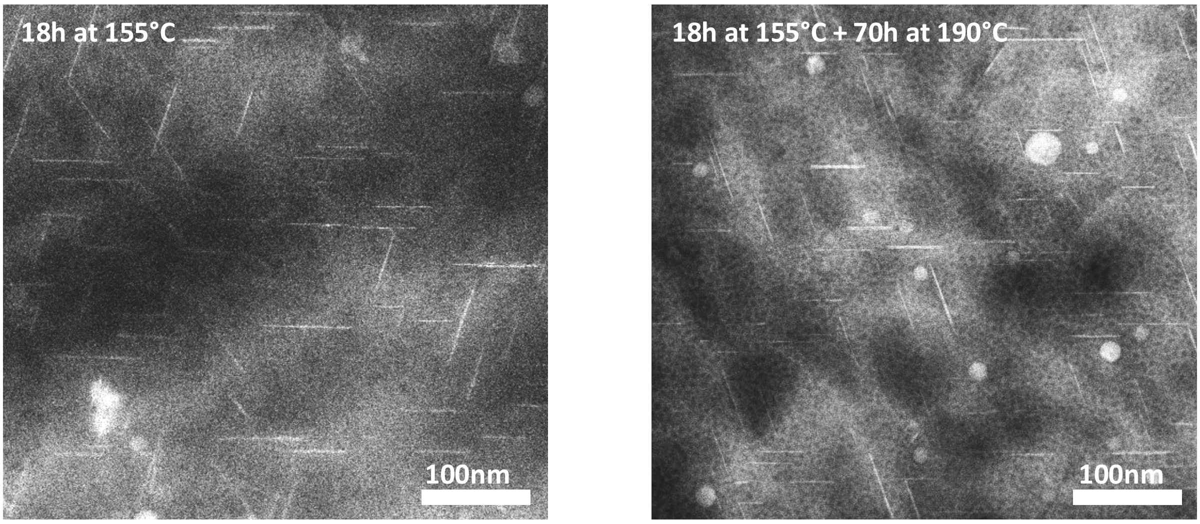

Figure 96: HAADF-STEM images taken along the <110> zone axis on (a) a sample heat treated for 18h at 155°C and (b) a sample heat treated for 18h at 155°C and then for 70h at 190°C.

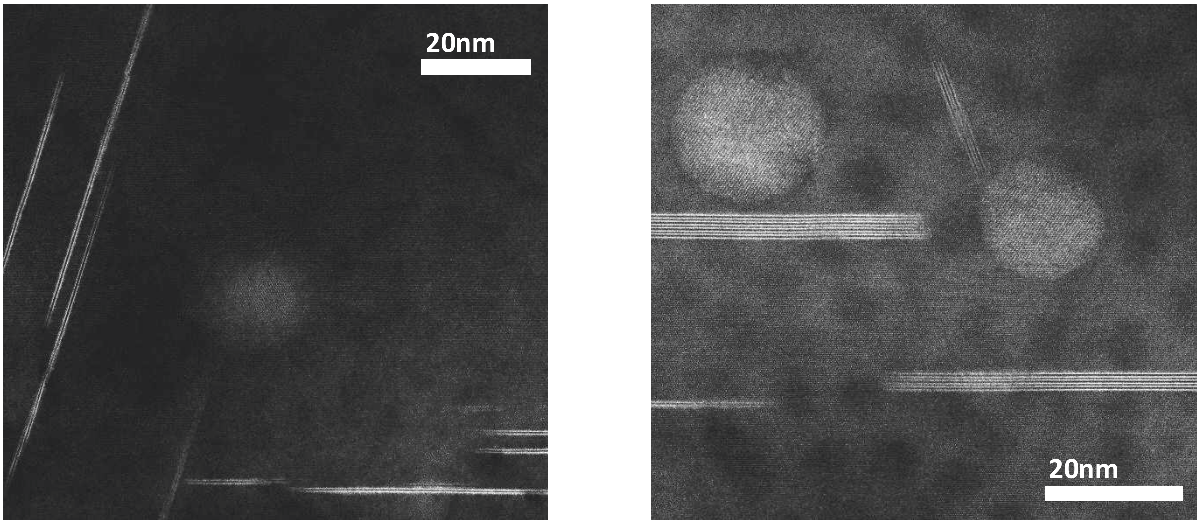

Figure 97: High resolution images performed in HAADF-STEM along the <110> zone axis on (a) a sample heat treated for 18h at 155°C and (b) a sample heat treated for 18h at 155°C and then for 70h at 190°C.

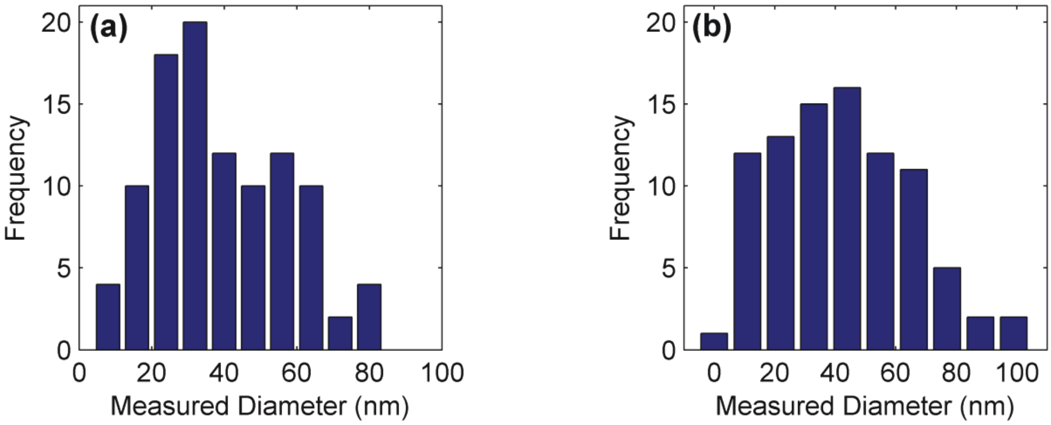

Figure 98: Measured T_1 diameter histograms. (a) sample heat treated for 18h at 155°C and (b) sample heat treated for 18h at 155°C and then for 70h at 190°C.

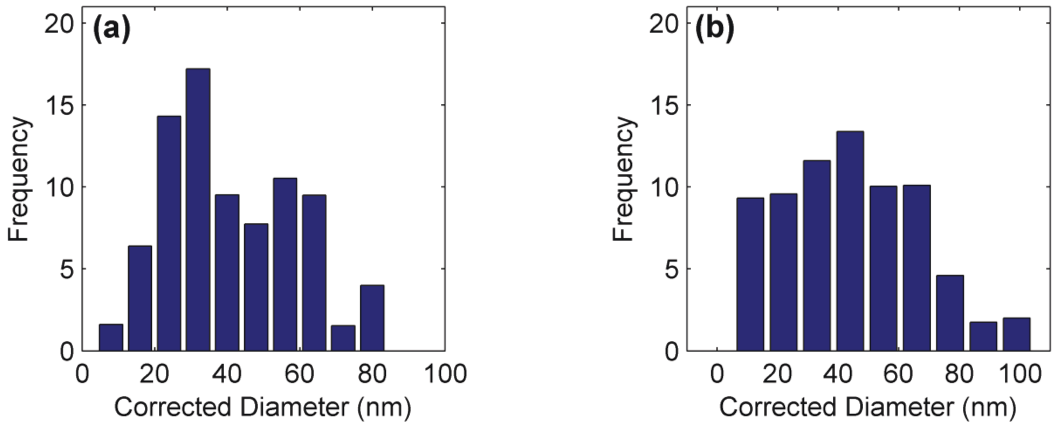

Figure 99: Corrected T_1 diameter distributions. (a) sample heat treated for 18h at 155°C and (b) sample heat treated for 18h at 155°C and then for 70h at 190°C.

3.2 Estimation of the T_1 volume fraction

The size distribution, in Figure 99, corresponds to the precipitates with their centres included inside the TEM sample. The volume fraction f_v of the T_1 precipitates can be defined as follow:

$$f_v = \frac{{V_{T_1}}^{tot}}{\mathrm{V_{sample}}} \qquad (54)$$

Where ${V_{T_1}}^{tot}$ is the total volume of precipitates included inside the TEM sample and $\mathrm{V_{sample}}$ is the volume of the observed area of the TEM sample, which can be written as $\mathrm{V_{sample}} = \mathrm{x} * \mathrm{y} * t$ where x and y are the dimensions of the TEM image. Three different configurations of precipitates have to be considered (precipitates 1, 2 and 3 in Figure 100). In the first configuration (1), the volume of the precipitate is entirely included inside the TEM sample. In configuration (2) and (3), the precipitates are sliced by the TEM sample edges and some of the precipitates are thus lying outside the TEM sample. However, in those two configurations, the volume of the precipitates that is outside the TEM sample is compensated by similar precipitates whose centre is located outside the TEM sample (precipitates 2', 3' and 3''). In terms of volume, we thus consider that V_{T_1} can be calculated as the whole volume of the precipitates after the distribution has been corrected.

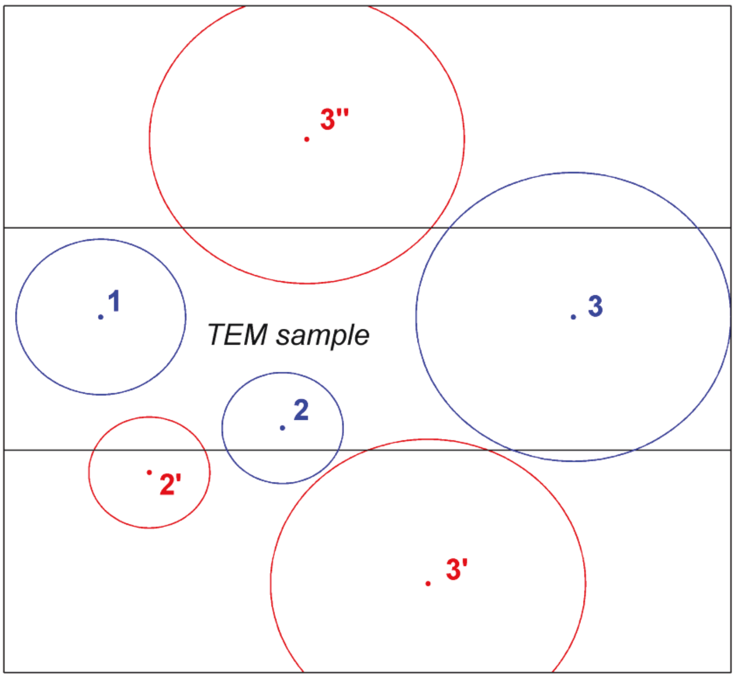

Figure 100: Schematic view of the different precipitate configurations.

The volume of a T_1 precipitate can be defined as follow

$$V_{T_1} = \frac{\pi d^2}{4} T \tag{55}$$

Where d is the diameter and T the thickness of the T_1 precipitate considered. The thickness of a one-layer precipitate can be approximated to the spacing of 5 {111} matrix planes, which corresponds to 1.15nm [7,8]. However, an additional layer of precipitate only adds an additional 4 {111} layers to the precipitates' thickness. As a result the thicknesses of one-layer to four-layer T_1 precipitates are respectively 1.15nm, 2.07nm, 2.99nm and 3.91nm. Considering this, we can now calculate an average T_1 thickness per class by using the ratio vector R_i (equation (53)). The average T_1 thickness for the class i, ${T_{avg}}^i$, can be defined such as:

$${T_{avg}}^i = 1.15 * R_i(1) + 2.07 * R_i(2) + 2.99 * R_i(3) + 3.91 * R_i(4) \tag{56}$$

We can now estimate the volume of the precipitates inside the TEM sample such as:

$${V_{T_1}}^{tot} = \sum_i \frac{\pi {d_i}^2}{4} {T_{avg}}^i \tag{57}$$

The volume fraction that we found, for the two samples presented previously, are respectively 2.6% and 3.6% for the 18h at 155°C and 18h at 155°C+70h at 190°C samples. This evolution of volume fraction was found to be in perfect agreement with the evolution found using the DSC evaluation method in a previous work [9]. In part 3.4, we will present APT results that confirm this evolution.

3.3 Influence of the number of classes on the corrected size distribution

If the correction method is sufficiently robust, the influence of the number of classes on the corrected size distribution should only be minor. We will estimate the impact of changing the number of classes by calculating the T_1 average diameter and volume fraction evolutions as a function of the number of classes. The number of classes was varied from 5, which is the minimum number recommended in the literature to a maximum of 13. The T_1 size distributions for 5 and 13 classes are represented for both samples before and after correction in Figure 101 and Figure 102.

The evolutions of the average T_1 diameter and volume fraction are plotted as a function of the number of classes for the 18h at 155°C and for the 18h at 155°C +70h at 190°C samples in Figure 103. We can see that the diameter and volume fraction stabilizes from 9 size classes. In contrast to what is usually recommended in the literature, we advise to use no less than 9 classes in order for the correction procedure to be accurate. Indeed, a large number of classes is not always favored. For instance, for the 18h at 155°C sample, we can notice that for 13 size classes, the size distribution is uneven and this can affect the correction procedure. We can see that both the average T_1 diameter and volume fraction also start to diverge for 13 size classes. These results justify our previous choice of 10 size classes. The maximum number of size classes should be different in each case depending on the measurement statistics.

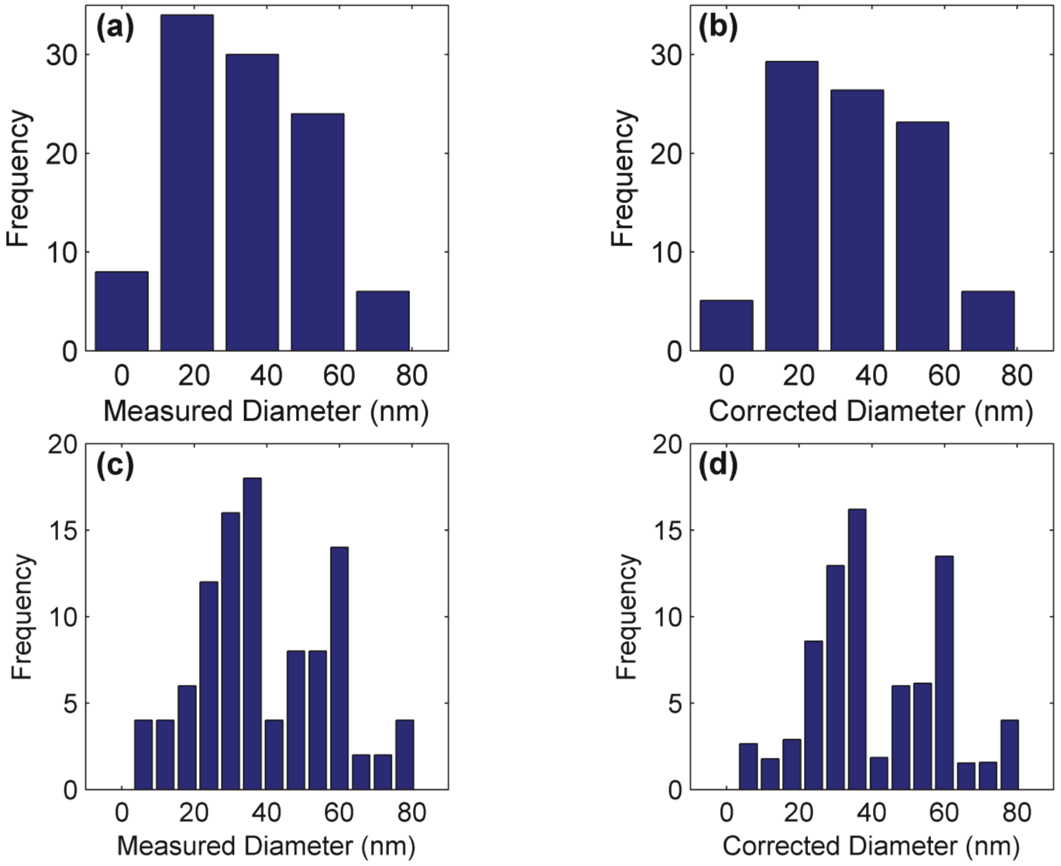

Figure 101: T_1 size distributions measured in HAADF-STEM on a AA2198 sample heat treated 18h at 155°C. (a) 5 size classes before correction and (b) after correction. (c) 13 size classes before correction and (d) after correction.

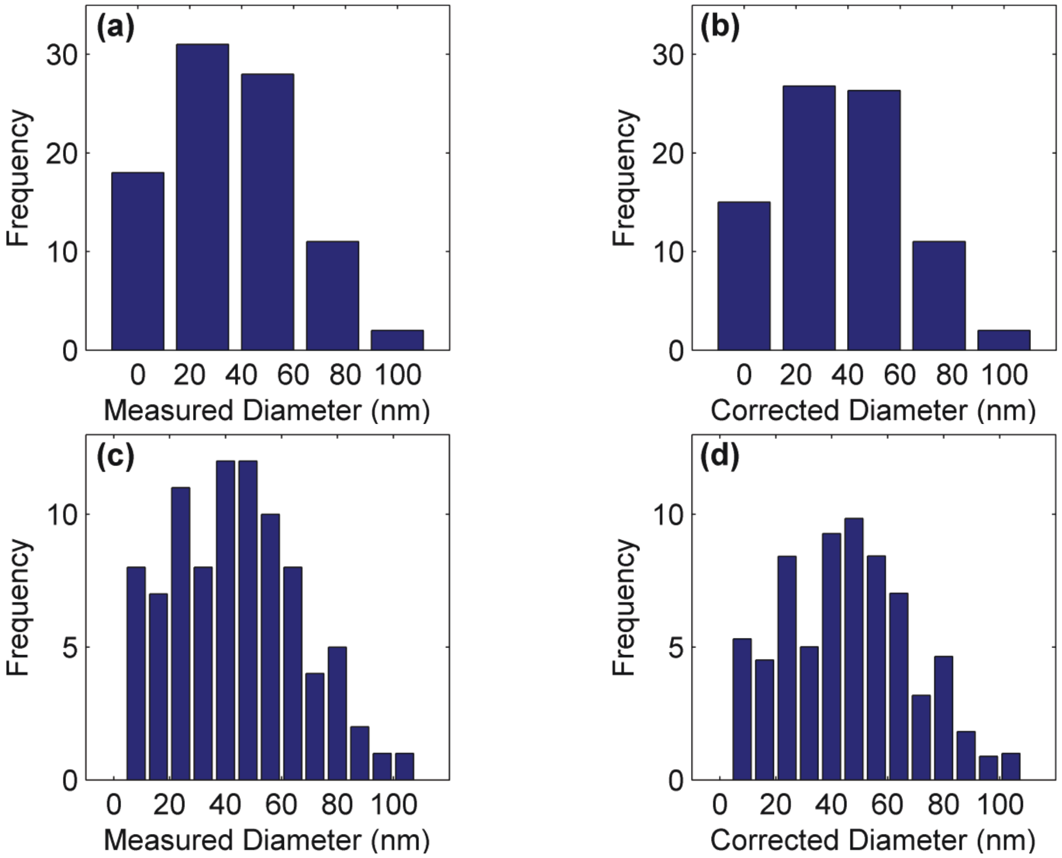

Figure 102: T_1 size distributions measured in HAADF-STEM on a AA2198 sample heat treated 18h at 155°C + 70h at 190°C. (a) 5 size classes before correction and (b) after correction. (c) 13 size classes before correction and (d) after correction.

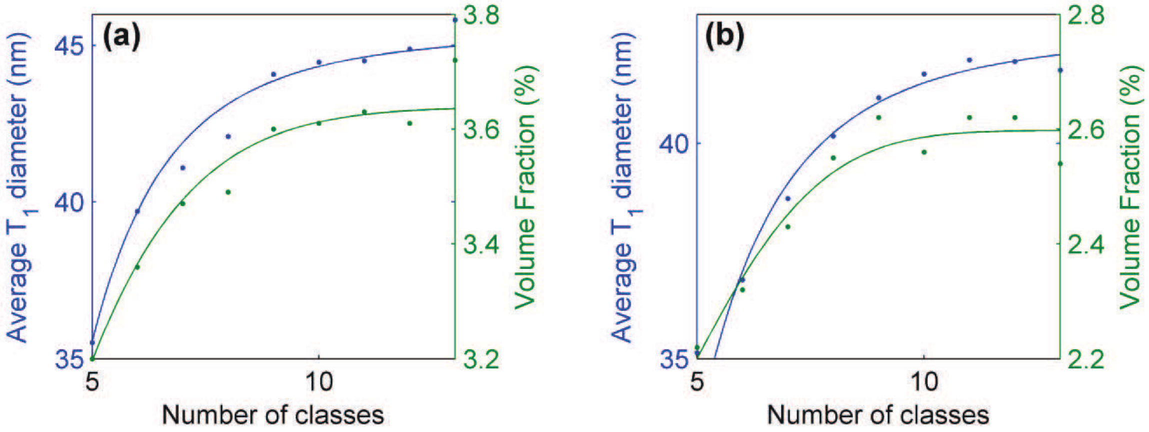

Figure 103: Evolution of the T_1 average diameter and volume fraction as a function of the number of classes for (a) the AA2198 sample heat treated for 18h at 155°C and (b) the AA2198 sample heat treated for 18h at 155°C and 70h at 190°C.

3.4 Alternative method to estimate the T_1 volume fraction: APT measurements

APT can be used as an alternative method to quantitatively estimate the T_1 volume fraction. This technique permits the evaluation of the concentrations of solute elements and the volume fraction of precipitates can then be deduced by making hypotheses on the precipitates' stoichiometry. The two volumes that were measured are represented in Figure 104. Those two volumes can be considered to be only solid solution as they do not highlight local concentration of atoms, which would be a sign of the presence of precipitates. The atomic concentrations found in both samples are displayed in Table 14. The detection of Li suffers from a number of uncertainties inherent to the technique so we will not consider it in our discussion. However, we can deduce a number of things by only looking at the Cu and Mg concentration. The global atomic concentrations in Cu and Mg in an AA2198 alloy were estimated to be respectively 1.35at% and 0.295at%, in a recent APT work [10]. If we now consider that all the Mg goes into the S'-phase of stoichiometry Al_2CuMg, the remaining available Cu is respectively 0.935at% and 1.113at% in the 18h at 155°C and the 18h at 155°C + 70h at 190°C samples. The remaining Cu goes mostly into the formation of the T_1-phase which is pre-dominant but could also go in a lesser extent into Al-cu phases such as θ' or Ω of stoichiometry Al_2Cu. If we first consider that all the Cu goes into the formation of T_1, the resulting T_1 volume fractions would respectively be 3.74% and 4.45%. Those values are higher than the ones found previously in part 3.2. However, a more realistic view is to account for the minor presence of θ'-like phases. If we assume that the results found with the HAADF-STEM observations are correct then it would mean that the volume fraction of θ'-like phases would be respectively 0.84% and 0.63% in respectively the 18h at 155°C and the 18h at 155°C+70h at 190°C samples.

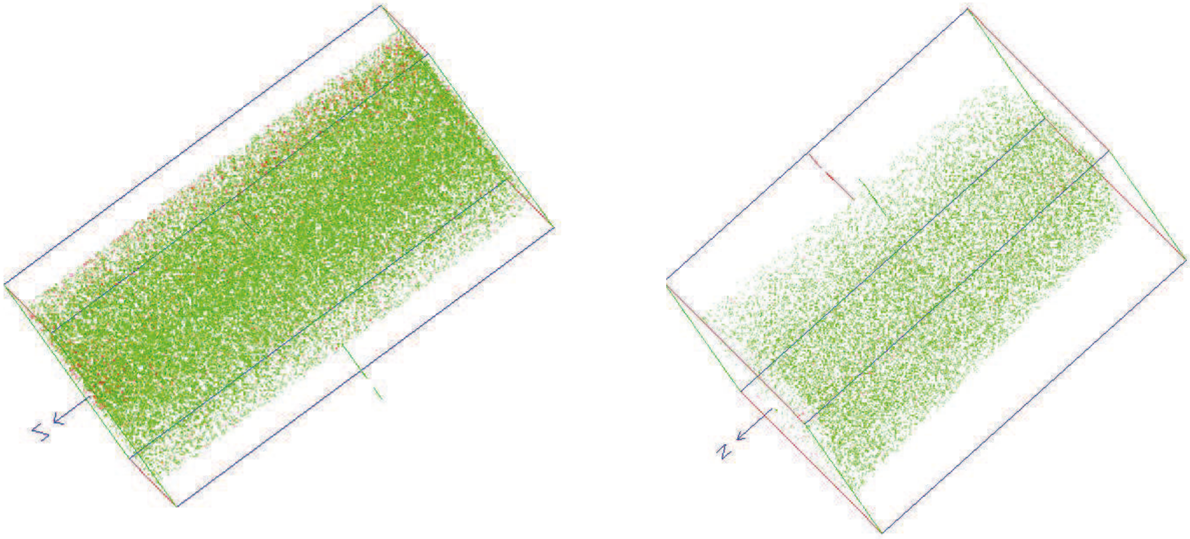

Figure 104: Atomic volumes of AA2198 samples, coming from APT measurements, highlighting the following atoms: Li (green), Cu (red) and Mg (pink). (a) 1,500,000 atoms of a sample heat treated 18h at 155°C and (b) 600,000 atoms of a sample heat treated 18h at 155°C and 70h at 190°C.

Table 14: Concentration in at% of the different elements comprised in the volume shown in Figure 104.

Element	Al	Li	Mg	Cu	Ag
Concentration (at%) 18hat155°C	96.247	3.153	0.209	0.334	0.057
Concentration (at%) 18hat155°C+70hat190°C	96.131	3.537	0.181	0.123	0.028

4. Conclusions

-We presented a successful correction method of the size distribution of disc-like precipitates as measured from TEM images. This method accounts for the sample’s thickness.

-No less than nine size classes should be used for the correction method to be accurate.

-The combined use of TEM, APT and DSC permits the accurate estimation of the T_1 volume fraction in the AA2198 alloy.

5. References

1. Scheil, A.: Z. Metallk 27, 199 (1935)

2. Schwartz, H. A.: Metals & Alloys, 139-140 (1934)

3. Saltykov, S. A.: Stereometric Metallurgy, 2nd edition. (1961)

4. Underwood, E. E.: Quantitative Microscopy: chapter 6. McGraw-Hill Book Co., New York (1968)

5. Jensen, D. G.: J. Phys. D.: App. Phys. 28, 549-558 (1995)

6. Egerton, R. F.: Plenum Press, New York (1996)

7. Donnadieu, P., Shao, Y., De Geuser, F., Botton, G. A., Lazar, S., Cheynet, M., de Boissieu, M., Deschamps, A.: Acta Mater. 59, 462-472 (2011)

8. Dwyer, C., Weyland, M., Chang, L. Y., Muddle, B. C.: Appl. Phys. Lett. 98 (2011)

9. Dorin, T., De Geuser, F., Lefebvre, W., Sigli, C., Deschamps, A.: Phil. Mag. in press (2013)

10. Araullo-Peters, V., Gault, B., De Geuser, F., Deschamps, A., Cairney, J.: Acta Mater. in press. (2013)

Mécanismes de durcissement structural par des précipités anisotropes dans un alliage Al-Li-Cu de troisième génération

Résumé

L'alliage AA2198 est un alliage à durcissement structural qui est principalement utilisé pour des applications aéronautiques. La phase anisotrope T_1 - Al_2LiCu est la principale phase durcissante dans ce système. L'objectif de cette étude est de comprendre les mécanismes de durcissement, en termes d'interaction dislocations/précipités, associés à la phase T_1 qui précipite sous forme de plaquettes. La première étape consiste au développement d'une méthode de caractérisation adaptée à la phase T_1 (caractérisation du diamètre, de l'épaisseur et de la fraction volumique des plaquettes). Le traitement thermomécanique est ajusté afin de varier les paramètres de la phase T_1 de manière indépendante et la limite d'élasticité est systématiquement mesuré ce qui permet de mieux comprendre le lien entre la microstructure de T_1 et la limite d'élasticité. La base de données expérimentale qui est générée permet de tester et d'améliorer les modèles de limite d'élasticité existants. Une approche énergétique du mécanisme de cisaillement permet de modéliser de manière précise la limite d'élasticité pour un grand nombre de microstructures. Le mécanisme de cisaillement permet d'expliquer la décroissance en limite d'élasticité après le pic de durcissement. L'observation des phénomènes de plasticité associés à la phase T_1, par l'étude des bandes cisaillements et du comportement en écrouissage, est la dernière étape de ce travail. L'ensemble des résultats permet d'identifier une transition cisaillement/contournement qui intervient longtemps après le pic de durcissement.

Strengthening mechanisms associated to anisotropic precipitates in an Al-Li-Cu alloy of third generation

Abstract

The age-hardening AA2198 alloy is mainly used in aeronautic applications. The anisotropic T_1 - Al_2LiCu phase gives the main contribution to strengthening in this system. The main objective of this study is to understand the strengthening mechanisms in terms of interactions between the dislocations and the T_1 plate-like precipitates. The first step consists in the development of a characterization procedure adapted to the T_1 phase (characterization of the diameter, thickness and volume fraction of the T_1 plates). The thermo-mechanical treatment is adapted in order to vary the T_1 parameters independently and the yield strength evolution is systematically measured and that permits the investigation of the relationship between the T_1 microstructure and the yield strength variations. The experimental data base that is generated allows testing and improving the existing yield strength models. An energetic approach of the shearing mechanisms is used to model precisely the yield strength evolution for a high number of microstructures. The decrease in yield strength after the peak is solely explained by invoking the shearing mechanism. The investigation of the plasticity phenomenon associated to the T1 phase, with the study of the shear bands and of the work hardening behavior, is the last step of this work. A shearing-to-by-passing transition is found to occur for long-over ageing times.